High velocity impact and fragmentation of concrete: Numerical simulation

Von der Fakultät Bau- und Umweltingenieurwissenschaften
der Universität Stuttgart zur Erlangung der Würde
eines Doktor-Ingenieurs (Dr.-Ing.)
genehmigte Abhandlung

Vorgelegt von
Barış İrhan
aus Ankara, Türkei

Hauptberichter: Prof. Dr.-Ing. habil. Joško Ožbolt
Mitberichter: Prof. Dr. Milan Jirásek
Mitberichter: Prof. Dr.-Ing. Jan Hofmann

Tag der mündlichen Prüfung: 26.09.2014

Institut für Werkstoffe im Bauwesen der Universität Stuttgart
2014

Acknowledgements

Difficult is easy. Easy is difficult. Prof. Joško Ožbolt has a very sound understanding of the computational and material science. It is the reason why he is able to solve apparently difficult problems by means of true simple tools. It is not only his great skills in computational mechanics but also his patient, determined and hard-working style that inspired me a lot during the period of our work together. In this respect I feel myself very lucky to be guided with such a good scientist and would like to thank him once more here that he trusted me and created an opportunity for me to do my doctoral study at IWB.

The project on impact and fire is funded by the German Research Foundation DFG. Their support is greatly acknowledged.

I would like to thank Prof. Milan Jirásek. He accepted to become the co-referee for my thesis and helped me a lot to improve the quality of my thesis with his very useful comments. Having Prof. Milan Jirásek as a co-referee was also very meaningful for me as I have studied his papers a lot during my master study at COMMAS. I would like to express my deepest appreciation to Prof. Jan Hofmann for letting me do my doctoral study staying in Turkey.

Josipa Bošnjak was always there to help. Her continuous support and friendship is gratefully acknowledged and will never be forgotten.

It was a pleasure to work with Daniela Ruta, Natalija Bede and Emiliano Sola. They helped me a lot to improve CIF program.

I would like to thank Dr. Goran Periškić for helping me to couple CIF program with MASA.

I would like to also thank Filip Oršanić, Dr. Akanshu Sharma, Marina Stipetić, Cenk Köse, Monika Werner, Gisela Baur, Silvia Choynacki and Kaipei Tian. I enjoyed every moment that we spent together during my visits to Stuttgart.

Finally I would like to express my deepest gratitude to my wife Itır Yeşim İrhan. Her existence in my life has made all what is happening now possible and come true. Without her patience, support and encouragement, it would not be possible to come to an end in this work. Last but not the least, I would like to express my heartfelt love to my little daughter İdil İrhan. Yeşim and İdil, I love you both so much.

Ankara, October 2014
Barış İrhan

Abstract

In this study load-rate dependent behavior of plain concrete has been investigated by means of numerical methods. To accomplish this, a three dimensional explicit Lagrangian finite element program has been developed for the simulation of contact, impact and fragmentation events based on mixed programming approach. In this respect a graphical user interface (GUI) has been developed using C++ programming language to carry out pre- and post-processing tasks. On the other hand, another program has been developed using FORTRAN programming language to carry out finite element computations. Communication in between GUI and FORTRAN program has been established using standard function import/export mechanism.

Microplane material model for concrete has been extended to account for large deformations, rate of loading and thermal effects. Stress locking observed under dominant tensile loading has been addressed by proper relaxation of the kinematical constraint. On the other hand mesh dependency, due to softening behavior present, has been tackled by crack-band regularization.

Kinematical contact constraints in normal and tangential directions have been formulated in both total and rate forms. Predictor-corrector type algorithm has been employed as method of constraint enforcement. Requirements for the exact satisfaction of constraints have been discussed. Mohr-Coulomb type frictional constitutive behavior is adopted in tangential direction. Classical radial return mapping algorithm, frequently used for elastic-plastic materials, has been used to perform constitutive update in tangential direction.

During high velocity contact-impact events, like projectile penetration, motion function loses its regularity around the impact region due to presence of very large deformations. In order to be able to continue simulations staying within Lagrangian framework, such material is simply removed with a technique based on adaptive element deletion. Maximum principal strain has been used as a deletion criterion. Topological data structures have been implemented to keep track of the evolving contact interface during simulations. Furthermore, to accelerate contact search a procedure based on so-called moving contact sphere has been developed.

Predictive capability of the numerical techniques proposed has been assessed by comparisons with some relevant experimental results from literature. Main conclusions have been drawn out and future research directions have been recommended.

Kurzfassung

In Rahmen dieser Arbeit wurde das lastrateabhängige Verhalten von Beton numerisch untersucht. In diesem Zusammenhang wurde ein dreidimensionales lagrangesches Finite-Elemente-Programm für die Simulation von Kontakt- und Impaktverhalten sowie Fragmentierung auf Basis von gemischter Programmierung entwickelt. Unter Anwendung der C++ Programmiersprache wurde eine graphische Oberfläche (GUI) für die Durchführung der Pre- und Post-processing-Aufgaben konzipiert. Ein weiteres Programm wurde für die Finite-Elemente-Berechnungen mit FORTRAN Programmiersprache entwickelt. Die Kommunikation zwischen GUI und FORTRAN-Programm fand durch Standardfunktion Import/Export Mechanismus statt.

Das Microplane-Modell für Beton wurde erweitert, um die großen Verformungen, die Belastungsrate und die thermischen Effekte zu berücksichtigen. Das bei der überwiegenden Zugbelastung beobachtete *„Stress-locking“* wurde durch eine geeignete Relaxation der kinematischen Bindungen vermieden. Die Netzempfindlichkeit, die Aufgrund der *„Softening“* (Erweichung) des Betons entsteht, wurde durch Anwendung der Rissbandmethode berücksichtigt.

Kinematische Bindungen für Kontakt in normaler und tangentialer Richtung wurden in absoluter und anteilmäßiger Form formuliert. Ein Prädiktor-Korrektor-Algorithmentyp wurde für die Durchsetzung der Bindungen angewendet. Die Bedingungen für die exakte Erfüllung der Bindungen wurden angesprochen. Das konstitutive Reibungsverhalten des Mohr-Coulomb-Types wurde für die tangentiale Richtung angenommen. Der klassische radiale Rückprojektionsalgorithmus, der oft für elastoplastische Materialen angewendet wird, wurde für die Durchführung der konstitutiven Aktualisierung in tangentialer Richtung eingesetzt.

Während der Kontakt–Impakt Hochgeschwindigkeitsereignisse, wie z.B. Geschosspenetration, verliert die Bewegungsfunktion ihre Regelmäßigkeit in der Nähe des Impaktbereiches infolge der großen Verformungen. Um die Simulationen in Rahmen des lagrangeschen Verfahrens fortsetzten zu können, wurde dieses Material gelöscht, wobei eine Technik basierend auf der adaptiven Elementlöschung eingesetzt wurde. Die maximalen Zugdehnungen wurden als Löschkriterium verwendet. Topologische Datenstrukturen wurden implementiert, um den Überblick über die entwickelnde Kontaktschnittstelle in Simulationen zu halten. Darüber hinaus wurde ein Verfahren basierend auf der sogenannten beweglichen Kontaktkugel entwickelt, um die Kontaktsuche zu beschleunigen. Die prädiktive Fähigkeit des vorgeschlagenen numerischen Verfahrens wurde durch Vergleich mit einigen relevanten experimentellen Ergebnissen aus der Literatur untersucht. Die wichtigsten Schlussfolgerungen wurden gezogen und künftige Forschungsrichtungen wurden empfohlen.

Contents

1 Introduction

1.1 Scope

Concrete structures, like offshore platforms, nuclear power plants, highway bridges etc., might be exposed to high intensity short duration time dependent loads due to impact, explosion or earthquake during their service life. Therefore it is of utmost importance to understand behavior of concrete under dynamic load in order to develop safety margins that enable the development of design procedures, which are reliable and economical at the same time.

Nowadays with the use of discrete or smeared modeling of cracks, adaptive discretization techniques, contact formulations and some others, complex three dimensional dynamic fracture of concrete structures exposed to time dependent loads, like impact, explosion or earthquake, can be studied in detail up to the complete failure numerically using finite element method. All these techniques are necessary but not sufficient. Still success of such simulations depends primarily on the capability of underlying constitutive equation to model material behavior at macro-scale under such complicated circumstances.

Concrete material undergoes progressive softening due to excessive amount of micro-cracking prior to propagation of macroscopic cracks. In this respect, dynamic response of concrete structures, which manifests itself with the presence of high loading rates, is quite different than their static response. At high rates of loading there are several reasons for this difference:

(i) At high strain rates micro-inertia forces are activated, which increase energy demand for micro-crack growth.

(ii) Due to the presence of water in concrete, viscous forces are activated, which significantly influences the response of concrete at high strain rates.

(iii) Due to the presence of inertial forces, stress state in the material might significantly change. As a consequence, depending upon the intensity of inertial forces, failure mode might change and crack branching could occur.

(iv) Considerable portion of the supplied external power is expended to raise kinetic energy of the material. As a consequence the part available to drive propagation of macro-cracks is reduced, phenomenon known as lateral inertial confinement.

(v) Large volume of structural elements undergo significant level of micro-cracking due to high amplitude stress waves propagating all over the body, even formation of the multiple fracture planes is possible.

(vi) Because of the presence of inertial forces, fracture plane might change and cracks might be forced to go through regions with high strength like those occupied by stiff aggregates.

Without exception, all of the phenomena listed above give rise to increase in energy demand and therefore strengthen the structure. As can be seen, some phenomena are all related with the presence of structural inertial forces. Therefore they can be automatically accounted for by conducting macro or meso-scale dynamic finite element analysis. On the other hand, phenomena summarized by first two items are taking place at micro-scale and, therefore, could only be directly accounted for by performing micro-scale finite element analysis. With the current level of technology, response of concrete structures with huge dimensions can only be analyzed numerically by performing macro-scale finite element simulations. For relatively small structures, like test specimens, meso-scale finite element simulations can be performed to get better insight about the underlying fracture mechanism leading to failure. Strictly speaking, response of a real concrete structure cannot be analyzed by meso and micro-scale finite element analysis at least for now.

Due to limitations mentioned above, micro-cracking, micro-inertia and viscous effects have to be incorporated into a macroscopic constitutive equation. Viscous effects can be handled to great extent by employing linear viscoelastic material models. On the other hand, micro-cracking can be modeled at macro-scale effectively by resorting to damage type constitutive equations. Constitutive equations of this class adopt initial elastic modulus, tensile strength, compressive strength and fracture energy as material parameters. Strengthening due to presence of micro-inertia forces should be reflected at macro-scale as a rate effect because they are activated only for relatively high loading rates and might be neglected otherwise. Normally rate effects are incorporated into the constitutive equations by multiplying each material parameter with a different factor which is a function of strain-rate.

Due to inadequacy of state of the art experimental techniques, it is not possible to establish a sound relationship between strain-rate and rate factor. Therefore theoretical and numerical investigations gain high importance. With numerical analysis it is possible to test range of applicability of different theoretical rate-dependency models. In addition, it is easy to filter out contribution of each factor to the rate-dependent structural resistance. It is only then possible, for example, to study reasons behind the progressive increase in structural resistance which is observed at high loading rates beyond a critical value. Is it due to material rate-dependency, or structural inertia forces, or combination of both? If both what is the contribution of each?

1.2 Objectives

The main objectives of the work are to:

(i) Develop a 3D finite element code to investigate load-rate dependent behavior of plain concrete structures.

(ii) Assess the general predictive capability of the numerical techniques proposed in the finite element code based on the results obtained from numerical simulation of some relevant experiments from the literature.

(iii) To study the role of structural inertia on the response of concrete in case of high loading rates.

(iv) To check whether the rate dependency model based on rate process theory can be used conveniently for full range of loading rates.

(v) To investigate whether material rate-dependency at high-loading rates (impact) plays an important role or can be ignored.

(vi) To confirm that experimental evaluation techniques based on one dimensional elastic wave propagation should at least take into account pre-damaging of material.

1.3 Outline

Thesis involves nine chapters overall. In Chapter-2, issues related with finite element modeling of dynamic fracture of concrete structures will be discussed. Chapter-3 basic principles of continuum mechanics will be given without going into much detail. In Chapter-4, finite element formulation of two-body contact problem will be presented in depth. First, strong and weak form of the governing initial boundary value problem will be discussed. Then concept of finite element interpolation will be motivated based on one dimensional set up. Afterwards, derivation of discrete dynamic nodal equilibrium equations will be given in detail. Explicit time integration scheme employed will be discussed next. This part will be followed by sections related with contact algorithm. In Chapter-5 the rate and temperature dependent microplane constitutive law for concrete and its generalization for finite strains are discussed. The thermo-mechanical coupling will be discussed in Chapter-6. Chapter-7 is devoted to computational tools and procedures used in different parts of the finite element program. First, topological data structures, which have been used extensively in contact and element deletion algorithms, will be presented. Then the idea of adaptive element deletion will be touched upon briefly. Concepts related with contact algorithm employed will be discussed next. Finally, structure of the new finite element program will be highlighted. Numerical case studies will be presented in Chapter-8. Adequacy of the new finite element program will be assessed based on the results obtained from the simulations of modified split Hopkinson bar test (Schuler et al. 2006),

compact tension specimen (CTS) test (Ožbolt et al. 2013b) and projectile penetration test (Cargile 1999). Finally in Chapter-9, main conclusions will be drawn out and further research directions will be recommended.

2 Dynamic Fracture of Concrete: Finite Element Method

In this chapter issues related with behavior and finite element modeling of dynamic fracture of concrete are briefly discussed and overviewed. Alternative approaches are considered and important literature is given.

2.1 Concrete

2.1.1 Tensile Fracture Mechanism

Concrete is the most commonly used construction material. It is so called frictional, quasi-brittle material, which is “strong” in compression and “weak” in tension. For this reason in engineering practice concrete is normally cast with reinforcing bars, which can take up tension and therefore increase the resistance of reinforced concrete (RC) composite against tensile forces. It is a man-made stone-like composite material, produced basically by mixing cement, water and aggregate particles in appropriate proportions. Cement enters into a chemical reaction with water (hydration process) and turns into cement paste (mortar) which hardens and binds aggregate particles together. Concrete gains its full strength in time. It is accepted that approximately 90% of its strength is gained within first 28 days. As the concrete is hardened and gains its strength uniformly distributed flaws are formed due to its heterogeneous structure, like pores in the hydrated cement paste or thermal and shrinkage cracks around large aggregates. Therefore even in its virgin unloaded state lots of defects (micro-cracks) are already present in concrete.

When mechanically loaded, in tension, compression or combination of both, failure of concrete material is initiated by the tensile fracture of most unfavorable micro-cracks, which are normally located at the interface between aggregates and the mortar (Stroeven 1973; Dhir et al. 1974; Mindess et al. 1982; van Mier 1984). Normally regions with high stress concentration are susceptible for the evolution of micro-cracks, like the one around the tip of an existing macro-crack. At this micro-level of observation propagation of micro-cracks can be assumed to be governed well by principles of linear elastic fracture mechanics relative to macro-level. Micro-cracking process can be divided into two consecutive stages as pre-cracking and post-cracking. During pre-cracking stage micro-crack evolution is confined to aggregate interfaces. For this reason material integrity is preserved and load can still be increased. With the increase of load new bond cracks form and those, which already exist, continue to grow along the aggregate boundaries. After a critical level of loading is reached growing micro-cracks infiltrate into the mortar. As a result a region populated with growing micro-cracks is formed. Such a transition region, in which progressive fracturing, propagation and coalescence of micro-cracks take place, is called as fracture process zone (FPZ). Size

of the FPZ is assumed to be a material property. For example its width is several times the maximum aggregate size for concrete (Bažant et al. 1983). After the formation of FPZ, post-cracking stage begins. During post-cracking stage material integrity is rapidly deteriorated. As a result deformation localizes inside the FPZ. As the post-cracking stage comes closer to an end, localized deformation starts rapidly increasing towards the center of the FPZ. Meanwhile width of the FPZ is narrowed. Upon completion of post-cracking stage, stress free crack surfaces form and tip of the existing macro-crack propagates further together with the FPZ. As already mentioned, macro-cracks cannot propagate suddenly while the micro-cracking is still in progress. This is especially true if the size of FPZ is not small as compared with the size of the overall structure.

During micro-cracking process in FPZ, a micro-crack starts to propagate as soon as supplied elastic energy release rate (or stress intensity factor) attains a critical value. For a medium with many randomly located micro-cracks of different size, determination of maximum elastic energy release rate for an individual micro-crack is impossible. Therefore onset of micro-crack propagation cannot be predicted. But what is known is that as soon as the critical value is reached for a micro-crack, it starts to propagate, either in a stable or unstable manner, and micro-stress in a specific region located around it suddenly released (dissipated). On the other hand, macro-stress transmitted through FPZ should not suddenly drop down to zero as the micro-cracking process is still in progress. Instead it is expected first to increase up to a peak during pre-cracking and then gradually reduce down to zero (stress softening) during post-cracking as all the material located inside the FPZ fully relaxes.

Total amount of elastic energy released during micro-cracking process for the creation of a stress free crack surface of unit area and maximum tensile stress that can be transmitted through FPZ during micro-cracking process are both assumed to be macroscopic material properties. They are called as fracture energy and tensile strength, respectively. These two material properties describe the response of material inside the FPZ at macro-level and therefore should be considered as default ingredients of relevant macroscopic constitutive models.

Materials possessing a FPZ, which undergoes progressive softening due to micro-cracking, are called as quasi-brittle. In some situations transversal (shear) deformations develop inside the FPZ in addition to tensile deformations depending upon the relaxation, geometry, loading and boundary conditions. In such a case there is a transition from tensile fracture to mixed mode tensile-shear fracture (Hassanzadeh 1992; Ortiz et al. 1999; de Borst 2002).

2.1.2 Constitutive Modeling

What is observed at the macro-level by looking at the FPZ is that structural integrity is gradually lost and, as a natural consequence, deformation localizes. All these phenomena can be modeled at macro-level by degradation of macroscopic elastic stiffness. Within the framework of continuum mechanics, complete failure process based on tensile (Mode-I) fracture of concrete, as described above, can be modeled successfully to a certain extent by continuum damage mechanics (Lemaitre 1984; Mazars et al. 1989; Ju 1990; Fichant et al. 1999; Pijaudier-Cabot et al. 2001; de Borst 2002) and to a great extent by anisotropic smeared-crack models (Rots et al. 1985; Rots 1988; Oliver 1989; Bažant et al. 1996b; Petrangeli et al. 1996; Jirásek et al. 1998a-b; de Borst et al. 2004).

Among anisotropic smeared-crack models, micromechanically motivated microplane material model is known to perform very well under different loading scenarios (Bažant et al. 1984b, 1988a-b, 2000b; Ožbolt et al. 2001; Pivonka et al. 2004). Microplane material model is not a macroscopic constitutive equation in the classical sense because there is no direct relationship between macro stresses and macro strains as usual. Macro stresses are computed from macro strains in three steps. In the first step total macro strain tensor is projected onto arbitrarily oriented microplanes (kinematic constraint). Microplanes may be imagined to represent weak planes in the microstructure like contact between aggregate and mortar. In contrast to fixed and rotating smeared crack models, decomposition of the strain tensor into concrete and crack parts does not take place at the macro level. Such a split is the natural outcome of the projection step. Since the cracking is resolved at microplane level it is possible to model micro-crack evolution and coalescence to a certain extent. In the second step traction vectors on each microplane are computed from projected strain vectors by employing simple one-dimensional inelastic constitutive equations for each component separately. Finally in the last step macro stress tensor is computed from traction vectors on each microplane through an averaging process based on the equivalence of micro and macro virtual work (Bažant et al. 1986).

2.1.3 Mesh Dependency

During fracture process, energy is dissipated (released) as the stress free crack surfaces open up, i.e. dissipation takes place over the measure of area. However in standard (local) numerical simulations, due to softening behavior present, crack (strain) localizes inside elements and energy is dissipated not over the crack surface but over the volume of element. Then total dissipated energy depends upon the element volume and therefore overall global response turns out to be mesh-dependent. Basically three remedies can be proposed to circumvent this handicap. (i) Crack-band approach (Rashid 1968; Bažant et al. 1983; Mazars et al. 1996; Ožbolt et al. 2002; Červenka et al. 2005; Jirásek

et al. 2012). (ii) Localization limiters (Bažant et al. 1984a, 1992, 1996b, 2002; Pijaudier-Cabot et al. 1987, 2001; Ožbolt et al. 1995; Petrangeli et al. 1996; Jirásek 1999; Jirásek et al. 2001, 2005; Grassl et al. 2006; Giry et al. 2011). (iii) Discrete techniques (Ortiz et al. 1993, 1999; Simo et al. 1993; Camacho et al. 1996; Oliver 1996a-b; Larsson et al. 1996; Dolbow et al. 1999; Ruiz et al. 2000; Wells et al. 2000, 2001; Jirásek 2000; Jirásek et al. 2002; Moës et al. 2002; İrhan 2003; de Borst 2003; de Borst et al. 2004; Linder et al. 2007).

2.1.4 Locking

Independent of whether modeled in a smeared way or discrete way, if the underlying displacement approximation is not able to explicitly account for discontinuous nature of displacement field across the crack faces, spurious stress transfer occurs at later stages of the failure process, i.e. stresses in the bulk material cannot relax down to zero (Rots 1988; Jirásek et al. 1998a; Jirásek 2000; Ožbolt et al. 2001).

In discrete setting one can resort to one of the two finite element formulations, namely cohesive finite elements and finite elements with embedded strong discontinuities, to kinematically model discontinuous displacement field along the faces of a discrete crack. All discrete techniques reserve room for the utilization of discrete traction-separation type material models assumed to be valid along the crack face (Hillerborg et al. 1976; Ortiz et al. 1993, 1999; Wells et al. 2001; de Borst 2003). Just because of this reason, energy dissipation takes place over the crack surface and numerical results turn out to be independent of the mesh automatically. Variational framework is obtained by adding contribution coming from the work of cohesive tractions, transmitted through crack surface, over virtual displacement jumps to standard virtual work expression (extended principle of virtual work). For the simulation of three dimensional dynamic fracture of concrete, the real advantages of formulations based on embedded strong discontinuities over the cohesive finite elements are not very much clear.

Within the context of cohesive finite elements, formation of the discrete cracks is restricted to take place along the element boundaries. As soon as proposed fracture initiation criteria is met, a cohesive finite element is inserted (or activated) along the corresponding element boundary and one or more of its nodes are cloned to enable discontinuous displacement components to evolve across the crack face in a natural way. As is obvious, this process requires finite element topology to be changed as the discrete cracks form and start to propagate and therefore calls for efficient data structures to be present (Martha et al. 1993; Pandolfi et al. 1998, 2002). Formulation results in somewhat constrained crack trajectories, which can be relaxed by supplementing it with adaptive techniques like continuous remeshing (Carter et al. 2000). Method has been used with success in two

dimensional (X.-P. Xu et al. 1994; Camacho et al. 1996) and three dimensional (Ruiz et al. 2000, 2001) fracture simulations.

Finite element formulations with embedded strong discontinuities can be divided into two broad categories, namely formulation based on elemental enrichment (Simo et al. 1993; Oliver 1996a-b) and formulation based on nodal enrichment (Dolbow et al. 1999). In both, standard continuous displacement approximation valid within element domain is enhanced with a discontinuous contribution. Therefore there is no need to adapt finite element discretization as the discontinuity propagates and enters into some other elements, i.e. in principle the initial finite element discretization can be used without any modification during the lifetime of simulation. Both formulations yield complete elements in the sense that they can represent rigid body motions without straining. Therefore they do not lock.

Elemental enrichment strategy results in non-conforming displacement interpolation which permits the condensation of internal parameters, corresponding to jump in the displacement field, at element level. However, in formal Galerkin set up, leading to symmetric formulation, there is an ambiguity in traction continuity along the crack surface, because it is enforced by equating sum of equivalent nodal internal forces at one side of the discrete crack to traction transmitted through it. In general, unless some special conditions are met by the crack geometry, traction obtained in this manner does not necessarily be equal to the one obtained by contracting stress tensor with the crack normal (Jirásek 2000; İrhan 2003). This issue can be resolved by resorting to Petrov-Galerkin type non-symmetric (irrespective of the underlying material model) finite element formulation where traction continuity along discontinuity is enforced in an averaged sense inside element domain (Simo et al. 1990; Jirásek 2000). In elemental enrichment strains on both sides of the crack are fully coupled. Therefore standard quadrature rules can still be used to perform numerical integrations.

In nodal enrichment strategy displacement interpolation is conforming, i.e. displacement jump is interelement continuous. Therefore it is easy to maintain zero displacement jump condition at the crack tip. Traction continuity along discontinuity is enforced globally in a weak sense and therefore it is not possible to condense out additional degrees of freedom assigned to the existing nodes of finite element discretization. Formulation is symmetric provided that the material tangent is also symmetric. Note that for elements cut by discontinuity material tangent is constructed by adding up contributions coming from bulk and cohesive surface. In nodal enrichment strains on both sides of the crack are partially uncoupled. Therefore standard quadrature rules should be modified in order to be able to integrate element contributions accurately.

In the continuum setting displacement field is not only continuous over the bulk material but also along the path of discrete crack. Crack formation (localization) is imitated reducing the material constants in the direction perpendicular to crack usually by resorting to anisotropic continuum smeared-crack models. Localization (crack opening) as well as softening (stress relaxation), in the direction perpendicular to crack, can be successfully modeled without any problem with this smeared approach. However with underlying continuous displacement approximation, resulting finite element formulation is not complete in the sense that it cannot represent rigid body motions without straining. Due to this deficiency in kinematical description, stress locking phenomena can be observed for material models based on continuum approach especially at later stages of failure process where full stress relaxation is expected to occur. If one wants to insist to stay in the continuum framework, some constitutive tricks must then be brought into the play. In the following three different representative examples will be briefly discussed.

In (Ožbolt et al. 2001) standard microplane material model based on kinematical constraint has been further extended to address aforementioned stress locking problem observed at dominant tensile loadings. In this study, this pathological behavior is attributed to the additive decomposition of microplane normal strain component into deviatoric and spherical parts and it is shown that if deviatoric stresses in the direction aligned with crack undergo elastic unloading non-physical lateral expansion is predicted. As a remedy kinematical constraint is relaxed by multiplying microplane strain components with a discontinuity function such that microplane deviatoric stiffness is proportional to the volumetric stiffness throughout the loading process. In a similar way it is ensured that all microplane stress components, deviatoric as well as shear, decay down to zero following the softening branch of constitutive equation at later stages of failure process, i.e. full stress relaxation is possible. However it should be mentioned that the reason for stress locking is more general and originated due to absence of proper kinematical description, which can reflect discontinuous nature of opening crack. If there is no strain in the bulk, there is no need to take any precautions.

In (Jirásek et al. 1998b), crack induced anisotropy has been modeled by rotating crack (RC) model at earlier stages of failure. After the formation of discrete crack, constitutive model is replaced with isotropic scalar damage (SD) model so that full relaxation of all stress components is possible and consequently pathological stress locking is avoided. This hybrid model is called as rotating crack model with transition to scalar damage (RC-SD).

In (Rots 1992), stress locking has been alleviated by deleting elements as soon as cracking strain reaches a critical value. Sudden removal of elements, which still carry some stress and therefore have contribution to the structural system, is not desirable from physical and numerical standpoints.

2.1.5 Rate Dependency

The response of concrete structures depends on time dependent loading through three different effects (Bischoff et al. 1991; Ožbolt et al. 2005b, 2006; Pedersen et al. 2006; Larcher 2009; Pedersen 2010), namely

(1) through the rate dependency of the growing micro-cracks (influence of inertia at the micro-crack level)
(2) through the viscous behavior of the bulk material between the cracks (creep of concrete or viscosity due to the water content) and
(3) through the influence of structural inertia forces which can significantly change the state of stresses and strains of the material.

The constitutive law can account for the first two effects and the third effect should be automatically accounted for through dynamic analysis where the constitutive law interacts with structural inertial forces. Depending on the material type and loading rate, the first, second or third effect may dominate. For quasi-brittle materials, such as concrete, which exhibit cracking and damage phenomena, the first two effects are important for relatively low and medium strain rates. However, for higher strain rates (impact) the last effect dominates.

There are different frameworks for modeling of rate dependent behavior of materials. The rate theory is employed to explain the first two above-mentioned reasons for strain rate sensitivity (micro-cracking and creep) (Mihashi et al. 1980; A. S. Krausz et al. 1988). The theory assumes that crack initiation on an atomic scale is governed by the activation energy, i.e. in a non-stressed material there are the same number of bond-breaking and bond-healing steps in time. When an external force acts on the material there is a surplus of energy, which causes more bond-breaking than bond-healing steps. Since the number of bond-breaking steps is assumed to be constant in time that means that a longer loading time causes more ruptures than a shorter loading time. Expressed in terms of strength, it means that sustained loading and creep causes a reduction of strength whereas very short loading causes an increase of strength. This means high loading rates increase the apparent strength of a material. According to (Mihashi et al. 1980) the increase of strength, compressive, tensile and flexural, can be expressed as

$$f_d/f_s = (\dot{\sigma}/\dot{\sigma}^0)^\alpha \qquad \text{(Eq. 2.1)}$$

where f_d is dynamic strength, f_s is static strength under monotonic load, $\dot{\sigma}$ is the applied load rate in terms of stress under dynamic load, $\dot{\sigma}^0$ is the applied load rate in terms of stress under static load

and α is a parameter dependent on load and type of material and the way of loading. Note that (Eq. 2.1) does not take into account the effect of macro-inertia forces.

The model of (Bažant et al. 2000a) is based on the same principle. Again, the influence of macro-inertia forces is not considered. The influence of the loading rate is divided in two parts: (i) the effect of viscosity and (ii) the effect of strain-rate dependent growth of micro-cracks. A relatively simple visco-elastic model describes the former effect. The influence of the strain-rate dependent growth of micro-cracks on the other hand is based on the theory of activation energy:

$$\sigma(\varepsilon) = \sigma^0(\varepsilon)\left[1 + C_2 \operatorname{asinh}\left[\frac{\dot{\varepsilon}}{C_1}\right]\right] \qquad \text{(Eq. 2.2)}$$

where σ is stress at dynamic load, σ^0 is stress at static load, $\dot{\varepsilon}$ is strain rate, C_1 and C_2 are constants determined from experiments. This model has been used in various forms in the microplane model for concrete (Bažant et al. 2000a; Ožbolt et al. 2006).

Inertia effects at the material macro-level are taken into account in the model of (Reinhardt et al. 1991) and (Lu et al. 2004). The authors look at a cluster of penny shaped cracks in a plane, which is perpendicular to the tensile loading direction. When a crack propagates into the material with a certain velocity the crack faces move. For this movement, the energy balance is computed which is the sum of external work W, deformation energy V, kinetic energy T, fracture energy D, and initial energy E_0 at time t_0, thus

$$-W + V + T + D - E_0 = 0 \qquad \text{(Eq. 2.3)}$$

The faster the crack propagates the larger is the kinetic energy and the deformation energy. The calculations show that the rate of energy supply becomes too high to be absorbed in the fracture process, resulting in an equilibrium in which a major part of the supplied energy is stored as kinetic and deformation energy around the crack tip. That means that the stress distribution around the crack tip changes and the stress intensity factor decreases with increasing loading rate. This is in agreement with (Freund 1972a-b) who predicts that the stress intensity factor even vanishes when the crack propagates with the speed of the Rayleigh wave. The consequence of this result is that the strength of a material increases with loading rate. The rate of strength increase is not constant for all loading rates, but is rather small for low and medium strain rates while there is a steep increase at high loading rates. At very high loading rates the strength increases with the cube root of strain rate (Kipp et al. 1980).

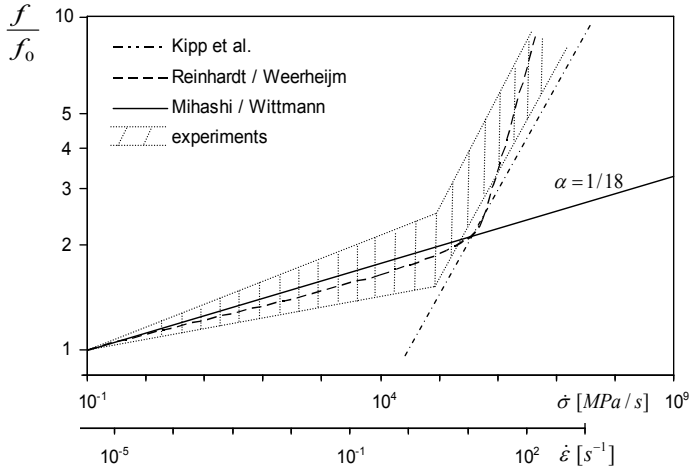

Fig. 2.1 The material resistance as a function of stress- and strain rate:
(a) (Mihashi et al. 1980), (b) (Reinhardt et al. 1991), (c) (Kipp et al. 1980)

The result of several theories is summarized in Fig. 2.1. As can be seen, the total resistance starts to increase progressively for strain rates larger than about $10\ \mathrm{s}^{-1}$. It has been recently demonstrated that for low and medium strain rates up to $10\ \mathrm{s}^{-1}$, the total resistance is controlled by viscosity and strain-rate dependent crack growth (Ožbolt et al. 2005b, 2006, 2011a, 2012, 2013b, 2014). At very high strain rates (impact), on the other hand, the macro-inertia forces dominate and cause progressive increase of structural resistance, having a dominant influence on failure mode and crack propagation (Ožbolt et al. 2005b, 2006, 2011a, 2012, 2013b, 2014).

Theoretical, experimental and numerical studies show that the failure mode, crack pattern and velocity of the crack propagation are influenced by the loading rate (Freund 1972a-b; Ožbolt et al. 2005b, 2006, 2011a, 2013b; Travaš et al. 2009). Principally, with increase of loading rate failure mode tends to change from Mode-I to mixed mode. The responsible for this are inertia forces, which homogenize material in the impact zone and force damage (crack) to move away from the zone of high inertia forces. Therefore, there is a change of Mode-I fracture to mixed mode. Moreover, when crack starts to propagate relatively fast, inertia forces at the crack tip tends to prevent crack propagation. Consequently, single crack split into two inclined cracks (branching), i.e. stress intensity factor at the crack tip decreases with increase of a crack speed.

The velocity of the crack propagation also depends on loading rate. The maximum theoretical crack velocity is equal to Rayleigh wave speed $v_R = C_R(G_c/\rho_c)^{0.5}$ where the constant $C_R$depends on Poisson's ratio, G_c is the shear modulus and ρ_c is specific weight of the material. For normal strength concrete Rayleigh wave speed is approximately equal to $2100\ \mathrm{m/s}$. However, experimental (Curbach et al. 1990), theoretical (Freund 1972a-b) and numerical investigations (Rabczuk et al. 2004; Ožbolt et al. 2011a, 2013b) indicate that a single Mode-I type of crack cannot reach this theoretical

speed of propagation. According to these investigations the maximum crack speed in normal strength concrete is between 500 and 600 $\mathrm{m/s}$. Moreover, after crack speed reaches certain critical value there is crack branching (Freund 1972a-b; Rabczuk et al. 2004; Kožar et al. 2010; Ožbolt et al. 2011a, 2013b).

Due to the complexity of the problem the above phenomena can be studied only numerically. In the numerical modeling, which can be of smeared or discrete type, different constitutive laws and modeling techniques can be used (Rabczuk et al. 2004; Ožbolt et al. 2006; Larcher 2009; Pedersen 2010). The influence of viscosity and strain rate dependent growth of micro-cracks is accounted for by the constitutive law. For this purpose some of the above discussed approaches can be used. The effect of structural inertia forces on the rate dependent crack growth should be automatically accounted for through dynamic analysis. However, it is important that constitutive law and (or) corresponding discretization method employed are able to account for realistic interaction between structural inertial forces and material constitutive law.

2.2 Contact

In experiments like free fall drop weight (X. Zhang et al. 2009), split Hopkinson bar (Schuler et al. 2006) and projectile penetration (Cargile 1999), concrete specimens are loaded by impact of a relatively rigid object. Normally impact events take place in a very short period of time, in the order of milliseconds, and momentum is transferred from one body to another through contact interactions. It is normally very difficult to take precise measurements in this kind of short-period events. For this reason numerical simulations become an attractive tool to gain more insight for such physical processes. Then from the numerical point of view contact problem must be addressed.

Contact interaction imposes some constraints on positions occupied by particles in contact (kinematical constraints) and on forces transmitted in between during contact (kinetical constraints). As is expressed in (Eq. 2.4), contact parasitic potential energy assumes different forms depending upon the method employed to enforce kinematical contact constraints.

$$\pi_c = \begin{cases} \boldsymbol{\lambda} \cdot \boldsymbol{g}_e & \rightarrow \text{Method of Lagrange Multipliers (LM)} \\ \dfrac{1}{2}\epsilon \boldsymbol{g}_e \cdot \boldsymbol{g}_e & \rightarrow \text{Penalty Formulation} \end{cases} \tag{Eq. 2.4}$$

where $\boldsymbol{\lambda}$ is Lagrange multiplier, which in our context corresponds to contact forces, ϵ is penalty parameter, a big number. In (Eq. 2.4), the elastic gap vector is defined as

$$\boldsymbol{g}_e = \boldsymbol{g} - \boldsymbol{g}_p \tag{Eq. 2.5}$$

where $\boldsymbol{g}$ is total gap vector and $\boldsymbol{g}_p$ is the accumulated slip along the tangential direction. Upon successful imposition of contact constraints elastic gap vector $\boldsymbol{g}_e$ is expected to diminish.

Upon differentiation with respect to $\boldsymbol{g}$, expressions for contact force are obtained as

$$\boldsymbol{\tau} = \partial \pi_c / \partial \boldsymbol{g} = \begin{cases} \boldsymbol{\lambda} & \rightarrow \text{LM} \\ \epsilon \boldsymbol{g}_e & \rightarrow \text{Penalty} \end{cases} \qquad \text{(Eq. 2.5)}$$

After taking the variation, contribution of contact to the structural system comes out to be

$$\delta \pi_c = \begin{cases} \boldsymbol{\lambda} \cdot \delta \boldsymbol{g} + \boldsymbol{g}_e \cdot \delta \boldsymbol{\lambda} & \rightarrow \text{LM} \\ \epsilon \boldsymbol{g}_e \cdot \delta \boldsymbol{g} & \rightarrow \text{Penalty} \end{cases} \qquad \text{(Eq. 2.6)}$$

In LM method, contact forces appear as additional unknowns since they are not expressed in terms particle positions via constitutive-like equations. However the system of equations is complete, because one can write as many additional equations as required by employing kinematical constraint equation

$$\boldsymbol{g}_e = \boldsymbol{0} \qquad \text{(Eq. 2.7)}$$

On the other hand, in penalty method (Eq. 2.7) is not directly enforced but used to relate contact forces to particle positions via linear relationship. Then one ends up with standard displacement based formulation, which can be handled in a conventional way. Here the proper choice of penalty parameter is essential such that at the end contact constraints are satisfied within a required accuracy, which is not an easy task to accomplish. Before passing note that hybrid formulations which combine LM and penalty methods are also available (Wriggers 2006).

(Eq. 2.7) states that normal as well as tangential component of elastic gap vector must be equal to zero in case the material particles collide each other. However in conventional approach this simple equation cannot be used, because contact pairs, pairs of particles in contact, are constructed by employing closest-point projection algorithm. By construction, the resulting gap vector does not have any component in tangential direction and therefore cannot be used to enforce kinematical contact constraint in that direction. Then one has to resort to another kinematical quantity. The natural choice of course is to switch to the rate in tangential direction. Then kinematical constraint equation (Eq. 2.7) turns out to be

$$\begin{aligned} g_{e_n} &= \boldsymbol{g}_e \cdot \boldsymbol{n} = 0 \\ \dot{g}_{e_s} &= \dot{\boldsymbol{g}}_e \cdot \boldsymbol{s} = 0 \end{aligned} \qquad \text{(Eq. 2.8)}$$

In (Eq. 2.8), $\dot{\boldsymbol{g}}_e = d\boldsymbol{g}_e/dt$ and $\boldsymbol{n}$, $\boldsymbol{s}$ denote, respectively, normal and tangent unit vectors along the contact surface. This rather odd approach is followed conventionally to formulate kinematical contact constraint in tangential direction. However, at least for predictor-corrector type contact formulations, it is possible to retain kinematical contact constraint equations in its original form given by (Eq. 2.7). This can be accomplished by switching to a trajectory based intersection algorithm (Travaš et al. 2009) to construct contact pairs. In addition to being more elegant, this algorithm also enjoys some real advantages. With this algorithm: (i) standard variational framework for contact can be utilized, (ii) trajectory of the contacting particles is respected firmly, (iii) it is possible to enforce stick condition by resorting to particle positions at first hand instead of particle velocities, which is, of course, geometrically more sound. In this study both possibilities are exploited and detailed derivations are given.

Contact imposes kinetical constraints too. In general Mohr-Coulomb type frictional constitutive model is adopted in tangential direction. Then by relying on this assumption we define bounding functions, which, in vector notation, read as

$$\begin{aligned}\boldsymbol{\phi} &= \phi_n \boldsymbol{n} + \phi_s \boldsymbol{s} \\ &= \tau_n \boldsymbol{n} + (\tau_s + \mu\tau_n)\boldsymbol{s}\end{aligned} \qquad \text{(Eq. 2.9)}$$

Then kinetical constraint equations can be expressed as

$$\begin{aligned}\phi_n &\leq 0 \\ \phi_s &\leq 0\end{aligned} \qquad \text{(Eq. 2.10)}$$

Note that (Eq. 2.10) is actually an inequality and defines the admissible region where contact forces can reside. $\phi_n \leq 0$ states that in case of contact normal component of the contact traction must be compressive. On the other hand, $\phi_s \leq 0$ states that tangential component of the contact force cannot be larger than the threshold posed by frictional law.

Kinematical and kinetical constraint equations can be written together in the form of Karush-Kuhn-Tucker (KKT) conditions as

$$\phi_n g_n = 0; \quad \phi_n \leq 0; \quad g_n \geq 0 \qquad \text{(Eq. 2.11)}$$

$$\begin{aligned}&\phi_s \dot{g}_s = 0; \quad \phi_s \leq 0; \quad \dot{g}_s \geq 0 \quad \rightarrow \text{Closest} - \text{Point Projection} \\ &\phi_s g_s = 0; \quad \phi_s \leq 0; \quad g_s \geq 0 \quad \rightarrow \text{Trajectory Intersection}\end{aligned} \qquad \text{(Eq. 2.12)}$$

Before passing attempts made to develop real constitutive equations for contact should be mentioned (Wriggers 2006). Depending upon the micromechanical properties, e.g. hardness and surface roughness, some sort of elastic energy can be stored along the contact interface in tangential as well as normal contact directions. These constitutive developments are very important because in this way it is possible to obtain objective macro elastic material parameters, which describe real material behavior. Then there is no need any more to contemplate ad-hoc user-prescribed big numbers or parameters derived from underlying finite element discretization.

2.3 High Velocity Impact

In this work it is also attempted to investigate behavior of plain concrete under very high-loading rates. Such rates are attained in experiments like projectile perforation where concrete specimen is pierced by a sharp rigid metallic object (Cargile 1999; Frank et al. 2012; Caner et al. 2014). The results obtained from perforation experiments on plain concrete slabs carried out by (Cargile 1999) reveal that failure mode is mainly the combination of brittle fracture, radial cracking and fragmentation. All these phenomena can be successfully modeled by employing microplane material model. Therefore for this set of experiments numerical simulations have been carried out using new finite element code developed within the context of this work.

During penetration process concrete material around the contact region experiences very large deformations for a very short period of time before it turns into powder. Therefore microplane material model is to be extended to the large strain regime (Bažant et al. 2000b). To our knowledge, there exists no rate form of constitutive equations developed for microplane model so far. In order to be able to track evolution of damage parameters total deformation, referred to initial configuration, is to be employed. For large deformation extension to be physically sound some simplifying assumptions are to be made. Relying on very limited deformation capacity (brittleness) of concrete, deformation gradient can be replaced by material rotation tensor during transformations in between initial and deformed configurations. That means that stress tensor rotates with material as well as the microplanes themselves. Then stress state referred to local material coordinate system is identical at initial and deformed configurations. In other words, co-rotated Cauchy stress and second Piola-Kirchhoff stress (PK2) becomes component wise equal to each other, which is very important for physical justification of the model. In addition, it can be shown that Green-Lagrange strain uniquely characterizes deformation on the individual microplanes (Bažant et al. 2000b) and can be approximately additively decomposed into volumetric and deviatoric parts (Bažant 1995). Therefore constitutive update can be conveniently performed by utilizing energetically conjugate couple, Green-Lagrange strain tensor and second Piola-Kirchhoff stress tensor.

Rate effects are incorporated into the microplane material model based on rate process theory (Mihashi et al. 1980; A. S. Krausz et al. 1988; Reinhardt et al. 1991; Bažant et al. 2000a-b; Ožbolt et al. 2005b, 2011a). It has been shown in (Ožbolt et al. 2011a, 2012, 2013b, 2014) that from low to medium strain rates this formulation performs very well to reflect the rate sensitivity of the material. Performance and adequacy of the rate sensitivity model proposed will be tested for very high strain rates which are attained around the contact region during penetration simulations.

Contact problem also becomes complicated at large deformations. In addition to possible material non-linearity along the contact interface, geometrical non-linearity is added. In solution methods based on implicit time integration equilibrium equation referred to an unknown state is considered. Since equilibrium state is not known beforehand, an iterative procedure starting from a guess state, which is usually set equal to equilibrium state corresponding to previous time step, has to be set up. Then, of course, material and geometrical nonlinearities are to be fully accounted. With implicit time integration, it is possible to obtain unconditionally stable time stepping algorithms (Hughes 2012). Therefore larger time increments can be used. Then it is very much possible that contact pairs change within equilibrium iterations, source of geometrical nonlinearity, which should be handled properly in order not to deteriorate convergence characteristics (Wriggers 2006). It is extremely difficult to find an equilibrium state for highly explosive contact-impact events with lots of fragments flying around. But having a quadratic convergence rate in such a case is a big one, which makes procedures based on equilibrium iterations even less attractive.

Contact nonlinearities as well as others can be bypassed if one refers to an equilibrium equation corresponding to a known state. If one resorts to dynamic nodal equilibrium equation corresponding to a known state and combines it with mass lumping, it is possible to advance dependent variables in time by performing explicit time integration without need to solve any system of equations. Naturally time integration is performed on a kinematically admissible state with all contact constraints already resolved. Since procedure involves no iteration, there is no guess that one can use to detect contact and handle it properly. Such a guess can be obtained if one employs predictor-corrector type algorithm (Carpenter et al. 1991; Marusich et al. 1995; Camacho et al. 1996, 1997; Erhart 2004; Erhart et al. 2006; Travaš et al. 2009). In predictor step unconstrained system is advanced in time by direct time integration assuming no contact. Then in corrector step, first a contact search is conducted with predicted positions at hand and contact pairs are constructed, if there exists any. Then contact constraints are enforced by computing corrector position increments. By using explicit time integration scheme employed and constraint equations together, it is possible to compute corrector position increments explicitly such that constraints are exactly satisfied at element level provided that it is not connected to any other contact element. Due to possible exact enforcement

one can call the method as Lagrange multiplier. But in fact it is purely penalty formulation. As will be shown, one can derive an explicit expression for penalty parameter, which is different for each contact element, such that exact satisfaction of contact constraints is ensured at element level for unconnected elements. But for connected elements an iterative procedure has to be set up (Carpenter et al. 1991; Travaš et al. 2009). Due to this iterative nature there always remains some amount of gap, which gives rise to storage of some amount of residual parasitic elastic energy along the contact interface. Due to actual underlying penalty formulation it is possible to regularize discontinuous Mohr-Coulomb law in the tangential direction and therefore to employ classical radial return mapping algorithms, frequently used for elastic-plastic material models (Simo et al. 1998), to perform constitutive updates. In solution methods based on explicit time integration, numerical stability issues put a very strict upper bound on the time increment that can be used, which is normally in the order of microseconds. But explicit time integration is the natural choice in short duration contact-impact problems, because everything happens just within milliseconds. Then time step required for resolving solution details fair enough falls already well below the stability limit.

Without a doubt, Lagrangian description fits perfectly well to describe motion of solids. Because path dependency is naturally accounted, the external boundaries can easily be tracked and, therefore, possible contact interactions can be precisely formulated. However, Lagrangian description puts strict constraints on the form of motion function. Motion function must be one-to-one and onto, i.e. invertible, and determinant of its Jacobian should be sign preserving, local impenetrability of matter. Actually these statements manifest that an assembly of particles can be called as solid as far as it moves regularly by fulfilling implied constraints. As soon as this assembly is not able to move regularly depending upon the level of external loading, it cannot be called as solid anymore, at least partly, but fluid-like solid or gas-like solid. If this happens, there are no restrictions on the form of motion function anymore and particle assembly can undergo arbitrarily complex motions like tearing, merging, splitting, vortex formation etc.

If motion function starts losing its regularity, then one should firstly consider if it is possible to heal motion function such that Lagrangian framework can be retained throughout the rest of deformation process. Within the context of the finite element method, possible change of material state during mechanical processes has been the driving force behind the development of several discretization techniques. If the material flow is not severe, one can employ Arbitrary Lagrangian-Eulerian (ALE) formulation to regularize the motion function. In this technique, underlying finite element discretization is respected and motion function is improved by repositioning the existing nodes (Hirt et al. 1974; Wall 1999; Linder 2003; Donea et al. 2004). During this repositioning phase, mass flows into (or out of) the boundaries of elements (convection) that is why the term Eulerian is appended.

As an alternative to ALE method one can consider techniques based on mesh adaptivity, like remeshing (Marusich et al. 1995; Camacho et al. 1997; Vaz Jr et al. 2001; A. Koch 2002; Erhart et al. 2006) and element deletion (Schwer et al. 1991; Chen 1994; Cargile 1999; Huang et al. 2005; Leppänen 2006; Y. Liu et al. 2009; Tu et al. 2010; Hansson et al. 2011; Frank et al. 2012). In remeshing underlying finite element discretization is replaced with another one such that an improved approximation to the motion function can be constructed. On the other hand, for technique based on adaptive element deletion underlying finite element discretization is kept in place. The problematic part of the body, where motion function started to lose its regularity, is simply removed from the system. Element deletion criteria play an important role and should be done with extreme care in order to avoid non-physical solutions.

During projectile penetration motion function starts immediately losing its regularity around the contact region. As a remedy ALE is not an option because the boundary of concrete specimen undergoes arbitrarily complex deformations due to explosive character of concrete. Then one has to resort to techniques based on mesh adaptivity. Remeshing should be avoided too, because: (i) it is difficult to generate meshes in three dimensions especially for bodies with arbitrarily complex boundaries automatically, (ii) it takes a lot of time, due to projection of nodal and history variables, which is prohibitive in solution methods based on explicit time integration and (iii) information is lost during projection due to numerical diffusion errors. Although it sounds awkward, adaptive technique based on element deletion seems to be only possible option left. Because, (i) with increasing number of elements exact solution is expected to be recovered (monotonic convergence), (ii) the extension from two dimensions to three dimensions does not bring any additional complexity, (iii) it is very fast and (iv) it couples with microplane material model based on smeared cracking in a natural way. Actually, all these statements explains why all conventional Lagrangian explicit finite element programs still employ this technique to handle highly distorted elements (Johnson 1977; L. M. Taylor et al. 1989; Whirley et al. 1993).

In hyper-velocity penetration events, i.e. for impact velocities larger than $3000\,\mathrm{m/s}$, the solid material evaporates, i.e. turns into gas, immediately after impact event occurs due to extremely high pressures present around the contact region. There is no time for material to deform and it does not make sense to employ Lagrangian framework staying within continuum setting, actually it is not possible. Then there exist two possible alternatives. One can either stay in continuum setting by employing Eulerian description of motion (Matuska et al. 1978; Couch et al. 1983; McGlaun et al. 1990), best suited for liquids and gasses but can also be used for solids, or switch to discontinuous mesh free Lagrangian techniques like Smoothed Particle Hydrodynamics (SPH) (Birnbaum et al. 1987; Hibbitt et al. 2001; Hallquist 2006).

Depending upon the impact conditions, like impact velocity, geometry of the projectile, attack angle, impact duration and material properties, considerable amount of heat could be generated due to friction along the contact surface and inelastic deformations in the bulk. Depending upon the level of heating, one might need to take into account coupling in between mechanical and non-mechanical processes (Armero et al. 1992; Zavarise et al. 1992, 1995, 2005; Wriggers et al. 1994; Marusich et al. 1995; Camacho et al. 1997; Pantuso 1997; Pantuso et al. 2000; Rieger et al. 2004; Periškic 2009; Ožbolt et al. 2013a; Bošnjak 2014). To investigate the significance of thermo mechanical coupling during penetration simulations, a simple staggered algorithm has also been implemented into the finite element code that is developed by the author in the framework of this work.

2.4 Solution Strategy

Within the context of this work an explicit finite element code capable of simulating real world impact events has been developed by the author. To accomplish this all formulations are rendered in three dimensions. Maximum impact velocity of $1000\ \mathrm{m/s}$ or less is targeted. Therefore pure Lagrangian finite element formulation has been employed. Current configuration is referred to as computational domain, i.e. element contributions are computed over the current configuration. However, in order to be able to track evolution of internal variables, the constitutive update is performed by referring to initial configuration. Large deformation frictional contact is treated by predictor-corrector type algorithm. Lagrange multiplier like penalty formulation is used to enforce contact constraints. Highly distorted elements on the way are removed with a technique based on adaptive element deletion. Explicit time integration with fixed time increment is used throughout the whole simulation. Time increment is computed based on stability limit first and then reduced with a factor of safety. Large deformation rate and temperature dependent microplane material model based on relaxed kinematical constraint, together with crack-band regularization, is used as a constitutive equation for concrete. For the conditions investigated, penetrating objects remain essentially undeformed during impact. Therefore for impacting objects simple Saint Venant-Kirchhoff hyperelastic material model is adopted.

3 Continuum Mechanics Preliminaries

In this chapter overview of continuum mechanics principles will be presented. Note that the following content is by no means complete and does not cover detailed derivations and discussions. In-depth information about these fundamental concepts can be found in the texts (Ogden 1997; Simo et al. 1998; Holzapfel 2000).

3.1 Kinematics

3.1.1 Motion

A continuum body $\mathcal{B}$ is defined by an open bounded set of continuum particles. The region occupied by the body is denoted as $\Omega \in \mathbb{R}^3$ (see Fig. 3.1). Such a body is said to be under relative motion if the position of some of the particles located inside is changing in time with respect to an observer, i.e.

$$\boldsymbol{x} = \boldsymbol{x}(t) \qquad \text{(Eq. 3.1)}$$

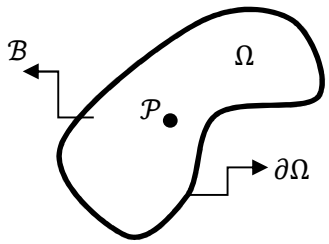

Fig. 3.1 Definition of Body

3.1.1.1 Frame of Observation: Lagrangian vs. Eulerian

In Lagrangian description of motion we observe the body from a fixed Cartesian coordinate system in general (see Fig. 3.2) and follow path of each particle, i.e.

$$\boldsymbol{x} = x_i(t)\mathbf{e}_i \qquad \text{(Eq. 3.2)}$$

Lagrangian description of motion gives us the possibility to measure relative deformation locally around material particles.

However in Eulerian description of motion we observe body from a control volume fixed in space at an arbitrary location. As can be seen from Fig. 3.3, the position $\boldsymbol{x}_{\mathcal{P}}$ fixed in space is occupied by different particles at different time instants. Due to this fact one cannot grab useful information for deformation experienced by the material particles using Eulerian description of the motion. Actually in Eulerian description one is not interested in the position and deformation but the evolution of

physical quantities, like rate of displacement (velocity), density, momentum, energy etc., within an arbitrary position fixed in space. Note also that there is no restriction on the motion in Eulerian description which means body of interest can undergo motions like tearing, merging, splitting, vortex formation etc., whereas, as will be shown in forthcoming sections, there are strict constraints on the form of motion in Lagrangian description.

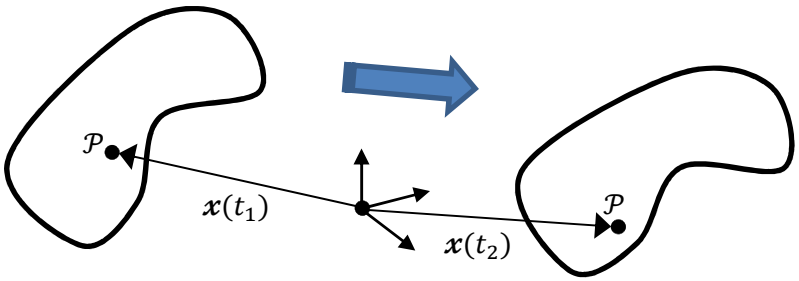

Fig. 3.2 Lagrangian Description of Motion

Lagrangian description of motion is best suited for bodies with moving (deforming) boundaries and made up of path-dependent materials which are the common statements encountered almost always in solid mechanics, whereas Eulerian description of motion is best suited for bodies with not moving (not deforming) boundaries and made up of path-independent materials which are the common statements encountered almost always in fluid mechanics. What happens if we have fluid-like solid or solid-like fluid drives the evolution of all complicated numerical solution procedures which are currently still under investigation. Since the main focus of the thesis is related with solid mechanics applications Lagrangian description of motion will be adopted for subsequent developments.

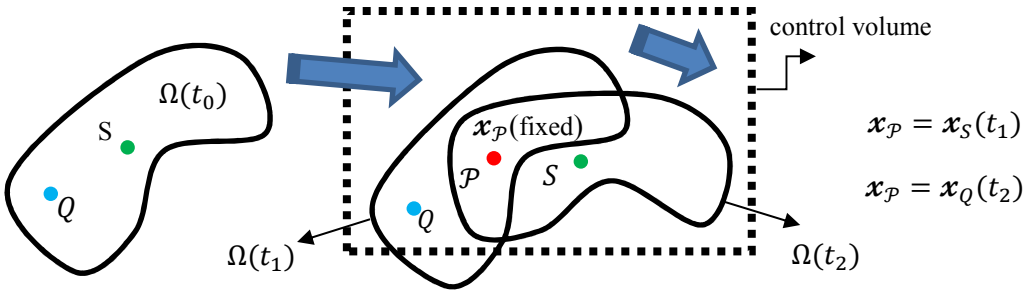

Fig. 3.3 Eulerian Description of Motion

3.1.2 Deformation

Deformation is a relative quantity. To be able to measure relative deformation around a material particle one needs to know a position for that particle where the total deformation is known. Such a position, if it exists, is called as reference position and is denoted by

$$\boldsymbol{X} = \boldsymbol{x}(T) \qquad \text{(Eq. 3.3)}$$

From now on capital letters will be devoted to quantities which refer to reference position. Here note that the time (T) corresponding to reference position is assumed to be same for all material particles.

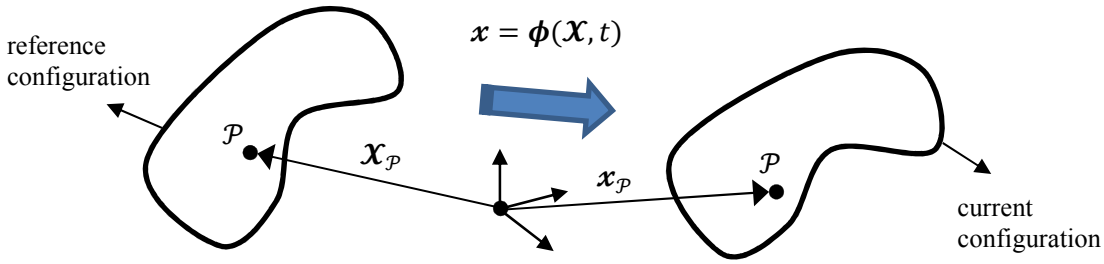

Fig. 3.4 Motion Function

Now follows some definitions. The region occupied by the body at time T is called as reference configuration, whereas that occupied by the body at generic time t is called as current configuration. Material or undeformed configuration can also be used interchangeably for reference configuration, whereas spatial or deformed configuration can be used in place of current configuration.

Next we assume that there exists a vector valued function $\boldsymbol{\phi}$ which maps the position of material particles at reference configuration to that at current configuration (see Fig. 3.4). It is called as motion function for body $\mathcal{B}$. Then one can write

$$\boldsymbol{x} = \boldsymbol{\phi}(\boldsymbol{X}, t) \qquad \text{(Eq. 3.4)}$$

It is assumed that $\boldsymbol{\phi}$ is one-to-one and onto which means that its inverse $\boldsymbol{\phi}^{-1}$ does exist and is unique. This statement implies that a position at current configuration cannot be occupied by more than one material particle at the same time and one material particle cannot occupy more than one position at current configuration at the same time. Additionally we pose that $\boldsymbol{\phi}$ is smooth and equipped with at least piecewise continuous derivatives with respect to space and time.

3.1.3 Displacement, Velocity and Acceleration

The displacement of a material particle measured from its position at undeformed configuration is given by

$$\boldsymbol{\mathcal{U}}(\boldsymbol{\mathcal{X}},t)=\boldsymbol{x}-\boldsymbol{\mathcal{X}}=\boldsymbol{\phi}(\boldsymbol{\mathcal{X}},t)-\boldsymbol{\mathcal{X}} \qquad \text{(Eq. 3.5)}$$

The velocity and acceleration of a material particle can be obtained by taking first and second total time derivative of motion function with respect to time as

$$\boldsymbol{\mathcal{V}}(\boldsymbol{\mathcal{X}},t)=\frac{D}{Dt}\boldsymbol{x}=\frac{D}{Dt}\boldsymbol{\phi}(\boldsymbol{\mathcal{X}},t)=\frac{\partial}{\partial t}\boldsymbol{\phi}(\boldsymbol{\mathcal{X}},t) \qquad \text{(Eq. 3.6)}$$

$$\boldsymbol{\mathcal{A}}(\boldsymbol{\mathcal{X}},t)=\frac{D}{Dt}\boldsymbol{\mathcal{V}}(\boldsymbol{\mathcal{X}},t)=\frac{D^2}{Dt^2}\boldsymbol{\phi}(\boldsymbol{\mathcal{X}},t)=\frac{\partial^2}{\partial t^2}\boldsymbol{\phi}(\boldsymbol{\mathcal{X}},t) \qquad \text{(Eq. 3.7)}$$

3.1.4 Deformation Gradient

3.1.4.1 Mapping of Differential Line Elements

A material particle $\mathcal{P}$ could realize if it undergoes deformation by looking at how the material particles located in the neighborhood are moving relative to it (see Fig. 3.5).

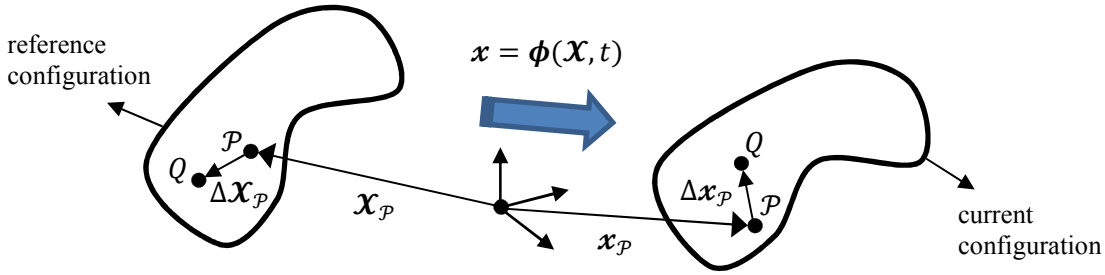

Fig. 3.5 Mapping od Differential Line Elements

Incremental line elements around a material particle $\mathcal{P}$ at its undeformed and deformed positions can be approximately related to each other with the first order linearization of the motion function around $\mathcal{P}$ as

$$\boldsymbol{\phi}(\boldsymbol{\mathcal{X}},t)\cong \mathrm{Lin}[\boldsymbol{\phi}(\boldsymbol{\mathcal{X}},t)]=\boldsymbol{\phi}(\boldsymbol{\mathcal{X}}_{\mathcal{P}},t)+\boldsymbol{\mathcal{F}}(\boldsymbol{\mathcal{X}}_{\mathcal{P}},t)(\boldsymbol{\mathcal{X}}-\boldsymbol{\mathcal{X}}_{\mathcal{P}}) \qquad \text{(Eq. 3.8)}$$

where

$$\boldsymbol{\mathcal{F}}(\boldsymbol{\mathcal{X}},t)=\frac{\partial\boldsymbol{\phi}(\boldsymbol{\mathcal{X}},t)}{\partial\boldsymbol{\mathcal{X}}}=\mathrm{Grad}\boldsymbol{\phi} \qquad \text{(Eq. 3.9)}$$

is called as deformation gradient. $\boldsymbol{\mathcal{F}}$ is in general not symmetric and contains all the necessary information to analyze deformation locally around the material particles. Now we define incremental line elements

$$\boldsymbol{\Delta X}_{\mathcal{P}} := \quad \boldsymbol{X} - \boldsymbol{X}_{\mathcal{P}}$$
$$\boldsymbol{\Delta x}_{\mathcal{P}} := \quad \boldsymbol{x} - \boldsymbol{x}_{\mathcal{P}} \qquad \text{(Eq. 3.10)}$$

around $\mathcal{P}$ at reference and current configurations. Taking into account above definitions and by inserting (Eq. 3.4) into (Eq. 3.8) we end up with a more compact form as

$$\boldsymbol{\Delta x}_{\mathcal{P}} \cong \boldsymbol{\mathcal{F}}(\boldsymbol{X}_{\mathcal{P}}, t)\boldsymbol{\Delta X}_{\mathcal{P}} \qquad \text{(Eq. 3.11)}$$

As in the limit $\boldsymbol{\Delta X}_{\mathcal{P}} \to \mathbf{0}$ an exact expression relating differential line elements is obtained as

$$\boldsymbol{dx}_{\mathcal{P}} = \boldsymbol{\mathcal{F}}(\boldsymbol{X}_{\mathcal{P}}, t)\boldsymbol{dX}_{\mathcal{P}} \qquad \text{(Eq. 3.12)}$$

$\boldsymbol{\mathcal{F}}$ can also be expressed in dyadic notation as

$$\boldsymbol{\mathcal{F}}(\boldsymbol{X}, t) = \mathcal{F}_{iI}\mathbf{e}_i \otimes \mathbf{E}_I; \quad \mathcal{F}_{iI} = \frac{\partial x_i}{\partial X_I} \qquad \text{(Eq. 3.13)}$$

(Eq. 3.13) reveals that $\boldsymbol{\mathcal{F}}$ is a two-point tensor with one base at current configuration and the other at reference configuration. Note that in general Cartesian basis $\mathbf{e}_i$ and $\mathbf{E}_I$ can be chosen independently from each other. We will keep this notation the same in order to identify association of physical quantities with reference and current configurations but assume the coincidence of both bases for subsequent developments to avoid unnecessary details. The following conditions must always hold for $\boldsymbol{\mathcal{F}}$ to be admissible.

$$\boldsymbol{\mathcal{F}}\mathbf{d}\boldsymbol{X} \neq \mathbf{0} \quad \forall \quad \boldsymbol{dX} \neq \mathbf{0}$$
$$\boldsymbol{\mathcal{F}}\mathbf{d}\boldsymbol{X} = \mathbf{0} \leftrightarrow \boldsymbol{dX} = \mathbf{0} \qquad \text{(Eq. 3.14)}$$

From physical standpoint above conditions state that a material line element with non-zero length cannot be reduced down to a zero length line element during deformation. This constraint implies that $\boldsymbol{\mathcal{F}}$ must be non-singular and therefore has non-zero determinant, i.e.

$$\det(\boldsymbol{\mathcal{F}}) \neq 0 \qquad \text{(Eq. 3.15)}$$

Recall that inverse of a tensor with non-zero determinant is well defined.

3.1.4.2 Mapping of Differential Volume Elements

Another important constraint will be put on $\boldsymbol{\mathcal{F}}$ when the mapping of differential volume elements from reference to current configuration is considered (see Fig. 3.6). The volume of differential volume elements spanned by differential line elements at reference and current configurations are given by the triple vector products as

$$\mathrm{d}\mathcal{V} = (\mathbf{d}\boldsymbol{X}_1 \times \mathbf{d}\boldsymbol{X}_2) \cdot \mathbf{d}\boldsymbol{X}_3 = (\mathbf{d}\boldsymbol{X}_2 \times \mathbf{d}\boldsymbol{X}_3) \cdot \mathbf{d}\boldsymbol{X}_1 = (\mathbf{d}\boldsymbol{X}_3 \times \mathbf{d}\boldsymbol{X}_1) \cdot \mathbf{d}\boldsymbol{X}_2 > 0$$
$$\mathrm{d}v = (\mathbf{d}\boldsymbol{x}_1 \times \mathbf{d}\boldsymbol{x}_2) \cdot \mathbf{d}\boldsymbol{x}_3 = (\mathbf{d}\boldsymbol{x}_2 \times \mathbf{d}\boldsymbol{x}_3) \cdot \mathbf{d}\boldsymbol{x}_1 = (\mathbf{d}\boldsymbol{x}_3 \times \mathbf{d}\boldsymbol{x}_1) \cdot \mathbf{d}\boldsymbol{x}_2 > 0 \quad \text{(Eq. 3.16)}$$

Note that we assume by convention that the line elements are positively oriented so that triple product attains a positive value. With the insertion of (Eq. 3.12) into (Eq. 3.16) and after some straightforward operations it is obtained that

$$\mathrm{d}v = \mathcal{J}\mathrm{d}\mathcal{V} > 0; \quad \mathcal{J} := \det(\boldsymbol{\mathcal{F}}) \quad \text{(Eq. 3.17)}$$

which implies

$$\det(\boldsymbol{\mathcal{F}}) > 0 \quad \text{(Eq. 3.18)}$$

Above condition states that line elements forming volume element must be mapped by preserving their relative orientations which is another way of saying that volume cannot change sign during mapping.

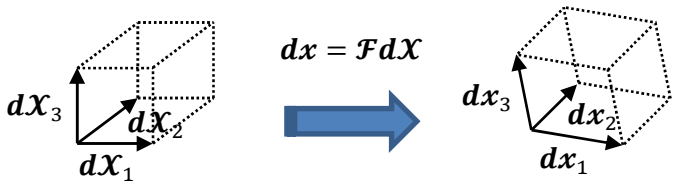

Fig. 3.6 Mapping of Volume Elements

3.1.4.3 Mapping of Differential Area Elements

The differential area elements at reference and current configurations spanned by two arbitrary differential line elements are defined as (see Fig. 3.7)

$$\mathbf{d}\boldsymbol{\mathcal{A}} = \mathbf{d}\boldsymbol{X}_1 \times \mathbf{d}\boldsymbol{X}_2 = d\mathcal{A}\boldsymbol{N}$$
$$\mathbf{d}\boldsymbol{a} = \mathbf{d}\boldsymbol{x}_1 \times \mathbf{d}\boldsymbol{x}_2 = da\boldsymbol{n} \quad \text{(Eq. 3.19)}$$

With the insertion of (Eq. 3.12) into (Eq. 3.19) and after some straightforward operations it is obtained that

$$\mathbf{d}\boldsymbol{a} = \mathcal{J}\boldsymbol{\mathcal{F}}^{-T}\mathbf{d}\boldsymbol{\mathcal{A}} \quad \text{(Eq. 3.20)}$$

Above expression is known as Nanson's formula.

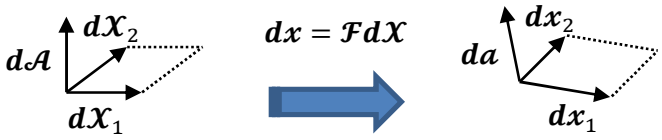

Fig. 3.7 Mapping of Area Elements

3.1.4.4 Total Time Derivative

Total time derivative of deformation gradient is given by the expression

$$\dot{\boldsymbol{\mathcal{F}}}(\boldsymbol{\mathcal{X}},t)=\frac{D}{Dt}\left(\frac{\partial\boldsymbol{\phi}(\boldsymbol{\mathcal{X}},t)}{\partial\boldsymbol{\mathcal{X}}}\right)=\frac{\partial}{\partial\boldsymbol{\mathcal{X}}}\boldsymbol{\mathcal{V}}(\boldsymbol{\mathcal{X}},t)=\mathrm{Grad}\big(\boldsymbol{\mathcal{V}}(\boldsymbol{\mathcal{X}},t)\big) \tag{Eq. 3.21}$$

Since $\boldsymbol{\phi}$ is invertible particle velocity can be written in terms of its position at current configuration, i.e.

$$\boldsymbol{\mathcal{V}}(\boldsymbol{\mathcal{X}},t)=\mathcal{V}_I(\boldsymbol{\mathcal{X}},t)\mathbf{E}_I=\mathcal{V}_I\big(\boldsymbol{\phi}^{-1}(\boldsymbol{x},t),t\big)\mathbf{E}_I=\mathcal{v}_i(\boldsymbol{x},t)\mathbf{e}_i=\boldsymbol{v}(\boldsymbol{x},t) \tag{Eq. 3.22}$$

Another useful expression for $\dot{\boldsymbol{\mathcal{F}}}$ can be obtained by using the alternative form for velocity function given by (Eq. 3.22) as

$$\dot{\boldsymbol{\mathcal{F}}}(\boldsymbol{\mathcal{X}},t)=\frac{\partial}{\partial\boldsymbol{\mathcal{X}}}\boldsymbol{v}(\boldsymbol{x}(\boldsymbol{\mathcal{X}},t),t)=\frac{\partial\boldsymbol{v}}{\partial\boldsymbol{x}}\frac{\partial\boldsymbol{x}}{\partial\boldsymbol{\mathcal{X}}}=\boldsymbol{\ell}\boldsymbol{\mathcal{F}} \tag{Eq. 3.23}$$

$$\boldsymbol{\ell}:=\frac{\partial\boldsymbol{v}}{\partial\boldsymbol{x}}=\mathrm{grad}\boldsymbol{v}$$

where $\boldsymbol{\ell}$ is spatial velocity gradient.

3.1.5 Right Cauchy-Green Deformation Tensor

Square length of differential line element at current configuration is given by

$$\boldsymbol{dx}\cdot\boldsymbol{dx}=\boldsymbol{\mathcal{F}}\boldsymbol{dX}\cdot\boldsymbol{\mathcal{F}}\boldsymbol{dX}=\boldsymbol{dX}\cdot\boldsymbol{\mathcal{C}}\boldsymbol{dX}>0 \tag{Eq. 3.24}$$

$$\boldsymbol{\mathcal{C}}:=\boldsymbol{\mathcal{F}}^T\boldsymbol{\mathcal{F}}=\mathcal{F}_{Ii}^T\mathcal{F}_{iJ}\mathbf{E}_I\otimes\mathbf{E}_J$$

where $\boldsymbol{\mathcal{C}}$ is called as right Cauchy-Green deformation tensor. (Eq. 3.24) implies that $\boldsymbol{\mathcal{C}}$ is symmetric positive-definite, an important property which will be exploited in subsequent sections. Before passing we note that all eigenvalues of a symmetric tensor are real, and corresponding eigenvectors form an orthogonal basis. If it is also positive-definite all eigenvalues become positive real numbers.

3.1.6 Polar Decomposition

Deformation gradient can be uniquely decomposed as the product of two second order tensors as

$$\boldsymbol{\mathcal{F}} = \boldsymbol{\mathcal{R}}\boldsymbol{\mathcal{U}} \tag{Eq. 3.25}$$

where, in general terms, $\boldsymbol{\mathcal{R}}$ is a second order orthogonal tensor and $\boldsymbol{\mathcal{U}}$ is a second order symmetric positive-semidefinite tensor. For our considerations $\boldsymbol{\mathcal{U}}$ becomes second order symmetric positive-definite since $\boldsymbol{\mathcal{F}}$ is non-singular and $\boldsymbol{\mathcal{R}}$ becomes proper orthogonal due to $\det(\boldsymbol{\mathcal{F}}) > 0$. In continuum mechanics nomenclature $\boldsymbol{\mathcal{R}}$ is called as material rotation tensor whereas $\boldsymbol{\mathcal{U}}$ is called as right stretch tensor.

For some numerical schemes $\boldsymbol{\mathcal{R}}$ must be explicitly known. Therefore the formal procedure to be followed for the determination of $\boldsymbol{\mathcal{R}}$ will be outlined next. First of all for a given $\boldsymbol{\mathcal{F}}$ we compute right Cauchy-Green deformation tensor $\boldsymbol{\mathcal{C}}$. With the insertion of (Eq. 3.25) into (Eq. 3.24) $\boldsymbol{\mathcal{C}}$ takes the form

$$\boldsymbol{\mathcal{C}} = \boldsymbol{\mathcal{F}}^T\boldsymbol{\mathcal{F}} = (\boldsymbol{\mathcal{U}}^T\boldsymbol{\mathcal{R}}^T)(\boldsymbol{\mathcal{R}}\boldsymbol{\mathcal{U}}) = \boldsymbol{\mathcal{U}}^T\boldsymbol{\mathcal{U}} = \boldsymbol{\mathcal{U}}^2 \tag{Eq. 3.26}$$

Then $\boldsymbol{\mathcal{U}}$ simply becomes

$$\boldsymbol{\mathcal{U}} = \sqrt{\boldsymbol{\mathcal{C}}} \tag{Eq. 3.27}$$

Square root of $\boldsymbol{\mathcal{C}}$ can easily be computed when expressed in spectral coordinates

$$\boldsymbol{\mathcal{C}} = \sum_{I=1}^{3} \lambda_I^{\mathcal{C}} \boldsymbol{\mathcal{N}}_I^{\mathcal{C}} \otimes \boldsymbol{\mathcal{N}}_I^{\mathcal{C}} \tag{Eq. 3.28}$$

where $\lambda_I^{\mathcal{C}}$ and $\boldsymbol{\mathcal{N}}_I^{\mathcal{C}}$ are, respectively, eigenvalues and eigenvectors of $\boldsymbol{\mathcal{C}}$. Recall that $\boldsymbol{\mathcal{C}}$ is symmetric positive-definite by definition. Therefore the following statements must hold

$$\begin{aligned} \lambda_I^{\mathcal{C}} &> 0 \\ \boldsymbol{\mathcal{N}}_I^{\mathcal{C}} \cdot \boldsymbol{\mathcal{N}}_J^{\mathcal{C}} &= \delta_{IJ} \\ \boldsymbol{\mathcal{N}}_I^{\mathcal{C}} &= \boldsymbol{\mathcal{R}}^{\mathcal{C}}\mathbf{E}_I \\ \boldsymbol{\mathcal{R}}^{\mathcal{C}} &:= \boldsymbol{\mathcal{N}}_Q^{\mathcal{C}} \otimes \mathbf{E}_Q = \mathcal{R}_{PQ}\mathbf{E}_P \otimes \mathbf{E}_Q \end{aligned} \tag{Eq. 3.29}$$

where $\boldsymbol{\mathcal{R}}^{\mathcal{C}}$ is a proper orthogonal material rotation tensor formed by eigenvectors of $\boldsymbol{\mathcal{C}}$. One can then easily express $\boldsymbol{\mathcal{C}}$ in Cartesian coordinate system by back substitution as

$$\boldsymbol{\mathcal{C}} = \sum_{I=1}^{3} \lambda_I^{\mathcal{C}} \boldsymbol{\mathcal{N}}_I^{\mathcal{C}} \otimes \boldsymbol{\mathcal{N}}_I^{\mathcal{C}} = \sum_{I=1}^{3} \lambda_I^{\mathcal{C}} \left(\boldsymbol{\mathcal{R}}^{\mathcal{C}}\mathbf{E}_I\right) \otimes \left(\boldsymbol{\mathcal{R}}^{\mathcal{C}}\mathbf{E}_I\right) = \sum_{I=1}^{3} \mathcal{R}_{PI}\lambda_I^{\mathcal{C}}\mathcal{R}_{IQ}^T\, \mathbf{E}_P \otimes \mathbf{E}_Q \tag{Eq. 3.30}$$

Then from (Eq. 3.27) $\boldsymbol{\mathcal{U}}$ simply becomes

$$\boldsymbol{\mathcal{U}} = \sqrt{\boldsymbol{\mathcal{C}}} = \sum_{I=1}^{3} \lambda_I^{\mathcal{U}} \boldsymbol{\mathcal{N}}_I^{\mathcal{U}} \otimes \boldsymbol{\mathcal{N}}_I^{\mathcal{U}} \tag{Eq. 3.31}$$

with

$$\begin{aligned} \lambda_I^{\mathcal{U}} &= \sqrt{\lambda_I^{\mathcal{C}}} \\ \boldsymbol{\mathcal{N}}_I^{\mathcal{U}} &= \boldsymbol{\mathcal{N}}_I^{\mathcal{C}} \end{aligned} \tag{Eq. 3.32}$$

Note that $\boldsymbol{\mathcal{C}}$, in general, poses more than one square root. We simply select the so called principal square root which is positive-definite. Finally rotation tensor $\boldsymbol{\mathcal{R}}$ is calculated from (Eq. 3.25) as

$$\boldsymbol{\mathcal{R}} = \boldsymbol{\mathcal{F}}\boldsymbol{\mathcal{U}}^{-1} \tag{Eq. 3.33}$$

Expression given by (Eq. 3.25) is called as right polar decomposition of $\boldsymbol{\mathcal{F}}$. Left polar decomposition of $\boldsymbol{\mathcal{F}}$ is also well defined but will not be discussed here.

3.1.7 Stretch

The linear map $\boldsymbol{\mathcal{U}}$ deforms (stretches) the material line element that it is applied to, whereas $\boldsymbol{\mathcal{R}}$ simply rotates it as a rigid line. Stretching, in general, changes the length and direction of material line element.

The line elements $\boldsymbol{dX}$ and $\boldsymbol{dx}$ can also be expressed in terms of corresponding unit vectors $\boldsymbol{\mathcal{M}}$ and $\boldsymbol{m}$ as

$$\begin{aligned} \boldsymbol{dX} &= |\boldsymbol{dX}|\boldsymbol{\mathcal{M}} \\ \boldsymbol{dx} &= |\boldsymbol{dx}|\boldsymbol{m} \end{aligned} \tag{Eq. 3.34}$$

By inserting (Eq. 3.34) into (Eq. 3.12) we obtain

$$|\boldsymbol{dx}|\boldsymbol{m} = |\boldsymbol{dX}|\boldsymbol{\mathcal{F}}\boldsymbol{\mathcal{M}} \tag{Eq. 3.35}$$

By equating the norm of the both sides we obtain

$$|\boldsymbol{dx}| = (|\boldsymbol{dX}|\boldsymbol{\mathcal{F}}\boldsymbol{\mathcal{M}} \cdot |\boldsymbol{dX}|\boldsymbol{\mathcal{F}}\boldsymbol{\mathcal{M}})^{1/2} = |\boldsymbol{dX}|(\boldsymbol{\mathcal{M}} \cdot \boldsymbol{\mathcal{U}}^{\boldsymbol{2}}\boldsymbol{\mathcal{M}})^{1/2} \tag{Eq. 3.36}$$

Then we define stretch in the direction of $\boldsymbol{\mathcal{M}}$ as

$$\lambda(\boldsymbol{\mathcal{M}}) := \frac{|\boldsymbol{dx}|}{|\boldsymbol{dX}|} = (\boldsymbol{\mathcal{M}} \cdot \boldsymbol{\mathcal{U}}^{\boldsymbol{2}}\boldsymbol{\mathcal{M}})^{1/2} \tag{Eq. 3.37}$$

$\boldsymbol{\mathcal{U}}$ takes the following form if all principal stretches are same.

$$\boldsymbol{\mathcal{U}} = \lambda_{\mathcal{U}} \sum_{I=1}^{3} \boldsymbol{\mathcal{N}}_I^{\mathcal{U}} \otimes \boldsymbol{\mathcal{N}}_I^{\mathcal{U}} = \lambda_{\mathcal{U}} \boldsymbol{I} \qquad \text{(Eq. 3.38)}$$

Insertion of above equation into (Eq. 3.37) then yields

$$\lambda(\boldsymbol{\mathcal{M}}) = (\boldsymbol{\mathcal{M}} \cdot {\lambda_{\mathcal{U}}}^2 \boldsymbol{\mathcal{M}})^{1/2} = \lambda_{\mathcal{U}} \qquad \text{(Eq. 3.39)}$$

which implies that stretches in all possible directions are same. Note also that the direction of the line element does not change during stretching but only its length.

If $\boldsymbol{\mathcal{M}}$ is aligned with one of the principal directions of $\boldsymbol{\mathcal{U}}$, i.e. $\boldsymbol{\mathcal{M}} = \boldsymbol{\mathcal{N}}_I^{\mathcal{U}}$, (Eq. 3.37) then takes the following form

$$\lambda(\boldsymbol{\mathcal{M}}) = (\boldsymbol{\mathcal{U}}\boldsymbol{\mathcal{N}}_I^{\mathcal{U}} \cdot \boldsymbol{\mathcal{U}}\boldsymbol{\mathcal{N}}_I^{\mathcal{U}})^{1/2} = \lambda_I^{\mathcal{U}} \qquad \text{(Eq. 3.40)}$$

which implies that stretch is equal to corresponding principal stretch. Note again that direction of the line element is also preserved in this case.

3.1.8 Green-Lagrange Strain

3.1.8.1 Definition

A material particle is called as unstrained if the length of a line element as well as the orientation of two line elements arbitrarily located around it does not change during mapping. These two conditions manifest themselves in the invariance of dot product taken between two arbitrary line elements during mapping, i.e.

$$\boldsymbol{d\hat{x}} \cdot \boldsymbol{d\tilde{x}} = \boldsymbol{d\hat{X}} \cdot \boldsymbol{d\tilde{X}} \qquad \text{(Eq. 3.41)}$$

which can be rewritten as

$$|\boldsymbol{d\hat{x}}||\boldsymbol{d\tilde{x}}| \cos\theta = \left|\boldsymbol{d\hat{X}}\right|\left|\boldsymbol{d\tilde{X}}\right| \cos\Theta \qquad \text{(Eq. 3.42)}$$

(Eq. 3.42), taking into account above prequisites, implies that

$$\begin{aligned} |\boldsymbol{d\hat{x}}| &= \left|\boldsymbol{d\hat{X}}\right| \\ |\boldsymbol{d\tilde{x}}| &= \left|\boldsymbol{d\tilde{X}}\right| \qquad \text{(Eq. 3.43)} \\ \cos\theta &= \cos\Theta \end{aligned}$$

The dot product of two vectors is invariant under mapping if and only if the transformation tensor is an orthogonal tensor, i.e.

$$\boldsymbol{\mathcal{F}} = \boldsymbol{\mathcal{R}}; \quad \boldsymbol{\mathcal{U}} = \mathbf{I} \qquad \text{(Eq. 3.44)}$$

By inserting (Eq. 3.12) into (Eq. 3.41) we obtain that

$$\boldsymbol{d\hat{x}} \cdot \boldsymbol{d\tilde{x}} - \boldsymbol{d\hat{X}} \cdot \boldsymbol{d\tilde{X}} = \boldsymbol{\mathcal{F}} \boldsymbol{d\hat{X}} \cdot \boldsymbol{\mathcal{F}} \boldsymbol{d\tilde{X}} - \boldsymbol{d\hat{X}} \cdot \boldsymbol{d\tilde{X}} = \boldsymbol{d\hat{X}} \cdot 2\boldsymbol{E} \boldsymbol{d\tilde{X}} = \boldsymbol{0}$$

$$\boldsymbol{E} := \frac{1}{2}(\boldsymbol{\mathcal{C}} - \boldsymbol{I}) \tag{Eq. 3.45}$$

where $\boldsymbol{E}$ is called Green-Lagrange strain. Factor $1/2$ in front of $\boldsymbol{E}$ is put for coincidence with small strain theory in case the deformations are small. Note that

$$\boldsymbol{E} = \boldsymbol{0} \quad \leftrightarrow \quad \boldsymbol{\mathcal{F}} = \boldsymbol{\mathcal{R}} \tag{Eq. 3.46}$$

and

$$\boldsymbol{E} = \frac{1}{2}(\boldsymbol{\mathcal{C}} - \boldsymbol{I}) = \frac{1}{2}(\boldsymbol{\mathcal{F}}^T \boldsymbol{\mathcal{F}} - \boldsymbol{I}) = \frac{1}{2}((\boldsymbol{\mathcal{U}}^T \boldsymbol{\mathcal{R}}^T)(\boldsymbol{\mathcal{R}} \boldsymbol{\mathcal{U}}) - \boldsymbol{I}) = \frac{1}{2}(\boldsymbol{\mathcal{U}}^2 - \boldsymbol{I}) \tag{Eq. 3.47}$$

which implies that $\boldsymbol{E}$ is not a function $\boldsymbol{\mathcal{R}}$.

Now we will interpret components of $\boldsymbol{E}$ with some examples. Consider the case where

$$\boldsymbol{d\hat{X}} = \boldsymbol{d\tilde{X}} = \boldsymbol{dX}$$

$$\boldsymbol{d\hat{x}} = \boldsymbol{d\tilde{x}} = \boldsymbol{dx} \tag{Eq. 3.48}$$

Putting (Eq. 3.48) into (Eq. 3.45) we obtain that

$$\boldsymbol{dx} \cdot \boldsymbol{dx} - \boldsymbol{dX} \cdot \boldsymbol{dX} = \boldsymbol{dX} \cdot 2\boldsymbol{E} \boldsymbol{dX}$$

$$|\boldsymbol{dx}|^2 - |\boldsymbol{dX}|^2 = |\boldsymbol{dX}|^2 \boldsymbol{\mathcal{M}} \cdot 2\boldsymbol{E}\boldsymbol{\mathcal{M}} \tag{Eq. 3.49}$$

$$\frac{1}{2}\frac{|\boldsymbol{dx}|^2 - |\boldsymbol{dX}|^2}{|\boldsymbol{dX}|^2} = \boldsymbol{\mathcal{M}} \cdot \boldsymbol{E}\boldsymbol{\mathcal{M}} = E_{\mathcal{M}\mathcal{M}}$$

where $E_{\mathcal{M}\mathcal{M}}$ can be interpreted as axial strain in the direction of $\boldsymbol{\mathcal{M}}$ defined as half relative change in square line length with respect to reference square line length.

Finally we consider

$$\boldsymbol{d\hat{X}} \cdot \boldsymbol{d\tilde{X}} = 0 \tag{Eq. 3.50}$$

which implies the case where reference line elements are perpendicular. With the insertion of (Eq. 3.50) into (Eq. 3.45) we, this time, obtain

$$\boldsymbol{d\hat{x}} \cdot \boldsymbol{d\tilde{x}} = \boldsymbol{d\hat{X}} \cdot 2\boldsymbol{E}\boldsymbol{d\tilde{X}}$$

$$|\boldsymbol{d\hat{x}}| \cdot |\boldsymbol{d\tilde{x}}| \cos\theta = \left|\boldsymbol{d\hat{X}}\right|\left|\boldsymbol{d\tilde{X}}\right|\widehat{\boldsymbol{\mathcal{M}}} \cdot 2\boldsymbol{E}\widetilde{\boldsymbol{\mathcal{M}}} \qquad \text{(Eq. 3.51)}$$

$$\frac{1}{2}\lambda\left(\widehat{\boldsymbol{\mathcal{M}}}\right)\lambda\left(\widetilde{\boldsymbol{\mathcal{M}}}\right)\cos\theta = E_{\widehat{\mathcal{M}}\widetilde{\mathcal{M}}}$$

where $E_{\widehat{\mathcal{M}}\widetilde{\mathcal{M}}}$ can be interpreted as a measure of the shear angle between directions $\widehat{\boldsymbol{\mathcal{M}}}$ and $\widetilde{\boldsymbol{\mathcal{M}}}$.

3.1.8.2 Total Time Derivative

Rate of Green-Lagrange strain can be obtained in two steps. Taking into account (Eq. 3.23) and (Eq. 3.24), one can easily obtain an expression for the rate of $\boldsymbol{\mathcal{C}}$ as

$$\dot{\boldsymbol{\mathcal{C}}} = \dot{\boldsymbol{\mathcal{F}}}^{\mathrm{T}}\boldsymbol{\mathcal{F}} + \boldsymbol{\mathcal{F}}^{\mathrm{T}}\dot{\boldsymbol{\mathcal{F}}} = \boldsymbol{\mathcal{F}}^{\mathrm{T}}\left(\boldsymbol{\ell}^{\mathrm{T}} + \boldsymbol{\ell}\right)\boldsymbol{\mathcal{F}} = \boldsymbol{\mathcal{F}}^{\mathrm{T}}2\boldsymbol{d}\boldsymbol{\mathcal{F}}$$

$$\boldsymbol{d} = \frac{1}{2}\left(\boldsymbol{\ell}^{\mathrm{T}} + \boldsymbol{\ell}\right) = \mathrm{sym}(\boldsymbol{\ell}) \qquad \text{(Eq. 3.52)}$$

where $\boldsymbol{d}$ is the symmetric part of the spatial velocity gradient $\boldsymbol{\ell}$ and called as rate of deformation tensor. It can be shown that

$$\frac{1}{|\boldsymbol{dx}|}\frac{\partial}{\partial \mathrm{t}}|\boldsymbol{dx}| = \boldsymbol{m} \cdot \boldsymbol{dm} = d_{mm} \qquad \text{(Eq. 3.53)}$$

(Eq. 3.53) suggests that diagonal terms of $\boldsymbol{d}$ can be interpreted as the measure of rate at which length of a line element at current configuration is changing with respect to time. One can also demonstrate that off diagonal terms of $\boldsymbol{d}$ can be used as a measure of rate of the shear angle between two arbitrary line elements at current configuration.

Finally, with the insertion of (Eq. 3.52), the rate of Green-Lagrange strain is obtained as

$$\dot{\boldsymbol{E}} = \frac{1}{2}\dot{\boldsymbol{\mathcal{C}}} = \boldsymbol{\mathcal{F}}^{\mathrm{T}}\boldsymbol{d}\boldsymbol{\mathcal{F}} \qquad \text{(Eq. 3.54)}$$

3.2 Kinetics

3.2.1 Stress

In section 3.1 kinematical aspects of continuum mechanics have been presented briefly without discussing the reasons causing body to move and deform. In terms of pure mechanical processes the motion is caused by the existence of external forces acting on a body either due to action from a distance or at vicinity (Fig. 3.8).

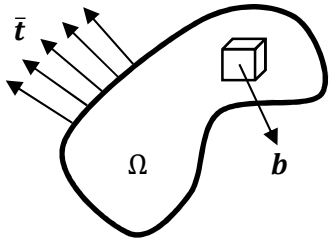

Fig. 3.8 Mechanical Loading

As the body moves under the effect of these external loads, internal forces develop due to resistance of the material against deformation. We denote these internal forces as $\boldsymbol{t}(\boldsymbol{x}, t)$ and call, by convention, as Cauchy (or true) traction vector measured as force per unit area at current configuration (see Fig. 3.9). According to Cauchy's postulate traction vector depends also on the surface orientation, i.e.

$$\boldsymbol{t} = \boldsymbol{t}(\boldsymbol{x}, t, \boldsymbol{n}) \qquad \text{(Eq. 3.55)}$$

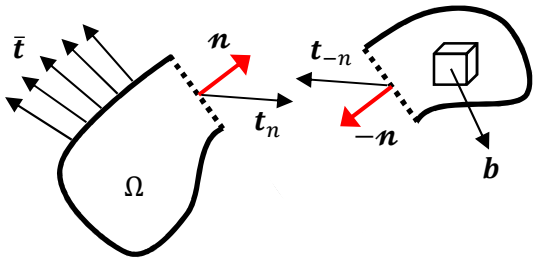

Fig. 3.9 Cauchy Traction Vector

To maintain the equilibrium of internal forces we assume that there exist a second-order tensor such that

$$\boldsymbol{t}(\boldsymbol{x}, t, \boldsymbol{n}) = \boldsymbol{\sigma}(\boldsymbol{x}, t)\boldsymbol{n} \qquad \text{(Eq. 3.56)}$$

which is known to be as Cauchy's stress theorem. In (Eq. 3.56), $\boldsymbol{\sigma}(\boldsymbol{x}, t)$ denotes a second-order spatial tensor field called as Cauchy stress.

Note that form given by (Eq. 3.56) automatically satisfies Newton's third law of action and reaction, i.e.

$$\boldsymbol{t}(\boldsymbol{x},t,\boldsymbol{n}) = -\boldsymbol{t}(\boldsymbol{x},t,-\boldsymbol{n}) \quad \text{(Eq. 3.57)}$$

(Eq. 3.57) is also known as Cauchy's lemma of traction continuity.

3.2.2 Alternative Stress Measures

We define first Piola-Kirchhoff (nominal) traction vector $\boldsymbol{T}$ by claiming that the equality

$$\mathbf{df} = \boldsymbol{t}da = \boldsymbol{T}dA \quad \text{(Eq. 3.58)}$$

holds for all area elements. Similar to Cauchy traction vector, one can write down

$$\boldsymbol{T} = \boldsymbol{T}(\boldsymbol{X},t,\boldsymbol{\mathcal{N}}) = \boldsymbol{P}(\boldsymbol{X},t)\boldsymbol{\mathcal{N}} \quad \text{(Eq. 3.59)}$$

where $\boldsymbol{P}$ is a second-order two-point unsymmetrical tensor called as first Piola-Kirchhoff (or nominal) stress. By employing Nanson's formula given by (Eq. 3.20), we can set the following relationship

$$\boldsymbol{P} = \mathcal{J}\boldsymbol{\sigma}\boldsymbol{\mathcal{F}}^{-T} \quad \text{(Eq. 3.60)}$$

in between two stress measures.

Kirchhoff stress, denoted by $\boldsymbol{\tau}$, is obtained by weighting Cauchy stress with $\mathcal{J} = \det(\boldsymbol{\mathcal{F}})$ as

$$\boldsymbol{\tau} = \mathcal{J}\boldsymbol{\sigma} \quad \text{(Eq. 3.61)}$$

Second Piola-Kirchhoff stress can then be obtained by applying pull-back operation on $\boldsymbol{\tau}$ as

$$\boldsymbol{\mathcal{S}} = \boldsymbol{\mathcal{F}}^{-1}\boldsymbol{\tau}\boldsymbol{\mathcal{F}}^{-T} \quad \text{(Eq. 3.62)}$$

Note that $\boldsymbol{\mathcal{S}}$ is a symmetric second order tensor living in reference configuration. In addition, as will be shown later, it is energetically conjugate with Green-Lagrange strain $\boldsymbol{E}$. All these characteristics make $\boldsymbol{\mathcal{S}}$ a very useful stress measure for the development of constitutive equations. Note also that components of $\boldsymbol{\mathcal{S}}$ do not have any direct physical interpretation. Taking into account (Eq. 3.60), (Eq. 3.61) and (Eq. 3.62) one can relate $\boldsymbol{\mathcal{P}}$ to $\boldsymbol{\mathcal{S}}$ as

$$\boldsymbol{\mathcal{P}} = \boldsymbol{\mathcal{F}}\boldsymbol{\mathcal{S}} \quad \text{(Eq. 3.63)}$$

Sometimes it is very useful to work in corotated coordinates defined by $\boldsymbol{\mathcal{R}}$ obtained from polar decomposition of $\boldsymbol{\mathcal{F}}$. Corotated Cauchy stress is obtained by expressing Cauchy stress in corotated coordinates as

$$\boldsymbol{\sigma} = \sigma_{ij}\mathbf{e}_i \otimes \mathbf{e}_j = \sigma_{ij}(\boldsymbol{\mathcal{R}}^T\hat{\mathbf{e}}_i) \otimes \left(\boldsymbol{\mathcal{R}}^T\hat{\mathbf{e}}_j\right) = \hat{\sigma}_{mn}\hat{\mathbf{e}}_m \otimes \hat{\mathbf{e}}_n = \hat{\boldsymbol{\sigma}}$$
$$\hat{\sigma}_{mn} = \mathcal{R}^T_{mi}\sigma_{ij}\mathcal{R}_{jn} \quad \text{(Eq. 3.64)}$$

where $\hat{\boldsymbol{\sigma}}$ is called as corotated Cauchy stress.

3.3 Balance Laws

3.3.1 Conservation of Mass

The amount of matter contained in a body is termed as total mass. In continuum mechanics total mass is assumed to be distributed over its volume and hence can be computed from

$$\mathcal{M}(t) = \int_{\Omega} \rho(\boldsymbol{x}, t) \; dv = \int_{\Omega} \rho(\boldsymbol{\phi}(\boldsymbol{X}, t), t) \; dv = \int_{\Omega} \bar{\rho}(\boldsymbol{X}, t) \; dv \tag{Eq. 3.65}$$

where $\rho(\boldsymbol{x}, t) = \bar{\rho}(\boldsymbol{X}, t)$ is called as the spatial mass density and measures the amount of matter per unit volume at deformed configuration. We assume that during the deformation process no matter enters or leaves from the boundary. Then the total mass becomes a conserved quantity. By denoting density field at reference configuration as

$$\rho_0(\boldsymbol{X}) := \rho(\boldsymbol{X}, T) \tag{Eq. 3.66}$$

conservation of total mass can be expressed in integral form as

$$\mathcal{M}(t) = \int_{\Omega} \rho(\boldsymbol{x}, t) \; dv = \int_{\Omega_0} \rho_0(\boldsymbol{X}) \; dV = \text{const.} \tag{Eq. 3.67}$$

The local form of the conservation equation can be obtained as follows. Using (Eq. 3.17), (Eq. 3.67) can be rewritten as

$$\int_{\Omega_0} [\mathcal{J}\rho(\boldsymbol{x}, t) - \rho_0(\boldsymbol{X})] \; dV = 0 \tag{Eq. 3.68}$$

Assuming sufficiently smooth variations of the integrand over the domain, local form of mass conservation equation, in total form, is obtained as

$$\rho(\boldsymbol{x}, t) = \frac{1}{\mathcal{J}} \rho_0(\boldsymbol{X}) \tag{Eq. 3.69}$$

3.3.2 Balance of Linear Momentum

Adaption of Newton's second law of motion to a continuous body manifests itself in the balance equation for linear momentum. Total linear momentum of the body is given by

$$\boldsymbol{\mathcal{L}}(t) = \int_{\Omega} \boldsymbol{v} \; dm = \int_{\Omega} \rho \boldsymbol{v} \; dv \tag{Eq. 3.70}$$

whereas total force acting on it is (see Fig. 3.8)

$$\boldsymbol{F}(t) = \int_{\Gamma} \boldsymbol{t}\ da + \int_{\Omega} \rho \boldsymbol{b}\ dv \qquad \text{(Eq. 3.71)}$$

In (Eq. 3.71), $\boldsymbol{t}$ represents the contact forces applied from the surroundings in the form of surface tractions, whereas $\boldsymbol{b}$ is the force field acting on the body by action from a distance like gravity. Balance of linear momentum states that temporal change of total linear momentum is equal to the total force acting on it, i.e.

$$\frac{D}{Dt}\boldsymbol{\mathcal{L}}(t) = \boldsymbol{F}(t) \qquad \text{(Eq. 3.72)}$$

Taking into account (Eq. 3.70) and by employing Reynold's transport theorem, the left hand side of (Eq. 3.72) can be written as

$$\frac{D}{Dt}\boldsymbol{\mathcal{L}}(t) = \int_{\Omega} \rho \dot{\boldsymbol{v}}\ dv \qquad \text{(Eq. 3.73)}$$

With the aid of divergence and Cauchy's stress theorems, total force acting on the body can be recast in a more useful form as

$$\boldsymbol{F}(t) = \int_{\Gamma} \boldsymbol{\sigma} \cdot \boldsymbol{da} + \int_{\Omega} \rho \boldsymbol{b}\ dv = \int_{\Omega} [\mathrm{div}(\boldsymbol{\sigma}) + \rho \boldsymbol{b}]\ dv \qquad \text{(Eq. 3.74)}$$

Inserting (Eq. 3.73) and (Eq. 3.74) into (Eq. 3.72) leads us to

$$\int_{\Omega} [\rho \dot{\boldsymbol{v}} - \mathrm{div}(\boldsymbol{\sigma}) - \rho \boldsymbol{b}]\ dv = 0 \qquad \text{(Eq. 3.75)}$$

Assuming smooth variation of the integrand, local form of the balance equation for linear momentum is obtained as

$$\rho \dot{\boldsymbol{v}} = \mathrm{div}(\boldsymbol{\sigma}) + \rho \boldsymbol{b} \qquad \text{(Eq. 3.76)}$$

By employing balance equation for angular momentum it can be shown that Cauchy's stress $\boldsymbol{\sigma}$ is to be symmetric.

3.3.3 First and Second Laws of Thermodynamics

First law of thermodynamics is known as energy equation. It establishes the relationship between the rate of total energy stored in the system and external power supplied from the surroundings due to mechanical and thermal loading. Second law of thermodynamics is called as entropy inequality and provides us a mathematical tool to describe the direction of energy transfer.

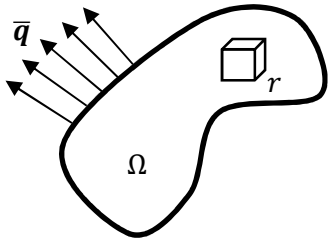

Fig. 3.10 Thermal Loading

3.3.3.1 First Law of Thermodnamics: Energy Equation

Under the effect of mechanical (see Fig. 3.8) and thermal loading (see Fig. 3.10) only, the external power supplied to the system is given by

$$\mathcal{P}_{ext} = \mathcal{P}_{ext}^{mechanical} + \mathcal{P}_{ext}^{thermal} \tag{Eq. 3.77}$$

In (Eq. 3.77), $\mathcal{P}_{ext}^{mechanical}$ is external mechanical power given by

$$\mathcal{P}_{ext}^{mechanical} = \int_{\Gamma} \boldsymbol{v} \cdot \boldsymbol{t} \ da + \int_{\Omega} \boldsymbol{v} \cdot \rho \boldsymbol{b} \ dv \tag{Eq. 3.78}$$

where, $\boldsymbol{t}$ represents the contact forces applied from the surroundings in the form of surface tractions, whereas $\boldsymbol{b}$ is the force field, measured per unit mass at current configuration, acting on the body by action from a distance like gravity. By employing divergence and Cauchy's stress theorems, external mechanical power can be expressed as

$$\mathcal{P}_{ext}^{mechanical} = \int_{\Omega} \boldsymbol{v} \cdot [\mathrm{div}(\boldsymbol{\sigma}) + \rho \boldsymbol{b}] \ dv + \int_{\Omega} \boldsymbol{\sigma} : \boldsymbol{\nabla v} \ dv \tag{Eq. 3.79}$$

By using symmetry of Cauchy stress and recognizing balance equation for linear momentum, (Eq. 3.79) can be recast into the final form as

$$\mathcal{P}_{ext}^{mechanical} = \int_{\Omega} \boldsymbol{v} \cdot \rho \dot{\boldsymbol{v}} \ dv + \int_{\Omega} \boldsymbol{\sigma} : \boldsymbol{d} \ dv \tag{Eq. 3.80}$$

In (Eq. 3.77), $\mathcal{P}_{ext}^{thermal}$ is external thermal power given by

$$\mathcal{P}_{ext}^{thermal} = \int_{\Gamma} -q_n \ da + \int_{\Omega} \rho r \ dv \tag{Eq. 3.81}$$

where $-q_n$ is the inward heat flux (heat per unit time) measured per unit area entering into body from its boundary, and r is heat source supplied per unit time for per unit mass at current configuration.

As the body is exposed to thermal loading internal heat fluxes develop due to resistance of the material against heating. We denote these internal heat fluxes as $\boldsymbol{q}(\boldsymbol{x},t)$ and call, by convention, as Cauchy (or true) heat flux vector measured per unit area at current configuration. According to Stoke's heat flux theorem internal heat flux vector depends also on the surface orientation, i.e.

$$q_n = \boldsymbol{q}(\boldsymbol{x},t,\boldsymbol{n}) \tag{Eq. 3.82}$$

To maintain the equilibrium of internal heat fluxes after steady-state temperature distribution has been reached, we postulate that the following relationship holds:

$$q_n(\boldsymbol{x},t,\boldsymbol{n}) = \boldsymbol{q}(\boldsymbol{x},t)\cdot\boldsymbol{n} \tag{Eq. 3.83}$$

By employing divergence and Stoke's heat flux theorems, external thermal power can be expressed as

$$\mathcal{P}_{ext}^{thermal} = \int_{\Gamma} -\boldsymbol{q}\cdot\boldsymbol{da} + \int_{\Omega} \rho r \; dv = \int_{\Omega} \left[-\mathrm{div}(\boldsymbol{q}) + \rho r\right] \; dv \tag{Eq. 3.84}$$

With the insertion of (Eq. 3.80) and (Eq. 3.84) into (Eq. 3.77), the total external power turns out to be

$$\mathcal{P}_{ext} = \int_{\Omega} \boldsymbol{v}\cdot\rho\dot{\boldsymbol{v}} \; dv + \int_{\Omega} \left[\boldsymbol{\sigma}\colon\boldsymbol{d} - \mathrm{div}(\boldsymbol{q}) + \rho r\right] \; dv \tag{Eq. 3.85}$$

The part of the total external power which is not expended on material drives the so called evolution of kinetic energy, denoted as $\mathcal{K}$, of the body as

$$\dot{\mathcal{K}} = \frac{D\mathcal{K}}{Dt} = \int_{\Omega} \boldsymbol{v}\cdot\rho\dot{\boldsymbol{v}} \; dv = \int_{\Omega} \rho(\boldsymbol{v}\cdot\dot{\boldsymbol{v}}) \; dv \tag{Eq. 3.86}$$

From Reynold's transport theorem it can be obtained that

$$\mathcal{K}(t) = \int_{\Omega} \rho(\frac{1}{2}\boldsymbol{v}\cdot\boldsymbol{v}) \; dv \tag{Eq. 3.87}$$

The part of the total external power which is expended on material drives the so called evolution of internal energy. Internal energy is an extensive quantity and given as

$$\mathcal{U}(t) = \int_{\Omega} \rho u(\boldsymbol{x},t) \; dv \tag{Eq. 3.88}$$

where $u(\boldsymbol{x},t)$ is internal energy density measured per unit mass.

Using (Eq. 3.85), (Eq. 3.88) and by employing Reynold's transport theorem, evolution equation for internal energy can be rewritten as

$$\dot{\mathcal{U}} = \frac{D\mathcal{U}}{Dt} = \int_{\Omega} \rho\dot{u}(\boldsymbol{x}, t) \; dv = \int_{\Omega} [\boldsymbol{\sigma}: \boldsymbol{d} - \mathrm{div}(\boldsymbol{q}) + \rho r] \; dv \qquad \text{(Eq. 3.89)}$$

By assuming the smoothness of the integrand, local form of the energy equation is obtained as

$$\rho\dot{u} = \boldsymbol{\sigma}: \boldsymbol{d} - \mathrm{div}(\boldsymbol{q}) + \rho r \qquad \text{(Eq. 3.90)}$$

3.3.3.2 Second Law of Thermodynamics: Entropy Inequality

The case $\boldsymbol{q} \neq \boldsymbol{0}$ implies that there is a heat flow. Energy equation alone neither gives any information about the heat flow nor puts any constraint on the form that $\boldsymbol{q}$ could assume. It only states that as a consequence of heat flow energy content of the material changes. But it is a universal fact gained from physical observations that heat always flows from hotter place towards warmer one. In case of irreversible mechanical processes some amount of energy is dissipated during inelastic deformations like micro-cracking, plastic flow or frictional sliding. It is a physical constraint that dissipated energy must be an ever non-decreasing function of time. To mathematically bring these facts into play we define another extensive quantity called as entropy and define it as

$$\mathcal{S}(t) = \int_{\Omega} \rho s(\boldsymbol{x}, t) \; dv \qquad \text{(Eq. 3.91)}$$

where $s(\boldsymbol{x}, t)$ is entropy density measured per unit mass. External entropy power is closely related to external thermal power as follows

$$\mathcal{P}_{\mathrm{ext}}^{\mathrm{entropy}} = \int_{\Gamma} \frac{-q_n}{\theta} \; da + \int_{\Omega} \frac{\rho r}{\theta} \; dv \qquad \text{(Eq. 3.92)}$$

where θ is called as absolute temperature. By employing divergence and Stoke's heat flux theorems, external entropy power can be expressed as

$$\mathcal{P}_{\mathrm{ext}}^{\mathrm{entropy}} = \int_{\Gamma} (-\frac{1}{\theta}\boldsymbol{q}) \cdot \boldsymbol{da} + \int_{\Omega} \frac{\rho r}{\theta} \; dv = \int_{\Omega} \left[\frac{-div(\boldsymbol{q}) + \rho r}{\theta} + \frac{1}{\theta^2}\boldsymbol{q} \cdot \boldsymbol{\nabla}\theta\right] \; dv \qquad \text{(Eq. 3.93)}$$

The difference between rate of change of entropy and external entropy power is defined as total entropy production per unit time, i.e.

$$\Gamma(t) = \frac{D\mathcal{S}}{Dt} - \mathcal{P}_{\mathrm{ext}}^{\mathrm{entropy}} \qquad \text{(Eq. 3.94)}$$

It is postulated that total entropy production for all thermodynamic processes is ever non-decreasing function of time, i.e.

$$\Gamma(t) \geq 0 \qquad \text{(Eq. 3.95)}$$

With the insertion of (Eq. 3.91) and (Eq. 3.93) into (Eq. 3.94) and taking into account the fact that absolute temperature θ is always positive, local form of the entropy inequality is obtained as

$$\rho\theta\dot{s} - \rho r + div(\boldsymbol{q}) - \frac{1}{\theta}\boldsymbol{q}\cdot\boldsymbol{\nabla}\theta \geq 0 \qquad \text{(Eq. 3.96)}$$

Note that inequality given by (Eq. 3.96) is known as Clausius-Duhem inequality. By employing energy equation given by (Eq. 3.90), (Eq. 3.96) can be rewritten as

$$\boldsymbol{\sigma}:\boldsymbol{d} - \rho\dot{u} + \rho\theta\dot{s} - \frac{1}{\theta}\boldsymbol{q}\cdot\boldsymbol{\nabla}\theta \geq 0 \qquad \text{(Eq. 3.97)}$$

Next we define Helmholtz free energy as

$$\Psi = u - \theta s \qquad \text{(Eq. 3.98)}$$

Taking total time derivative of (Eq. 3.98), it is obtained that

$$\dot{u} - \theta\dot{s} = \dot{\Psi} + s\dot{\theta} \qquad \text{(Eq. 3.99)}$$

Plugging (Eq. 3.99) into (Eq. 3.97), an alternative form for Clausius-Duhem inequality is obtained as

$$\boldsymbol{\sigma}:\boldsymbol{d} - \rho\dot{\Psi} + \rho s\dot{\theta} - \frac{1}{\theta}\boldsymbol{q}\cdot\boldsymbol{\nabla}\theta \geq 0 \qquad \text{(Eq. 3.100)}$$

The last expression in (Eq. 3.100) is the entropy production term due to heat conduction. Based on physical observations heat always flows from hotter place towards warmer one. Therefore entropy production due to heat conduction must be non-negative. Knowing that θ is non-negative, we then obtain

$$\boldsymbol{q}\cdot\boldsymbol{\nabla}\theta \leq 0 \qquad \text{(Eq. 3.101)}$$

which is known as heat conduction inequality. It is known by physical observations that

$$\boldsymbol{q} = \boldsymbol{0} \quad \leftrightarrow \quad \boldsymbol{\nabla}\theta = \boldsymbol{0} \qquad \text{(Eq. 3.102)}$$

(Eq. 3.101) and (Eq. 3.102) indicate direct dependence of heat flux on temperature gradient, i.e.

$$\boldsymbol{q} = \boldsymbol{q}(\boldsymbol{\nabla}\theta) \qquad \text{(Eq. 3.103)}$$

Assuming that the material is thermally isotropic a simple constitutive equation for $\boldsymbol{q}$ in terms of $\boldsymbol{\nabla}\theta$ can be postulated as

$$\boldsymbol{q} = -k\boldsymbol{\nabla}\theta \qquad \text{(Eq. 3.104)}$$

where k is called as coefficient of thermal conductivity measured in watt per meter Kelvin. (Eq. 3.104) is known as Fourier's law of heat conduction. Note that inserting (Eq. 3.104) into (Eq. 3.101) we obtain the constraint on the material coefficient that

$$k > 0 \qquad \text{(Eq. 3.105)}$$

According to (Eq. 3.101), Clausius-Duhem inequality collapses down to stronger form of the second law of thermodynamics

$$\boldsymbol{\sigma}:\boldsymbol{d} - \rho\dot{\Psi} + \rho s\dot{\theta} \geq 0 \qquad \text{(Eq. 3.106)}$$

which is known as Clausius-Planck inequality. The local form of entropy inequality given by (Eq. 3.106) gives us the possibility to construct a general framework for the development of thermomechanically consistent constitutive models to predict material response for a given state of deformation. The formal procedure is called as internal variable formulation which will not be discussed here (Simo et al. 1998).

3.3.4 Heat Equation

In the absence of stress power, internal energy is proportional to the temperature, i.e.

$$u = c_v\theta \qquad \text{(Eq. 3.107)}$$

where c_v is the heat capacity at constant volume and assumed to be a material constant. Plugging (Eq. 3.107) into (Eq. 3.90), heat equation is then obtained as

$$\rho c_v\dot{\theta} = -\mathrm{div}(\boldsymbol{q}) + \rho r \qquad \text{(Eq. 3.108)}$$

Heat equation takes the form given by (Eq. 3.109) by assuming that the material obeys isotropic heat conduction law given by (Eq. 3.104).

$$\rho c_v\dot{\theta} = k\Delta\theta + \rho r \qquad \text{(Eq. 3.109)}$$

Note that in (Eq. 3.109) Δ is Laplace operator.

4 Finite Element Formulation

4.1 Description of the Problem

To begin with, we consider bodies $\mathcal{B}^1$ and $\mathcal{B}^2$ depicted in Fig. 4.1 at their reference and current configurations. We assume that deformations are large and contact interactions might take place between the bodies within time interval $\mathbb{I} = [0, t]$ during their motions. For notational convenience, an individual body or the union of the bodies, depending upon the context, will be referred to as $\mathcal{B}$ unless otherwise is necessary. The motion function for body $\mathcal{B}$ is then defined as

$$\begin{aligned} \boldsymbol{x} &= \phi(\boldsymbol{X}, t) \\ \Omega &= \phi(\Omega_0, t) \end{aligned} \qquad \text{(Eq. 4.1)}$$

In (Eq. 4.1) ϕ is the motion function, $\boldsymbol{x}$ and $\boldsymbol{X}$ are current and reference positions, Ω_0 and Ω are current and reference domains, for body $\mathcal{B}$. Note that the expressions given by (Eq. 4.1) define family of configurations parameterized in terms of time t.

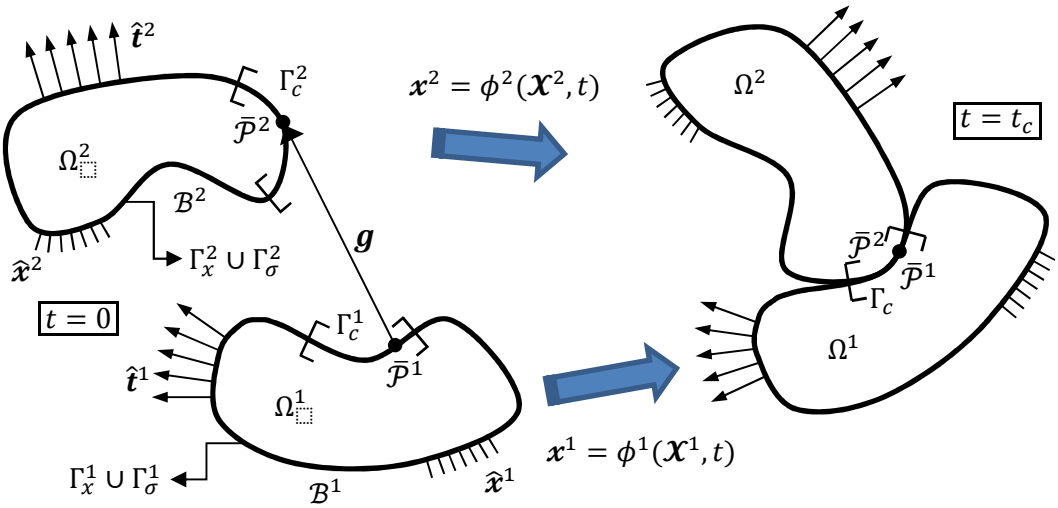

Fig. 4.1 Description of the Problem

4.2 Strong (Differential) Form of the Initial Boundary Value Problem (IBVP)

The strong (differential) form of the linear momentum equation for body $\mathcal{B}$ at current configuration, together with boundary and initial conditions, reads as

$$\begin{aligned}
\rho\ddot{\boldsymbol{x}} &= \operatorname{div}(\boldsymbol{\sigma}) + \rho\boldsymbol{b} && \forall \boldsymbol{X} \in \Omega_0 \;\rightarrow\; \text{linear momentum equation} \\
\boldsymbol{\sigma}\cdot\boldsymbol{n} &= \hat{\boldsymbol{t}} && \forall \boldsymbol{X} \in \Gamma_\sigma \;\rightarrow\; \text{boundary conditions} \\
\boldsymbol{x} &= \hat{\boldsymbol{x}} && \forall \boldsymbol{X} \in \Gamma_x \;\nearrow \\
\boldsymbol{x}|_{t=0} &= \boldsymbol{x}_0 = \boldsymbol{X} && \forall \boldsymbol{X} \in \Omega_0 \;\rightarrow\; \text{initial conditions} \\
\dot{\boldsymbol{x}}|_{t=0} &= \boldsymbol{V}_0 && \forall \boldsymbol{X} \in \Omega_0 \;\nearrow
\end{aligned} \qquad \text{(Eq. 4.2)}$$

In (Eq. 4.2), ρ is the spatial mass density, div is divergence operator in current configuration, $\boldsymbol{\sigma}$ is Cauchy (true) stress, $\boldsymbol{b}$ is body force field per unit mass, $\boldsymbol{n}$ is unit outward normal in current configuration, $\hat{\boldsymbol{t}}$ and $\hat{\boldsymbol{x}}$ are, respectively, prescribed surface tractions and positions, $\boldsymbol{x}_0 (= \boldsymbol{X})$ and $\boldsymbol{V}_0$ are initial conditions in terms of position and velocity.

In addition we propose that bodies of interest might possibly interact, i.e. come into contact, during their motions. For this purpose we identify some portion of outer boundary $\partial\Omega_0$ as contact boundary and denote it as Γ_c. Furthermore we assume that we know, beforehand, particle $\bar{\mathcal{P}}^1 \in \Gamma_c^1$ will come into contact with $\bar{\mathcal{P}}^2 \in \Gamma_c^2$ at some unknown time instant t_c, time of contact, during the motion (see Fig. 4.1). To be able to detect contact event in between we define vector valued gap functions as

$$\begin{aligned}
\boldsymbol{g}^{21} &= \bar{\boldsymbol{x}}^{\,2} - \bar{\boldsymbol{x}}^1 \\
\boldsymbol{g}^{12} &= \bar{\boldsymbol{x}}^1 - \bar{\boldsymbol{x}}^2
\end{aligned} \qquad \text{(Eq. 4.3)}$$

where $\bar{\boldsymbol{x}}^1$, $\bar{\boldsymbol{x}}^2$ are, respectively, current positions of particles $\bar{\mathcal{P}}^1$ and $\bar{\mathcal{P}}^2$. In the continuous setting we have $\boldsymbol{g}^{21} = -\boldsymbol{g}^{12}$, therefore one can resort to either $\boldsymbol{g}^{21}$ by taking body $\mathcal{B}^1$ as reference, or vice versa. However in discrete setting $\boldsymbol{g}^{21} \neq -\boldsymbol{g}^{12}$ since it cannot be guaranteed that finite element discretization is matching along Γ_c. Therefore a choice should be made. In the light of above discussion we take body $\mathcal{B}^1$ as reference and continue with gap function $\boldsymbol{g}^{21}$ by denoting it as $\boldsymbol{g}$ for the sake of convenience.

If bodies come into contact then they cannot penetrate into each other. This kinematical statement is known as impenetrability constraint and can be expressed as

$$g_n = \boldsymbol{g}\cdot\mathbf{n} \geq 0 \qquad \text{(Eq. 4.4)}$$

where $\boldsymbol{n}$ is the outward unit normal placed at $\bar{\boldsymbol{x}}^1$.

As the contact takes place bodies apply forces to each other to prevent penetration and sliding. We denote those forces as $\boldsymbol{\tau}$ in the form of surface tractions. To enforce impenetrability constraint normal component of the contact tractions must be compressive, i.e.

$$\tau_n = \boldsymbol{\tau} \cdot \boldsymbol{n} \leq 0 \qquad \text{(Eq. 4.5)}$$

From (Eq. 4.4) and (Eq. 4.5) conditions for contact can be written as

$$\begin{aligned} \text{contact} \rightarrow & \begin{vmatrix} g_n &= 0 \\ \tau_n &\leq 0 \end{vmatrix} \\ \text{no contact} \rightarrow & \begin{vmatrix} g_n &\geq 0 \\ \tau_n &= 0 \end{vmatrix} \end{aligned} \qquad \text{(Eq. 4.6)}$$

Contact conditions given by (Eq. 4.6) can be brought together as

$$\tau_n \, g_n = 0; \quad \tau_n \leq 0; \quad g_n \geq 0 \qquad \text{(Eq. 4.7)}$$

The form given by (Eq. 4.7) is called as Karush -Kuhn-Tucker conditions. The solution of the problem stated by (Eq. 4.2) must respect the inequality constraints given by (Eq. 4.7) too.

The outer boundary $\partial\Omega_0$ of Ω_0 is decomposed into union of non-overlapping parts as

$$\partial\Omega_0 = \Gamma_\sigma \cup \Gamma_x \cup \Gamma_c \qquad \text{(Eq. 4.8)}$$

and it is assumed that

$$\Gamma_\sigma \cap \Gamma_x = \Gamma_x \cap \Gamma_c = \Gamma_c \cap \Gamma_\sigma = \emptyset \qquad \text{(Eq. 4.9)}$$

In (Eq. 4.8), Γ_σ, Γ_x are, respectively, portions of the boundary where tractions and positions are prescribed, Γ_c is contact boundary.

For the set of equations given in (Eq. 4.2) to be complete, Cauchy stress $\boldsymbol{\sigma}$ must be expressed in terms of particle positions $\boldsymbol{x}$. In general $\boldsymbol{\sigma}$ is function of a strain measure plus set of internal variables, like plastic strain, damage parameters, etc., in case of inelasticity. Strain measure can be expressed in terms of $\boldsymbol{x}$ via well-established kinematical relationships already. However, one needs extra set of equations for the determination of internal variables. Constitutive model for $\boldsymbol{\sigma}$ as well as evolution equations for internal variables can be obtained by exploiting the local form of entropy inequality.

At large deformations, material behavior can be highly nonlinear as well as evolution equations for internal variables. In addition kinematical operators turn out to be nonlinear too. Contact problem

also becomes nonlinear at large deformations. In the presence of contact interactions, nonlinearities arise due to time dependency of contact boundary and non-smooth material behavior in the tangential direction. Moreover, bodies of interest occupy arbitrary domains, in general, for real world applications. Within the context of above statements, it is impossible to obtain a closed form analytical solution to the differential form of initial boundary value problem described by (Eq. 4.2) and (Eq. 4.7). Therefore one has to resort to numerical solution methods, like finite element or finite difference methods. In this study finite element method is used to solve momentum balance equation together with contact constraints due to its wide range of applicability and vast amount of solution techniques embodied (Simo et al. 1998; Belytschko et al. 1999; Donea et al. 2003; Zienkiewicz et al. 2005; Hughes 2012).

4.3 Weak (Integral) Form of IBVP

The weak (integral) form of the linear momentum equation provides us a framework for the development of a numerical solution procedure based on finite element method. It can be obtained as follows. First of all, local differential form is weighted with the variations of the primary variables, current positions $\boldsymbol{x}$ of the material particles, and then resulting expression is integrated over the domain. By enforcing the result obtained to vanish, we get

$$\int_{\Omega} \delta\boldsymbol{x} \cdot [\rho\ddot{\boldsymbol{x}} - \mathrm{div}(\boldsymbol{\sigma}) - \rho\boldsymbol{b}]dv = 0 \qquad \text{(Eq. 4.10)}$$

With (Eq. 4.10) the linear momentum equation is enforced to hold in a weak (integral) sense. However, as can be seen, this form is not suitable for the imposition of boundary conditions. Moreover, it involves, in general, second order partial derivatives with respect to $\boldsymbol{x}$ due to presence of divergence term $\mathrm{div}(\boldsymbol{\sigma})$. Due to this term higher order continuity requirements must be met for the approximations constructed for $\boldsymbol{x}$. Therefore we need to take another step and perform integration by parts. We proceed as follows. First we rewrite the term involving divergence as

$$\delta\boldsymbol{x} \cdot \mathrm{div}(\boldsymbol{\sigma}) = \mathrm{div}(\boldsymbol{\sigma} \cdot \delta\boldsymbol{x}) - \boldsymbol{\sigma} : \boldsymbol{\nabla}\delta\boldsymbol{x} \qquad \text{(Eq. 4.11)}$$

Putting above expression into (Eq. 4.10), and then applying divergence and Cauchy's stress theorems, we obtain

$$\int_{\Omega} \delta\boldsymbol{x} \cdot \rho\ddot{\boldsymbol{x}}\ dv + \int_{\Omega} \boldsymbol{\nabla}\delta\boldsymbol{x} : \boldsymbol{\sigma}\ dv \boxed{- \int_{\Gamma_c^1} \delta\overline{\boldsymbol{x}}^1 \cdot \boldsymbol{\tau}^1\ da - \int_{\Gamma_c^2} \delta\overline{\boldsymbol{x}}^2 \cdot \boldsymbol{\tau}^2\ da} =$$
$$\int_{\Omega} \delta\boldsymbol{x} \cdot \rho\boldsymbol{b}\ dv + \int_{\Gamma_\sigma} \delta\boldsymbol{x} \cdot \hat{\boldsymbol{t}}\ da + \int_{\Gamma_x} \delta\boldsymbol{x} \cdot \boldsymbol{t}_{rea}\ da \qquad \text{(Eq. 4.12)}$$

With the aid of Cauchy's lemma of traction continuity, i.e. $\boldsymbol{\tau}^1 = -\boldsymbol{\tau}^2 = \boldsymbol{\tau}$, and recognizing the fact that

$$\Gamma_c^1 = \Gamma_c^2 = \Gamma_c \tag{Eq. 4.13}$$

during contact, (Eq. 4.12) can be rewritten as

$$\int_\Omega \delta\boldsymbol{x} \cdot \rho\ddot{\boldsymbol{x}}\ dv + \int_\Omega \boldsymbol{\nabla}\delta\boldsymbol{x} : \boldsymbol{\sigma}\ dv + \int_{\Gamma_c} \delta\boldsymbol{g} \cdot \boldsymbol{\tau}\ da = \int_\Omega \delta\boldsymbol{x} \cdot \rho\boldsymbol{b}\ dv + \int_{\Gamma_\sigma} \delta\boldsymbol{x} \cdot \hat{\boldsymbol{t}}\ da + \boxed{\int_{\Gamma_x} \delta\boldsymbol{x} \cdot \boldsymbol{t}_{rea}\ da} \tag{Eq. 4.14}$$

In (Eq. 4.14), $\delta\boldsymbol{g}$ is the variation of gap function given by (Eq. 4.3), $\boldsymbol{\nabla}\delta\boldsymbol{x}$ is virtual strain. As can be seen, now, prescribed boundary tractions $\hat{\boldsymbol{t}}$ appear in the expression, and, hence, can easily be enforced. However it seems it is still not possible to enforce prescribed positions. In addition there exists a term representing reactions, secondary variables, due to prescribed positions. We resolve these issues by imposing conditions on the form of $\delta\boldsymbol{x}$ and $\boldsymbol{x}$. We simply make $\delta\boldsymbol{x}$ belong to a function space defined as

$$\boldsymbol{\mathcal{V}} = \{\boldsymbol{w} \mid \boldsymbol{w} \in H^1,\ \boldsymbol{w} = \boldsymbol{0}\ \ \forall \boldsymbol{X} \in \Gamma_x\} \tag{Eq. 4.15}$$

With this definition the term corresponding to reactions automatically drops down from (Eq. 4.14). Next we define the function space for $\boldsymbol{x}$ as

$$\boldsymbol{\mathcal{S}} = \{\boldsymbol{u} \mid \boldsymbol{u} \in H^1,\ \boldsymbol{u} = \hat{\boldsymbol{x}}\ \ \forall \boldsymbol{X} \in \Gamma_x\} \tag{Eq. 4.16}$$

The form given by (Eq. 4.16) ensures that the solution to the weak form will respect prescribed positions too. Note that H^1, appearing in (Eq. 4.15) and (Eq. 4.16), denotes functions equipped with square-integrable derivatives up to first order. With the function spaces defined for $\delta\boldsymbol{x}$ and $\boldsymbol{x}$ at hand, we obtain the final version of the weak form as

$$\boxed{\int_\Omega \delta\boldsymbol{x} \cdot \rho\ddot{\boldsymbol{x}}\ dv + \int_\Omega \boldsymbol{\nabla}\delta\boldsymbol{x} : \boldsymbol{\sigma}\ dv + \int_{\Gamma_c} \delta\boldsymbol{g} \cdot \boldsymbol{\tau}\ da = \int_\Omega \delta\boldsymbol{x} \cdot \rho\boldsymbol{b}\ dv + \int_{\Gamma_\sigma} \delta\boldsymbol{x} \cdot \hat{\boldsymbol{t}}\ da} \tag{Eq. 4.17}$$

In mechanics, (Eq. 4.17) is called as equation of virtual work. Namely, we define

$$\begin{aligned}
\delta W^{inertia} &:= \int_{\Omega} \delta \boldsymbol{x} \cdot \rho \ddot{\boldsymbol{x}} \; dv \\
\delta W^{stress} &:= \int_{\Omega} \boldsymbol{\nabla} \delta \boldsymbol{x} : \boldsymbol{\sigma} \; dv \\
\delta W^{contact} &:= \int_{\Gamma_c} \delta \boldsymbol{g} \cdot \boldsymbol{\tau} \; da \\
\delta W^{external} &:= \int_{\Omega} \delta \boldsymbol{x} \cdot \rho \boldsymbol{b} \; dv + \int_{\Gamma_\sigma} \delta \boldsymbol{x} \cdot \hat{\boldsymbol{t}} \; da
\end{aligned} \qquad \text{(Eq. 4.18)}$$

where $\delta W^{inertia}$, δW^{stress}, $\delta W^{contact}$ and $\delta W^{external}$ are, respectively, virtual work of inertial forces, stresses, contact and external forces. By defining internal virtual work as

$$\delta W^{internal} := \delta W^{stress} + \delta W^{contact} \qquad \text{(Eq. 4.19)}$$

and plugging it, together with definitions in (Eq. 4.18), into (Eq. 4.17), we obtain

$$\delta W^{inertia} + \delta W^{internal} = \delta W^{external} \qquad \text{(Eq. 4.20)}$$

(Eq. 4.20) states that sum of the virtual work of inertial and internal forces are in equilibrium with the virtual work of external forces.

4.4 Finite Element Approximation

4.4.1 Motivation

Consider an arbitrary scalar single-valued continuous function f of single scalar argument s (see Fig. 4.2). Suppose that function values are given at n distinctive points, i.e.

$$f_i := f(s_i) \longrightarrow \text{known} \quad (i = 1, \dots, n) \qquad \text{(Eq. 4.21)}$$

and we want to compute area enclosed by f for the range $s \in [s_1, s_n]$ defined by sampling points. The expression for area is given by the integral

$$I = \int_{s_1}^{s_n} f(s) \; ds \qquad \text{(Eq. 4.22)}$$

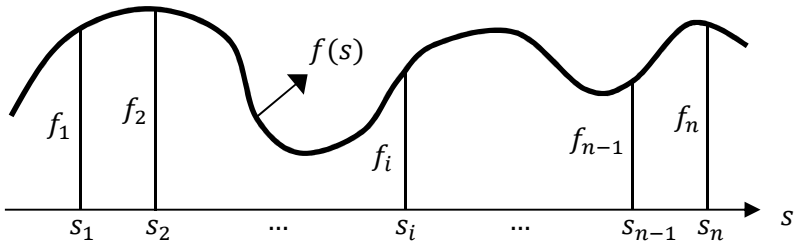

Fig. 4.2 Continuous Function

Since the form of f is not given, one has to evaluate I numerically. The first step in numerical integration is the construction of an approximation $\tilde{f} \cong f$ valid within $s \in [s_1, s_n]$. With $\tilde{f}$ at hand, the integral expression then becomes

$$I \cong \int_{s_1}^{s_n} \tilde{f}(s)\ ds \tag{Eq. 4.23}$$

With the help of sampling points, a polynomial approximation to f can be constructed as

$$\tilde{f}(s) = \sum_{i=1}^{n} u_i^p f_i \tag{Eq. 4.24}$$

where $u_i^p := u_i^p(s)$ is the interpolation (or base) polynomial of order $p < n$ associated with f_i. There are some conditions to be satisfied for the set of interpolation functions given by $\left[u_1^p,\ u_2^p,\ \cdots\ u_n^p\right]$ to be admissible. First of all interpolation functions must be linearly independent. Linear independence can be ensured by imposing the condition that

$$u_i^p(s_j) = \delta_{ij} \tag{Eq. 4.25}$$

In addition, if the function f itself is a polynomial function of order q, the approximation given by (Eq. 4.24) must be exact for $q \leq p$, i.e.

$$f(s) \overset{!}{=} \tilde{f}(s) = \sum_{i=1}^{n} u_i^p f_i \quad \Leftrightarrow \quad q \leq p \tag{Eq. 4.26}$$

For example for $q = 1$, the approximation given by (Eq. 4.24) must be exact for functions 1 and s, i.e.

$$\begin{aligned} f(s) = 1 &= \sum_{i=1}^{n} u_i^p 1 \\ f(s) = s &= \sum_{i=1}^{n} u_i^p s_i \end{aligned} \tag{Eq. 4.27}$$

Set of interpolation functions satisfying (Eq. 4.26) is called as complete. It can be shown that p th derivative, $\frac{\partial^p \tilde{f}}{\partial s^p}$, of complete interpolations assumes constant values, at least in a piecewise manner, in $s \in [s_1, s_n]$. This property is crucial to converge to the exact function in the limit as the number of sampling points goes to infinity.

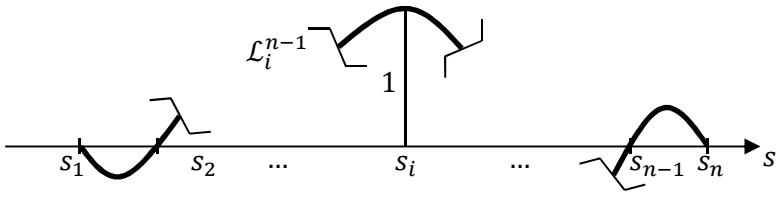

Fig. 4.3 Lagrange Polynomial $\boldsymbol{\mathcal{L}_i^{n-1}}$

4.4.2 Lagrange Polynomials

Lagrange polynomials can be used as an interpolation basis, i.e. one can choose

$$u_i^p = \mathcal{L}_i^{n-1} = \prod_{\substack{j=1 \\ j \neq i}}^{n} \frac{s - s_j}{s_i - s_j} \tag{Eq. 4.28}$$

Note that order of Lagrange polynomial is $(n-1)$ and

$$\mathcal{L}_i^{n-1}(s_j) = \delta_{ij} \tag{Eq. 4.29}$$

From (Eq. 4.25) and (Eq. 4.29) it can easily be seen that Lagrange polynomials are linearly independent. From (Eq. 4.28), Lagrange polynomials for $n = 2$, i.e. for two sampling points only, can be written as

$$\mathcal{L}_1^1 = \frac{s - s_2}{s_1 - s_2}$$
$$\mathcal{L}_2^1 = \frac{s - s_1}{s_2 - s_1} \tag{Eq. 4.30}$$

Plugging these functions into (Eq. 4.27), we obtain

$$\sum_{i=1}^{2} \mathcal{L}_i^1 = \mathcal{L}_1^1 + \mathcal{L}_2^1 = \frac{s - s_2}{s_1 - s_2} + \frac{s - s_1}{s_2 - s_1} = 1$$
$$\sum_{i=1}^{2} \mathcal{L}_i^1 s_i = \mathcal{L}_1^1 s_1 + \mathcal{L}_2^1 s_2 = \frac{s - s_2}{s_1 - s_2} s_1 + \frac{s - s_1}{s_2 - s_1} s_2 = s \tag{Eq. 4.31}$$

(Eq. 4.31) implies that interpolation basis constructed by Lagrange polynomials is complete, therefore is admissible.

4.4.3 Piecewise Polynomial Functions

Next we consider the decomposition of function domain $[s_1, s_n]$ into the union of disjoint finite elements as

$$[s_1, s_n] := \Omega = \bigcup_{i=1}^{n-1} \Omega_i \qquad \text{(Eq. 4.32)}$$

where

$$\Omega_i := [s_i, s_{i+1}] \qquad \text{(Eq. 4.33)}$$

is the region occupied by i th finite element. In addition, on purpose, we name sampling point located at $s_i (i = 1, \dots, n)$ as node i. Note that for our case we have total n nodes and $(n-1)$ finite elements. To simplify the notation we will denote i th node as nd_i and i th finite element as el_i.

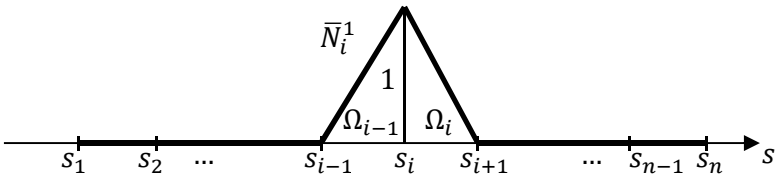

Fig. 4.4 Piecewise Linear Polynomial $\bar{\boldsymbol{N}}_{\boldsymbol{i}}^{\boldsymbol{1}}$

As can be inferred from Fig. 4.3, Lagrange interpolation function $\mathcal{L}_i^{n-1}$ does have contribution in each finite element domain, although it vanishes identically at all nodes except nd_i, where it is one. Therefore, for the evaluation of I, its integral has to be taken over the whole domain Ω, i.e.

$$I \cong \int_{s_1}^{s_n} \tilde{f}(s)\ ds = \sum_{i=1}^{n} \left[f_i \int_{s_1}^{s_n} \mathcal{L}_i^{n-1}\ ds \right] \qquad \text{(Eq. 4.34)}$$

For this reason we call approximation constructed by Lagrange polynomials as global interpolation. Integrating polynomial function $\mathcal{L}_i^{n-1}$ is easy if it is expressed in expanded form

$$\mathcal{L}_i^{n-1} = \sum_{i=1}^{n-1} c_i s^i \qquad \text{(Eq. 4.35)}$$

which requires the computation of coefficients c_i starting from (Eq. 4.28). This step is computationally demanding, especially if a new sampling point is added (refinement), or an existing one is removed (coarsening), or location of an existing one is changed (remeshing). For the partitioning defined by (Eq. 4.32), a polynomial basis resulting in local finite element level interpolation, insensitive to refinement, coarsening and remeshing, can be constructed based on piecewise linear polynomials, see Fig. 4.4, as

$$u_i^p = \bar{N}_i^1 = \begin{cases} \dfrac{s - s_{i-1}}{s_i - s_{i-1}}, & \forall s \in \Omega_{i-1} \\ \dfrac{s - s_{i+1}}{s_i - s_{i+1}}, & \forall s \in \Omega_i \\ 0, & \text{elsewhere} \end{cases} \qquad \text{(Eq. 4.36)}$$

Following the same procedure, as for Lagrange polynomials, it can be shown that piecewise linear polynomials are linearly independent and corresponding interpolation basis is complete.

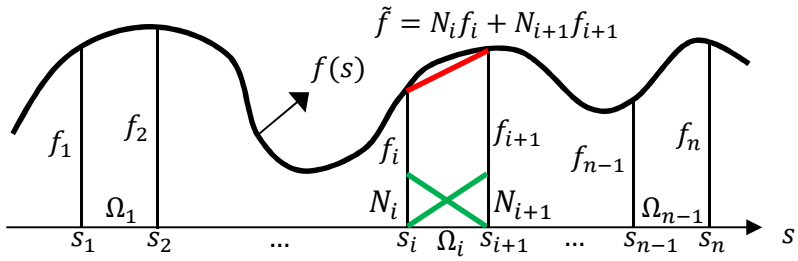

Fig. 4.5 Finite Element Interpolation

4.4.4 Finite Element Interpolation

With piecewise linear polynomials defined by (Eq. 4.36), approximation $\tilde{f}$ valid within el_i turns out to be

$$\tilde{f}(s) = N_i f_i + N_{i+1} f_{i+1} \qquad \text{(Eq. 4.37)}$$

In (Eq. 4.37), N_i and N_{i+1} are finite element interpolation functions given by

$$N_i = \frac{s - s_{i+1}}{s_i - s_{i+1}}$$
$$N_{i+1} = \frac{s - s_i}{s_{i+1} - s_i} \qquad \text{(Eq. 4.38)}$$

As can be seen from Fig. 4.5, approximation given by (Eq. 4.37) is nothing else but a straight line connecting f_i to f_{i+1}. Note also that the interpolation provided by (Eq. 4.37) is local in the sense that it only depends on the function values associated with nodes connected to el_i. Therefore the integral I can be computed as the sum of integrals evaluated over each finite element, i.e.

$$I \cong \int_{s_1}^{s_n} \tilde{f}(s)\ ds = \sum_{i=1}^{n-1} I_i \qquad \text{(Eq. 4.39)}$$

where

$$I_i := \int_{s_i}^{s_{i+1}} [N_i f_i + N_{i+1} f_{i+1}]\ ds \qquad \text{(Eq. 4.40)}$$

(Eq. 4.39) is the well-known trapezoidal rule used for numerical integration.

Evaluation of integral (Eq. 4.40) can be further simplified by coordinate transformation. For this purpose, we reparameterize s in el_i in terms of single local coordinate $\xi \in [0,1]$ as

$$s = \sum_{j=1}^{2} N_j(\xi) s_j \qquad \text{(Eq. 4.41)}$$

where s_j is the coordinate of node associated with j th local node of el_i, and $N_j(\xi)$ is corresponding coordinate interpolation function given by

$$\begin{aligned} N_1(\xi) &= 1 - \xi \\ N_2(\xi) &= \xi \end{aligned} \qquad \text{(Eq. 4.42)}$$

Jacobian of coordinate transformation, given by (Eq. 4.41), is obtained from

$$J = \frac{ds}{d\xi} = l_i \qquad \text{(Eq. 4.43)}$$

where $l_i = s_{i+1} - s_i$ is the length of el_i. By expanding (Eq. 4.41), we obtain

$$s = s_i + \xi l_i \qquad \text{(Eq. 4.44)}$$

Plugging (Eq. 4.44) into (Eq. 4.38) then, we obtain

$$\begin{aligned} N_i &= \frac{s - s_{i+1}}{s_i - s_{i+1}} = \frac{(s_i + \xi l_i) - s_{i+1}}{s_i - s_{i+1}} = \frac{-l_i + \xi l_i}{-l_i} = 1 - \xi \overset{!}{=} N_1(\xi) \\ N_{i+1} &= \frac{s - s_i}{s_{i+1} - s_i} = \frac{(s_i + \xi l_i) - s_i}{s_{i+1} - s_i} = \frac{\xi l_i}{l_i} = \xi \overset{!}{=} N_2(\xi) \end{aligned} \qquad \text{(Eq. 4.45)}$$

Note that base functions used to interpolate $\tilde{f}$ inside el_i turn out to be exactly the same as those used for coordinate interpolation. We call such elements, where dependent variables (f) and coordinate (s) are interpolated using same shape functions as isoparametric finite elements.

Within the context of (Eq. 4.43) and (Eq. 4.45), the integral expression given by (Eq. 4.40) can be rewritten as

$$I_i = \int_{s_i}^{s_{i+1}} [N_i f_i + N_{i+1} f_{i+1}] \; ds = \sum_{j=1}^{2} I_j \, f_j \qquad \text{(Eq. 4.46)}$$

where

$$I_j := \int_0^1 N_j(\xi) \;\; l_j d\xi \qquad \text{(Eq. 4.47)}$$

Within the context of isoparametric formulation, the approximation $\tilde{f}$ valid inside el_i can be expressed in a more general form as

$$\tilde{f}(s) = \sum_{j=1}^{npe} N_j(\xi) \, f_j \qquad \text{(Eq. 4.48)}$$

where, in local numbering, $N_j(\xi)$ and f_j are, respectively, isoparametric finite element shape function and function value associated with j th node of el_i, npe is number of node per finite element. For our case, $npe = 2$ and, therefore, resulting finite element shape functions are linear polynomials. To emphasize these properties, we name the underlying finite element in our example as either 2-noded or linear line element. As can be inferred from (Eq. 4.48), finite element approximation is totally independent of node locations. Node locations come into play in the computation of Jacobian which directly enters into the integral expression given by (Eq. 4.47). Therefore, refinement, coarsening and remeshing operations does not bring any complications into the finite element interpolation. Note that for subsequent developments we will denote isoparametric shape functions simply as N_j, instead of $N_j(\xi)$, for simplicity.

4.4.5 Linear Tetrahedral Finite Element

In this thesis finite element method has been used to tackle fully transient three dimensional (3D) numerical simulations of colliding bodies. Therefore there is a need to construct approximations in space based on 3D finite element discretization of the bodies. Linear tetrahedral element is the simplest, at the same time most efficient, element to perform 3D discretization. Denoting 3D position vector as $\boldsymbol{x}$, the coordinate interpolation for linear tetrahedral element can be expressed as

$$\boldsymbol{x} = \sum_{j=1}^{4} N_j \boldsymbol{x}_j \qquad \text{(Eq. 4.49)}$$

where, in local numbering, N_j and $\boldsymbol{x}_j$ are, respectively, isoparametric finite element shape function and coordinate vector associated with j th node of element. Note that linear tetrahedral element has flat faces, and therefore it is not possible to discretize curved, i.e. higher order, boundaries exactly with it. Such discretization errors can be minimized either by decreasing the element size or by increasing the approximation order around such problematic regions.

Volume coordinate associated with j th local node of tetrahedral element is defined as

$$\xi_j := \frac{V_j}{V} \tag{Eq. 4.50}$$

where V_j is the volume associated with node j, see Fig. 4.6, and V is total volume of tetrahedral element. In a similar way, one can assign a volume coordinate to each node. However one of them is redundant and can be expressed in terms of others due to the fact that

$$\sum_{j=1}^{4} \xi_j = \frac{1}{V}\sum_{j=1}^{4} V_j = \frac{V}{V} = 1 \tag{Eq. 4.51}$$

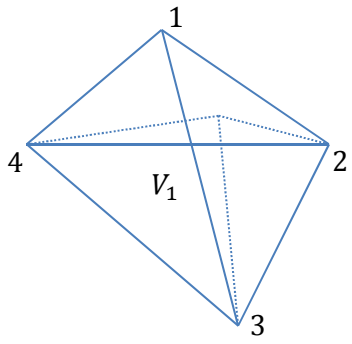

Fig. 4.6 Volume Associated with Node 1

Since there exist three independent coordinates in 3D, shape function N_j must be a function of three independent local coordinates. One can choose, without loss of generality, volume coordinates defined above as local coordinates. Then isoparametric shape functions turn out to be

$$\begin{aligned} N_1 &= \xi_1 \\ N_2 &= \xi_2 \\ N_3 &= \xi_3 = 1 - (\xi_1 + \xi_2 + \xi_4) \\ N_4 &= \xi_4 \end{aligned} \tag{Eq. 4.52}$$

where for the third shape function constraint given by (Eq. 4.51) has been employed. The reason why ξ_3 is condensed out, instead of ξ_4, is to maintain an orientation preserving mapping between

isoparametric and real coordinate spaces so that determinant of the Jacobian attains a positive value as conventional. Note also that shape function N_j varies between 0 and 1. It is equal to 1 at node j and vanishes at all other nodes of element. As discussed in section 4.4, this property of the shape functions ensures that interpolation functions are linearly independent and resulting approximation is conforming, i.e. interelement continuous.

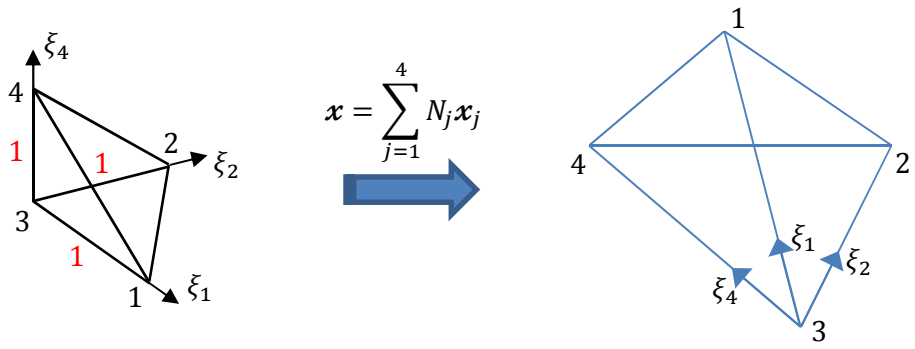

Fig. 4.7 Isoparametric Mapping

With the insertion of (Eq. 4.52), the coordinate interpolation, given by (Eq. 4.49), turns out to be

$$\boldsymbol{x} = \sum_{j=1}^{4} N_j \boldsymbol{x}_j = \boldsymbol{x}_3 + \xi_1 \boldsymbol{x}_{13} + \xi_2 \boldsymbol{x}_{23} + \xi_4 \boldsymbol{x}_{43} \qquad \text{(Eq. 4.53)}$$

where $\boldsymbol{x}_{13}$, $\boldsymbol{x}_{23}$ and $\boldsymbol{x}_{43}$ are defined as

$$\begin{aligned} \boldsymbol{x}_{13} &:= \boldsymbol{x}_1 - \boldsymbol{x}_3 \\ \boldsymbol{x}_{23} &:= \boldsymbol{x}_2 - \boldsymbol{x}_3 \\ \boldsymbol{x}_{43} &:= \boldsymbol{x}_4 - \boldsymbol{x}_3 \end{aligned} \qquad \text{(Eq. 4.54)}$$

Jacobian of the coordinate transformation is given by

$$\boldsymbol{\mathcal{J}} = \boldsymbol{\nabla} \boldsymbol{x} = \frac{\partial \boldsymbol{x}}{\partial \boldsymbol{\xi}} = x_{i,j} \mathbf{e}_i \otimes \bar{\mathbf{e}}_j \qquad \text{(Eq. 4.55)}$$

where $\boldsymbol{\nabla}$ is gradient vector associated with local coordinates, $\mathbf{e}_i$ and $\bar{\mathbf{e}}_j$ are, respectively, Cartesian and local coordinate bases and $x_{i,j} := \partial x_i / \partial \xi_j$. Note that although gradient operator appears at left-hand side of $\boldsymbol{x}$, it is applied from right as usual. By employing (Eq. 4.49) and (Eq. 4.52), (Eq. 4.55) can be expressed as

$$\boldsymbol{\mathcal{J}} = \boldsymbol{\nabla} \boldsymbol{x} = \boldsymbol{\nabla} \left(\sum_{j=1}^{4} N_j \boldsymbol{x}_j \right) = \sum_{j=1}^{4} \boldsymbol{x}_j \otimes \boldsymbol{\nabla} N_j = \boldsymbol{x}_{13} \otimes \bar{\mathbf{e}}_1 + \boldsymbol{x}_{23} \otimes \bar{\mathbf{e}}_2 + \boldsymbol{x}_{43} \otimes \bar{\mathbf{e}}_4 \qquad \text{(Eq. 4.56)}$$

Note that (Eq. 4.56) can also be derived directly from (Eq. 4.53). For subsequent developments we express (Eq. 4.56) in matrix notation as

$$\boldsymbol{\mathcal{J}} = \begin{bmatrix} \uparrow & \uparrow & \uparrow \\ \boldsymbol{x}_{13} & \boldsymbol{x}_{23} & \boldsymbol{x}_{43} \\ \downarrow & \downarrow & \downarrow \end{bmatrix} \mathbf{e}_i \otimes \bar{\mathbf{e}}_j \tag{Eq. 4.57}$$

In (Eq. 4.57), notation given by (Eq. 4.58) is used for convenience.

$$\begin{bmatrix} x_{13}^1 & & \\ x_{13}^2 & \dots & \\ x_{13}^3 & & \end{bmatrix} := \begin{bmatrix} \uparrow & & \\ \boldsymbol{x}_{13} & \dots & \\ \downarrow & & \end{bmatrix} \tag{Eq. 4.58}$$

Note that determinant of the Jacobian is equal to the triple vector product taken between $\boldsymbol{x}_{13}$, $\boldsymbol{x}_{23}$ and $\boldsymbol{x}_{43}$, i.e.

$$\det(\boldsymbol{\mathcal{J}}) = \boldsymbol{x}_{13} \cdot (\boldsymbol{x}_{23} \times \boldsymbol{x}_{43}) \tag{Eq. 4.59}$$

Triple vector product given in (Eq. 4.59) is equal to the volume of the parallelepiped formed by those vectors. Volume is positive since the corresponding vectors are properly oriented (see Fig. 4.8). Finally note that volume of parallelepiped is equal to six times the volume of tetrahedral element, i.e. we have

$$\det(\boldsymbol{\mathcal{J}}) = 6V > 0 \tag{Eq. 4.60}$$

In forthcoming sections we will need an expression for gradient vector, $\boldsymbol{\nabla}^x$, with respect to real coordinates $\boldsymbol{x}$. $\boldsymbol{\nabla}^x$ can be obtained from transformation

$$\boldsymbol{\nabla}^x = \frac{\partial}{\partial \boldsymbol{x}} = \frac{\partial}{\partial \boldsymbol{\xi}} \cdot \frac{\partial \boldsymbol{\xi}}{\partial \boldsymbol{x}} = \boldsymbol{\nabla} \cdot \boldsymbol{\mathcal{J}}^{-1} \tag{Eq. 4.61}$$

(Eq. 4.61) requires the inversion of the Jacobian. It can be obtained as follows. First we write $\boldsymbol{\mathcal{J}}^{-1}$ in matrix notation as

$$\boldsymbol{\mathcal{J}}^{-1} = \begin{bmatrix} \leftarrow & \boldsymbol{r}_1 & \rightarrow \\ \leftarrow & \boldsymbol{r}_2 & \rightarrow \\ \leftarrow & \boldsymbol{r}_4 & \rightarrow \end{bmatrix} \bar{\mathbf{e}}_i \otimes \mathbf{e}_j \tag{Eq. 4.62}$$

In (Eq. 4.62), notation given by (Eq. 4.63) is used for convenience.

$$\begin{bmatrix} r_1^1 & r_1^2 & r_1^3 \\ & \vdots & \end{bmatrix} := \begin{bmatrix} \leftarrow & \boldsymbol{r}_1 & \rightarrow \\ & \vdots & \end{bmatrix} \qquad \text{(Eq. 4.63)}$$

Since $\boldsymbol{\mathcal{J}} \cdot \boldsymbol{\mathcal{J}}^{-1} = \boldsymbol{I}$, the following relations must hold for $\boldsymbol{r}_1$

$$\left.\begin{aligned} \boldsymbol{r}_1 \cdot \boldsymbol{x}_{23} &= 0 \\ \boldsymbol{r}_1 \cdot \boldsymbol{x}_{43} &= 0 \end{aligned}\right\} \Longrightarrow \boldsymbol{r}_1 \overset{!}{=} \gamma_1 \boldsymbol{n}_1 \quad (\gamma_1 \in \mathbb{R}^1) \qquad \text{(Eq. 4.64)}$$

$$\boldsymbol{r}_1 \cdot \boldsymbol{x}_{13} = 1 \Longrightarrow \gamma_1 = \frac{1}{\boldsymbol{n}_1 \cdot \boldsymbol{x}_{13}} = \frac{A_1}{\boldsymbol{A}_1 \cdot \boldsymbol{x}_{13}} = -\frac{A_1}{6V}$$

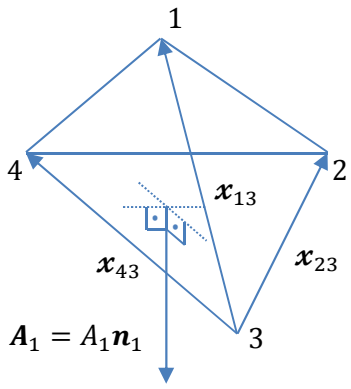

Fig. 4.8 Surface Element Associated with Node 1

In (Eq. 4.64), $\boldsymbol{n}_1$ is unit outward normal to the surface opposing node 1, A_1 is the area of that surface and $\boldsymbol{A}_1 := A_1\boldsymbol{n}_1$ is the associated surface vector (see Fig. 4.8). Applying the same procedure for $\boldsymbol{r}_2$ and $\boldsymbol{r}_4$, we finally obtain

$$\begin{aligned} \boldsymbol{r}_1 &= -\frac{1}{6V}\boldsymbol{A}_1 \\ \boldsymbol{r}_2 &= -\frac{1}{6V}\boldsymbol{A}_2 \\ \boldsymbol{r}_4 &= -\frac{1}{6V}\boldsymbol{A}_4 \end{aligned} \qquad \text{(Eq. 4.65)}$$

Taking into account (Eq. 4.62) and (Eq. 4.65), one can express $\boldsymbol{\mathcal{J}}^{-1}$ in dyadic notation as

$$\boldsymbol{\mathcal{J}}^{-1} = -\frac{1}{6V}\bar{\mathbf{e}}_1 \otimes \boldsymbol{A}_1 - \frac{1}{6V}\bar{\mathbf{e}}_2 \otimes \boldsymbol{A}_2 - \frac{1}{6V}\bar{\mathbf{e}}_4 \otimes \boldsymbol{A}_4 \qquad \text{(Eq. 4.66)}$$

With the insertion of (Eq. 4.66) into (Eq. 4.61), gradient vector $\boldsymbol{\nabla}^x$ can be put into final explicit form as

$$\boldsymbol{\nabla}^x(\dots) = -\frac{1}{6V}\frac{\partial}{\partial \xi_1}(\dots)\boldsymbol{A}_1 - \frac{1}{6V}\frac{\partial}{\partial \xi_2}(\dots)\boldsymbol{A}_2 - \frac{1}{6V}\frac{\partial}{\partial \xi_4}(\dots)\boldsymbol{A}_4 \qquad \text{(Eq. 4.67)}$$

Using (Eq. 4.67), in view of (Eq. 4.52), one can express spatial gradient of shape functions as

$$\begin{aligned}
\boldsymbol{\nabla}^x N_1 &= -\frac{1}{6V}\boldsymbol{A}_1 \\
\boldsymbol{\nabla}^x N_2 &= -\frac{1}{6V}\boldsymbol{A}_2 \\
\boldsymbol{\nabla}^x N_3 &= -\frac{1}{6V}(-\boldsymbol{A}_1 - \boldsymbol{A}_2 - \boldsymbol{A}_4) = -\frac{1}{6V}\boldsymbol{A}_3 \\
\boldsymbol{\nabla}^x N_4 &= -\frac{1}{6V}\boldsymbol{A}_4
\end{aligned} \qquad \text{(Eq. 4.68)}$$

Note that use of divergence theorem has been made for the derivation of $\boldsymbol{\nabla}^x N_3$. As can be inferred from (Eq. 4.68), spatial gradient, $\boldsymbol{\nabla}^x N_j$, of a shape function is aligned with its corresponding surface element $\boldsymbol{A}_j$. It does not come as a surprise because the shape function is constant on any plane perpendicular to $\boldsymbol{A}_j$.

4.5 Discretization of the Weak Form

To obtain the so called semi-discrete version of the weak form, we, first, construct global continuous piecewise linear interpolation functions in space based on finite element discretization of the bodies with linear tetrahedral elements. With the help of these interpolation functions, the spatial position vector $\boldsymbol{x}$ and its variation $\delta\boldsymbol{x}$ can be approximated within an element from nodal values as

$$\begin{aligned}
\boldsymbol{x} &\cong {}^h_e\boldsymbol{x} = \sum_{i=1}^{4} N_i \boldsymbol{x}_I \\
\delta\boldsymbol{x} &\cong {}^h_e\delta\boldsymbol{x} = \sum_{i=1}^{4} N_i \delta\boldsymbol{x}_I
\end{aligned} \qquad \text{(Eq. 4.69)}$$

In (Eq. 4.69), in local numbering, N_i , $\boldsymbol{x}_I$ and $\delta\boldsymbol{x}_I$ are, respectively, isoparametric finite element shape function, global position vector and its variation associated with i th node of element. $I = con(e, i)$ is a mapping between local and global node numbers for element e. Note that resulting global approximation functions ${}^h\boldsymbol{x}$ and ${}^h\delta\boldsymbol{x}$ belong to the function spaces ${}^h\boldsymbol{\mathcal{S}} \in \boldsymbol{\mathcal{S}}$ and ${}^h\boldsymbol{\mathcal{V}} \in \boldsymbol{\mathcal{V}}$, respectively, defined by

$$
{}^{h}\boldsymbol{\mathcal{S}} = \left\{ {}^{h}\boldsymbol{u} \mid \ {}^{h}\boldsymbol{u} \in H^1, \ {}^{h}\boldsymbol{u} = \hat{\boldsymbol{x}} \ \forall \boldsymbol{\mathcal{X}} \in \ {}^{h}\Gamma_x \right\}
$$

$$
{}^{h}\boldsymbol{\mathcal{V}} = \left\{ {}^{h}\boldsymbol{w} \mid \ {}^{h}\boldsymbol{w} \in H^1, \ {}^{h}\boldsymbol{w} = \boldsymbol{0} \ \forall \boldsymbol{\mathcal{X}} \in \ {}^{h}\Gamma_x \right\} \qquad \text{(Eq. 4.70)}
$$

Next based on approximations given by (Eq. 4.69), we will investigate virtual work expressions introduced by (Eq. 4.18) one by one.

4.5.1 Virtual Work Expressions

4.5.1.1 Virtual Work of Inertial Forces

Within the context of (Eq. 4.69), the element-wise approximation to particle acceleration $\ddot{\boldsymbol{x}}$ takes the form

$$
\ddot{\boldsymbol{x}} \cong {}^{h}_{e}\ddot{\boldsymbol{x}} = \sum_{i=1}^{4} N_i \ddot{\boldsymbol{x}}_I \qquad \text{(Eq. 4.71)}
$$

In (Eq. 4.71), $\ddot{\boldsymbol{x}}_I$ is acceleration vector associated with i th node of element e. With the insertion of (Eq. 4.69) and (Eq. 4.71), virtual work of the inertial forces is then approximated as

$$
\delta W^{inertia} \cong {}^{h}\delta W^{inertia} = \sum_{e=1}^{nel} {}^{h}_{e}\delta W^{inertia} \qquad \text{(Eq. 4.72)}
$$

where

$$
{}^{h}_{e}\delta W^{inertia} := \int_{{}^{h}_{e}\Omega} {}^{h}_{e}\delta \boldsymbol{x} \cdot \rho_e \, {}^{h}_{e}\ddot{\boldsymbol{x}} \ dv = \sum_{i=1}^{4} \left[\delta \boldsymbol{x}_I \cdot \sum_{j=1}^{4} \left[\int_{{}^{h}_{e}\Omega} \rho_e N_i N_j \ddot{\boldsymbol{x}}_J \ dv \right] \right] \qquad \text{(Eq. 4.73)}
$$

and nel is total number of finite elements.

Next mass lumping based on row-sum technique is applied (Hughes 2012). In row-sum technique, it is assumed that while evaluating expression in bracket for i th node in (Eq. 4.73), all nodes of the element have the same acceleration which is equal to the acceleration of i th node, i.e.

$$
\ddot{\boldsymbol{x}}_J (j = 1, \dots, 4) = \ddot{\boldsymbol{x}}_I \qquad \text{(Eq. 4.74)}
$$

Then by inserting (Eq. 4.74) into (Eq. 4.73) we end up with

$$
{}^{h}_{e}\delta W^{inertia} = \sum_{i=1}^{4} \left[\delta \boldsymbol{x}_I \cdot \left[\int_{{}^{h}_{e}\Omega} \rho_e N_i \sum_{j=1}^{4} N_j \ dv \right] \ddot{\boldsymbol{x}}_I \right] = \sum_{i=1}^{4} \delta \boldsymbol{x}_I \cdot \boldsymbol{f}_I^{inertia} \qquad \text{(Eq. 4.75)}
$$

where

$$
\boldsymbol{f}_I^{inertia} := m_I \ddot{\boldsymbol{x}}_I \qquad \text{(Eq. 4.76)}
$$

with

$$m_I := \int_{{}^h_e\Omega} \rho_e N_i \; dv = \frac{\rho_e V_e}{4} = \frac{m_e}{4} \tag{Eq. 4.77}$$

In (Eq. 4.76), $\boldsymbol{f}_I^{inertia}$ and m_I are, respectively, inertial force vector and mass associated with i th node of element e. In obtaining (Eq. 4.77), we make use of partition of unity property of finite element shape functions, i.e.

$$\sum_{j=1}^{4} N_j = 1 \tag{Eq. 4.78}$$

Recall that (Eq. 4.78) implies completeness of underlying interpolation functions. In addition the integral in (Eq. 4.77) has been computed using the formula

$$\int_{{}^h_e\Omega} N_1^a N_2^b N_3^c N_4^d \; dv = \frac{a!\, b!\, c!\, d!}{(a+b+c+3)!} 6V_e \tag{Eq. 4.79}$$

where a, b, c and d are all non-negative integers. Note also that mass of the element is distributed equally over its nodes.

4.5.1.2 Virtual Work of Stresses

In view of (Eq. 4.68) and (Eq. 4.69), the element-wise approximation to virtual strain $\boldsymbol{\nabla}\delta\boldsymbol{x}$ can be expressed as

$$\boldsymbol{\nabla}\delta\boldsymbol{x} \cong \boldsymbol{\nabla}_e^h \delta\boldsymbol{x} = \sum_{i=1}^{4} \delta\boldsymbol{x}_I \otimes \boldsymbol{\nabla}^{\boldsymbol{x}} N_i = -\frac{1}{6V_e} \sum_{i=1}^{4} \delta\boldsymbol{x}_I \otimes \boldsymbol{A}_i \tag{Eq. 4.80}$$

With the insertion of (Eq. 4.69) and (Eq. 4.80), virtual work of the stresses is then approximated as

$$\delta W^{stress} \cong {}^h\delta W^{stress} = \sum_{e=1}^{nel} {}^h_e\delta W^{stress} \tag{Eq. 4.81}$$

where

$${}^h_e\delta W^{stress} := \int_{{}^h_e\Omega} \boldsymbol{\nabla}_e^h \delta\boldsymbol{x} : \boldsymbol{\sigma}_e \; dv = \sum_{i=1}^{4} \delta\boldsymbol{x}_I \cdot \boldsymbol{f}_I^{stress} \tag{Eq. 4.82}$$

Assuming that $\boldsymbol{\sigma}_e$ is constant inside element domain, we obtain

$$\boldsymbol{f}_I^{stress} := -\frac{1}{6V_e} \int_{{}^h_e\Omega} \boldsymbol{\sigma}_e \cdot \boldsymbol{A}_i \; dv = -\boldsymbol{\sigma}_e \cdot \boldsymbol{A}_i = -\boldsymbol{t}_i A_i \tag{Eq. 4.83}$$

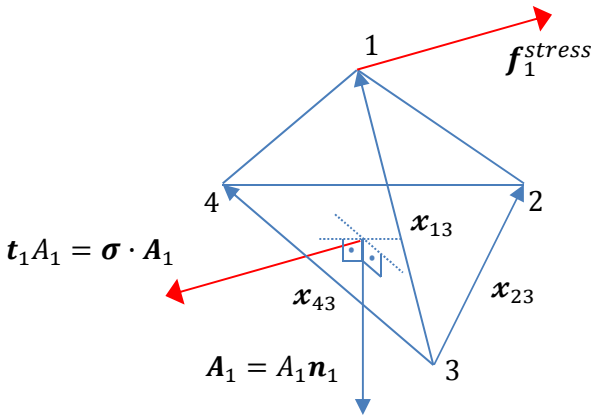

Fig. 4.9 Internal Force due to Stress Associated with Node 1

In (Eq. 4.83), $\boldsymbol{f}_I^{stress}$ is the internal force vector due to stress associated with i th node of element e. As can be inferred from (Eq. 4.83), $\boldsymbol{f}_I^{stress}$ is nothing else but the minus traction force acting on opposite face oriented with surface element $\boldsymbol{A}_i$ (see Fig. 4.9). (Eq. 4.83) reveals the fact that linear tetrahedral element behaves like a material particle contained within a finite volume. Therefore one expects to recover exact solution in the limit as the element size goes to zero. It is also noteworthy to point out that (Eq. 4.83) also implies equilibrium of nodal internal forces at element level, i.e.

$$\sum_{i=1}^{4} \boldsymbol{f}_I^{stress} = \sum_{i=1}^{4} -\boldsymbol{\sigma}_e \cdot \boldsymbol{A}_i = -\boldsymbol{\sigma}_e \cdot \sum_{i=1}^{4} \boldsymbol{A}_i = -\boldsymbol{\sigma}_e \cdot \boldsymbol{0} = \boldsymbol{0} \qquad \text{(Eq. 4.84)}$$

4.5.1.3 Virtual Work of Contact Forces

4.5.1.3.1 Finite Element Approximation

The approximation to the gap function $\boldsymbol{g}$ and its variation $\delta\boldsymbol{g}$ can be written as

$$\begin{aligned} \boldsymbol{g} &\cong {}^{h}\boldsymbol{g} = {}^{h}\overline{\boldsymbol{x}}^{2} - {}^{h}\overline{\boldsymbol{x}}^{1} \\ \delta\boldsymbol{g} &\cong {}^{h}\delta\boldsymbol{g} = {}^{h}\delta\overline{\boldsymbol{x}}^{2} - {}^{h}\delta\overline{\boldsymbol{x}}^{1} \end{aligned} \qquad \text{(Eq. 4.85)}$$

In reality, it is impossible to construct a finite element discretization which is conforming along the contact boundary Γ_c all the time, especially in the large deformation regime. Therefore the equivalence of the contact boundaries Γ_c^1 and Γ_c^2 during contact, which holds for continuous formulation, is not valid anymore in discrete setting. Furthermore, in addition to space discretization based on finite elements, as will be discussed in forthcoming sections, we also discretize time domain, usually, by employing finite difference schemes. Due to discrete nature of time it is also impossible to capture exact instance where the contact takes place between generic particles $\overline{\mathcal{P}}^1$

and $\bar{\mathcal{P}}^2$. Actually from numerical standpoint we need the violation of impenetrability constraint, i.e. $\boldsymbol{g} \cdot \mathbf{n} < 0$, to be able to detect and then handle contact numerically. These problems, introduced due to discretization errors in space and time, calls for the development of well-posed numerical techniques for contact formulation. The simplest and widely used approach is the employment of an auxiliary contact discretization based on so-called node-to-surface (NTS) finite elements (Wriggers 2006). One can then formulate contact problem, taking Γ_c^1 as reference, on this overlaying discretization and compute contact contributions. In this approach gap function is constructed using the penetrated particles from body $\mathcal{B}^2$ positioned at the boundary nodes belonging to Γ_c^2 only. Confronting particle, however, can be arbitrarily located on the contact boundary Γ_c^1. One can then approximate to particle position $\bar{\boldsymbol{x}}^1$ and its variation $\delta\bar{\boldsymbol{x}}^1$ by taking into account the fact that a material particle which is in contact must be positioned inside an element face located on contact boundary Γ_c^1. Then one can resort to two-dimensional (2D) isoparametric shape functions associated with corresponding linear triangular element to construct necessary approximations.

Similar to linear tetrahedral element, one can define area coordinates for linear triangular element as

$$\zeta_i := \frac{A_i}{A} \tag{Eq. 4.86}$$

where A_i is the area associated with i th node of element and A is total area of triangular element (see Fig. 4.10). Following the same procedure, as for linear tetrahedral element, the isoparametric shape functions for linear triangular element are obtained as

$$\begin{aligned} N_1(\boldsymbol{\zeta}) &= \zeta_1 \\ N_2(\boldsymbol{\zeta}) &= \zeta_2 \\ N_3(\boldsymbol{\zeta}) &= \zeta_3 = 1 - (\zeta_1 + \zeta_2) \end{aligned} \tag{Eq. 4.87}$$

By denoting the local coordinates of contacting particle $\bar{\mathcal{P}}^1$ as $\bar{\boldsymbol{\zeta}} = (\bar{\zeta}_1, \bar{\zeta}_2)$ and in view of (Eq. 4.87), the approximations to $\bar{\boldsymbol{x}}^1$ and $\delta\bar{\boldsymbol{x}}^1$ are expressed as

$$\begin{aligned} \bar{\boldsymbol{x}}^1 &\cong {}^h\bar{\boldsymbol{x}}^1 = \sum_{i=1}^{3} \bar{N}_i \boldsymbol{x}_I^1 \\ \delta\bar{\boldsymbol{x}}^1 &\cong {}^h\delta\bar{\boldsymbol{x}}^1 = \sum_{i=1}^{3} \bar{N}_i \delta\boldsymbol{x}_I^1 \end{aligned} \tag{Eq. 4.88}$$

In (Eq. 4.88), $\bar{N}_i = N_i(\bar{\boldsymbol{\zeta}})$, $\boldsymbol{x}_I$ and $\delta\boldsymbol{x}_I$ are, respectively, position vector and its variation associated with i th node of triangular element e. As pointed out earlier, due to discrete nature of time it is not

possible to fulfill impenetrability constraint exactly at discrete time points. We can only figure out, with the help of gap function and by performing in-out or projection tests, that particle $\bar{\mathcal{P}}^2$ has penetrated into body $\mathcal{B}^1$ within a given time increment. The task is then to set up a numerical procedure such that contact constraints will have been satisfied, almost exactly, at the end of time increment.

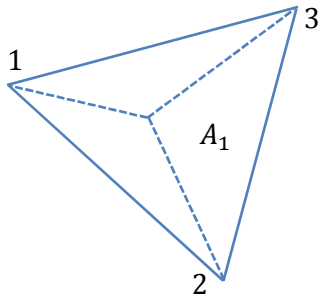

Fig. 4.10 Area Associated with Node 1

4.5.1.3.2 Computation of Local Coordinates

If it is found that $\bar{\mathcal{P}}^2$ has penetrated, one can then compute, approximately, local coordinates $\bar{\boldsymbol{\zeta}}$ by employing one of the two alternative methods which will be discussed next.

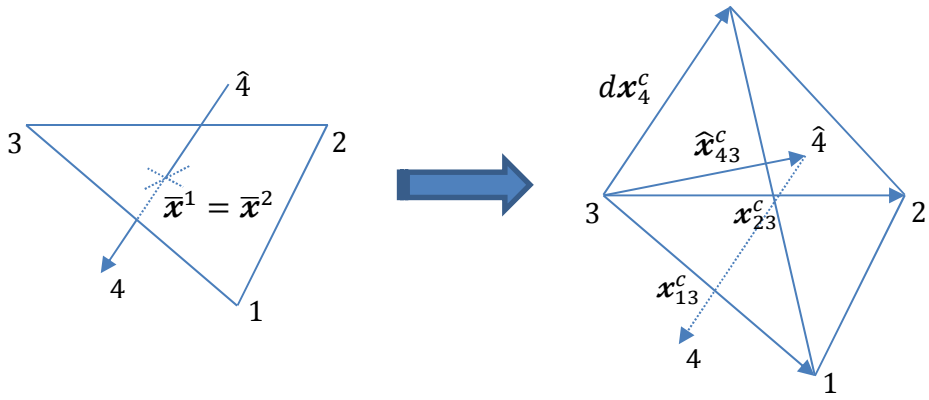

Fig. 4.11 Line-Surface Intersection. Analogy with Tetrahedral Element

4.5.1.3.2.1 Line-Surface Intersection (LSI)

Local coordinates $\bar{\boldsymbol{\zeta}}$ can be set using the position of $\bar{\mathcal{P}}^2$ at the beginning and end of corresponding generic time increment $\Delta t^k := t^{k+1} - t^k$. By assuming that the trajectory of $\bar{\mathcal{P}}^2$ is a straight line within Δt^k, its position can be approximated as

$$\boldsymbol{x}^2 \cong (1-\beta)\ {}^k\boldsymbol{x}^2 + \beta\ {}^{k+1}_{p}\boldsymbol{x}^2 \qquad \text{(Eq. 4.89)}$$

where k and $k+1$ denote time steps at the beginning and end of generic time increment Δt^k, superscript p stands for predicted position and $\beta \in [0,1]$ is local coordinate introduced to interpolate position of particle $\bar{\mathcal{P}}^2$ within Δt^k. With (Eq. 4.89) at hand, $\bar{\boldsymbol{\zeta}}$ can be determined uniquely by solving the resulting line-surface intersection problem, see Fig. 4.11, which reads as

$$\bar{\boldsymbol{x}}^2 - \bar{\boldsymbol{x}}^1 = \mathbf{0}$$

$$\bar{\boldsymbol{x}}^2 = {}^k\boldsymbol{x}^2 + \bar{\beta}\left({}^{k+1}_{p}\boldsymbol{x}^2 - {}^k\boldsymbol{x}^2\right) \tag{Eq. 4.90}$$

$$\bar{\boldsymbol{x}}^1 = {}^{k+1}_{p}\boldsymbol{x}^1_{con(e,3)} + \bar{\zeta}_1\,{}^{k+1}_{p}\boldsymbol{x}^1_{13} + \bar{\zeta}_2\,{}^{k+1}_{p}\boldsymbol{x}^1_{23}$$

where ${}^{k+1}_{p}\boldsymbol{x}^1_{ij} := {}^{k+1}_{p}\boldsymbol{x}^1_{con(e,i)} - {}^{k+1}_{p}\boldsymbol{x}^1_{con(e,j)}$. To simplify expressions we introduce following notation for node positions, namely

$$\begin{aligned}
\boldsymbol{x}^c_1 &:= {}^{k+1}_{p}\boldsymbol{x}^1_{con(e,1)} \\
\boldsymbol{x}^c_2 &:= {}^{k+1}_{p}\boldsymbol{x}^1_{con(e,2)} \\
\boldsymbol{x}^c_3 &:= {}^{k+1}_{p}\boldsymbol{x}^1_{con(e,3)} \\
\boldsymbol{x}^c_4 &:= {}^{k+1}_{p}\boldsymbol{x}^2
\end{aligned} \tag{Eq. 4.91}$$

and denote ${}^k\boldsymbol{x}^2$ as $\hat{\boldsymbol{x}}^c_4$ to imply that it is a known quantity coming from previous time step. With the insertion of (Eq. 4.91), (Eq. 4.90) can then be expressed as

$$\hat{\boldsymbol{x}}^c_4 + \bar{\beta}(\boldsymbol{x}^c_4 - \hat{\boldsymbol{x}}^c_4) = \boldsymbol{x}^c_3 + \bar{\zeta}_1\,\boldsymbol{x}^c_{13} + \bar{\zeta}_2\,\boldsymbol{x}^c_{23} \tag{Eq. 4.92}$$

With the definitions

$$\begin{aligned}
\hat{\boldsymbol{x}}^c_{43} &:= \hat{\boldsymbol{x}}^c_4 - \boldsymbol{x}^c_3 \\
d\boldsymbol{x}^c_4 &:= \hat{\boldsymbol{x}}^c_4 - \boldsymbol{x}^c_4 \\
\bar{\boldsymbol{\eta}} &:= [\bar{\zeta}_1 \quad \bar{\zeta}_2 \quad \bar{\beta}]^T
\end{aligned} \tag{Eq. 4.93}$$

(Eq. 4.92) can be put into matrix form as

$$\hat{\boldsymbol{x}}^c_{43} = \boldsymbol{K}\bar{\boldsymbol{\eta}} \tag{Eq. 4.94}$$

where $\boldsymbol{K}$ is defined as

$$\boldsymbol{K} = \begin{bmatrix} \uparrow & \uparrow & \uparrow \\ \boldsymbol{x}^c_{13} & \boldsymbol{x}^c_{23} & d\boldsymbol{x}^c_4 \\ \downarrow & \downarrow & \downarrow \end{bmatrix} \mathbf{e}_i \otimes \bar{\mathbf{e}}_j = \boldsymbol{x}^c_{13} \otimes \bar{\mathbf{e}}_1 + \boldsymbol{x}^c_{23} \otimes \bar{\mathbf{e}}_2 + d\boldsymbol{x}^c_4 \otimes \bar{\mathbf{e}}_4 \tag{Eq. 4.95}$$

Finally, $\bar{\boldsymbol{\eta}}$ is obtained from

$$\bar{\boldsymbol{\eta}} = \boldsymbol{K}^{-1}\hat{\boldsymbol{x}}_{43}^{c} \tag{Eq. 4.96}$$

$\boldsymbol{K}^{-1}$ can easily be computed analytically, in correlation with linear tetrahedral element, as

$$\boldsymbol{K}^{-1} = -\frac{1}{6V^{c}}\begin{bmatrix} \leftarrow & \boldsymbol{A}_1^{c} & \rightarrow \\ \leftarrow & \boldsymbol{A}_2^{c} & \rightarrow \\ \leftarrow & \boldsymbol{A}_4^{c} & \rightarrow \end{bmatrix}\bar{\mathbf{e}}_i \otimes \mathbf{e}_j = -\frac{1}{6V^{c}}[\bar{\mathbf{e}}_1 \otimes \boldsymbol{A}_1^{c} + \bar{\mathbf{e}}_2 \otimes \boldsymbol{A}_2^{c} + \bar{\mathbf{e}}_4 \otimes \boldsymbol{A}_4^{c}] \tag{Eq. 4.97}$$

where $6V^{c} = \boldsymbol{x}_{13}^{c} \cdot (\boldsymbol{x}_{23}^{c} \times d\boldsymbol{x}_{4}^{c})$ and

$$\begin{aligned} \boldsymbol{A}_1^{c} &= -\boldsymbol{x}_{23}^{c} \times d\boldsymbol{x}_{4}^{c} \\ \boldsymbol{A}_2^{c} &= -d\boldsymbol{x}_{4}^{c} \times \boldsymbol{x}_{13}^{c} \\ \boldsymbol{A}_4^{c} &= -\boldsymbol{x}_{13}^{c} \times \boldsymbol{x}_{23}^{c} \end{aligned} \tag{Eq. 4.98}$$

With the insertion of (Eq. 4.97) into (Eq. 4.96), $\bar{\boldsymbol{\zeta}}$ is computed as

$$\bar{\boldsymbol{\zeta}} = \bar{\zeta}_1\bar{\mathbf{e}}_1 + \bar{\zeta}_2\bar{\mathbf{e}}_2 = \left[-\frac{1}{6V^{c}}\boldsymbol{A}_1^{c} \cdot \hat{\boldsymbol{x}}_{43}^{c}\right]\bar{\mathbf{e}}_1 + \left[-\frac{1}{6V^{c}}\boldsymbol{A}_2^{c} \cdot \hat{\boldsymbol{x}}_{43}^{c}\right]\bar{\mathbf{e}}_2 \tag{Eq. 4.99}$$

4.5.1.3.2.2 Closest-Point Projection (CPP)

Conventionally, local coordinates $\bar{\boldsymbol{\zeta}}$ are set as those corresponding to closest-point (CP) on triangular element to $\boldsymbol{x}_4^{c}$. CP is obtained by normal projection of $\boldsymbol{x}_4^{c}$ onto triangular element (see Fig. 4.12). A vector is said to be perpendicular to a given plane if it is perpendicular to two linearly independent vectors located on that plane (see Fig. 4.12). Based on this definition, CPP problem can be formulated, with the help of linearly independent vectors $\boldsymbol{x}_{13}^{c}$ and $\boldsymbol{x}_{23}^{c}$, as

$$\begin{aligned} (\boldsymbol{x}_4^{c} - \boldsymbol{x}_P^{c}) \cdot \boldsymbol{x}_{13}^{c} &= 0 \\ (\boldsymbol{x}_4^{c} - \boldsymbol{x}_P^{c}) \cdot \boldsymbol{x}_{23}^{c} &= 0 \\ \boldsymbol{x}_P^{c} &= \boldsymbol{x}_3^{c} + \bar{\zeta}_1\,\boldsymbol{x}_{13}^{c} + \bar{\zeta}_2\,\boldsymbol{x}_{23}^{c} \end{aligned} \tag{Eq. 4.100}$$

where $\boldsymbol{x}_P^{c}$ is the position of particle obtained from CPP. Plugging third equation into first and second one in (Eq. 4.100) and after making some arrangements, we end up with system of linear equations as

$$\boldsymbol{b} = \boldsymbol{K}\bar{\boldsymbol{\zeta}} \tag{Eq. 4.101}$$

where

$$\boldsymbol{b} := \begin{bmatrix} b_1 \\ b_2 \end{bmatrix} = \begin{bmatrix} \boldsymbol{x}_{43}^c \cdot \boldsymbol{x}_{13}^c \\ \\ \boldsymbol{x}_{43}^c \cdot \boldsymbol{x}_{23}^c \end{bmatrix} \tag{Eq. 4.102}$$

and

$$\boldsymbol{K} := \begin{bmatrix} k_{11} & k_{12} \\ \\ k_{21} & k_{22} \end{bmatrix} = \begin{bmatrix} \boldsymbol{x}_{13}^c \cdot \boldsymbol{x}_{13}^c & \boldsymbol{x}_{23}^c \cdot \boldsymbol{x}_{13}^c \\ \\ \boldsymbol{x}_{13}^c \cdot \boldsymbol{x}_{23}^c & \boldsymbol{x}_{23}^c \cdot \boldsymbol{x}_{23}^c \end{bmatrix} \tag{Eq. 4.103}$$

$\bar{\boldsymbol{\zeta}}$ is then obtained from (Eq. 4.101) as

$$\bar{\boldsymbol{\zeta}} = \boldsymbol{K}^{-1}\boldsymbol{b} \tag{Eq. 4.104}$$

Determinant of $\boldsymbol{K}$ is given by expression

$$\det \boldsymbol{K} = \ k_{11}k_{22} - k_{12}k_{21} \tag{Eq. 4.105}$$

By applying standard vector algebra it can be shown that

$$\det \boldsymbol{K} = 4A^2 \tag{Eq. 4.106}$$

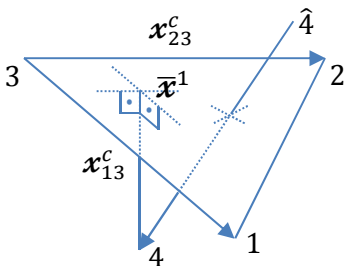

Fig. 4.12 Closest-Point Projection

With the insertion of (Eq. 4.105), $\boldsymbol{K}^{-1}$ is obtained as

$$\boldsymbol{K}^{-1} = \frac{1}{k_{11}k_{22} - k_{12}k_{21}} \begin{bmatrix} k_{22} & -k_{12} \\ \\ -k_{21} & k_{11} \end{bmatrix} = \frac{1}{4A^2} \begin{bmatrix} \boldsymbol{x}_{23}^c \cdot \boldsymbol{x}_{23}^c & -\boldsymbol{x}_{13}^c \cdot \boldsymbol{x}_{23}^c \\ \\ -\boldsymbol{x}_{23}^c \cdot \boldsymbol{x}_{13}^c & \boldsymbol{x}_{13}^c \cdot \boldsymbol{x}_{13}^c \end{bmatrix} \tag{Eq. 4.107}$$

Plugging (Eq. 4.102) and (Eq. 4.107) into (Eq. 4.104), $\bar{\boldsymbol{\zeta}}$ is computed analytically as

$$\bar{\boldsymbol{\zeta}} = \frac{1}{4A^2} \begin{bmatrix} \boldsymbol{x}_{23}^c \cdot \boldsymbol{x}_{23}^c & -\boldsymbol{x}_{13}^c \cdot \boldsymbol{x}_{23}^c \\ \\ -\boldsymbol{x}_{23}^c \cdot \boldsymbol{x}_{13}^c & \boldsymbol{x}_{13}^c \cdot \boldsymbol{x}_{13}^c \end{bmatrix} \begin{bmatrix} \boldsymbol{x}_{43}^c \cdot \boldsymbol{x}_{13}^c \\ \\ \boldsymbol{x}_{43}^c \cdot \boldsymbol{x}_{23}^c \end{bmatrix} \tag{Eq. 4.108}$$

4.5.1.3.3 Node-To-Surface (NTS) Contact Finite Element

Next, after computing $\bar{\boldsymbol{\zeta}}$, we carry the information provided by (Eq. 4.88), which is extracted from underlying 3D discretization, together with penetrating particle $\bar{\mathcal{P}}^2$ to the contact discretization and construct corresponding 4-node NTS contact finite element which is compatible with linear tetrahedra. To achieve this goal, first of all, we introduce another mapping, given by (Eq. 4.109), in addition to that introduced by (Eq. 4.91).

$$\begin{aligned}
\bar{\alpha}_1(\bar{\boldsymbol{\zeta}}) &= -\bar{N}_1 = -\bar{\zeta}_1 \\
\bar{\alpha}_2(\bar{\boldsymbol{\zeta}}) &= -\bar{N}_2 = -\bar{\zeta}_2 \\
\bar{\alpha}_3(\bar{\boldsymbol{\zeta}}) &= -\bar{N}_3 = -[1-(\bar{\zeta}_1+\bar{\zeta}_2)] \\
\bar{\alpha}_4(\bar{\boldsymbol{\zeta}}) &= 1
\end{aligned} \tag{Eq. 4.109}$$

With the notations provided by (Eq. 4.91) and (Eq. 4.109) at hand, one can rewrite (Eq. 4.85) as

$$\begin{aligned}
\boldsymbol{g} \cong \ {}^h\boldsymbol{g} &= \sum_{i=1}^{4} \bar{\alpha}_i \boldsymbol{x}_I^c \\
\delta\boldsymbol{g} \cong \ {}^h\delta\boldsymbol{g} &= \sum_{i=1}^{4} \bar{\alpha}_i \delta\boldsymbol{x}_I^c + \sum_{i=1}^{4} \delta\bar{\alpha}_i \boldsymbol{x}_I^c
\end{aligned} \tag{Eq. 4.110}$$

The form given by (Eq. 4.110) is useful especially in computing contact contributions to the connected nodes. In (Eq. 4.110), $\delta\bar{\alpha}_i$ is the variation of $\bar{\alpha}_i$ and can be computed from

$$\delta\bar{\alpha}_i = \boldsymbol{\nabla}\bar{\alpha}_i \cdot \delta\bar{\boldsymbol{\zeta}} \tag{Eq. 4.111}$$

Within the context of (Eq. 4.109) and (Eq. 4.111), we obtain

$$\begin{aligned}
\delta\bar{\alpha}_1 &= -\delta\bar{\zeta}_1 \\
\delta\bar{\alpha}_2 &= -\delta\bar{\zeta}_2 \\
\delta\bar{\alpha}_3 &= \delta\bar{\zeta}_1 + \delta\bar{\zeta}_2 \\
\delta\bar{\alpha}_4 &= 0
\end{aligned} \tag{Eq. 4.112}$$

With the insertion of (Eq. 4.112), ${}^h\delta\boldsymbol{g}$ then takes the form

$${}^h\delta\boldsymbol{g} = \sum_{i=1}^{4} \bar{\alpha}_i \delta\boldsymbol{x}_I^c - \delta\bar{\zeta}_1 \boldsymbol{x}_{13}^c - \delta\bar{\zeta}_2 \boldsymbol{x}_{23}^c \tag{Eq. 4.113}$$

4.5.1.3.4 Computation of Variation of Local Coordinates

As can be inferred from (Eq. 4.113), one needs an explicit expression for the variation of local coordinates $\bar{\boldsymbol{\zeta}}$ in order to compute ${}^{h}\delta\boldsymbol{g}$. For completeness we will derive expressions for $\delta\bar{\boldsymbol{\zeta}}$ based on LSI and CPP.

4.5.1.3.4.1 Based on LSI

$\delta\bar{\boldsymbol{\zeta}}$ can easily be computed by exploiting (Eq. 4.94). Taking the variation of both sides in (Eq. 4.94), we end up with

$$\delta\hat{\boldsymbol{x}}_{43}^{c} = \delta\boldsymbol{K}\bar{\boldsymbol{\eta}} + \boldsymbol{K}\delta\bar{\boldsymbol{\eta}} \tag{Eq. 4.114}$$

From (Eq. 4.114), $\delta\bar{\boldsymbol{\eta}}$ is then obtained as

$$\delta\bar{\boldsymbol{\eta}} = \boldsymbol{K}^{-1}(\delta\hat{\boldsymbol{x}}_{43}^{c} - \delta\boldsymbol{K}\bar{\boldsymbol{\eta}}) \tag{Eq. 4.115}$$

In view of (Eq. 4.95), $\delta\boldsymbol{K}$ is expressed as

$$\delta\boldsymbol{K} = \begin{bmatrix} \uparrow & \uparrow & \uparrow \\ \delta\boldsymbol{x}_{13}^{c} & \delta\boldsymbol{x}_{23}^{c} & \delta d\boldsymbol{x}_{4}^{c} \\ \downarrow & \downarrow & \downarrow \end{bmatrix} \mathbf{e}_i \otimes \bar{\mathbf{e}}_j \tag{Eq. 4.116}$$

Within the context of (Eq. 4.93) and (Eq. 4.116), the bracket term in (Eq. 4.115) is expressed as

$$\delta\hat{\boldsymbol{x}}_{43}^{c} - \delta\boldsymbol{K}\bar{\boldsymbol{\eta}} = \bar{\beta}\delta\boldsymbol{x}_{4}^{c} - \delta\boldsymbol{x}_{3}^{c} - \bar{\zeta}_1\delta\boldsymbol{x}_{13}^{c} - \bar{\zeta}_2\delta\boldsymbol{x}_{23}^{c} = \sum_{i=1}^{4}\tilde{\alpha}_i\delta\boldsymbol{x}_{I}^{c} \tag{Eq. 4.117}$$

where coefficients $\tilde{\alpha}_i$ are defined as

$$\begin{aligned} \tilde{\alpha}_1 &= \bar{\alpha}_1 \\ \tilde{\alpha}_2 &= \bar{\alpha}_2 \\ \tilde{\alpha}_3 &= \bar{\alpha}_3 \\ \tilde{\alpha}_4 &= \bar{\beta} \end{aligned} \tag{Eq. 4.118}$$

Note that coefficients $\bar{\alpha}_i$ and $\tilde{\alpha}_i$ are identical if and only if $\bar{\beta} = 1$. With the insertion of (Eq. 4.97) and (Eq. 4.117) into (Eq. 4.115), $\delta\bar{\boldsymbol{\zeta}}$ is obtained as

$$\delta\bar{\boldsymbol{\zeta}} = -\frac{1}{6V^{c}}\sum_{i=1}^{2}\left[\bar{\mathbf{e}}_i \otimes \sum_{j=1}^{4}\boldsymbol{A}_{i}^{c}\cdot\tilde{\alpha}_j\delta\boldsymbol{x}_{j}^{c}\right] \tag{Eq. 4.119}$$

Inserting (Eq. 4.119) into (Eq. 4.113), we finally end up with

$$ {}^{h}\delta \boldsymbol{g} = \sum_{i=1}^{4} \bar{\alpha}_i \delta \boldsymbol{x}_I^c + \frac{1}{6V^c} \left\{ \left[\sum_{i=1}^{4} \boldsymbol{A}_1^c \cdot \tilde{\alpha}_i \delta \boldsymbol{x}_I^c \right] \boldsymbol{x}_{13}^c + \left[\sum_{i=1}^{4} \boldsymbol{A}_2^c \cdot \tilde{\alpha}_i \delta \boldsymbol{x}_I^c \right] \boldsymbol{x}_{23}^c \right\} \quad \text{(Eq. 4.120)} $$

4.5.1.3.4.2 Based on CPP

One can make use of (Eq. 4.101) to compute $\delta\bar{\boldsymbol{\zeta}}$. Taking the variation of both sides in (Eq. 4.101), we obtain

$$ \delta \boldsymbol{b} = \delta \boldsymbol{K} \bar{\boldsymbol{\zeta}} + \boldsymbol{K} \delta \bar{\boldsymbol{\zeta}} \quad \text{(Eq. 4.121)} $$

From (Eq. 4.121), $\delta\bar{\boldsymbol{\zeta}}$ can be extracted as

$$ \delta \bar{\boldsymbol{\zeta}} = \boldsymbol{K}^{-1} (\delta \boldsymbol{b} - \delta \boldsymbol{K} \bar{\boldsymbol{\zeta}}) \quad \text{(Eq. 4.122)} $$

In view of (Eq. 4.102) and (Eq. 4.103), $\delta\boldsymbol{b}$ and $\delta\boldsymbol{K}$ are expressed as

$$ \delta \boldsymbol{b} = \begin{bmatrix} \delta \boldsymbol{x}_{43}^c \cdot \boldsymbol{x}_{13}^c \\ \\ \delta \boldsymbol{x}_{43}^c \cdot \boldsymbol{x}_{23}^c \end{bmatrix} + \begin{bmatrix} \boldsymbol{x}_{43}^c \cdot \delta \boldsymbol{x}_{13}^c \\ \\ \boldsymbol{x}_{43}^c \cdot \delta \boldsymbol{x}_{23}^c \end{bmatrix} \quad \text{(Eq. 4.123)} $$

$$ \delta \boldsymbol{K} := \begin{bmatrix} \delta \boldsymbol{x}_{13}^c \cdot \boldsymbol{x}_{13}^c & \delta \boldsymbol{x}_{13}^c \cdot \boldsymbol{x}_{23}^c \\ \\ \delta \boldsymbol{x}_{23}^c \cdot \boldsymbol{x}_{13}^c & \delta \boldsymbol{x}_{23}^c \cdot \boldsymbol{x}_{23}^c \end{bmatrix} + \begin{bmatrix} \boldsymbol{x}_{13}^c \cdot \delta \boldsymbol{x}_{13}^c & \boldsymbol{x}_{13}^c \cdot \delta \boldsymbol{x}_{23}^c \\ \\ \boldsymbol{x}_{23}^c \cdot \delta \boldsymbol{x}_{13}^c & \boldsymbol{x}_{23}^c \cdot \delta \boldsymbol{x}_{23}^c \end{bmatrix} \quad \text{(Eq. 4.124)} $$

Plugging (Eq. 4.123) and (Eq. 4.124), the bracket term in (Eq. 4.122) turns out to

$$ \delta \boldsymbol{b} - \delta \boldsymbol{K} \bar{\boldsymbol{\zeta}} = \begin{bmatrix} \delta \boldsymbol{x}_{13}^c \cdot \sum_{i=1}^{4} \bar{\alpha}_i \boldsymbol{x}_i^c \\ \\ \delta \boldsymbol{x}_{23}^c \cdot \sum_{i=1}^{4} \bar{\alpha}_i \boldsymbol{x}_i^c \end{bmatrix} + \begin{bmatrix} \boldsymbol{x}_{13}^c \cdot \sum_{i=1}^{4} \bar{\alpha}_i \delta \boldsymbol{x}_i^c \\ \\ \boldsymbol{x}_{23}^c \cdot \sum_{i=1}^{4} \bar{\alpha}_i \delta \boldsymbol{x}_i^c \end{bmatrix} = \begin{bmatrix} \delta \boldsymbol{x}_{13}^c \cdot {}^{h}\boldsymbol{g} \\ \\ \delta \boldsymbol{x}_{23}^c \cdot {}^{h}\boldsymbol{g} \end{bmatrix} + \begin{bmatrix} \boldsymbol{x}_{13}^c \cdot {}^{h}\delta \boldsymbol{g}(\bar{\boldsymbol{\zeta}}) \\ \\ \boldsymbol{x}_{23}^c \cdot {}^{h}\delta \boldsymbol{g}(\bar{\boldsymbol{\zeta}}) \end{bmatrix} \quad \text{(Eq. 4.125)} $$

where

$$ {}^{h}\delta \boldsymbol{g}(\bar{\boldsymbol{\zeta}}) := \sum_{i=1}^{4} \bar{\alpha}_i \delta \boldsymbol{x}_i^c \quad \text{(Eq. 4.126)} $$

With the insertion of (Eq. 4.107) and (Eq. 4.125) into (Eq. 4.122), $\delta\bar{\boldsymbol{\zeta}}$ is then obtained as

$$ \delta \bar{\boldsymbol{\zeta}} = \begin{bmatrix} \delta \bar{\zeta}_1 \\ \\ \delta \bar{\zeta}_2 \end{bmatrix} = \begin{bmatrix} \delta \boldsymbol{\gamma} \cdot {}^{h}\boldsymbol{g} + \boldsymbol{\gamma} \cdot {}^{h}\delta \boldsymbol{g}(\bar{\boldsymbol{\zeta}}) \\ \\ \delta \boldsymbol{\theta} \cdot {}^{h}\boldsymbol{g} + \boldsymbol{\theta} \cdot {}^{h}\delta \boldsymbol{g}(\bar{\boldsymbol{\zeta}}) \end{bmatrix} \quad \text{(Eq. 4.127)} $$

where

$$\boldsymbol{\gamma} := \frac{1}{4A^2}(k_{22}\boldsymbol{x}_{13}^c - k_{12}\boldsymbol{x}_{23}^c) = \sum_{i=1}^{4} \alpha_i^{\gamma}\boldsymbol{x}_i^c$$

$$\delta\boldsymbol{\gamma} := \sum_{i=1}^{4} \alpha_i^{\gamma}\delta\boldsymbol{x}_i^c \qquad \text{(Eq. 4.128)}$$

$$\alpha_1^{\gamma} = \frac{k_{22}}{4A^2}; \quad \alpha_2^{\gamma} = -\frac{k_{12}}{4A^2}; \quad \alpha_3^{\gamma} = -(\alpha_1^{\gamma} + \alpha_2^{\gamma}); \quad \alpha_4^{\gamma} = 0;$$

and

$$\boldsymbol{\theta} := \frac{1}{4A^2}(-k_{21}\boldsymbol{x}_{13}^c + k_{11}\boldsymbol{x}_{23}^c) = \sum_{i=1}^{4} \alpha_i^{\theta}\boldsymbol{x}_i^c$$

$$\delta\boldsymbol{\theta} := \sum_{i=1}^{4} \alpha_i^{\theta}\delta\boldsymbol{x}_i^c \qquad \text{(Eq. 4.129)}$$

$$\alpha_1^{\theta} := -\frac{k_{21}}{4A^2}; \ \alpha_2^{\theta} := \frac{k_{11}}{4A^2}; \ \alpha_3^{\theta} = -(\alpha_1^{\theta} + \alpha_2^{\theta}); \ \alpha_4^{\theta} = 0;$$

Taking into account (Eq. 4.127), (Eq. 4.113) is rewritten as

$${}^{h}\delta\boldsymbol{g} = \sum_{i=1}^{4} \bar{\alpha}_i\delta\boldsymbol{x}_i^c - \left[\delta\boldsymbol{\gamma}\cdot\ {}^{h}\boldsymbol{g} + \boldsymbol{\gamma}\cdot\ {}^{h}\delta\boldsymbol{g}(\bar{\boldsymbol{\zeta}})\right]\boldsymbol{x}_{13}^c - \left[\delta\boldsymbol{\theta}\cdot\ {}^{h}\boldsymbol{g} + \boldsymbol{\theta}\cdot\ {}^{h}\delta\boldsymbol{g}(\bar{\boldsymbol{\zeta}})\right]\boldsymbol{x}_{23}^c \qquad \text{(Eq. 4.130)}$$

4.5.1.3.5 Computation of Nodal Contact Forces

With the insertion of (Eq. 4.113), virtual work of the contact forces is then approximated as

$$\delta W^{contact} \cong {}^{h}\delta W^{contact} = \sum_{e=1}^{nelc} {}^{h}_{e}\delta W^{contact} \qquad \text{(Eq. 4.131)}$$

where

$${}^{h}_{e}\delta W \ := \int_{{}^{h}_{e}\Gamma_c} {}^{h}_{e}\delta\boldsymbol{g}\cdot\boldsymbol{\tau}_e \ da = \sum_{i=1}^{4} \delta\boldsymbol{x}_I^c\cdot\boldsymbol{f}_I^{contact} \qquad \text{(Eq. 4.132)}$$

and $nelc$ is total number of contact finite elements. Assuming that contact tractions are piecewise linear, one can write

$$\boldsymbol{\lambda}_e = \int_{{}^{h}_{e}\Gamma_c} \boldsymbol{\tau}_e \ da \qquad \text{(Eq. 4.133)}$$

where $\boldsymbol{\lambda}_e$ is contact force acting on triangular surface.

In (Eq. 4.132), $\boldsymbol{f}_I^{contact}$ is the internal force vector due to contact associated with i th node of element. $\boldsymbol{f}_I^{contact}$ has different shapes depending upon the method utilized to compute local coordinates. For method based on LSI, it has the form

$$\boldsymbol{f}_I^{contact} = \bar{\alpha}_i \boldsymbol{\lambda}_e + \tilde{\alpha}_i \left[\frac{1}{6V^c} (\boldsymbol{\lambda}_e \cdot \boldsymbol{x}_{13}^c) \boldsymbol{A}_1^c + \frac{1}{6V^c} (\boldsymbol{\lambda}_e \cdot \boldsymbol{x}_{23}^c) \boldsymbol{A}_2^c \right] \quad \text{(Eq. 4.134)}$$

whereas, for CPP algorithm it turns out to

$$\boldsymbol{f}_I^{contact} = \bar{\alpha}_i [\boldsymbol{\lambda}_e - (\boldsymbol{\lambda}_e \cdot \boldsymbol{x}_{13}^c)\boldsymbol{\gamma} - (\boldsymbol{\lambda}_e \cdot \boldsymbol{x}_{23}^c)\boldsymbol{\theta}] - \alpha_i^{\gamma} (\boldsymbol{\lambda}_e \cdot \boldsymbol{x}_{13}^c) \ {}^h\boldsymbol{g} - \alpha_i^{\theta} (\boldsymbol{\lambda}_e \cdot \boldsymbol{x}_{23}^c) \ {}^h\boldsymbol{g} \quad \text{(Eq. 4.135)}$$

Note that for LSI we have

$$\sum_{i=1}^{4} \tilde{\alpha}_i = 1 - \bar{\beta} \neq 0 \quad \text{(Eq. 4.136)}$$

(Eq. 4.136) implies that element level equilibrium of contact forces is not maintained unless $\bar{\beta} = 1$ for LSI. On the other hand, for CPP contact forces are elementwise in equilibrium due to the fact that

$$\sum_{i=1}^{4} \bar{\alpha}_i = \sum_{i=1}^{4} \alpha_i^{\gamma} = \sum_{i=1}^{4} \alpha_i^{\theta} = 0 \quad \text{(Eq. 4.137)}$$

For transient contact-impact simulations the size of the time increment is to be selected as a very small value in the order of microseconds due to numerical stability issues which emerge when an explicit time integration scheme is employed to integrate resulting dynamic nodal equilibrium equations in time. Based on this fact we can assume conveniently that $\bar{\boldsymbol{\zeta}}$ is constant within a time increment. Therefore for the incremental solution procedure its variation is taken to be zero. Hence the expression for nodal contact force simplifies to (Fig. 4.13)

$$\boldsymbol{f}_I^{contact} = \bar{\alpha}_i \boldsymbol{\lambda}_e \quad \text{(Eq. 4.138)}$$

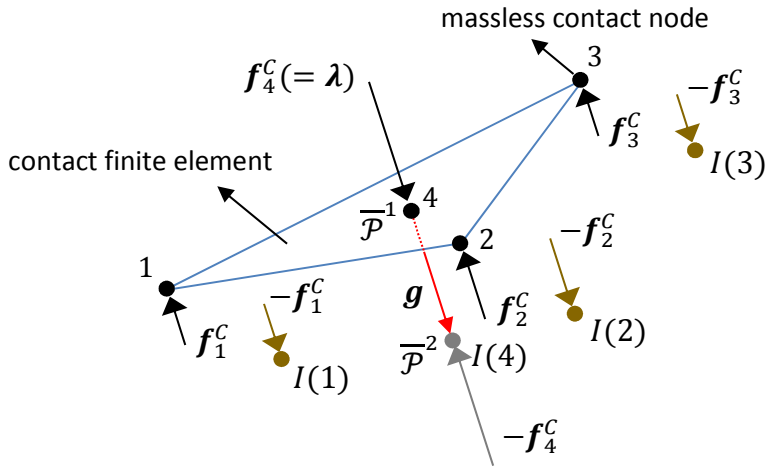

Fig. 4.13 Distribution and Transmission of Contact Forces

4.5.1.4 Virtual Work of External Forces

With the insertion of (Eq. 4.69), virtual work of the external forces is approximated as

$$\delta W^{external} \cong {}^{h}\delta W^{external} = \sum_{e=1}^{nel} {}^{h}_{e}\delta W^{external} \tag{Eq. 4.139}$$

where

$${}^{h}_{e}\delta W^{external} := \int_{{}^{h}_{e}\Omega} {}^{h}_{e}\delta \boldsymbol{x} \cdot \rho_e \boldsymbol{b}_e \; dv + \int_{{}^{h}_{e}\Gamma} {}^{h}_{e}\delta \boldsymbol{x} \cdot \hat{\boldsymbol{t}}_e \; da = \sum_{i=1}^{4} \delta \boldsymbol{x}_I \cdot \boldsymbol{f}_I^{external} \tag{Eq. 4.140}$$

If one assumes that $\boldsymbol{b}_e$ is constant inside element domain and $\hat{\boldsymbol{t}}_e$ is so on element face located at boundary, if there exists any connected to node i, we obtain

$$\begin{aligned} \boldsymbol{f}_I^{external} &:= \left[\int_{{}^{h}_{e}\Omega} \rho_e N_i \; dv\right] \boldsymbol{b}_e + \left[\int_{{}^{h}_{e}\Gamma} N_i \; da\right] \hat{\boldsymbol{t}}_e \\ &:= \frac{m_e}{4} \boldsymbol{b}_e + \frac{1}{3} A \hat{\boldsymbol{t}}_e \end{aligned} \tag{Eq. 4.141}$$

In (Eq. 4.141), $\boldsymbol{f}_I^{external}$ is the nodal force vector due to external loading associated with i th node of element.

4.5.2 Nodal Equilibrium Equations

Virtual work expressions exploited above can be rewritten equivalently as

$$\begin{aligned} {}^{h}\delta W^{inertia} &= \sum_{e=1}^{nel}\sum_{i=1}^{4} \delta \boldsymbol{x}_{con(e,i)} \cdot \boldsymbol{f}_{con(e,i)}^{inertia} = \sum_{I=1}^{nnd}\left[\delta \boldsymbol{x}_I \cdot \sum_{e=1}^{nel(I)} \boldsymbol{f}_{con(E(e),i(I))}^{inertia}\right] \\ {}^{h}\delta W^{stress} &= \sum_{e=1}^{nel}\sum_{i=1}^{4} \delta \boldsymbol{x}_{con(e,i)} \cdot \boldsymbol{f}_{con(e,i)}^{stress} = \sum_{I=1}^{nnd}\left[\delta \boldsymbol{x}_I \cdot \sum_{e=1}^{nel(I)} \boldsymbol{f}_{con(E(e),i(I))}^{stress}\right] \\ {}^{h}\delta W^{contact} &= \sum_{e=1}^{nelc}\sum_{i=1}^{4} \delta \boldsymbol{x}_{con(e,i)} \cdot \boldsymbol{f}_{con(e,i)}^{contact} = \sum_{I=1}^{nndc}\left[\delta \boldsymbol{x}_I \cdot \sum_{e=1}^{nel(I)} \boldsymbol{f}_{con(E(e),i(I))}^{contact}\right] \\ {}^{h}\delta W^{external} &= \sum_{e=1}^{nel}\sum_{i=1}^{4} \delta \boldsymbol{x}_{con(e,i)} \cdot \boldsymbol{f}_{con(e,i)}^{external} = \sum_{I=1}^{nnd}\left[\delta \boldsymbol{x}_I \cdot \sum_{e=1}^{nel(I)} \boldsymbol{f}_{con(E(e),i(I))}^{external}\right] \end{aligned} \tag{Eq. 4.142}$$

In (Eq. 4.142), $nel(I)$ returns the total number of elements connected to global node I, $E(e)$ returns element id for e th element connected to global node I and $i(I), i = 1 \dots 4$, denotes local node number matching with global node I for e th element connected to it. Plugging (Eq. 4.142) into (Eq. 4.20) then, we obtain

$$\sum_{I=1}^{nnd} \delta \boldsymbol{x}_I \cdot \left[{}^{inertia}\boldsymbol{f}_I + {}^{str}\boldsymbol{f}_I + {}^{con}\boldsymbol{f}_I - {}^{ext}\boldsymbol{f}_I \right] = 0 \qquad \text{(Eq. 4.143)}$$

where

$$\begin{aligned} {}^{inertia}\boldsymbol{f}_I &= \sum_{e=1}^{nel(I)} \boldsymbol{f}^{inertia}_{con(E(e),i(I))} = m_I \ddot{\boldsymbol{x}}_I \\ {}^{str}\boldsymbol{f}_I &= \sum_{e=1}^{nel(I)} \boldsymbol{f}^{stress}_{con(E(e),i(I))} \\ {}^{con}\boldsymbol{f}_I &= \sum_{e=1}^{nel(I)} \boldsymbol{f}^{contact}_{con(E(e),i(I))} \\ {}^{ext}\boldsymbol{f}_I &= \sum_{e=1}^{nel(I)} \boldsymbol{f}^{external}_{con(E(e),i(I))} \end{aligned} \qquad \text{(Eq. 4.144)}$$

In (Eq. 4.144), nodal mass m_I is computed from the expression

$$m_I = \sum_{e=1}^{nel(I)} m_{con(E(e),i(I))} = \sum_{e=1}^{nel(I)} \frac{m_{E(e)}}{4} \qquad \text{(Eq. 4.145)}$$

Note that although the density of an element changes in time as the body deforms, its mass remains constant since the Lagrangian description of motion is adapted to analyze the dynamic contact-impact problem at hand. As we know in Lagrangian description of motion finite element mesh deforms together with the material and no mass transfer is allowed through its boundaries. Therefore assembled nodal masses are also constant and, consequently, can be computed only once at the beginning of simulation during pre-processing phase.

Finally, considering independent variations of nodal positions, (Eq. 4.143) results in nodal dynamic equilibrium equations of the form

$$m_I \boldsymbol{a}_I = {}^{ext}\boldsymbol{f}_I - \left[{}^{str}\boldsymbol{f}_I + {}^{con}\boldsymbol{f}_I \right] \quad (I = 1 \dots nnd) \qquad \text{(Eq. 4.146)}$$

where we denote $\ddot{\boldsymbol{x}}_I$ as $\boldsymbol{a}_I$ for convenience.

4.6 Explicit Time Integration

4.6.1 Central Difference Approximation

(Eq. 4.146) is a second order nonlinear ordinary differential equation (ODE) of independent time variable and can be solved numerically using finite difference method. Method requires the division of timeline into increments. Such an increment corresponding to generic time step t^k is expressed as

$$\Delta t^k = t^{k+1} - t^k \qquad \text{(Eq. 4.147)}$$

where t^{k+1}, t^k are, respectively, discrete time at the beginning and end of time increment. For subsequent developments we define following quantities:

$$\Delta t^a := (\Delta t^k + \Delta t^{k-1})/2$$
$$\Delta t^d := (\Delta t^k - \Delta t^{k-1})/2 \qquad \text{(Eq. 4.148)}$$

By using increments Δt^{k-1} and Δt^k, one can construct a quadratic approximation to the node positions valid within time interval $[t^{k-1}, t^{k+1}]$ based on Lagrange polynomials as

$$\boldsymbol{x}_I(t) \cong {}^h\boldsymbol{x}_I(t) = \sum_{i=k-1}^{k+1} \mathcal{L}_i(t)\, \boldsymbol{x}_I^i = \sum_{i=k-1}^{k+1} \mathcal{L}_i\, \boldsymbol{x}_I^i \qquad \text{(Eq. 4.149)}$$

where $\mathcal{L}_i$and x_I^i are, respectively, the Lagrangian polynomial and node position associated with time step t^i. In view of (Eq. 4.149), Lagrangian interpolation functions are expressed as

$$\mathcal{L}_{k-1}(t) = \frac{(t - t^k)(t - t^{k+1})}{2\Delta t^{k-1}\Delta t^a}$$
$$\mathcal{L}_k(t) = -\frac{(t - t^{k-1})(t - t^{k+1})}{\Delta t^{k-1}\Delta t^k} \qquad \text{(Eq. 4.150)}$$
$$\mathcal{L}_{k+1}(t) = \frac{(t - t^{k-1})(t - t^k)}{2\Delta t^k\Delta t^a}$$

Taking the first and second time derivative of (Eq. 4.149), nodal velocity and acceleration at $t = t^k$ are obtained as

$$\boldsymbol{v}_I^k \cong \frac{-\Delta t^k\Delta t^k\boldsymbol{x}_I^{k-1} + \Delta t^a\Delta t^d\boldsymbol{x}_I^k + \Delta t^{k-1}\Delta t^{k-1}\boldsymbol{x}_I^{k+1}}{2\Delta t^{k-1}\Delta t^k\Delta t^a}$$
$$\boldsymbol{a}_I^k \cong \frac{\Delta t^k\boldsymbol{x}_I^{k-1} - 2\Delta t^a\boldsymbol{x}_I^k + \Delta t^{k-1}\boldsymbol{x}_I^{k+1}}{\Delta t^{k-1}\Delta t^k\Delta t^a} \qquad \text{(Eq. 4.151)}$$

For a uniform grid, where $\Delta t^{k-1} = \Delta t^k = \Delta t^a = \Delta t; \quad \Delta t^d = 0$, the expressions for nodal velocity and acceleration reduce down to

$$\boldsymbol{v}_I^k \cong \frac{\Delta\boldsymbol{x}_I^k + \Delta\boldsymbol{x}_I^{k-1}}{2\Delta t}$$
$$\boldsymbol{a}_I^k \cong \frac{\Delta\boldsymbol{x}_I^k - \Delta\boldsymbol{x}_I^{k-1}}{\Delta t^2} \qquad \text{(Eq. 4.152)}$$

where

$$\Delta \boldsymbol{x}_I^k = \boldsymbol{x}_I^{k+1} - \boldsymbol{x}_I^k$$
$$\Delta \boldsymbol{x}_I^{k-1} = \boldsymbol{x}_I^k - \boldsymbol{x}_I^{k-1} \quad \text{(Eq. 4.153)}$$

are position increments corresponding to time increments Δt^k and Δt^{k-1}, respectively. For future use, we also derive an expression for velocity at time step t^{k+1} from the following relationship:

$$\begin{aligned} \boldsymbol{v}_I^{k+1} &= \boldsymbol{v}_I^k + \Delta \boldsymbol{v}_I^k = \boldsymbol{v}_I^k + \Delta t \mathbf{a}_I^k \\ &= \frac{\Delta \boldsymbol{x}_I^k + \Delta \boldsymbol{x}_I^{k-1}}{2\Delta t} + \Delta t \frac{\Delta \boldsymbol{x}_I^k - \Delta \boldsymbol{x}_I^{k-1}}{\Delta t^2} \\ &= \frac{3\Delta \boldsymbol{x}_I^k - \Delta \boldsymbol{x}_I^{k-1}}{2\Delta t} \end{aligned} \quad \text{(Eq. 4.154)}$$

(Eq. 4.154) is valid because for the approximation given by (Eq. 4.149) acceleration is constant within the time interval $[t^{k-1}, t^{k+1}]$. Approximation given by (Eq. 4.152) is second order accurate and called as central difference approximation. Then the overall problem turns out to be the determination of $\Delta \boldsymbol{x}_I^k$ for the current time step t^k. Since the mass lumping is used in obtaining (Eq. 4.146), with the proposed algorithm positions can be updated explicitly without need to solve any system of equations. With the insertion of (Eq. 4.152) into (Eq. 4.146), it is obtained that

$$\mathbf{a}_I^k \cong \frac{\Delta \boldsymbol{x}_I^k - \Delta \boldsymbol{x}_I^{k-1}}{\Delta t^2} = \frac{{}^{tot}\boldsymbol{f}_I^k}{m_I} \quad \Longrightarrow \quad \Delta \boldsymbol{x}_I^k = \frac{\Delta t^2}{m_I} {}^{tot}\boldsymbol{f}_I^k + \Delta \boldsymbol{x}_I^{k-1} \quad \text{(Eq. 4.155)}$$

where total nodal force ${}^{tot}\boldsymbol{f}_I^k$ is defined as

$${}^{tot}\boldsymbol{f}_I^k := {}^{ext}\boldsymbol{f}_I^k - {}^{str}\boldsymbol{f}_I^k - {}^{con}\boldsymbol{f}_I^k \quad \text{(Eq. 4.156)}$$

In the presence of contact interactions, however, position update cannot be performed in single step because contact forces are not known beforehand. One can remedy such a situation by setting up a predictor-corrector type multi-step algorithm. As can be inferred from (Eq. 4.155), such an additive split is possible because discrete nodal dynamic equilibrium equation is linear in $\Delta \boldsymbol{x}_I^k$ and all other force terms. Taking this fact into account, one can decompose $\Delta \boldsymbol{x}_I^k$ additively as

$$\Delta \boldsymbol{x}_I^k = {}_p\Delta \boldsymbol{x}_I^k + {}_c\Delta \boldsymbol{x}_I^k \quad \text{(Eq. 4.157)}$$

where ${}_p\Delta \boldsymbol{x}_I^k$, ${}_c\Delta \boldsymbol{x}_I^k$ are, respectively, predictor and corrector position increments.

4.6.2 Predictor-Corrector Algorithm

4.6.2.1 Predictor Step

In the predictor step we perform node-level updates assuming that no contact takes place within the current time increment. Therefore for generic node I we have

$$
\begin{aligned}
&{}^{tot}_{p}\boldsymbol{f}_I^k = {}^{ext}\boldsymbol{f}_I^k - {}^{str}\boldsymbol{f}_I^k \\
&{}^{con}\boldsymbol{f}_I^k \overset{!}{=} \mathbf{0}
\end{aligned}
\qquad \text{(Eq. 4.158)}
$$

where ${}^{tot}_{p}\boldsymbol{f}_I^k$ is total predictor force acting on node I. From (Eq. 4.155), predictor position increment is then obtained as

$$
{}_p\mathbf{a}_I^k = \frac{{}_p\Delta\boldsymbol{x}_I^k - \Delta\boldsymbol{x}_I^{k-1}}{\Delta t^2} = \frac{{}^{tot}_{p}\boldsymbol{f}_I^k}{m_I} \quad \Longrightarrow \quad {}_p\Delta\boldsymbol{x}_I^k = \frac{\Delta t^2}{m_I}\,{}^{tot}_{p}\boldsymbol{f}_I^k + \Delta\boldsymbol{x}_I^{k-1} \qquad \text{(Eq. 4.159)}
$$

With the insertion of (Eq. 4.159) into (Eq. 4.154), predictor nodal velocity is computed as

$$
{}_p\boldsymbol{v}_I^{k+1} = \frac{3\,{}_p\Delta\boldsymbol{x}_I^k - \Delta\boldsymbol{x}_I^{k-1}}{2\Delta t} \qquad \text{(Eq. 4.160)}
$$

Plugging (Eq. 4.159) into (Eq. 4.153), the predictor position of node I at time step t^{k+1} turns out to be

$$
{}_p\boldsymbol{x}_I^{k+1} = \boldsymbol{x}_I^k + {}_p\Delta\boldsymbol{x}_I^k \qquad \text{(Eq. 4.161)}
$$

Next, based on predictor position given by (Eq. 4.161), we perform a global contact search and check if there are some nodes for which impenetrability constraint, given by (Eq. 4.4), is violated. Presupposed assumption made at the beginning, see (Eq. 4.158), holds for node I if it comes out that it does not violate impenetrability constraint. Then node-level update can be completed without taking another extra step (see Box 4.1).

4.6.2.2 Corrector Step

On the other hand, if node I violates impenetrability constraint, one has to take another step and correct relevant quantities by computing corrector position increment ${}_c\Delta\boldsymbol{x}_I^k$. If node I is in contact then there must be a contact force exerted on it, i.e. ${}^{con}\boldsymbol{f}_I^k \neq \mathbf{0}$, in order to satisfy related contact constraints. Let us for the moment presuppose that we are able to compute resulting contact force using the predictor positions, or predictor velocities, of contributing nodes in some way. Note that computation of the contact force will be discussed in detail in forthcoming section. With ${}^{con}\boldsymbol{f}_I^k$ at hand, we can compute corrector increment from (Eq. 4.159) as

$$
{}_c\mathbf{a}_I^k = \frac{{}_c\Delta\boldsymbol{x}_I^k}{\Delta t^2} = \frac{-{}^{con}\boldsymbol{f}_I^k}{m_I} \quad \Longrightarrow \quad {}_c\Delta\boldsymbol{x}_I^k = -\frac{\Delta t^2}{m_I}\,{}^{con}\boldsymbol{f}_I^k \qquad \text{(Eq. 4.162)}
$$

Plugging (Eq. 4.162) into (Eq. 4.154), corrector velocity is computed as

$$
{}_c\boldsymbol{v}_I^{k+1} \cong \frac{3\,{}_c\Delta\boldsymbol{x}_I^k}{2\Delta t} \qquad \text{(Eq. 4.163)}
$$

Node-level update is completed by incorporating contributions due to predictor position increment ${}_c\Delta\boldsymbol{x}_I^k$. The overall predictor-corrector algorithm is summarized in Box 4.1.

Box 4.1 Predictor-Corrector Algorithm

GIVEN → $\left| x_I^{k-1}, x_I^k, {}^{str}f_I^k, {}^{ext}f_I^k \right.$

PREDICTORS: $\boxed{{}^{con}\boldsymbol{f}_I^k = \boldsymbol{0}}$ →

$$\left|\begin{aligned}
{}^{tot}_{p}\boldsymbol{f}_I^k &= {}^{ext}\boldsymbol{f}_I^k - {}^{str}\boldsymbol{f}_I^k \\
{}_p\boldsymbol{a}_I^k &= \frac{{}_p\Delta\boldsymbol{x}_I^k - \Delta\boldsymbol{x}_I^{k-1}}{\Delta t^2} = \frac{{}^{tot}_{p}\boldsymbol{f}_I^k}{m_I} \\
{}_p\Delta\boldsymbol{x}_I^k &= \Delta t^2 \frac{{}^{tot}_{p}\boldsymbol{f}_I^k}{m_I} + \Delta\boldsymbol{x}_I^{k-1} \\
{}_p\boldsymbol{v}_I^{k+1} &= \frac{3\ {}_p\Delta\boldsymbol{x}_I^k - \Delta\boldsymbol{x}_I^{k-1}}{2\Delta t} \\
{}_p\boldsymbol{x}_I^{k+1} &= \boldsymbol{x}_I^k + {}_p\Delta\boldsymbol{x}_I^k
\end{aligned}\right.$$

CONTACT SEARCH …

DOES NODE I CONTRIBUTE TO CONTACT?

NO: FINALIZE →

$$\left|\begin{aligned}
\boldsymbol{a}_I^k &= {}_p\boldsymbol{a}_I^k \\
\Delta\boldsymbol{x}_I^k &= {}_p\Delta\boldsymbol{x}_I^k \\
\boldsymbol{v}_I^{k+1} &= {}_p\boldsymbol{v}_I^{k+1} \\
\boldsymbol{x}_I^{k+1} &= {}_p\boldsymbol{x}_I^{k+1}
\end{aligned}\right.$$

YES: CORRECTOR: $\boxed{{}^{con}\boldsymbol{f}_I^k \neq \boldsymbol{0}}$ →

COMPUTE ${}^{con}\boldsymbol{f}_I^k$

CORRECTORS →

$$\left|\begin{aligned}
{}_c\boldsymbol{a}_I^k &= \frac{{}_c\Delta\boldsymbol{x}_I^k}{\Delta t^2} = \frac{-{}^{con}\boldsymbol{f}_I^k}{m_I} \\
{}_c\Delta\boldsymbol{x}_I^k &= -\frac{\Delta t^2}{m_I}\,{}^{con}\boldsymbol{f}_I^k \\
{}_c\boldsymbol{v}_I^{k+1} &= \frac{3\ {}_c\Delta\boldsymbol{x}_I^k}{2\Delta t}
\end{aligned}\right.$$

FINALIZE →

$$\left|\begin{aligned}
\boldsymbol{a}_I^k &= {}_p\boldsymbol{a}_I^k + \boxed{{}_c\boldsymbol{a}_I^k} \\
\Delta\boldsymbol{x}_I^k &= {}_p\Delta\boldsymbol{x}_I^k + \boxed{{}_c\Delta\boldsymbol{x}_I^k} \\
\boldsymbol{v}_I^{k+1} &= {}_p\boldsymbol{v}_I^{k+1} + \boxed{{}_c\boldsymbol{v}_I^{k+1}} \\
\boldsymbol{x}_I^{k+1} &= \boldsymbol{x}_I^k + \Delta\boldsymbol{x}_I^k = {}_p\boldsymbol{x}_I^{k+1} + \boxed{{}_c\Delta\boldsymbol{x}_I^k}
\end{aligned}\right.$$

4.6.3 Computation of the Reactions

In formal setup discrete nodal equilibrium equations corresponding to the nodes located on the boundary Γ_x, where positions are prescribed, are deactivated since the nodal variation of positions is designed to vanish there, see (Eq. 4.70). However, within the framework of predictor-corrector algorithm described in previous section one can determine reaction forces in a straightforward manner by activating corresponding nodal equilibrium equations. The procedure is as follows. First we write down a typical discrete equilibrium equation corresponding to a node belonging to Γ_x, namely

$$m_I \boldsymbol{a}_I = \left[{}^{ext}\boldsymbol{f}_I - {}^{str}\boldsymbol{f}_I \right] + {}^{rea}\boldsymbol{f}_I \quad (I \in \Gamma_x) \tag{Eq. 4.164}$$

Note that (Eq. 4.164) is constructed based on the assumption that $\Gamma_x \cap \Gamma_c = \emptyset$, and therefore we have ${}^{con}\boldsymbol{f}_I = \boldsymbol{0}$. Predicting ${}^{rea}\boldsymbol{f}_I = \boldsymbol{0}$ and by utilizing (Eq. 4.158), (Eq. 4.159) and (Eq. 4.161), predictor position ${}_p\boldsymbol{x}_I^{k+1}$ can easily be computed. Corrector position increment for node I is then given by the expression

$${}_c\Delta\boldsymbol{x}_I^k = \hat{\boldsymbol{x}}_I^{k+1} - {}_p\boldsymbol{x}_I^{k+1} \tag{Eq. 4.165}$$

where $\hat{\boldsymbol{x}}_I^{k+1}$ is the prescribed (known) position for node I. Within the context of (Eq. 4.162) and (Eq. 4.165), reaction forces are finally obtained as

$${}_c\mathbf{a}_I^k = \frac{{}_c\Delta\boldsymbol{x}_I^k}{\Delta t^2} = \frac{{}^{rea}\boldsymbol{f}_I^k}{m_I} \quad \Longrightarrow \quad {}^{rea}\boldsymbol{f}_I^k = \frac{m_I}{\Delta t^2}\ {}_c\Delta\boldsymbol{x}_I^k \tag{Eq. 4.166}$$

4.6.4 Numerical Stability

Note that explicit time integration scheme applied is only conditionally stable. Stability limit is given by the well-known Courant-Friedrichs-Lewy (CFL) condition, which can be written as

$$c_d \leq \frac{{}^h l_{min}}{\Delta t_{crit}} \tag{Eq. 4.167}$$

where c_d is the dilatational wave velocity, ${}^h l_{min}$ is the minimum characteristic length extracted from the underlying finite element discretization and Δt_{crit} is critical time increment. (Eq. 4.167) states that the distance travelled by an elastic dilatational wave cannot exceed ${}^h l_{min}$ within one time increment. For wave propagation in inelastic medium, elastic wave speed is not constant and to be computed from updated elastic material properties. In addition, characteristic length also changes as the Lagrangian finite element method is used. Therefore critical time step is to be monitored and altered appropriately if necessary.

4.6.5 Starting Values

Explicit integration scheme based on central difference approximation is not self-starting. One needs position of node I at time step t^{-1} to be able to start time integration. This position can be approximately computed by backward Taylor series expansion around time step t^0, namely

$$\boldsymbol{x}_I^{-1} \cong \boldsymbol{x}_I^0 - \Delta t \boldsymbol{v}_I^0 + \frac{\Delta t^2}{2} \boldsymbol{a}_I^0 \qquad \text{(Eq. 4.168)}$$

In (Eq. 4.168), $\boldsymbol{x}_I^0$, $\boldsymbol{v}_I^0$ are, respectively, known initial conditions in terms of position and velocity for node I and $\boldsymbol{a}_I^0$ is the acceleration of node I at time step t^0 which can be computed from

$$\mathbf{a}_I^0 = \frac{{}^{ext}\boldsymbol{f}_I^0}{m_I} \qquad \text{(Eq. 4.169)}$$

In (Eq. 4.169), it is assumed that ${}^{str}\boldsymbol{f}_I^0 = {}^{con}\boldsymbol{f}_I^0 = \mathbf{0}$ at the beginning of the simulation.

4.6.6 Energy Transfer

In the absence of external forces total energy of the contacting bodies is constant, i.e. we have

$$E = \mathcal{K}(t) + \mathcal{U}(t) + \mathcal{D}(t) = \text{const.} \qquad \text{(Eq. 4.170)}$$

where

$$\begin{aligned} \mathcal{K}(t) &= \int_\Omega \rho(\frac{1}{2}\boldsymbol{v} \cdot \boldsymbol{v}) \; dv \\ \mathcal{U}(t) &= \int_\Omega \rho u_b \; dv + \int_{\Gamma_c} u_c \; da \\ \mathcal{D}(t) &= \int_\Omega \rho d_b \; dv + \int_{\Gamma_c} d_c \; da \end{aligned} \qquad \text{(Eq. 4.171)}$$

In (Eq. 4.171), $\mathcal{K}$ is the total kinetic energy, $\mathcal{U}$ is the sum of energy stored (reversible) in the bulk and along contact interface. $\mathcal{D}$ is the sum of energy dissipated (irreversible) in the bulk and along contact interface. Denoting $\mathcal{W} := \mathcal{U} + \mathcal{D}$, energy equation for thermally frozen state reads as

$$\frac{d\mathcal{K}}{dt} + \frac{d\mathcal{W}}{dt} = \int_\Omega \rho \boldsymbol{a} \cdot \boldsymbol{v} \; dv + \int_\Omega \boldsymbol{\sigma} : \boldsymbol{d} \; dv + \int_{\Gamma_c} \boldsymbol{\tau} \cdot \dot{\boldsymbol{g}} \; da \qquad \text{(Eq. 4.172)}$$

From (Eq. 4.172), we deduce that

$$\begin{aligned} \frac{d\mathcal{K}}{dt} &= \int_\Omega \rho \boldsymbol{a} \cdot \boldsymbol{v} \; dv \\ \frac{d\mathcal{W}}{dt} &= \int_\Omega \boldsymbol{\sigma} : \boldsymbol{d} \; dv + \int_{\Gamma_c} \boldsymbol{\tau} \cdot \dot{\boldsymbol{g}} \; da \end{aligned} \qquad \text{(Eq. 4.173)}$$

Based on finite element discretization of the bodies, (Eq. 4.173) takes the form

$$\frac{d\,{}^{h}\mathcal{K}}{dt} = \sum_{I=1}^{nnd} \boldsymbol{v}_I \cdot m_I \boldsymbol{a}_I$$
$$\frac{d\,{}^{h}\mathcal{W}}{dt} = \sum_{I=1}^{nnd} \boldsymbol{v}_I \cdot \left[{}^{str}\boldsymbol{f}_I + {}^{con}\boldsymbol{f}_I\right] \qquad \text{(Eq. 4.174)}$$

From (Eq. 4.174), it automatically comes out that

$$\frac{d\,{}^{h}E}{dt} = \frac{d\,{}^{h}\mathcal{K}}{dt} + \frac{d\,{}^{h}\mathcal{W}}{dt} = \sum_{I=1}^{nnd} \boldsymbol{v}_I \cdot \underbrace{\left[m_I \boldsymbol{a}_I + {}^{str}\boldsymbol{f}_I + {}^{con}\boldsymbol{f}_I\right]}_{=0\ (\text{Eq.}4.146)} = 0 \qquad \text{(Eq. 4.175)}$$

Energy increments corresponding to a typical time step t^k can be written as

$$\Delta\,{}^{h}\mathcal{K}^k = {}^{h}\mathcal{K}^{k+1} - {}^{h}\mathcal{K}^k = \sum_{I=1}^{nnd} \Delta\boldsymbol{x}_I^k \cdot m_I \boldsymbol{a}_I^k$$
$$\Delta\,{}^{h}\mathcal{W}^k = {}^{h}\mathcal{W}^{k+1} - {}^{h}\mathcal{W}^k = \sum_{I=1}^{nnd} \Delta\boldsymbol{x}_I^k \cdot \left[{}^{str}\boldsymbol{f}_I^k + {}^{con}\boldsymbol{f}_I^k\right] \qquad \text{(Eq. 4.176)}$$

(Eq. 4.176) corresponds to forward Euler update of energies and therefore is highly prone to instabilities especially in case of large position increments. Therefore in (Eq. 4.176), instead of $\Delta\boldsymbol{x}_I^k$, energy increments are computed using mean increments $\Delta\bar{\boldsymbol{x}}_I^k$ which are defined as

$$\Delta\bar{\boldsymbol{x}}_I^k := \frac{1}{2}\left(\Delta\boldsymbol{x}_I^{k-1} + \Delta\boldsymbol{x}_I^k\right) \qquad \text{(Eq. 4.177)}$$

4.7 Contact Algorithm

4.7.1 Contact Constraints

Among several other possibilities, we employ Lagrange multiplier method to enforce normal and tangential kinematical contact constraints (KCC). KCCs assume different forms depending upon the method utilized to compute local coordinates $\bar{\boldsymbol{\zeta}}$. In addition one should also take necessary precautions as passing from continuous setting to the discrete one.

4.7.1.1 Continuous Setting

4.7.1.1.1 Based on LSI

For method based on LSI one can put gap vector $\boldsymbol{g}$ in charge to construct KCCs in both normal and tangential directions. KCC in the normal direction is known as impenetrability constraint and can be expressed as

$$\boldsymbol{g}_n = (\boldsymbol{g} \cdot \bar{\mathbf{n}}^1)\bar{\mathbf{n}}^1 = g_n \bar{\mathbf{n}}^1 = \mathbf{0} \quad \Longrightarrow \quad g_n = 0 \tag{Eq. 4.178}$$

KCC in tangential direction is written, similar to the normal direction, as

$$\boldsymbol{g}_s = \boldsymbol{g} - \boldsymbol{g}_n = \|\boldsymbol{g}_s\| \frac{\boldsymbol{g}_s}{\|\boldsymbol{g}_s\|} = g_s \bar{\boldsymbol{s}}^1 = \mathbf{0} \quad \Longrightarrow \quad g_s = 0 \tag{Eq. 4.179}$$

(Eq. 4.178), (Eq. 4.179) imply, respectively, that relative normal and tangential motion of particle $\bar{\mathcal{P}}^2$ with respect to $\bar{\mathcal{P}}^1$ is zero in case of contact, i.e. they stick together. Based on this statement, one can conveniently bring (Eq. 4.178) and (Eq. 4.179) together and write down a single equation for KCC as

$$\boldsymbol{g} = \boldsymbol{g}_n + \boldsymbol{g}_s = g_n \bar{\mathbf{n}}^1 + g_s \bar{\boldsymbol{s}}^1 = \mathbf{0} \tag{Eq. 4.180}$$

Note that (Eq. 4.179) represents perfect stick case. In case of frictional sliding, however, gap vector is to be equal to the resulting slip vector, i.e. we should have

$$\boldsymbol{g} = g_s^{slip} \bar{\boldsymbol{s}}^1 \tag{Eq. 4.181}$$

4.7.1.1.2 Based on CPP

For method based on CPP, tangential component of the gap vector does not exist by construction, i.e. we have

$$\boldsymbol{g}_s = \mathbf{0} \tag{Eq. 4.182}$$

But, of course, (Eq. 4.182) does not mean that there is no relative motion in tangential direction. Therefore one has to resort to another kinematical quantity to enforce KCCs. The natural choice is to employ relative velocities. One can express relative velocity of the particle $\bar{\mathcal{P}}^2$ with respect $\bar{\mathcal{P}}^1$ as

$$\dot{\boldsymbol{g}} = \sum_{i=1}^{4} \bar{\alpha}_i \boldsymbol{v}_i^c \tag{Eq. 4.183}$$

KCC in the normal direction then takes the form

$$\dot{\boldsymbol{g}}_n = (\dot{\boldsymbol{g}} \cdot \bar{\mathbf{n}}^1)\bar{\mathbf{n}}^1 = \dot{g}_n \bar{\mathbf{n}}^1 = \mathbf{0} \quad \Longrightarrow \quad \dot{g}_n = 0 \tag{Eq. 4.184}$$

KCC in tangential direction can be expressed, in a similar fashion, as

$$\dot{\boldsymbol{g}}_s = \dot{\boldsymbol{g}} - \dot{\boldsymbol{g}}_n = \|\dot{\boldsymbol{g}}_s\| \frac{\dot{\boldsymbol{g}}_s}{\|\dot{\boldsymbol{g}}_s\|} = \dot{g}_s \bar{\boldsymbol{s}}^1 = \mathbf{0} \quad \Longrightarrow \quad \dot{g}_s = 0 \tag{Eq. 4.185}$$

(Eq. 4.184), (Eq. 4.185) imply, respectively, that relative normal and tangential velocity of particle $\bar{\mathcal{P}}^2$ with respect to $\bar{\mathcal{P}}^1$ is zero in case of contact. Based on this statement, one can conveniently bring (Eq. 4.184) and (Eq. 4.185) together and write down a single equation for KCC as

$$\dot{\boldsymbol{g}} = \dot{\boldsymbol{g}}_n + \dot{\boldsymbol{g}}_s = \dot{g}_n \overline{\mathbf{n}}^1 + \dot{g}_s \overline{\boldsymbol{s}}^1 = \mathbf{0} \qquad \text{(Eq. 4.186)}$$

Note that (Eq. 4.185) resembles perfect stick case. In case of frictional sliding, however, relative velocity is to be equal to the resulting slip velocity, i.e. we should have

$$\dot{\boldsymbol{g}} = \dot{g}_s^{slip} \overline{\boldsymbol{s}}^1 \qquad \text{(Eq. 4.187)}$$

4.7.1.2 Discrete Setting

In continuous setting, from pure geometrical point of view, the following relationship holds for stick case:

$$\boldsymbol{g} = \dot{\boldsymbol{g}} = \mathbf{0} \qquad \text{(Eq. 4.188)}$$

As will be shown later (Eq. 4.188) does not hold for discrete setting. For a formulation based on total form, i.e. in terms of $\boldsymbol{g}$, we have

$$\begin{aligned} \boldsymbol{g} &= 0 \\ \dot{\boldsymbol{g}} &\neq 0 \end{aligned} \qquad \text{(Eq. 4.189)}$$

whereas for one build on rate form, i.e. in terms of $\dot{\boldsymbol{g}}$, we have

$$\begin{aligned} \dot{\boldsymbol{g}} &= 0 \\ \boldsymbol{g} &\neq 0 \end{aligned} \qquad \text{(Eq. 4.190)}$$

From numerical standpoint it is always desirable to have better accuracy in primary variable, which in our case turns out to be $\boldsymbol{g}$. Therefore we prefer (Eq. 4.189) to construct discrete version of the KCCs. However it is not always possible as is the case for CPP due to absence of tangential component of gap vector. But still (Eq. 4.189) can be used in the normal direction and actually it has to be used to ensure that impenetrability constraint is precisely enforced. Some gap can be tolerated in the tangential direction but not in the normal direction. Then, for CPP, KCC in normal direction, given by (Eq. 4.185), should be replaced with (Eq. 4.179). On top of this discussion we summarize final version of the KCCs obtained based on LSI and CPP in Box 4.2.

Box 4.2 Contact Constraints

$$\begin{aligned} \text{LSI} \rightarrow \;& \text{STICK} \rightarrow \; \boldsymbol{g} = \mathbf{0} \\ & \text{SLIP} \rightarrow \; \boldsymbol{g} = g_s^{slip} \overline{\boldsymbol{s}}^1 \;\; (g_s^{slip} > 0) \\ \text{CPP} \rightarrow \;& \text{STICK} \rightarrow \; \boldsymbol{g}_n = \mathbf{0} \\ & \qquad\qquad\;\; \dot{\boldsymbol{g}}_s = \mathbf{0} \\ & \text{SLIP} \rightarrow \; \boldsymbol{g}_n = \mathbf{0} \\ & \qquad\qquad\;\; \dot{\boldsymbol{g}}_s = \dot{g}_s^{slip} \overline{\boldsymbol{s}}^1 \;\; (\dot{g}_s^{slip} > 0) \end{aligned}$$

4.7.2 Constitutive Modeling

As the characteristic of Lagrange multiplier method, one cannot express normal and tangential components of the contact force $\boldsymbol{\lambda}$, Lagrange multiplier, in terms of constitutive equations based on relevant kinematical quantities, like gap vector $\boldsymbol{g}$ or its rate $\dot{\boldsymbol{g}}$. Instead, as will be discussed in the next section, one can exploit extra set of equations provided by KCCs and explicit time integration scheme employed to compute $\boldsymbol{\lambda}$.

To be able to differentiate between stick and slip cases, we adopt non-regularized (discontinuous) Mohr-Coulomb type constitutive behavior in the tangential direction. First of all, for subsequent developments, we decompose $\boldsymbol{\lambda}$ into its normal and tangential components as

$$\begin{aligned} \boldsymbol{\lambda} &= \boldsymbol{\lambda}_n + \boldsymbol{\lambda}_s \\ \boldsymbol{\lambda}_n &= (\boldsymbol{\lambda} \cdot \bar{\mathbf{n}}^1)\bar{\mathbf{n}}^1 = -\lambda_n \bar{\boldsymbol{n}}^1 \\ \boldsymbol{\lambda}_s &= \boldsymbol{\lambda} - \boldsymbol{\lambda}_n = \|\boldsymbol{\lambda}_s\| \frac{\boldsymbol{\lambda}_s}{\|\boldsymbol{\lambda}_s\|} = \lambda_s \bar{\boldsymbol{s}}^1 \end{aligned} \qquad \text{(Eq. 4.191)}$$

Note that according to kinetical contact constraint introduced by (Eq. 4.5), we have

$$-\lambda_n < 0 \quad \Longrightarrow \quad \lambda_n > 0 \qquad \text{(Eq. 4.192)}$$

In addition, due to proposed decomposition given by (Eq. 4.191), we also have

$$\lambda_s > 0 \qquad \text{(Eq. 4.193)}$$

For Mohr-Coulomb type of constitutive model limit (yield) value $\overline{\boldsymbol{\lambda}}_s$ for the tangential component of $\boldsymbol{\lambda}$ is defined as

$$\overline{\boldsymbol{\lambda}}_s = \mu \lambda_n \bar{\boldsymbol{s}}^1 \qquad \text{(Eq. 4.194)}$$

where μ is the coefficient of friction. With the help of (Eq. 4.194), a yield function bounding the admissible tangential contact forces is defined as

$$\phi(\lambda_s, \lambda_n) = \lambda_s - \mu \lambda_n \qquad \text{(Eq. 4.195)}$$

Next we define stick-slip conditions. In view of (Eq. 4.195), we have a stick case if

$$\phi \leq 0 \quad \Leftrightarrow \quad \begin{cases} g_s = 0 & \text{for LSI} \\ \dot{g}_s = 0 & \text{for CPP} \end{cases} \qquad \text{(Eq. 4.196)}$$

On the other hand, in case of slip the following relation holds:

$$\phi = 0 \quad \Leftrightarrow \quad \begin{cases} g_s = g_s^{slip} \geq 0 & \text{for LSI} \\ \dot{g}_s = \dot{g}_s^{slip} \geq 0 & \text{for CPP} \end{cases} \qquad \text{(Eq. 4.197)}$$

(Eq. 4.195), (Eq. 4.196) and (Eq. 4.197) can be brought together under one equation, in the form of Karush-Kuhn-Tucker conditions, as

$$\phi g_s = 0; \quad \phi \leq 0; \quad g_s \geq 0; \quad \text{for LSI}$$
$$\phi \dot{g}_s = 0; \quad \phi \leq 0; \quad \dot{g}_s \geq 0; \quad \text{for CPP} \qquad \text{(Eq. 4.198)}$$

4.7.3 Computation of Contact Force

In Lagrange multiplier method contact forces appear as additional unknowns in corresponding nodal equilibrium equations, which makes the system indeterminate, i.e. available number of equations is less than total number of unknowns. Therefore nodal equilibrium equations must be supplemented with some extra equations so that the overall system becomes determinate again. Within the context of Box 4.2, for each unknown contact force, one can write down a constraint equation based on impenetrability and stick. Next we will show that based on these constraint equations and with the help of explicit time integration scheme proposed, it is possible to obtain closed-form expressions for contact forces. For a given contact finite element, in view of (Eq. 4.138) and (Eq. 4.162), corrector position increment corresponding to its i th node is computed as

$$_c\Delta \boldsymbol{x}_i^k = -\Delta t^2 \gamma_i \boldsymbol{\lambda}; \quad \gamma_i := \frac{\overline{\alpha}_i}{m_i} \qquad \text{(Eq. 4.199)}$$

Corresponding predictor gap vector and predictor gap rate are expressed as

$$_p\boldsymbol{g} = \sum_{i=1}^{4} \overline{\alpha}_i \; {}_p\boldsymbol{x}_i^{k+1} \qquad \text{(Eq. 4.200)}$$

$$_p\dot{\boldsymbol{g}} = \sum_{i=1}^{4} \overline{\alpha}_i \; {}_p\boldsymbol{v}_i^{k+1} \qquad \text{(Eq. 4.201)}$$

4.7.3.1 Based on LSI

For LSI we compute Lagrange multiplier by employing constraint equation given by (Eq. 4.180). The procedure is as follows. We first linearize (Eq. 4.200) and obtain an expression for corrector increment in $\boldsymbol{g}$ as

$$_c\boldsymbol{g} = \sum_{i=1}^{4} \overline{\alpha}_i \; {}_c\Delta \boldsymbol{x}_i^k \qquad \text{(Eq. 4.202)}$$

With the insertion of (Eq. 4.199), (Eq. 4.202) can be recast in a form

$$_c\boldsymbol{g} = -\Delta t^2 \overline{\theta} \boldsymbol{\lambda}; \quad \overline{\theta} := \sum_{i=1}^{4} \overline{\alpha}_i \overline{\gamma}_i = \sum_{i=1}^{4} \overline{\alpha}_i^2 / m_i \qquad \text{(Eq. 4.203)}$$

One can then compute Lagrange multiplier by enforcing corrected value of the penetration be equal to zero, i.e.

$$\boldsymbol{g} = {}_p\boldsymbol{g} + {}_c\boldsymbol{g} \overset{!}{=} \mathbf{0} \Longrightarrow {}_c\boldsymbol{g} = -{}_p\boldsymbol{g} \tag{Eq. 4.204}$$

Rearranging (Eq. 4.204) by taking into account (Eq. 4.203) leads us to a closed form expression for predictor Lagrange multiplier as

$$\boldsymbol{\lambda} = \boldsymbol{\lambda}_n + {}_p\boldsymbol{\lambda}_s = \frac{1}{\Delta t^2 \bar{\theta}} \boldsymbol{g}_n + \frac{1}{\Delta t^2 \bar{\theta}} {}_p\boldsymbol{g}_s \tag{Eq. 4.205}$$

Note that $\boldsymbol{g} = 0$ does not necessarily imply that $\dot{\boldsymbol{g}} = 0$. This can easily be shown. Rewriting (Eq. 4.204) in expanded form, we obtain

$$\boldsymbol{g} = \sum_{i=1}^{4} \overline{\alpha}_i ({}_p\boldsymbol{x}_i^{k+1} + {}_c\Delta\boldsymbol{x}_i^k) = \sum_{i=1}^{4} \overline{\alpha}_i \boldsymbol{x}_i^{k+1} = \mathbf{0} \tag{Eq. 4.206}$$

Plugging (Eq. 4.206) into (Eq. 4.201), it is obtained that

$$\dot{\boldsymbol{g}} = \sum_{i=1}^{4} \frac{\overline{\alpha}_i (3\boldsymbol{x}_i^{k+1} - 4\boldsymbol{x}_i^k + \boldsymbol{x}_i^{k-1})}{2\Delta t} = -\frac{1}{2\Delta t} \sum_{i=1}^{4} \overline{\alpha}_i \left(4\boldsymbol{x}_i^k - \boldsymbol{x}_i^{k-1}\right) \neq \mathbf{0} \tag{Eq. 4.207}$$

Therefore, (Eq. 4.206) and (Eq. 4.207) imply that contact constraints written in total form, see (Eq. 4.180), and in rate form, see (Eq. 4.186), cannot be satisfied at the same time in discrete setting.

With back-substituting (Eq. 4.205) into (Eq. 4.199), corrector position increment is obtained as

$$\begin{aligned} {}_c\Delta\boldsymbol{x}_i^k &= -\Delta t^2 \gamma_i \boldsymbol{\lambda} \\ &= -\Delta t^2 \gamma_i \frac{1}{\Delta t^2 \bar{\theta}} {}_p\boldsymbol{g} \\ &= -\frac{\gamma_i}{\bar{\theta}} {}_p\boldsymbol{g} \end{aligned} \tag{Eq. 4.208}$$

As can be grabbed from (Eq. 4.208), integration coefficient Δt^2, consistent with central difference approximation employed, drops out during back-substitution. This cancellation reveals the fact that integration coefficient does affect the magnitude of contact force but actually has no role in the computation of position increments. Therefore its value does not change overall global pure mechanical response of the system.

4.7.3.2 Based on CPP

For CPP, KCC based on total form is used in normal direction (see Box 4.2). Following a similar procedure presented in previous section, normal component of the contact force is obtained as

$$\boldsymbol{\lambda}_n = \frac{1}{\Delta t^2 \bar{\theta}} \boldsymbol{g} \tag{Eq. 4.209}$$

Note for CPP $\boldsymbol{g}_n = \boldsymbol{g}$. To compute tangential component of the contact force we employ KCC written in rate form (see Box 4.2) due to obvious reasons. The procedure is as follows. We first linearize (Eq. 4.201) and obtain an expression for corrector increment in gap rate ${}_c\dot{\boldsymbol{g}}_s$ as

$$ {}_c\dot{\boldsymbol{g}} = \frac{3}{2\Delta t}\sum_{i=1}^{4} \overline{\alpha}_i \; {}_c\Delta\boldsymbol{x}_i^k \quad \Longrightarrow \quad {}_c\dot{\boldsymbol{g}}_s = {}_c\dot{\boldsymbol{g}} - \left({}_c\dot{\boldsymbol{g}} \cdot \overline{\boldsymbol{n}}^1 \right)\overline{\boldsymbol{n}}^1 = \; {}_c\dot{g}_s \overline{\boldsymbol{s}}^1 \tag{Eq. 4.210} $$

With the insertion of (Eq. 4.199), (Eq. 4.210) can be recast in a form

$$ {}_c\dot{\boldsymbol{g}}_s = -\frac{3\Delta t\overline{\theta}}{2} \; {}_p\boldsymbol{\lambda}_s \tag{Eq. 4.211} $$

One can then compute tangential contact force by enforcing updated value of the tangential gap rate be equal to zero, i.e.

$$ \dot{\boldsymbol{g}}_s = \; {}_p\dot{\boldsymbol{g}}_s + \; {}_c\dot{\boldsymbol{g}}_s \stackrel{!}{=} \boldsymbol{0} \Longrightarrow \; {}_c\dot{\boldsymbol{g}}_s = - \; {}_p\dot{\boldsymbol{g}}_s \tag{Eq. 4.212} $$

Rearranging (Eq. 4.212) by taking into account (Eq. 4.211) leads us to a closed form expression for predictor contact force as

$$ {}_p\boldsymbol{\lambda}_s = \frac{1}{\frac{3\Delta t}{2}\bar{\theta}} \; {}_p\dot{\boldsymbol{g}}_s \tag{Eq. 4.213} $$

Within the context of (Eq. 4.163), (Eq. 4.199) and (Eq. 4.213), corrector velocity is computed as

$$ \begin{aligned} {}_c^s\Delta\boldsymbol{x}_i^k = \; -\Delta t^2\gamma_i \; {}_p\boldsymbol{\lambda}_s \quad &\Longrightarrow \; {}_c^s\boldsymbol{v}_i^{k+1} = \; \frac{3}{2\Delta t} \; {}_c\Delta\boldsymbol{x}_I^k \\ = \; -\frac{2\Delta t}{3}\frac{\gamma_i}{\bar{\theta}} \; {}_p\boldsymbol{v}_s \quad &= \; -\frac{\gamma_i}{\bar{\theta}} \; {}_p\dot{\boldsymbol{g}}_s \end{aligned} \tag{Eq. 4.214} $$

From (Eq. 4.213) and (Eq. 4.214), it comes out that for CPP contact force as well as position increment depends on integration coefficients given by, respectively, $3\Delta t/2$ and $2\Delta t/3$.

Combining (Eq. 4.209) and (Eq. 4.213) together, we obtain an expression for total contact force as

$$ \boldsymbol{\lambda} = \boldsymbol{\lambda}_n + \; {}_p\boldsymbol{\lambda}_s = \frac{1}{\Delta t^2\bar{\theta}}\boldsymbol{g} + \frac{1}{\frac{3\Delta t}{2}\bar{\theta}} \; {}_p\dot{\boldsymbol{g}}_s \tag{Eq. 4.215} $$

Finally we bring (Eq. 4.205) and (Eq. 4.215) together and write down

$$ \boldsymbol{\lambda} = \boldsymbol{\lambda}_n + \; {}_p\boldsymbol{\lambda}_s = \begin{cases} \frac{1}{\Delta t^2\bar{\theta}}\boldsymbol{g}_n \; + \; \frac{1}{\Delta t^2\bar{\theta}} \; {}_p\boldsymbol{g}_s & \text{for LSI} \\ \frac{1}{\Delta t^2\bar{\theta}}\boldsymbol{g} \; + \; \frac{1}{\frac{3\Delta t}{2}\bar{\theta}} \; {}_p\dot{\boldsymbol{g}}_s & \text{for CPP} \end{cases} \tag{Eq. 4.216} $$

4.7.4 Constitutive Update

Expressions for tangential contact force given by (Eq. 4.216) are derived based on stick assumption. One should validate if this assumption is true and, if it is not, should correct tangential component of the contact force and compute resulting total slip or slip velocity. Return mapping algorithm used to for rate-independent plasticity material model can be adapted to perform constitutive update in tangential direction (Simo et al. 1998). The procedure is as follows. First we decompose tangential component of the gap vector additively into stick and slip parts as

$$ {}_p\boldsymbol{g}_s = {}^{stick}_{p}\boldsymbol{g}_s + {}^{slip}_{p}\boldsymbol{g}_s \qquad \text{(Eq. 4.217)} $$

With the insertion of (Eq. 4.217) into (Eq. 4.216), the expression for contact force can be recast in a form

$$ \boldsymbol{\lambda}_s = \frac{1}{\Delta t^2 \bar{\theta}} {}^{stick}_{p}\boldsymbol{g}_s = \frac{1}{\Delta t^2 \bar{\theta}} ({}_p\boldsymbol{g}_s - {}^{slip}_{p}\boldsymbol{g}_s) \qquad \text{(Eq. 4.218)} $$

Yield value for tangential contact force is computed from (Eq. 4.194). Constitutive update is performed based on stick-predictor-slip-corrector algorithm. In stick-predictor step we assume that there is no slip, i.e. we presuppose

$$ {}^{slip}_{p}\boldsymbol{g}_s = \mathbf{0} \qquad \text{(Eq. 4.219)} $$

With the insertion of (Eq. 4.219) into (Eq. 4.218), predictor for tangential contact force is obtained as

$$ \boldsymbol{\lambda}_s = {}_p\boldsymbol{\lambda}_s = \frac{1}{\Delta t^2 \bar{\theta}} {}_p\boldsymbol{g}_s = {}_p\lambda_s \bar{\boldsymbol{s}}^1 \qquad \text{(Eq. 4.220)} $$

Next we should check if stick assumption is correct. For this purpose we first compute so called over-stress from

$$ \Delta\boldsymbol{\lambda}_s = \big({}_p\lambda_s - \mu\lambda_n \big)\bar{\boldsymbol{s}}^1 = {}_p\phi\,\bar{\boldsymbol{s}}^1 \qquad \text{(Eq. 4.221)} $$

Note that use of (Eq. 4.195) is made to obtain (Eq. 4.221). Now we recall (Eq. 4.198) which defines stick-slip conditions in the form of inequality constraints. For stick we must fulfill

$$ {}_p\phi \leq 0 \qquad \text{(Eq. 4.222)} $$

in addition to (Eq. 4.219). If (Eq. 4.222) holds, it means that stick assumption is correct and relationships given by (Eq. 4.219) and (Eq. 4.220) are valid. On the other hand, if (Eq. 4.222) is not valid, we need to take another step and compute corrector tangential force and resulting amount of slip. First we compute corrector tangential force emanating from the constraint equation

$$ \phi = {}_p\phi + {}_c\phi = 0 \quad \Longrightarrow \quad {}_p\phi + {}_c\lambda_s = 0 \qquad \text{(Eq. 4.223)} $$

which is valid for slip case, see (Eq. 4.198), as

$$ {}_c\lambda_s = -\,{}_p\phi \tag{Eq. 4.224}$$

From (Eq. 4.218) we can write

$$ {}_c\boldsymbol{\lambda}_s = -\frac{1}{\Delta t^2\bar{\theta}}\,{}^{slip}_{c}\boldsymbol{g}_s = -\frac{{}_c g_s^{slip}}{\Delta t^2\bar{\theta}}\bar{\boldsymbol{s}}^1 = {}_c\lambda_s\bar{\boldsymbol{s}}^1 \tag{Eq. 4.225}$$

Plugging (Eq. 4.224) into (Eq. 4.225), we obtain

$$ -\,{}_p\phi = -\frac{{}_c g_s^{slip}}{\Delta t^2\bar{\theta}} \quad \Longrightarrow \quad {}_c g_s^{slip} = \Delta t^2\bar{\theta}\;{}_p\phi \tag{Eq. 4.226}$$

Finally, with corrected values, we have

$$\begin{aligned} \boldsymbol{\lambda}_s &= {}_p\boldsymbol{\lambda}_s + {}_c\boldsymbol{\lambda}_s \qquad = \mu\lambda_n\bar{\boldsymbol{s}}^1 \\ {}^{slip}\boldsymbol{g}_s &= {}^{slip}_{p}\boldsymbol{g}_s + {}^{slip}_{c}\boldsymbol{g}_s = \left(\Delta t^2\bar{\theta}\;{}_p\phi\right)\bar{\boldsymbol{s}}^1 \end{aligned} \tag{Eq. 4.227}$$

The overall predictor-corrector algorithm for tangential contact based on total form of KCC is summarized in Box 4.3, whereas in Box 4.4 algorithm based on rate from of KCC is presented.

4.7.5 Gauss-Seidel Iteration

If the triangular faces belonging to contact finite elements are not connected to each other, the global contact problem reduces down to local contact problem at element level. Therefore with contact algorithm discussed above contact constraints can be resolved at element level and exactly satisfied without any problem. On the other hand, if there are some faces connected to each other, one has to first assemble contact forces computed from (Eq. 4.138) at common nodes and then compute the corrector displacement increments accordingly from (Eq. 4.162). However with such an update corresponding displacement increment will be the summation coming from all neighbor contact finite elements. It is obvious that with such an update it is not possible to fulfill contact constraints within neighbor elements. Therefore an iterative solution procedure has to be considered. An assembly-based iteration is not smooth and therefore not preferred. Instead we propose an alternative robust method based on elemental updates in the form of Gauss-Seidel iteration (Carpenter et al. 1991; Travaš et al. 2009). The algorithmic set up is given in Box 4.5, where nec, nnc are, respectively, total number of elements and nodes of corresponding contact discretization, $I(n)$ maps n th node of contact discretization to corresponding node of underlying body discretization, $n(i)$ maps i th local node of contact finite element to corresponding node of contact discretization. The iteration is of Gauss-Seidel type because each element in the list is

processed with the updated positions of the contact nodes. During iteration, contact might be lost in some of the elements. Therefore contact release case must be handled properly. Note that after converged state has been reached, there still remains, within each connected element, some amount of penetration, magnitude of which depends on the tolerance value used to terminate iteration. This, of course, contradicts with the nature of Lagrange multiplier method employed for the solution of contact problem. In addition, from (Eq. 4.216), it comes out that contact forces are expressed as a function of gap vector or its rate, i.e. one can derive an expression for penalty parameter for each contact element separately such that contact constraints are exactly satisfied for those which are not connected. Therefore it is better to call method of constraint enforcement described out here as penalty with varying parameters instead of Lagrange multiplier.

Box 4.3 Constitutive Update for Tangential Contact: Total Form

GIVEN →

$$
\begin{aligned}
{}_p\boldsymbol{g} &= \boldsymbol{g}_n + {}_p\boldsymbol{g}_s \\
\boldsymbol{g}_n &= \left({}_p\boldsymbol{g}\cdot\bar{\boldsymbol{n}}^1\right)\bar{\boldsymbol{n}}^1 = g_n\bar{\boldsymbol{n}}^1 \\
{}_p\boldsymbol{g}_s &= {}_p\boldsymbol{g} - \boldsymbol{g}_n = g_s\bar{\boldsymbol{s}}^1
\end{aligned}
$$

DECOMPOSE →

$$
{}_p\boldsymbol{g}_s = {}^{stick}_{p}\boldsymbol{g}_s + {}^{slip}_{p}\boldsymbol{g}_s
$$

PREDICTORS: $\boxed{{}^{slip}_{p}\boldsymbol{g}_s = \boldsymbol{0}}$ →

$$
\begin{aligned}
{}_p\boldsymbol{\lambda} &= \boldsymbol{\lambda}_n + {}_p\boldsymbol{\lambda}_s \\
&= \tfrac{1}{\Delta t^2\bar{\theta}}\boldsymbol{g}_n + \tfrac{1}{\Delta t^2\bar{\theta}}\,{}_p\boldsymbol{g}_s \\
&= -\lambda_n\bar{\boldsymbol{n}}^1 + {}_p\lambda_s\bar{\boldsymbol{s}}^1 \qquad (\lambda_n > 0;\ {}_p\lambda_s > 0)
\end{aligned}
$$

COMPUTE →

$$
\begin{aligned}
\Delta\boldsymbol{\lambda}_s &= \left({}_p\lambda_s - \mu\lambda_n\right)\bar{\boldsymbol{s}}^1 \\
&= {}_p\phi\bar{\boldsymbol{s}}^1
\end{aligned}
$$

IS $\boxed{{}_p\phi \le 0}$? →

YES → STICK →

$$
\begin{aligned}
\boldsymbol{\lambda}_s &= {}_p\boldsymbol{\lambda}_s \\
\boldsymbol{g}_s &= {}_p\boldsymbol{g}_s
\end{aligned}
$$

NO → SLIP →

$$
\begin{aligned}
{}_c\boldsymbol{\lambda}_s &= -\,{}_p\phi\bar{\boldsymbol{s}}^1 \\
{}^{slip}_{c}\boldsymbol{g}_s &= \Delta t^2\bar{\theta}\,{}_p\phi\bar{\boldsymbol{s}}^1 \\
{}^{slip}\boldsymbol{g}_s &= {}^{slip}_{p}\boldsymbol{g}_s + {}^{slip}_{c}\boldsymbol{g}_s = {}^{slip}_{c}\boldsymbol{g}_s \\
\boldsymbol{\lambda}_s &= {}_p\boldsymbol{\lambda}_s + {}_c\boldsymbol{\lambda}_s = \mu\lambda_n\bar{\boldsymbol{s}}^1 \\
\boldsymbol{g}_s &= {}_p\boldsymbol{g}_s - {}^{slip}\boldsymbol{g}_s
\end{aligned}
$$

Box 4.4 Constitutive Update for Tangential Contact: Rate Form

GIVEN →

$$\boldsymbol{g} = \boldsymbol{g}_n$$

$${}_p\dot{\boldsymbol{g}}_s = {}_p\dot{\boldsymbol{g}} - \dot{\boldsymbol{g}}_n = \dot{g}_s\bar{\boldsymbol{s}}^1$$

DECOMPOSE →

$${}_p\dot{\boldsymbol{g}}_s = {}^{stick}_{\ p}\dot{\boldsymbol{g}}_s + {}^{slip}_{\ p}\dot{\boldsymbol{g}}_s$$

PREDICTORS: $\boxed{{}^{slip}_{\ p}\dot{\boldsymbol{g}}_s = \boldsymbol{0}}$ →

$$\begin{aligned} {}_p\boldsymbol{\lambda} &= \boldsymbol{\lambda}_n + {}_p\boldsymbol{\lambda}_s \\ &= \frac{1}{\Delta t^2\bar{\theta}}\boldsymbol{g}_n + \frac{1}{\frac{3\Delta t}{2}\bar{\theta}}\,{}_p\dot{\boldsymbol{g}}_s \\ &= -\lambda_n\bar{\boldsymbol{n}}^1 + {}_p\lambda_s\bar{\boldsymbol{s}}^1 \qquad (\lambda_n > 0;\ {}_p\lambda_s > 0) \end{aligned}$$

COMPUTE →

$$\begin{aligned} \Delta\boldsymbol{\lambda}_s &= \left({}_p\lambda_s - \mu\lambda_n\right)\bar{\boldsymbol{s}}^1 \\ &= {}_p\phi\bar{\boldsymbol{s}}^1 \end{aligned}$$

IS $\boxed{{}_p\phi \le 0}$? →

YES → STICK →

$$\begin{aligned} \boldsymbol{\lambda}_s &= {}_p\boldsymbol{\lambda}_s \\ \dot{\boldsymbol{g}}_s &= {}_p\dot{\boldsymbol{g}}_s \end{aligned}$$

NO → SLIP →

$$\begin{aligned} {}_c\boldsymbol{\lambda}_s &= -\,{}_p\phi\bar{\boldsymbol{s}}^1 \\ {}^{slip}_{\ c}\dot{\boldsymbol{g}}_s &= \frac{3\Delta t}{2}\bar{\theta}\,{}_p\phi\bar{\boldsymbol{s}}^1 \\ {}^{slip}\dot{\boldsymbol{g}}_s &= {}^{slip}_{\ p}\dot{\boldsymbol{g}}_s + {}^{slip}_{\ c}\dot{\boldsymbol{g}}_s = {}^{slip}_{\ c}\dot{\boldsymbol{g}}_s \\ \boldsymbol{\lambda}_s &= {}_p\boldsymbol{\lambda}_s + {}_c\boldsymbol{\lambda}_s = \mu\lambda_n\bar{\boldsymbol{s}}^1 \\ \dot{\boldsymbol{g}}_s &= {}_p\dot{\boldsymbol{g}}_s - {}^{slip}\dot{\boldsymbol{g}}_s \end{aligned}$$

Box 4.5 Gauss-Seidel Iteration

$$
\begin{aligned}
&\text{INITIALIZE} \rightarrow \Big[\text{LOOP}_{e=1}^{nec} \rightarrow \Big| \; \boldsymbol{g}_e = \mathbf{0} \\
&\qquad \boldsymbol{g}_e^{slip} = \mathbf{0} \\
&\qquad \Delta\boldsymbol{\lambda}_e = \mathbf{0} \\
&\qquad \text{LOOP}_{i=1}^{4} \rightarrow \Big| \text{COMPUTE} \rightarrow \bar{\alpha}_e^i \\
&\qquad\qquad\qquad\quad \Big| \text{COMPUTE} \rightarrow \bar{\gamma}_e^i \\
&\qquad \text{COMPUTE} \rightarrow \bar{\theta}_e \\
&\qquad \text{LOOP}_{n=1}^{nnc} \rightarrow \Big| \; \boldsymbol{x}_n = {}_p\boldsymbol{x}_{I(n)}^{k+1} \\
&\qquad\qquad\qquad\quad \Delta\boldsymbol{x}_n = \mathbf{0} \\
&\qquad\qquad\qquad\quad \boldsymbol{\lambda}_n = \mathbf{0} \\
&\qquad\qquad\qquad\quad \Delta\boldsymbol{\lambda}_n = \mathbf{0}
\end{aligned}
$$

$$
\begin{aligned}
&\text{ITERATE} \rightarrow \Big[\text{LOOP}_{e=1}^{nec} \rightarrow \Big| \; \boldsymbol{g}_e = \sum_{i=1}^{4} \bar{\alpha}_e^i \boldsymbol{x}_{n(i)} - \boldsymbol{g}_e^{slip} \\
&\qquad\qquad\qquad\quad \Delta\boldsymbol{\lambda}_e = \frac{1}{\Delta t^2 \bar{\theta}} \boldsymbol{g}_e \\
&\qquad\qquad\qquad\quad \boldsymbol{\lambda}_e = \boldsymbol{\lambda}_{n(1)} + \Delta\boldsymbol{\lambda}_e \\
&\qquad\qquad\qquad\quad \text{CALL } \underbrace{\text{MATMODEL}(\boldsymbol{\lambda}_e, \boldsymbol{g}_e, \boldsymbol{g}_e^{slip})}_{\text{Box 4.3}} \\
&\qquad\qquad\qquad\quad \Delta\boldsymbol{\lambda}_e = \boldsymbol{\lambda}_e - \boldsymbol{\lambda}_{n(1)} \\
&\qquad\qquad\qquad\quad \text{LOOP}_{i=1}^{4} \rightarrow \Big| \; \boldsymbol{\lambda}_{n(i)} = \boldsymbol{\lambda}_{n(i)} + \bar{\alpha}_e^i \Delta\boldsymbol{\lambda}_e \\
&\qquad\qquad\qquad\qquad\qquad\quad \Big| \; \Delta\boldsymbol{\lambda}_{n(i)} = \Delta\boldsymbol{\lambda}_{n(i)} + \bar{\alpha}_e^i \Delta\boldsymbol{\lambda}_e \\
&\qquad\qquad\qquad\qquad\qquad\quad \Big| \; \Delta\boldsymbol{x}_{n(i)} = -\Delta t^2 \bar{\gamma}_e^i \Delta\boldsymbol{\lambda}_e \\
&\qquad\qquad\qquad\qquad\qquad\quad \Big| \; \boldsymbol{x}_{n(i)} = \boldsymbol{x}_{n(i)} + \Delta\boldsymbol{x}_{n(i)} \\
&\qquad \text{CHECK} \rightarrow \\
&\qquad \|\Delta\boldsymbol{\lambda}\| = \left[\sum_{n=1}^{nnc} (\Delta\boldsymbol{\lambda}_n \cdot \Delta\boldsymbol{\lambda}_n) \right]^{1/2} \\
&\qquad \|\boldsymbol{\lambda}\| = \left[\sum_{n=1}^{nnc} (\boldsymbol{\lambda}_n \cdot \boldsymbol{\lambda}_n) \right]^{1/2} \\
&\qquad \boxed{\frac{\|\Delta\boldsymbol{\lambda}\|}{\|\boldsymbol{\lambda}\|} < TOL} \quad \Rightarrow \quad \text{EXIT}
\end{aligned}
$$

5 Microplane Material Model

In this chapter rate and temperature dependent microplane model for concrete will be briefly overviewed. Detailed discussion of the concepts can be found in (Ožbolt et al. 2001, 2006; Periškic 2009). The large deformation extension of the model is the subject of this work and therefore is here discussed in more detail.

5.1 General Framework

The constitutive law employed for concrete in this work is the microplane material model with relaxed kinematic constraint, which is proposed by (Ožbolt et al. 2001) and successfully used in a number of numerical simulations of concrete and reinforced concrete structures. The model utilizes the strength of both macroscopic and microscopic models and therefore is known to provide results which are in very good agreement with the experiments, e.g. (Ožbolt et al. 2002). The model is able to realistically describe micro-structural phenomena such as cohesion, friction and aggregate interlock etc.

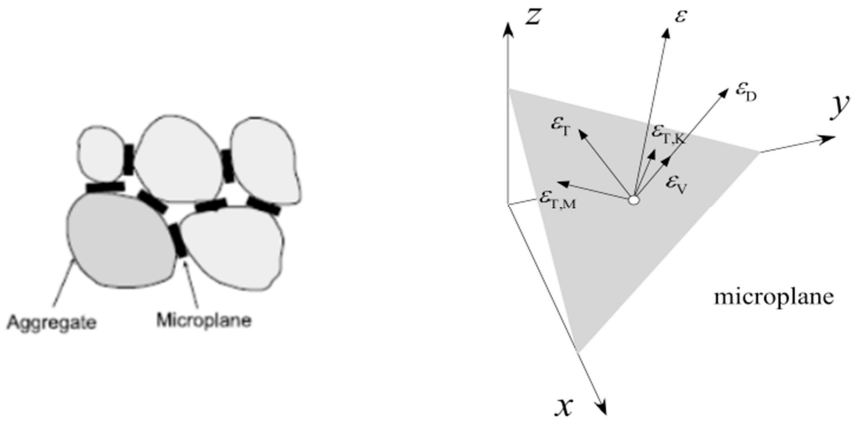

Fig. 5.1 Microplane model: Idealized contact planes (left) and Projection of the total macroscopic strain tensor onto the microplane (right)

Contrary to classical macroscopic type of constitutive laws, which are based on tensorial invariants of stresses and strains, in the microplane model the material response is calculated based on the monitoring of uniaxial stresses and strains in a number of predefined directions. Integrating microplane stresses in a thermodynamically consistent way, it is possible to calculate macroscopic stress tensor. Principally, the constitutive framework is similar to discrete type of the models, e.g. random particle model, with the difference that the model is formulated within the framework of continuum mechanics. The physical concept behind the microplane model was already discussed at the beginning of last century by (Mohr 1900) and (G. I. Taylor 1938). The microplanes may be

imagined to represent damage or weak planes in the microstructure, such as those that exist at the contact between aggregate and the cement matrix or slip planes in the theory of plasticity as shown in Fig. 5.1 (Ožbolt et al. 2001).

Generally, in macroscopic models, the macroscopic strain tensor is related to the macroscopic stress tensor through a constitutive relationship valid at macro level. In microplane model, there are few more steps involved. Basically, in the model the macroscopic strain tensor $\boldsymbol{\varepsilon} = \varepsilon_{ij}\mathbf{e}_i \otimes \mathbf{e}_j$ is first projected onto microplanes (kinematic constraint) and then decomposed into components on mutually perpendicular directions that are used to characterize material behaviour for that direction (see Fig. 5.2). In the model microplane is defined by its unit normal vector $\boldsymbol{n} = n_i\mathbf{e}_i$. Let $\boldsymbol{k} = k_i\mathbf{e}_i$ and $\boldsymbol{m} = m_i\mathbf{e}_i$ denote predefined mutually perpendicular unit vectors corresponding to shear directions on a microplane such that

$$\boldsymbol{k} = \boldsymbol{m} \times \boldsymbol{n} \tag{Eq. 5.1}$$

Then normal and shear strain components on the microplane can be computed by projection of the macroscopic strain tensor as

$$\begin{aligned} e_n &= \boldsymbol{n}\cdot\boldsymbol{\varepsilon}\cdot\boldsymbol{n} &&= \mathbb{P}_n{:}\boldsymbol{\varepsilon} \\ e_k &= \boldsymbol{k}\cdot\boldsymbol{\varepsilon}\cdot\boldsymbol{n} &&= \mathbb{P}_k{:}\boldsymbol{\varepsilon} \\ e_m &= \boldsymbol{m}\cdot\boldsymbol{\varepsilon}\cdot\boldsymbol{n} &&= \mathbb{P}_m{:}\boldsymbol{\varepsilon} \end{aligned} \tag{Eq. 5.2}$$

where projection tensors for each component are defined as

$$\begin{aligned} \mathbb{P}_n &:= \boldsymbol{n}\otimes\boldsymbol{n} \\ \mathbb{P}_k &:= \boldsymbol{k}\otimes\boldsymbol{n} \\ \mathbb{P}_m &:= \boldsymbol{m}\otimes\boldsymbol{n} \end{aligned} \tag{Eq. 5.3}$$

Since normal microplane directions and corresponding shear directions are fixed, projection tensors given by (Eq. 5.3) can be computed and stored at the beginning of the finite element analysis. To realistically model concrete response, the normal microplane strain component is further decomposed into volumetric (e_V) and deviatoric (e_D) parts as

$$e_n = e_V + e_D \tag{Eq. 5.4}$$

Volumetric part is obtained from macroscopic strain tensor as

$$e_V = \frac{1}{3}\varepsilon_{kk} \tag{Eq. 5.5}$$

In the version of the microplane model used in this work, the kinematic constraint is relaxed in order to prevent unrealistic material response under dominant tensile load (Ožbolt et al. 2001). Namely,

for strong localization of strains due to crack opening (Mode-I fracture), the kinematic constraint is physically meaningless. Therefore an additional function, called as discontinuity function, is introduced. By means of discontinuity function, the microplane stresses and strains for all microplane directions gradually relaxes down to zero in case of crack opening for dominant macroscopic tension. In this way the material becomes fully unloaded and stress locking is prevented at the finite element level.

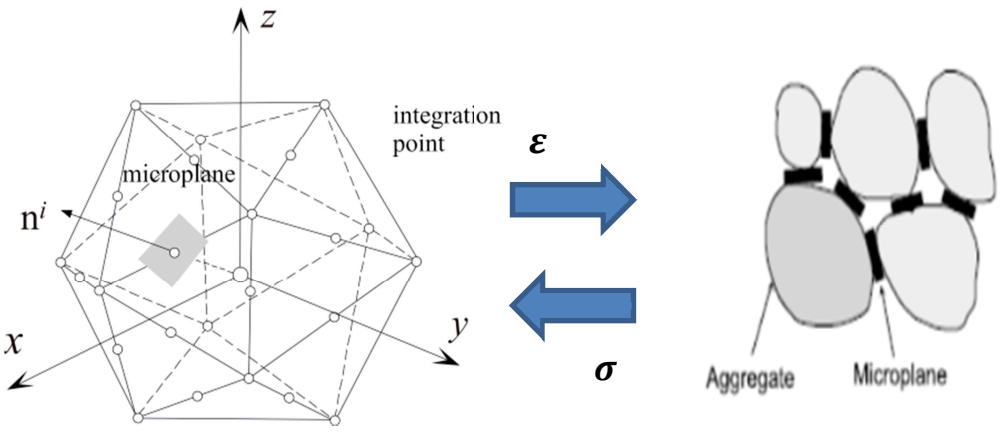

Fig. 5.2 Concept of microplane model (Ožbolt et al. 2001)

After obtaining microplane strain components, microplane stress components σ_V, σ_D, σ_k and σ_m are computed by employing one-dimensional inelastic constitutive equations (Ožbolt et al. 2001). In the present model, except for volumetric compression, the one-dimensional constitutive stress-strain relationship for volumetric, deviatoric and shear directions are based on the scalar damage theory. The curves are defined by exponential functions. Typical uniaxial stress-strain curves for volumetric, deviatoric and both shear components are shown in Fig. 5.3. Finally, using the principle of virtual work, a numerical integration over the total number of microplanes representing the material point is performed to determine the macroscopic stress components. At an integration point, total number of microplanes can be an arbitrary number. Obviously, larger number of microplanes will produce more accurate results but at the same time will need much higher computational effort. A good balance between the computational time and accuracy can be obtained by considering 21 microplanes (Bažant et al. 1986) as shown in Fig. 5.2. Since microplanes with different spatial orientations are considered, the tensorial invariant restrictions are automatically fulfilled and they need not be directly enforced. Based on the micro-macro work conjugacy of volumetric-deviatoric split and using in advance defined microplane stress-strain constitutive laws, the macroscopic stress tensor is calculated as an integral over all possible predefined microplane orientations:

$$\sigma_{ij} = \sigma_V \delta_{ij} + \frac{3}{2\pi} \int_S \left[\sigma_D \left(n_i n_j - \frac{\delta_{ij}}{3} \right) + \frac{\sigma_k}{2} \left(k_i n_j + k_j n_i \right) + \frac{\sigma_m}{2} \left(m_i n_j + m_j n_i \right) \right] dS \qquad \text{(Eq. 5.6)}$$

where S denotes the surface of the unit radius sphere and δ_{ij} denotes Kronecker delta.

In its original form the model has a number of internal parameters which cannot be explicitly related to the macroscopic properties of concrete, such as strength and fracture energy. This is actually the main disadvantage of the model. To overcome this inconvenience, a computer code is written, which for known macroscopic properties of concrete (Young's modulus, Poisson's ratio, uni-axial tensile and compressive strength and fracture energy) generates corresponding microplane model parameters (Ožbolt et al. 2001). In order to obtain results that are objective with respect to the size of finite elements, the local version of the microplane model is used together with regularization based on the energy (crack band method). Consequently, at the start of the analysis the constitutive law has to be adopted for each finite element.

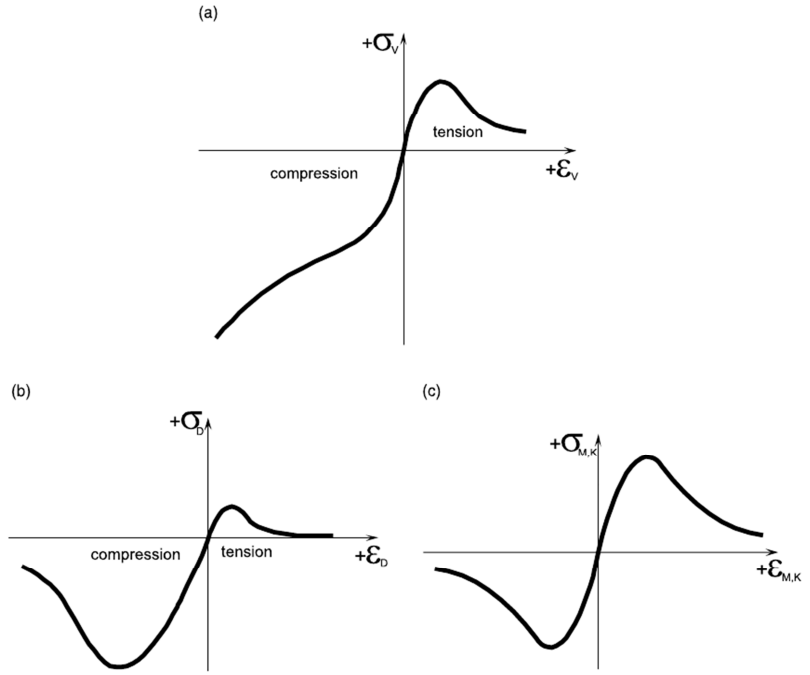

Fig. 5.3 Schematic plot of microplane stress-strain relationships for virgin load: (a) volumetric component (V). (b) deviatoric component (D) and (c) shear stress-strain components (m and k).

Contrary to the standard tensorial type of macroscopic models, the main advantage of the microplane model is the fact that the model accounts for the interaction between different orientations in the material. From this point of view the model is very similar to the discrete models. As will be demonstrated on several numerical examples, together with simple standard finite elements, the model is able to realistically predict complex phenomena related to dynamic fracture of concrete without any additional energy criteria.

5.2 Rate Effects

The rate dependency in the here presented version of the microplane model for concrete accounts for two effects: (i) the rate dependency related to the formation (propagation) of the micro-cracks, which is the effect of inertia forces at the level of the micro-crack tip, and (ii) the rate dependency due to the viscosity of concrete (bulk material) between the micro-cracks. In the rate dependent microplane model proposed by (Bažant et al. 2000a), these effects are modeled by two separate contributions, i.e. viscosity is represented by a simple viscoelastic model and the rate dependent growth of micro-cracks is modeled by rate process theory, which results in the following relationship between stress and strain rate:

$$\sigma(\varepsilon) = \sigma^0(\varepsilon)\left[1 + C_2 \operatorname{asinh}\left(\frac{\dot{\varepsilon}}{C_1}\right)\right] \qquad \text{(Eq. 5.7)}$$

where σ is stress at dynamic load, σ^0 is stress at static load, $\dot{\varepsilon}$ is strain rate, C_1 and C_2 are constants determined from experiments (Bažant et al. 2000a).

In the present model, both effects are modeled in the integral sense based on the rate process theory, similar to the concept proposed by (Mihashi et al. 1980). It is assumed that the micro-cracks start to grow immediately after the application of load. The initial stiffness, which is in experiments always measured as secant stiffness, is assumed to be controlled by the rate of growing micro-cracks. Since in the model the out-coming strength is proportional to the initial stiffness, an increase in initial stiffness, because of higher strain rate, also causes an increase in strength. The influence of inertia at the macro scale (e.g. inertia at the macro crack tip or structural inertia) on the rate dependency is not and should not be a part of the constitutive law. As will be demonstrated later, this effect is automatically accounted for in dynamic analysis in which the constitutive law interacts with forces due to structural inertia.

The rate of strain $\dot{\varepsilon}$ in a continuum with a number of parallel cohesive cracks can be expressed as

$$\dot{\varepsilon} = \frac{\dot{w}}{s_{cr}} + \frac{\dot{\sigma}}{E} \approx \frac{\dot{w}}{s_{cr}} \qquad \text{(Eq. 5.8)}$$

where ε is average macroscopic strain normal to the direction of parallel cracks, s_{cr} is spacing of the parallel cracks, E is effective Young's modulus of bulk material and $\dot{\sigma}/E$ is the elastic strain rate which can be neglected as compared to the crack opening rate $\dot{w}$. After introducing a few reasonable simplifications into the concept that is based on the energy activation theory (A. S. Krausz et al. 1988), the influence of the rate effect on the rate independent stress-strain relation $\sigma^0(\varepsilon)$ can be calculated according to (Eq. 5.7).

(a) (b)

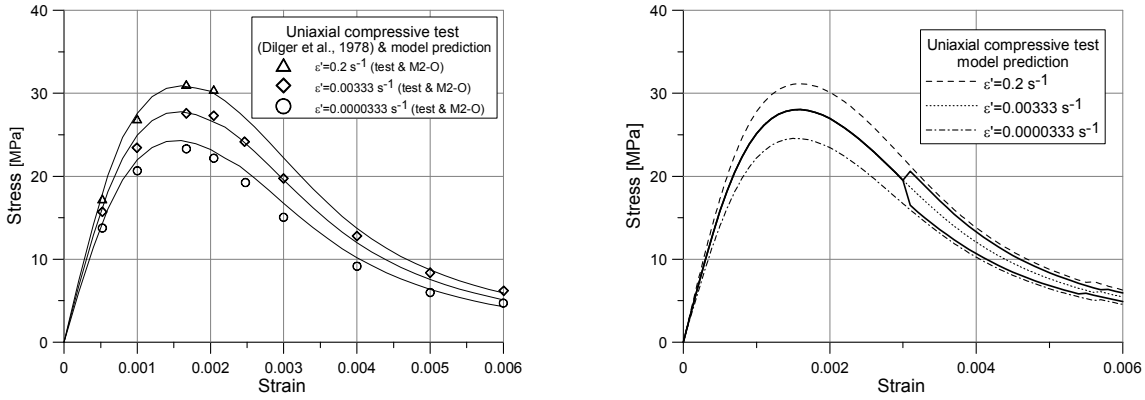

Fig. 5.4 Uniaxial compressive test (Ožbolt et al. 2006):
(a) model prediction and test data (Dilger et al. 1978) and
(b) model prediction – increase and decrease of the loading rate in the softening region

In the microplane model macroscopic response is obtained by integrating normal and shear microplane stresses over all microplanes. The rate independent microplane stress components $\sigma_{Mp}^{0}(e_{Mp})$, where Mp stands for, respectively, microplane volumetric, deviatoric and shear components, are calculated from the known microplane strains e_{Mp} using pre-defined microplane uniaxial stress-strain constitutive relations (Ožbolt et al. 2001). The strain rate independent model parameters are: Young's modulus, Poisson's ratio, uniaxial compressive and tensile strengths and fracture energy. These macroscopic properties are related to internal microplane parameters (Ožbolt et al. 2001). It seems reasonable to assume that the rate effect on each microplane component is of the same type as given by (Eq. 5.7). Consequently, the rate dependency for each microplane component reads (Ožbolt et al. 2006)

$$\sigma_{Mp}(e_{Mp}) = \sigma_{Mp}^{0}(e_{Mp})\left[1 + c_2\,\mathrm{asinh}\left(\frac{\dot{\gamma}}{c_1}\right)\right] \quad \text{with} \quad \dot{\gamma} = \sqrt{\frac{1}{2}\dot{\varepsilon}_{ij}\dot{\varepsilon}_{ij}} \quad c_1 = \frac{c_0}{s_{cr}} \qquad \text{(Eq. 5.9)}$$

where c_0 and c_2 are material rate constants which have to be calibrated by fitting test data, $\dot{\varepsilon}_{ij}$ are components of the macroscopic strain rate tensor. From (Eq. 5.9) it is obvious that the rate magnitude is not measured on the individual microplanes, which would not be objective otherwise, but on the macro-scale. Furthermore, (Eq. 5.9) applies to all microplane components except to volumetric compression, which is assumed to be rate insensitive. This is because for volumetric compression there is no crack development, i.e. the material is compacted.

The model parameters from (Eq. 5.9) are calibrated (Ožbolt et al. 2006) based on the uniaxial compressive tests performed by (Dilger et al. 1984). The tests have been carried out for three loading rates: $0.2\ \mathrm{s}^{-1}$, $3.33\mathrm{x}10^{-3}\ \mathrm{s}^{-1}$ and $3.33\mathrm{x}10^{-5}\ \mathrm{s}^{-1}$. Assuming average crack spacing of $s_{cr} = 100\ \mathrm{mm}$, the following values are obtained from the calibration procedure: $c_0 = 0.0004\ \mathrm{mm/s}$ and

$c_2 = 0.032$ (Ožbolt et al. 2006). Using these parameters, the rate dependent uniaxial compressive stress-strain curves are plotted for three different loading rates in Fig. 5.4a. together with the test results. Fig. 5.4b shows the model response in the case of a sudden increase and decrease of the strain rate for the compression softening. Similar behavior was observed in the experiments (Bažant et al. 2000a). The influence of strain rate on the uniaxial compressive strength and initial Young's modulus is shown in Fig. 5.5. In both figures, the static strength and the static Young's modulus correspond to the strain rate of $10^{-5}\ \mathrm{s}^{-1}$ for which the average test value of the ratio between dynamic and static strengths is equal to one. As can be seen, for medium strain rates up to approximately $1.0\ \mathrm{s}^{-1}$ the microplane model prediction agrees well with the average trend observed in the experiments.

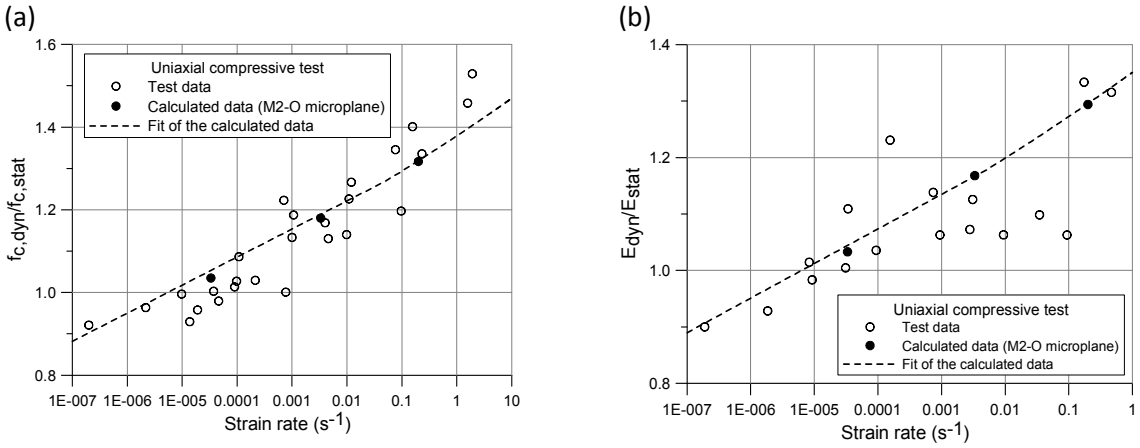

Fig. 5.5 Uniaxial compressive test (Ožbolt et al. 2006):
(a) rate dependent compressive strength – test data and model prediction and
(b) rate dependent initial Young's modulus - test data and model prediction

As mentioned above, the influence of structural inertia on the rate sensitive response is not a part of the constitutive model. By a number of numerical studies (Ožbolt et al. 2005b, 2006, 2012, 2013b, 2014) it was demonstrated that inertia effects, which cause a kind of homogenization of the material, is accounted for automatically in dynamic analysis through the interaction between inertia forces (stresses) and constitutive law. The effect is here illustrated on the example of a concrete cylinder (Young's modulus $E_c = 35000\ \mathrm{MPa}$, Poisson's ratio $\nu = 0.18$, tensile strength $f_t = 2.25\ \mathrm{MPa}$, uniaxial compressive strength $f_c = 23\ \mathrm{MPa}$ and concrete fracture energy $G_F = 0.08\ \mathrm{N/mm}$; cylinder diameter $D = 50\ \mathrm{mm}$ and height $H = 100\ \mathrm{mm}$) loaded by different strain rates. To demonstrate the influence of inertia, rate sensitive static and dynamic analysis were carried out. The relation between the relative compressive strength (resistance) and strain rate is plotted in Fig. 5.6. The results of the rate dependent static analysis show almost linear increase of relative strength as a function of strain rate (log-log scale). The outcome of the rate sensitive dynamic analysis shows for medium strain rates the same tendency. However, similar to experiments (Bischoff et al. 1991), the increase of resistance becomes progressive for strain rates higher than approximately $10\ \mathrm{s}^{-1}$. Obviously, the

results clearly show that inertia forces are responsible for the progressive increases obtained in the dynamic analysis. For comparison a curve proposed by CEB (1988) is also shown. The agreement between test data, CEB prediction formula and numerical results is very good.

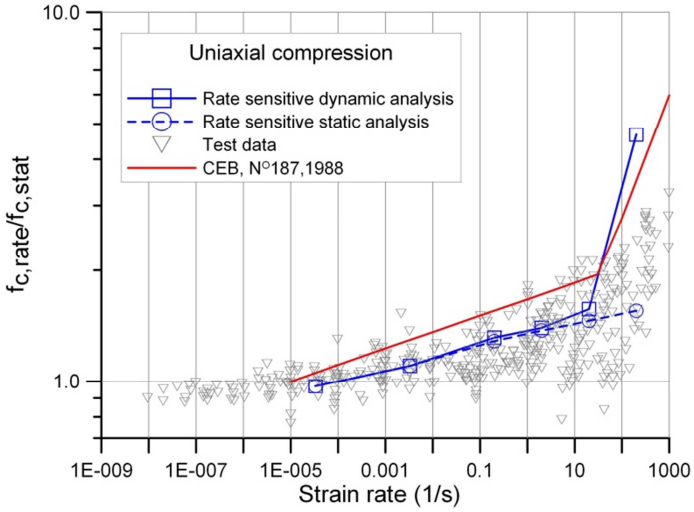

Fig. 5.6 Relative compressive strength as a function of strain rate (Ožbolt et al. 2006)

5.3 Thermal Effects

To account for the effect of temperature the macroscopic mechanical properties of concrete need to be temperature dependent. In the present work the thermo-mechanical model proposed by (Ožbolt et al. 2005a, 2008, 2013a; Periškic 2009; Bošnjak 2014) is adopted.

5.3.1 Young's Modulus

The experiments indicate that with the temperature increase Young's modulus E decreases as shown by Schneider (1982). It is assumed that at relatively low temperatures, decrease of E is caused by the loss of capillary water (vaporization). However, at higher temperatures decrease of E is due to the decomposition of individual concrete components (cement paste and aggregate). In the present model, temperature dependent Young's modulus follows the proposition of Stabler (2000), i.e. E is assumed to be a scalar function of temperature, see Fig. 5.7, which reads as

$$
\begin{aligned}
E &= \left(1 - \max(\omega_{t,E})\right) E^{20} \\
\omega_{t,E} &= 0.2\,\theta - 0.01\,\theta^2 \qquad \text{for } 0 \le \theta \le 10.0 \\
\omega_{t,E} &= 1.0 \qquad \text{for } \theta > 10.0
\end{aligned}
\qquad \text{(Eq. 5.10)}
$$

where E^{20} is Young's modulus at temperature $T_0 = 20\ ^{\circ}C$, $\theta = (T - T_0)/100\ ^{\circ}C$ is the normalized relative temperature and history parameter $\max(\omega_{t,E})$ is the maximum value of $\omega_{t,E}$ attained during temperature loading/unloading.

5.3.2 Compressive Strength

According to the experimental evidence by Schneider (1982) at temperatures up to $300\ ^{\circ}C$ the concrete compressive strength remains almost constant. However, with further temperature increase, the concrete strength decreases almost linearly. Namely, at lower temperatures ($< \sim 300\ ^{\circ}C$) hydration of cement paste is more advanced. Moreover, due to the thermal strains the frictional and aggregate locking phenomena are stronger than for the concrete at normal temperature. Due to these effects the compressive strength does not decrease. At high temperature micro-cracks, vaporization and decomposition of cement paste and aggregate cause decrease of the concrete compressive strength. In the present model it is assumed that up to $T = 300\ ^{\circ}C$ the cylinder compressive strength f_c is temperature independent and for higher temperature it decreases as a linear function of temperature, i.e.

$$
\begin{aligned}
f_c(T) &= \max\left(\omega_{t,f_c}\right) f_c^{20} \\
\omega_{t,f_c} &= 1.0 \qquad\qquad \text{for } 0 \le \theta \le 2.8 \\
\omega_{t,f_c} &= 1.43 - 0.153\,\theta \quad \text{for } \theta > 2.8
\end{aligned}
\qquad \text{(Eq. 5.11)}
$$

where f_c^{20} is uniaxial compressive strength at $T = 20\ ^{\circ}C$ (see Fig. 5.7).

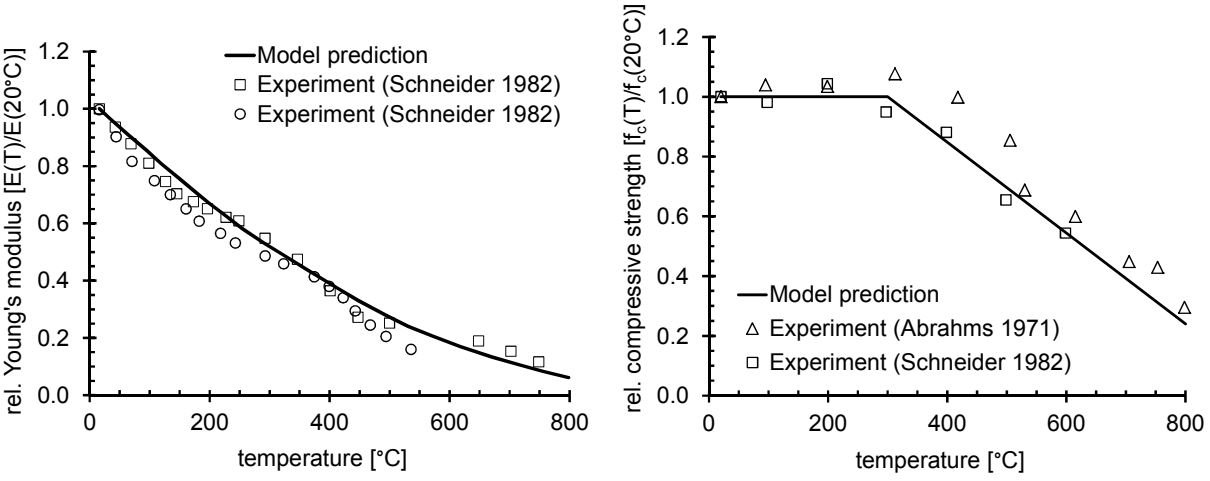

Fig. 5.7 The dependency of the Young's modulus of concrete (left) and concrete compressive strength (right) on temperature

5.3.3 Tensile Strength

The experimental evidence indicates that the tensile strength of concrete decreases almost linearly with increase of temperature as shown by Schneider (1982) and B. Zhang et al. (2002). At lower temperatures thermal strains lead to micro cracking and damage of the aggregate-cement paste interface that reduces tensile strength of concrete. With temperature increase, micro-cracks, vaporization and decomposition of cement paste and aggregate also lead to decrease of the concrete tensile strength.

In the present model the following dependency of tensile strength on temperature is adopted:

$$f_t(T) = \max\left(\omega_{t,f_t}\right) f_t^{20}$$
$$\omega_{t,f_t} = 1.0 - 0.13\,\theta \qquad \text{(Eq. 5.12)}$$

where f_t^{20} is uniaxial tensile strength at $T = 20\ ^{\circ}C$ (see Fig. 5.8).

5.3.4 Fracture Energy

The experimental data (B. Zhang et al. 2002) show that with the temperature increase up to approximately $300\ ^{\circ}C$ the concrete fracture energy increases for approximately 60%. However, with further temperature increase it starts to decrease and at approximately $600\ ^{\circ}C$ reaches about 60% of its initial value. This can be attributed to the fact that at temperatures lower than approximately $300\ ^{\circ}C$ the hydration of cement paste is more advanced than at normal room temperature. Moreover, at this stage temperature strains contribute to the frictional effects and aggregate interlock what also increases ductility. At higher temperatures the micro-cracks, vaporization and decomposition of cement paste and aggregate cause decrease in fracture energy. In the present model, the dependency of the concrete fracture energy G_F on the temperature is obtained by fitting of test data of B. Zhang et al. (2002). The adopted dependency reads as

$$G_F(T) = \max\left(\omega_{t,G_F}\right) G_F^{20}$$
$$\omega_{t,G_F} = 1.0 + 0.407\,\theta - 0.0727\,\theta^2 \quad \text{for } 0 \le \theta \le 2.8 \qquad \text{(Eq. 5.13)}$$
$$\omega_{t,G_F} = 0.917 + 0.467\,\theta - 0.0833\,\theta^2 \quad \text{for } \theta > 2.8$$

where G_F^{20} is concrete fracture energy at $T = 20\ ^{\circ}C$ (see Fig. 5.8).

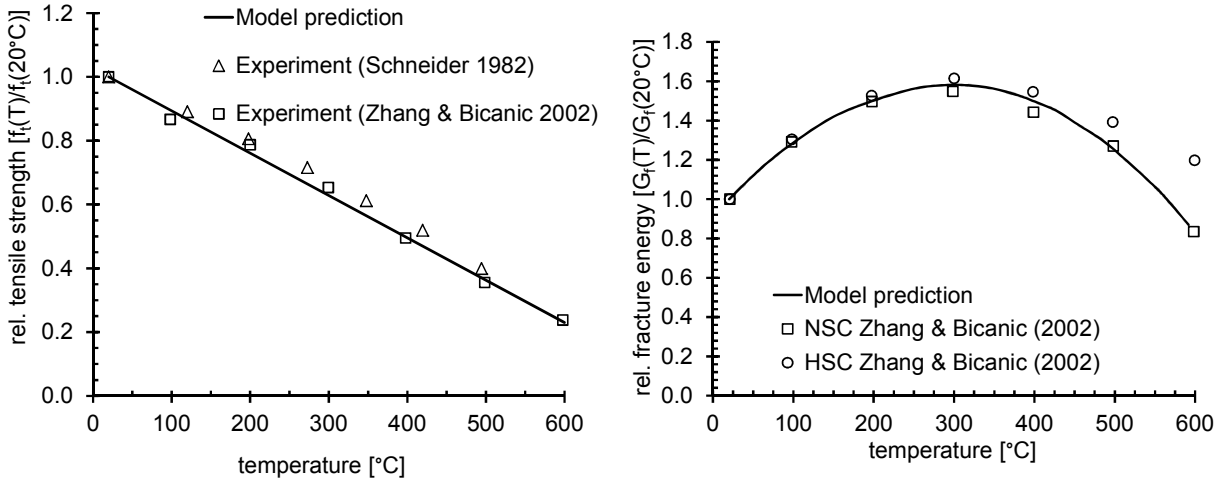

Fig. 5.8 Relative tensile strength of concrete as a function of temperature (left) and relative concrete fracture energy of concrete as a function of temperature (residual conditions) (right)

5.3.5 Strains

5.3.5.1 Decomposition of Strain Tensor

In the present model the total strain tensor ε_{ij} for stressed concrete exposed to high temperature can be decomposed additively as

$$\varepsilon_{ij} = \varepsilon_{ij}^{m}(T, \sigma_{kl}) + \varepsilon_{ij}^{ft}(T) + \varepsilon_{ij}^{lits}(T, \sigma_{kl}) \qquad \text{(Eq. 5.14)}$$

where ε_{ij}^{m} are mechanical strain components obtained from kinematical relationships, ε_{ij}^{ft} are free thermal strain components and ε_{ij}^{lits} are load-induced thermal strain components (Khoury et al. 1985). In general, the mechanical strain components can be further decomposed into elastic, plastic and damage parts. In the present model these strain components are obtained from the constitutive law. The free thermal strain is stress independent and is experimentally obtained by measurements on the load-free specimens. In such experiments it is not possible to isolate shrinkage of cement paste, therefore the temperature dependent shrinkage is contained in the free thermal strain. The load-induced thermal strain is stress and temperature dependent (Khoury 2006a–c). It appears only during the first heating and not during subsequent cooling and heating cycles. This strain is irrecoverable and can cause severe tensile stresses during cooling in concrete structures. It generally comprises several components including transient strain (consisting of transitional thermal creep and drying creep), time-dependent creep and changes in elastic strain that occur during heating under load. Due to the fact that these components have similar properties – they are all irrecoverable – and are hard to be individually identified in an experiment, it is common practice to model them mutually in a single strain tensor. However, it should be noted that in case of very fast loading, such as impact, these strains cannot be realized.

5.3.5.2 Free Thermal Strain

The experimental evidence by (Schneider 1982) indicates that the free thermal strains in concrete specimen mainly depend on the type and amount of the aggregate. Although the experiments indicate that the free thermal strain depends on the heating rate, in the present model it is assumed that this strain depends only on temperature. Moreover, it is assumed that in the case of a stress free specimen, the thermal strains are equal in all three mutually perpendicular directions (isotropy). The temperature dependency of the free thermal strain, as adopted in the present model, reads as

$$\dot{\varepsilon}_{ij}^{ft} = \alpha \dot{T} \delta_{ij}$$

$$\alpha = \begin{cases} \dfrac{6.0\text{x}10^{-5}}{7.0 - \theta} & \text{for } 0 \le \theta \le 6.0 \\ 0 & \text{for } \theta > 6.0 \end{cases} \qquad \text{(Eq. 5.15)}$$

This temperature dependency approximately corresponds to experimental data obtained for sandstone aggregates. However, it is also possible to input a desired temperature dependent path for free thermal strain in order to account for the effect of different aggregates or to model the thermal strain of different concrete constituents.

5.3.5.3 Load-Induced Thermal Strain

When a concrete specimen is loaded before heating (heating of stressed specimen), the resulting thermal strain (i.e. all the contributions to the total strain, induced by high temperature) is different from that occurring in an unloaded specimen (heating of unstressed specimen) (Khoury 2006a–c). The difference can be obtained if the free thermal strain is subtracted from the resulting thermal strain, which results in the so called load-induced thermal strain. It is relatively insensitive to aggregate type and cement paste since it originates from cement gel and mismatch between aggregates and mortar. Due to its similarity for different concrete types, a common "master" LITS curve is taken to exist up to temperatures of about $450\ ^{\circ}C$. In the present model the bi-parabolic function is used for representing load induced thermal strain (Nielsent et al. 2004), which reads as

$$\dot{\varepsilon}^{lits}(T,\sigma) = \frac{\sigma}{f_c^{20}}\beta\dot{T} \quad (\sigma \rightarrow \text{maximum principal compression})$$
$$\beta = \begin{cases} 0.02A\theta + B & \text{for } 0 \le \theta \le \theta^*(=4.5) \\ 0.02C(\theta-\theta^*) + 2A\theta^* + B & \text{for } \theta > \theta^* \end{cases} \qquad \text{(Eq. 5.16)}$$

where θ^* is a dimensionless transition temperature corresponding to $470\ ^{\circ}C$ with $T_0 = 20\ ^{\circ}C$. The two expressions above are introduced to account for abrupt change in behavior detected in the experiments. Constants A, B and C are experimentally obtained constants and are set as: $A = 0.0005$, $B = 0.00125$ and $C = 0.0085$ in the present model.

The presented implementation of load induced thermal strain is valid for the macro-scale modeling approach, when concrete is idealized as a homogeneous material. However, when modeling concrete at meso-scale, load induced thermal strains were not explicitly accounted for in the model, since the largest part of these strains comes automatically from the meso-scale model.

5.4 Extension to Large Deformations

5.4.1 Appropriate Strain Measure

In the rate and temperature dependent microplane material model overviewed in previous sections, constitutive equation for each microplane stress component is defined by a simple one-dimensional scalar damage type material model of the generic form

$$\sigma = (1-\omega)Ee \qquad \text{(Eq. 5.17)}$$

where σ , e represent, respectively, generic microplane stress and strain components, E, is generic virgin elastic modulus, ω is generic scalar damage variable controlling degradation of stiffness. Due to thermodynamical restrictions, i.e. for positive dissipation, damage rate must be always greater than or equal to zero, i.e.

$$\dot{\omega} \geq 0 \qquad \text{(Eq. 5.18)}$$

In addition, damage is assumed to grow if and only if e exceeds its maximum value e_{max} that has been reached so far. It implies that damage variable is a function of e_{max}, i.e. $\omega = f(e_{max})$, and

$$e \leq e_{max} \quad \Longrightarrow \quad \phi := e - e_{max} \leq 0 \qquad \text{(Eq. 5.19)}$$

Definition in (Eq. 5.19) is made for convenience. Based on (Eq. 5.18) and (Eq. 5.19), conditions for damage evolution can be written as

$$\begin{aligned} \text{damage} \rightarrow & \begin{vmatrix} \phi &= 0 \\ \dot{\omega} &\geq 0 \end{vmatrix} \\ \text{no damage} \rightarrow & \begin{vmatrix} \phi &\leq 0 \\ \dot{\omega} &= 0 \end{vmatrix} \end{aligned} \qquad \text{(Eq. 5.20)}$$

Equations for damage evolution, also known as loading/unloading conditions, can be expressed in the form of Karush-Kuhn-Tucker conditions as

$$\phi\dot{\omega} = 0; \quad \phi \leq 0; \quad \dot{\omega} \geq 0 \qquad \text{(Eq. 5.21)}$$

With (Eq. 5.17) and (Eq. 5.21) material behavior under general loading scenarios is fully described.

To be able to track evolution of ω, e must be related to a strain measure which refers to initial reference configuration. One can then conveniently choose among Seth-Hill family of generalized strain tensors given by

$$\boldsymbol{E}_m = \frac{1}{2m}(\boldsymbol{U}^{2m} - \boldsymbol{I}) = \frac{1}{2m}(\boldsymbol{C}^m - \boldsymbol{I}) \qquad \text{(Eq. 5.22)}$$

Setting $m = 1, 1/2, 0$, we obtain, respectively, Green-Lagrangian (GL), Biot and Hencky (True) strain tensors. A finite strain measure should be able to characterize stretches along a given microplane independent of the stretches that belong to some others. This condition is satisfied only for Green-Lagrangian strain tensor (Bažant et al. 2000b). Therefore it has to be put in charge for large deformation generalization of microplane material model (Bažant et al. 2000b).

5.4.1.1 Additive Deviatoric-Volumetric Split

Original microplane model is formulated based on deviatoric-volumetric split of the microplane normal strain component. At small deformations this split has additive form, whereas at large deformations it is generally multiplicative. For concrete the change in volume at large deformations is always small. Based on this fact approximate additive decomposition of GL strain tensor into deviatoric and volumetric parts is possible (Bažant 1995; Bažant et al. 1996a, 2000b), i.e. one can write

$$E_{ij} = E_{D\,ij} + E_V \delta_{ij} \qquad \text{(Eq. 5.23)}$$

In (Eq. 5.23), $E_{D\,ij}$ are deviatoric components and E_V is the approximate volumetric strain given by

$$E_V = E_0 + \frac{1}{2} E_0^2 \qquad \text{(Eq. 5.24)}$$

with

$$E_0 = \mathcal{J}^{1/3} - 1 \qquad \text{(Eq. 5.25)}$$

5.4.2 Appropriate Stress Measure

Second Piola-Kirchhoff (PK2) stress tensor, which is work-conjugate to the GL strain tensor, is the natural choice to be used as a stress measure. But one must be careful that stress components, for a given microplane, obtained from the projection of Cauchy stress and PK2 must be equal to each other for microplane model to make a physical sense (Bažant et al. 2000b). This strict requirement can be fulfilled by realizing the fact that concrete, as a quasi-brittle material, cannot sustain large deformations. Based on this observation one can write

$$\begin{aligned} &\boldsymbol{\mathcal{F}} \cong \boldsymbol{\mathcal{R}} \\ &\mathcal{J} \cong 1 \end{aligned} \qquad \text{(Eq. 5.26)}$$

Within context of (Eq. 5.26), Cauchy stress is obtained as

$$\boldsymbol{\sigma} = \frac{1}{\mathcal{J}} \boldsymbol{\mathcal{F}} \boldsymbol{\mathcal{S}} \boldsymbol{\mathcal{F}}^T \cong \boldsymbol{\mathcal{R}} \boldsymbol{\mathcal{S}} \boldsymbol{\mathcal{R}}^T \quad \Longrightarrow \quad \sigma_{ij} = \mathcal{R}_{ik} s_{kl} \mathcal{R}_{lj}^T \qquad \text{(Eq. 5.27)}$$

Co-rotated Cauchy stress $\hat{\boldsymbol{\sigma}}$ can be expressed in terms of $\boldsymbol{\sigma}$ as

$$\begin{aligned} &\boldsymbol{\sigma} = \sigma_{ij} \mathbf{e}_i \otimes \mathbf{e}_j = \sigma_{ij} (\boldsymbol{\mathcal{R}}^T \hat{\mathbf{e}}_i) \otimes \left(\boldsymbol{\mathcal{R}}^T \hat{\mathbf{e}}_j \right) = \hat{\sigma}_{mn} \hat{\mathbf{e}}_m \otimes \hat{\mathbf{e}}_n = \hat{\boldsymbol{\sigma}} \\ &\hat{\sigma}_{mn} = \mathcal{R}_{mi}^T \sigma_{ij} \mathcal{R}_{jn} \end{aligned} \qquad \text{(Eq. 5.28)}$$

With the insertion of (Eq. 5.28) into (Eq. 5.27), it is obtained that

$$\hat{\sigma}_{mn} = \mathcal{R}_{mi}^T \sigma_{ij} \mathcal{R}_{jn} = \mathcal{R}_{im} \mathcal{R}_{ik} s_{kl} \mathcal{R}_{jl} \mathcal{R}_{jn} = \delta_{mk} \delta_{ln} s_{kl} = s_{mn} \qquad \text{(Eq. 5.29)}$$

(Eq. 5.29) states that components of PK2 in global Cartesian coordinate system are equal to the components of co-rotated Cauchy stress referred to rotated coordinate system (see Fig. 5.9).

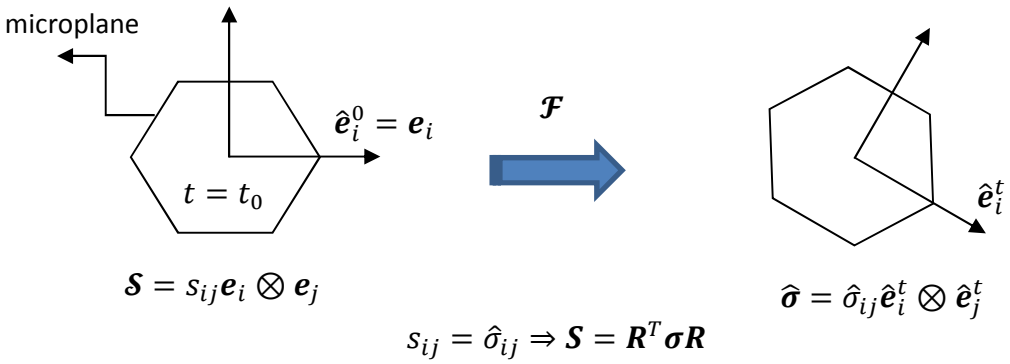

Fig. 5.9 Co-rotated Cauchy stress

In addition, by exploiting the Nanson's formula for normal map, we obtain the following relationship between microplane normal at reference and current configurations:

$$\begin{aligned} \mathbf{d}\boldsymbol{a} = \mathcal{J}\boldsymbol{\mathcal{F}}^{-T}\boldsymbol{d}\boldsymbol{\mathcal{A}} \quad \Longrightarrow \quad \boldsymbol{n} \;&\cong \boldsymbol{\mathcal{R}}^{-T}\boldsymbol{N} \quad \Longrightarrow \quad n_i = \mathcal{R}_{ij}N_j \\ &= (\boldsymbol{\mathcal{R}}^T)^T\boldsymbol{N} \\ &= \boldsymbol{\mathcal{R}}\boldsymbol{N} \end{aligned} \tag{Eq. 5.30}$$

Microplane normal in rotated coordinate system can be expressed as

$$\boldsymbol{n} = n_i\mathbf{e}_i = n_i\left(\boldsymbol{\mathcal{R}}^T\hat{\mathbf{e}}_i^t\right) = \hat{n}_m\hat{\mathbf{e}}_m^t; \quad \hat{n}_m = \mathcal{R}_{mi}^T n_i \tag{Eq. 5.31}$$

Plugging (Eq. 5.30) into (Eq. 5.31), we get

$$\hat{n}_m = \mathcal{R}_{mi}^T n_i = \mathcal{R}_{im}\mathcal{R}_{ij}N_j = \delta_{mj}N_j = N_m \tag{Eq. 5.32}$$

(Eq. 5.32) indicates that components of microplane normal, referred to global Cartesian coordinate system, at reference configuration are equal to those, referred to rotated coordinate system, at current configuration.

The components of a microplane traction vector, referred to reference configuration, oriented with surface normal $\boldsymbol{N}$ are expressed as

$$\boldsymbol{T} = T_i\mathbf{e}_i = \boldsymbol{S}\boldsymbol{N} = s_{ij}N_j\mathbf{e}_i \tag{Eq. 5.33}$$

whereas those, referred to current configuration, oriented with surface normal $\boldsymbol{n}$ have the form

$$\boldsymbol{t} = \hat{t}_i\hat{\mathbf{e}}_i^t = \hat{\boldsymbol{\sigma}}\hat{\boldsymbol{n}} = \hat{\sigma}_{ij}\hat{n}_j\hat{\mathbf{e}}_i^t \tag{Eq. 5.34}$$

With the insertion of (Eq. 5.29), (Eq. 5.32) and (Eq. 5.33), (Eq. 5.34) can be rewritten as

$$\boldsymbol{t} = s_{ij}N_j\hat{\mathbf{e}}_i^t = T_i\hat{\mathbf{e}}_i^t \tag{Eq. 5.35}$$

Within the context of (Eq. 5.34) and (Eq. 5.35), we conclude that

$$\hat{t}_i = T_i \tag{Eq. 5.36}$$

(Eq. 5.36) implies that microplane traction vectors referred to initial reference and current rotated coordinate systems, respectively, are component-wise equal. Therefore PK2 can be conveniently used as a stress measure for large deformation extension of the microplane material model for concrete.

5.4.3 Algorithmic Framework

Stress update is performed after node level update has been completed. With the corrected positions of particles corresponding to time step t^{k+1} at hand, first of all increment in Green-Lagrangian strain tensor is to be computed. Increment in GL strain can be computed in two different ways, by using either direct linearization or total formulation. In the former case we consider first order linearization of GL strain around $\boldsymbol{\mathcal{F}}_0^k = \partial \boldsymbol{x}^k / \partial \boldsymbol{\mathcal{X}}$ given by (Eq. 5.37).

$$\boldsymbol{E}(\boldsymbol{\mathcal{F}}) \cong \mathrm{Lin}[\boldsymbol{E}(\boldsymbol{\mathcal{F}})] = \boldsymbol{E}_0^k + \frac{1}{2}\left[\left(\Delta\boldsymbol{\mathcal{F}}_0^k\right)^T \boldsymbol{\mathcal{F}}_0^k + \boldsymbol{\mathcal{F}}_0^{k\,T}\left(\Delta\boldsymbol{\mathcal{F}}_0^k\right)\right] \tag{Eq. 5.37}$$

If (Eq. 5.37) is evaluated at time step t^{k+1}, the increment in GL strain turns out to be

$$\Delta\boldsymbol{E}_0^k := \boldsymbol{E}_0^{k+1} - \boldsymbol{E}_0^k = \frac{1}{2}\left[\left(\Delta\boldsymbol{\mathcal{F}}_0^k\right)^T \boldsymbol{\mathcal{F}}_0^k + \boldsymbol{\mathcal{F}}_0^{k\,T}\left(\Delta\boldsymbol{\mathcal{F}}_0^k\right)\right] \tag{Eq. 5.38}$$

where

$$\Delta\boldsymbol{\mathcal{F}}_0^k := \boldsymbol{\mathcal{F}}_0^{k+1} - \boldsymbol{\mathcal{F}}_0^k \tag{Eq. 5.39}$$

By applying chain rule on $\boldsymbol{\mathcal{F}}_0^{k+1}$, (Eq. 5.39) can be rewritten as

$$\begin{aligned} \Delta\boldsymbol{\mathcal{F}}_0^k &= (\boldsymbol{\mathcal{F}}_k^{k+1} - \boldsymbol{I})\boldsymbol{\mathcal{F}}_0^k \\ &= \left(\boldsymbol{\nabla}^k \Delta\boldsymbol{x}^k\right)\boldsymbol{\mathcal{F}}_0^k \end{aligned} \tag{Eq. 5.40}$$

In (Eq. 5.40), $\Delta\boldsymbol{x}^k := \boldsymbol{x}^{k+1} - \boldsymbol{x}^k$ and $\boldsymbol{\nabla}^k := \partial / \partial \boldsymbol{x}^k$. With the insertion of (Eq. 5.40) into (Eq. 5.38), it is obtained that

$$\Delta\boldsymbol{E}_0^k = \boldsymbol{\mathcal{F}}_0^{k\,T} \boldsymbol{\varepsilon}^k \boldsymbol{\mathcal{F}}_0^k \tag{Eq. 5.41}$$

where

$$\boldsymbol{\varepsilon}^k = \frac{1}{2}\left[\left(\boldsymbol{\nabla}^k \Delta\boldsymbol{x}^k\right) + \left(\boldsymbol{\nabla}^k \Delta\boldsymbol{x}^k\right)^T\right] \tag{Eq. 5.42}$$

is the engineering strain referred to configuration at time step t^k. In the latter case increment in GL strain is computed by subtracting GL strain at t^k from GL strain in t^{k+1}, i.e.

$$\Delta \boldsymbol{E}_0^k := \boldsymbol{E}_0^{k+1} - \boldsymbol{E}_0^k = \frac{1}{2}\left({\boldsymbol{\mathcal{F}}_0^{k+1}}^T \boldsymbol{\mathcal{F}}_0^{k+1} - \boldsymbol{I}\right) - \frac{1}{2}({\boldsymbol{\mathcal{F}}_0^k}^T \boldsymbol{\mathcal{F}}_0^k - \boldsymbol{I}) \tag{Eq. 5.43}$$

With the insertion of (Eq. 5.40) into (Eq. 5.43) and after applying some straightforward operations, it is obtained that

$$\begin{aligned} \Delta \boldsymbol{E}_0^k &= {\boldsymbol{\mathcal{F}}_0^k}^T \boldsymbol{E}_k^{k+1} \boldsymbol{\mathcal{F}}_0^k \\ &= {\boldsymbol{\mathcal{F}}_0^k}^T \boldsymbol{\varepsilon}^k \boldsymbol{\mathcal{F}}_0^k + \boxed{\frac{1}{2} \Delta {\boldsymbol{\mathcal{F}}_0^k}^T \Delta \boldsymbol{\mathcal{F}}_0^k} \end{aligned} \tag{Eq. 5.44}$$

If (Eq. 5.41) and (Eq. 5.44) are compared, it can easily be seen that they differ only by an amount given in the boxed expression in (Eq. 5.44). In the implementation increment in GL strain is computed by employing (Eq. 5.44). Note that to be able to compute strain increments from (Eq. 5.44), $\boldsymbol{\mathcal{F}}_0^k$ must be kept as a history parameter.

In the next step, strain increment computed from (Eq. 5.44) are sent to microplane material routine together with $\boldsymbol{E}_0^k$ and microplane history variables controlling the degradation of stiffness at microplane level. In general, for the constitutive update passing $\boldsymbol{E}_0^{k+1}$ and history variables to the material routine should be enough. However this is not the case for rate dependent microplane material model because

- Some algorithmic considerations are necessary as passing from tension to compression or vice versa at microplane level. To be able detect such a case, $\boldsymbol{E}_0^k$ is to be available.
- Strain increment $\Delta \boldsymbol{E}_0^k$ must also be provided to compute strain rate from which rate factor is computed.

Based on provided input, increment in PK2 stress is then computed and history update is performed. Finally by employing (Eq. 5.29) co-rotated Cauchy stress corresponding to time step t^{k+1} is obtained as

$$\boldsymbol{\mathcal{S}}^{k+1} = s_{ij}^{k+1} \mathbf{e}_i \otimes \mathbf{e}_j \quad \underbrace{\Longrightarrow}_{\text{(Eq.5.29)}} \quad \widehat{\boldsymbol{\sigma}}^{k+1} = s_{ij}^{k+1} \hat{\mathbf{e}}_m^{k+1} \otimes \hat{\mathbf{e}}_n^{k+1} \tag{Eq. 5.45}$$

Since the internal forces are calculated at current configuration, see (Eq. 4.83), one has to take another step and compute $\boldsymbol{\sigma}^{k+1}$. As is obvious from (Eq. 5.28), computation of $\boldsymbol{\sigma}^{k+1}$ from $\widehat{\boldsymbol{\sigma}}^{k+1}$ requires the computation of $\boldsymbol{\mathcal{R}}_0^{k+1}$. $\boldsymbol{\mathcal{R}}_0^{k+1}$ is computed from left polar decomposition of $\boldsymbol{\mathcal{F}}_0^{k+1} = \boldsymbol{\mathcal{F}}_k^{k+1} \boldsymbol{\mathcal{F}}_0^k$ as discussed in section 3.1.6.

5.5 Bulk Viscosity Pressure

Artificial viscosity is applied to the numerical solution for two reasons (L. M. Taylor et al. 1989); (i) to prevent elements from collapsing down due to high velocity gradients, (ii) to quiet truncation frequency "ringing". Ideally it is desirable to add viscosity to the highest mode of the element, but it is not practical. Instead viscosity is added to the volumetric (bulk) response. Then bulk viscosity pressure p is computed in terms of volumetric strain rate as

$$p = \rho l_c [b_1 c_d \dot{\epsilon}_{vol} - b_2 l_c (\dot{\epsilon}_{vol})^2] \quad \text{(Eq. 5.46)}$$

In (Eq. 5.46), b_1, b_2 are damping coefficients, ρ is material density, c_d is dilatational wave speed, l_c is an element characteristic length and $\dot{\epsilon}_{vol}$ is the volumetric strain rate. The term linear in $\dot{\epsilon}_{vol}$ is computed for both negative and positive volumetric strain rates. For positive and negative strain rates, tensile and compressive pressures are produced, respectively. On the other hand, the term quadratic in $\dot{\epsilon}_{vol}$ is computed only for negative volumetric strain rates and ignored otherwise. Note that bulk viscosity pressure is not a part of the material constitutive response, i.e. the expression given by (Eq. 5.46) can be used conveniently for all material models. Therefore it is a good practice to compute bulk viscosity pressure not in the material routine, where stress update is performed, but at some other place.

In the finite element code developed in this work, default values for b_1 and b_2 are set to be 0.06 and 1.5, respectively and l_c is taken as the smallest segment of the element. For microplane material model, dilatational wave velocity c_d is computed from

$$c_d = \sqrt{\frac{3\mathrm{K}}{\rho}\frac{(1-\nu)}{(1+\nu)}} \quad \text{(Eq. 5.47)}$$

In (Eq. 5.47), K, ν are, respectively, bulk modulus and Poisson's ratio. ν is assumed to be equal to its initial value, whereas K is reduced (damaged) bulk modulus and computed from

$$\mathrm{K} = (1 - \omega_V)\mathrm{K}_0 \quad \text{(Eq. 5.48)}$$

In (Eq. 5.48), ω_V is damage parameter controlling degradation of bulk modulus and K_0 is the initial (undamaged) bulk modulus. Note that response of concrete material for volumetric deformations is same for all microplanes in contrast to all other components. Therefore volumetric response is not computed at microplane level but at Gauss point level.

It will be shown in numerical simulations performed for concrete perforation experiments that the strengthening due to rate dependency of micro-crack growth (material rate sensitivity) itself is not

sufficient to produce necessary resistance for concrete. In addition bulk viscosity effects should also be present.

As an alternative to the approach proposed in this work, in (Bažant et al. 2014; Caner et al. 2014) authors have developed a theoretical foundation for a rate effect based on comminution of concrete at very high strain rates. Based on this theory they developed a rate sensitive microplane model by additionally incorporating rate effects due to comminution of concrete and obtained good correlation with experiments which otherwise was not possible. Note that in contrast to the strategy followed in this work, bulk viscosity pressure is not included in their computations.

6 Thermal Effects

During high-velocity contact-impact events substantial amount of heat might be generated due to frictional sliding along the contact interface and inelastic deformations in the bulk. Depending upon the level of heating the mechanical properties of concrete material might drastically change which in turn affects the overall mechanical response of the structure. In this chapter finite element formulation of the heat problem will be presented by taking into account only the heat generated due to frictional sliding.

6.1 Strong (Differential) Form of the Initial Boundary Value Problem (IBVP)

The differential equation which governs the evolution of temperature is energy equation. The strong (differential) form of the energy equation for body $\mathcal{B}$ at current configuration, together with boundary and initial conditions, reads as

$$\begin{array}{llll} \rho c_v \dot{\theta} = -\mathrm{div}(\boldsymbol{q}) + \rho r & \forall \boldsymbol{\mathcal{X}} \in \Omega_0 & \rightarrow & \text{energy equation} \\ \boldsymbol{q} \cdot \boldsymbol{n} = \hat{q} & \forall \boldsymbol{\mathcal{X}} \in \Gamma_q & \rightarrow & \text{boundary conditions} \\ \theta = \hat{\theta} & \forall \boldsymbol{\mathcal{X}} \in \Gamma_\theta & \nearrow & \\ \theta|_{t=0} = \theta_0 & \forall \boldsymbol{\mathcal{X}} \in \Omega_0 & \rightarrow & \text{initial conditions} \end{array} \qquad \text{(Eq. 6.1)}$$

In (Eq. 6.1), ρ is the spatial mass density, div is divergence operator in current configuration, $\boldsymbol{q}$ is internal heat flux vector, $\boldsymbol{r}$ is heat source supplied per unit time for per unit mass at current configuration, $\boldsymbol{n}$ is unit outward normal in current configuration, $\hat{q}$ and $\hat{\theta}$ are, respectively, prescribed heat fluxes and temperatures along the boundary, θ_0 is initial temperature distributions, Γ_q, Γ_θ are, respectively, portions of the boundary where heat fluxes and temperatures are prescribed.

For the set of equations given in (Eq. 6.1) to be complete, internal heat flux $\boldsymbol{q}$ must be expressed in terms of temperature θ. For the materials of interest we assume that Fourier's law of heat conduction holds, i.e. we have

$$\boldsymbol{q} = -k\boldsymbol{\nabla}\theta \qquad \text{(Eq. 6.2)}$$

where k is coefficient of thermal conductivity measured in watt per meter Kelvin.

6.2 Weak (Integral) Form of IBVP

The weak (integral) form of the energy equation provides us a framework for the development of a numerical solution procedure based on finite element method. It can be obtained as follows. First of all, local differential form is weighted with the variations of the primary variables, temperatures θ of the material particles, and then resulting expression is integrated over the domain. By enforcing the result obtained to vanish, we get

$$\int_{\Omega} \delta\theta\left[\rho c_v \dot{\theta} + \mathrm{div}(\boldsymbol{q}) - \rho r\right] dv = 0 \qquad \text{(Eq. 6.3)}$$

To make integral expression given by (Eq. 6.3) suitable for the imposition of essential and natural boundary conditions we take another step and perform integration by parts. We proceed as follows. First we rewrite the term involving divergence as

$$\delta\theta \ \mathrm{div}(\boldsymbol{q}) = \mathrm{div}(\delta\theta \boldsymbol{q}) - \boldsymbol{\nabla}\delta\theta \cdot \boldsymbol{q} \qquad \text{(Eq. 6.4)}$$

Putting above expression into (Eq. 6.3), and then applying divergence and Stoke's heat flux theorems, we obtain

$$\int_{\Omega} \delta\theta \ \rho c_v \dot{\theta} \ \ dv - \int_{\Omega} \boldsymbol{\nabla}\delta\theta \cdot \boldsymbol{q} \ \ dv \boxed{+ \int_{\Gamma_c^1} \delta\bar{\theta}^1 \ q^1 \ \ da + \int_{\Gamma_c^2} \delta\bar{\theta}^2 \ q^2 \ \ da} =$$
$$\int_{\Omega} \delta\theta \ \rho r \ \ dv - \int_{\Gamma_q} \delta\theta \, \widehat{q} \ \ da - \int_{\Gamma_\theta} \delta\theta \ q_{rea} \ \ da \qquad \text{(Eq. 6.5)}$$

In (Eq. 6.5) q^1 and q^2 are surface heat fluxes generated due to frictional sliding of the form

$$q^1 = \alpha^1 q_c$$
$$q^2 = \alpha^2 q_c \qquad \text{(Eq. 6.6)}$$

with

$$q_c = \boldsymbol{\tau} \cdot {}^{slip}\boldsymbol{g}_s \qquad \text{(Eq. 6.7)}$$

Heat distribution coefficients, $\alpha^1$and α^2, appearing in (Eq. 6.6) are taken to be equal as 0.5. In (Marusich et al. 1995) an expression for the computation of these distribution factors from thermal and physical properties of contacting bodies is given.

Note that in (Eq. 6.6), possible exchange of heat due to conduction through spots and convection through air particles trapped in micro-cavities along the contact interface has been neglected. With (Eq. 6.6) and recognizing the fact that

$$\Gamma_c^1 = \Gamma_c^2 = \Gamma_c \qquad \text{(Eq. 6.8)}$$

during contact, (Eq. 6.5) can be rewritten as

$$\int_\Omega \delta\theta\ \rho c_v \dot{\theta}\ \ dv - \int_\Omega \boldsymbol{\nabla}\delta\theta \cdot \boldsymbol{q}\ \ dv + \int_{\Gamma_c} \delta\theta_c\ q_c\ \ da =$$

$$\int_\Omega \delta\theta\ \rho r\ \ dv - \int_{\Gamma_q} \delta\theta\ \hat{q}\ \ da - \boxed{\int_{\Gamma_\theta} \delta\theta\ q_{rea}\ \ da} \qquad \text{(Eq. 6.9)}$$

In (Eq. 6.9), $\delta\theta_c$ is the temperature variation given by

$$\delta\theta_c = \alpha^1 \delta\bar{\theta}^1 + \alpha^2 \delta\bar{\theta}^2 \qquad \text{(Eq. 6.10)}$$

and $\boldsymbol{\nabla}\delta\theta$ is spatial gradient of temperature variations. As can be seen from (Eq. 6.9), now, prescribed boundary heat fluxes $\hat{q}$ appear in the expression, and, hence, can easily be enforced. However it seems it is still not possible to enforce prescribed temperatures. In addition there exists a term representing reactions, secondary variables, due to prescribed temperatures. We resolve these issues by imposing conditions on the form of $\delta\theta$ and θ. We simply make $\delta\theta$ belong to function space defined as

$$\mathcal{V} = \{w \mid w \in H^1,\ w = 0\ \ \forall \boldsymbol{X} \in \Gamma_\theta\} \qquad \text{(Eq. 6.11)}$$

With this definition the term corresponding to reactions automatically drops down from (Eq. 6.9). Next we define the function space for θ as

$$\mathcal{S} = \{u \mid u \in H^1,\ u = \hat{\theta}\ \ \forall \boldsymbol{X} \in \Gamma_\theta\} \qquad \text{(Eq. 6.12)}$$

The form given by (Eq. 6.12) ensures that the solution to the weak form will respect prescribed temperatures too. With the function spaces defined for $\delta\theta$ and θ at hand, we obtain the final version of the weak form as

$$\boxed{\begin{aligned} &\int_\Omega \delta\theta\ \rho c_v \dot{\theta}\ \ dv - \int_\Omega \boldsymbol{\nabla}\delta\theta \cdot \boldsymbol{q}\ \ dv + \int_{\Gamma_c} \delta\theta_c\ q_c\ \ da = \\ &\int_\Omega \delta\theta\ \rho r\ \ dv - \int_{\Gamma_q} \delta\theta\ \hat{q}\ \ da \end{aligned}} \qquad \text{(Eq. 6.13)}$$

Next we define

$$\delta H^{capacity} := \int_{\Omega} \delta\theta\ \rho c_v \dot{\theta}\ \ dv$$

$$\delta H^{conduction} := \int_{\Omega} -\boldsymbol{\nabla}\delta\theta \cdot \boldsymbol{q}\ \ dv$$

$$\delta H^{contact} := \int_{\Gamma_c} \delta\theta_c\ q_c\ \ da \qquad \text{(Eq. 6.14)}$$

$$\delta H^{external} := \int_{\Omega} \delta\theta\ \rho r\ \ dv - \int_{\Gamma_q} \delta\theta\ \hat{q}\ \ da$$

With the definition

$$\delta H^{internal} := \delta H^{conduction} + \delta H^{contact} \qquad \text{(Eq. 6.15)}$$

and plugging it, together with definitions in (Eq. 6.14), into (Eq. 6.13), we finally obtain

$$\delta H^{capacity} + \delta H^{internal} = \delta H^{external} \qquad \text{(Eq. 6.16)}$$

6.3 Discretization of the Weak Form

To obtain the so called semi-discrete version of the weak form, we, first, construct global continuous piecewise linear interpolation functions in space based on finite element discretization of the bodies with linear tetrahedral elements. With the help of these interpolation functions, the temperature θ and its variation $\delta\theta$ can be approximated within an element from nodal values as

$$\theta \cong {}^{h}_{e}\theta = \sum_{i=1}^{4} N_i \theta_I$$

$$\delta\theta \cong {}^{h}_{e}\delta\theta = \sum_{i=1}^{4} N_i \delta\theta_I \qquad \text{(Eq. 6.17)}$$

In (Eq. 6.17), in local numbering, N_i , θ_I and $\delta\theta_I$ are, respectively, isoparametric finite element shape function, temperature and its variation associated with i th node of element. Note that resulting global approximation functions ${}^{h}\theta$ and ${}^{h}\delta\theta$ belong to the function spaces ${}^{h}\mathcal{S} \in \mathcal{S}$ and ${}^{h}\mathcal{V} \in \mathcal{V}$, respectively, defined by

$${}^{h}\mathcal{S} = \left\{ {}^{h}u \mid\ {}^{h}u \in H^1,\ {}^{h}u = \hat{\theta}\ \forall \boldsymbol{x} \in\ {}^{h}\Gamma_\theta \right\}$$

$${}^{h}\mathcal{V} = \left\{ {}^{h}w \mid\ {}^{h}w \in H^1,\ {}^{h}w = 0\ \forall \boldsymbol{x} \in\ {}^{h}\Gamma_\theta \right\} \qquad \text{(Eq. 6.18)}$$

Next based on approximations given by (Eq. 6.17), we will investigate weak form expressions introduced by (Eq. 6.14) one by one.

6.3.1 Weak Form Expressions

6.3.1.1 Heat Capacity

Within the context of (Eq. 6.17), the element-wise approximation to temperature rate $\dot{\theta}$ takes the form

$$\dot{\theta} \cong {}^{h}_{e}\dot{\theta} = \sum_{i=1}^{4} N_i \dot{\theta}_I \qquad \text{(Eq. 6.19)}$$

In (Eq. 6.19), $\dot{\theta}_I$ is temperature rate associated with i th node of element. With the insertion of (Eq. 6.17) and (Eq. 6.19), weak form expression due to heat capacity is then approximated as

$$\delta H^{capacity} \cong {}^{h}\delta H^{capacity} = \sum_{e=1}^{nel} {}^{h}_{e}\delta H^{capacity} \qquad \text{(Eq. 6.20)}$$

where

$${}^{h}_{e}\delta H^{capacity} := \int_{{}^{h}_{e}\Omega} {}^{h}_{e}\delta\theta \; \rho_e c_{v_e} {}^{h}_{e}\dot{\theta} \; dv = \sum_{i=1}^{4} \left[\delta\theta_I \sum_{j=1}^{4} \left[\int_{{}^{h}_{e}\Omega} \rho_e c_{v_e} N_i N_j \dot{\theta}_J \; dv \right] \right] \qquad \text{(Eq. 6.21)}$$

and nel is total number of finite elements.

Then we apply capacity lumping based on row-sum technique (Hughes 2012) and obtain

$${}^{h}_{e}\delta H^{capacity} = \sum_{i=1}^{4} \left[\delta\theta_I \left[\int_{{}^{h}_{e}\Omega} \rho_e c_{v_e} N_i \sum_{j=1}^{4} N_j \; dv \right] \dot{\theta}_I \right] = \sum_{i=1}^{4} \delta\theta_I \; h_I^{capacity} \qquad \text{(Eq. 6.22)}$$

where

$$h_I^{capacity} := m_I c_{v_e} \dot{\theta}_I \qquad \text{(Eq. 6.23)}$$

In (Eq. 6.23), $h_I^{capacity}$ is capacity heat flux associated with i th node of element.

6.3.1.2 Heat Conduction

In view of (Eq. 4.68) and (Eq. 6.17), the element-wise approximation to temperature gradient $\boldsymbol{\nabla}\delta\theta$ can be expressed as

$$\boldsymbol{\nabla}\delta\theta \cong \boldsymbol{\nabla}^{h}_{e}\delta\theta = \sum_{i=1}^{4} \delta\theta_I \; \boldsymbol{\nabla}^{\boldsymbol{x}} N_i = -\frac{1}{6V_e} \sum_{i=1}^{4} \delta\theta_I \; \boldsymbol{A}_i \qquad \text{(Eq. 6.24)}$$

With the insertion of (Eq. 6.17) and (Eq. 6.24), weak form expression due to heat conduction is then approximated as

$$\delta H^{conduction} \cong {}^{h}\delta H^{conduction} = \sum_{e=1}^{nel} {}^{h}_{e}\delta H^{conduction} \tag{Eq. 6.25}$$

where

$${}^{h}_{e}\delta H^{conduction} := -\int_{{}^{h}_{e}\Omega} \boldsymbol{\nabla}^{h}_{e}\delta\theta \cdot \boldsymbol{q}_e \; dv = \sum_{i=1}^{4} \delta\theta_I \; h_I^{conduction} \tag{Eq. 6.26}$$

Assuming that $\boldsymbol{q}_e$ is constant inside element domain, we obtain

$$h_I^{conduction} := \frac{1}{6V_e}\int_{{}^{h}_{e}\Omega} \boldsymbol{q}_e \cdot \boldsymbol{A}_i \; dv = \boldsymbol{q}_e \cdot \boldsymbol{A}_i \tag{Eq. 6.27}$$

In (Eq. 6.27), $h_I^{conduction}$ is the conduction heat flux associated with i th node of element. Note that (Eq. 6.27) implies equilibrium of nodal heat fluxes at element level due to conduction, i.e.

$$\sum_{i=1}^{4} h_I^{conduction} = \sum_{i=1}^{4} \boldsymbol{q}_e \cdot \boldsymbol{A}_i = \boldsymbol{q}_e \cdot \sum_{i=1}^{4} \boldsymbol{A}_i = \boldsymbol{q}_e \cdot \boldsymbol{0} = 0 \tag{Eq. 6.28}$$

6.3.1.3 Contact

First we define coefficients

$$\begin{aligned}
\bar{\beta}_1(\bar{\boldsymbol{\zeta}}) &= \alpha^1 \bar{N}_1 = \alpha^1 \bar{\zeta}_1 \\
\bar{\beta}_2(\bar{\boldsymbol{\zeta}}) &= \alpha^1 \bar{N}_2 = \alpha^1 \bar{\zeta}_2 \\
\bar{\beta}_3(\bar{\boldsymbol{\zeta}}) &= \alpha^1 \bar{N}_3 = \alpha^1 [1 - (\bar{\zeta}_1 + \bar{\zeta}_2)] \\
\bar{\beta}_4(\bar{\boldsymbol{\zeta}}) &= \alpha^2
\end{aligned} \tag{Eq. 6.29}$$

With the notation provided by (Eq. 6.29) at hand, one can write down the following approximation for $\delta\theta_c$, namely

$$\delta\theta_c \cong {}^{h}\delta\theta_c = \sum_{i=1}^{4} \bar{\beta}_i \delta\theta_I \tag{Eq. 6.30}$$

With the insertion of (Eq. 6.17) and (Eq. 6.30), weak form expression due to contact is then approximated as

$$\delta H^{contact} \cong {}^{h}\delta H^{contact} = \sum_{e=1}^{nelc} {}^{h}_{e}\delta H^{contact} \quad \text{(Eq. 6.31)}$$

where

$$ {}^{h}_{e}\delta H \;:= \int_{{}^{h}_{e}\Gamma_c} {}^{h}_{e}\delta\theta_c \, q_{c_e} \; da = \sum_{i=1}^{4} \delta\theta_I \; h_I^{contact} \quad \text{(Eq. 6.32)}$$

Assuming that contact heat fluxes are piecewise linear, one can write

$$h_{c_e} = \int_{{}^{h}_{e}\Gamma_c} q_{c_e} \; da \quad \text{(Eq. 6.33)}$$

where h_{c_e} is contact heat flux entering into triangular surface. In (Eq. 6.32), $h_I^{contact}$ is the heat flux due to contact associated with i th node of contact finite element and has the form

$$h_I^{contact} = \bar{\beta}_i h_{c_e} \quad \text{(Eq. 6.34)}$$

6.3.1.4 External Heating

With the insertion of (Eq. 6.17), weak form expression for external heat fluxes is approximated as

$$\delta H^{external} \cong {}^{h}\delta H^{external} = \sum_{e=1}^{nel} {}^{h}_{e}\delta H^{external} \quad \text{(Eq. 6.35)}$$

where

$$ {}^{h}_{e}\delta H^{external} := \int_{{}^{h}_{e}\Omega} {}^{h}_{e}\delta\theta \; \rho_e r_e \; dv - \int_{{}^{h}_{e}\Gamma} {}^{h}_{e}\delta\theta \; \hat{q}_e \; da = \sum_{i=1}^{4} \delta\theta_I \; h_I^{external} \quad \text{(Eq. 6.36)}$$

If one assumes that r_e is constant inside element domain and $\hat{q}_e$ is so on element face located at boundary, if there exists any connected to node i, we obtain

$$\begin{aligned} h_I^{external} &:= \left[\int_{{}^{h}_{e}\Omega} \rho_e N_i \; dv\right] r_e - \left[\int_{{}^{h}_{e}\Gamma} N_i \; da\right] \hat{q}_e \\ &:= \frac{m_e}{4} r_e - \frac{1}{3} A \hat{q}_e \end{aligned} \quad \text{(Eq. 6.37)}$$

In (Eq. 6.36), $h_I^{external}$ is the heat flux due to external loading associated with i th node of element.

6.3.2 Nodal Thermal Equilibrium Equations

Weak form expressions exploited above can be rewritten equivalently as

$$
\begin{aligned}
{}^{h}\delta H^{capacity} &= \sum_{e=1}^{nel}\sum_{i=1}^{4} \delta\theta_{con(e,i)}\, h_{con(e,i)}^{capacity} &&= \sum_{I=1}^{nnd}\left[\delta\theta_I \sum_{e=1}^{nel(I)} h_{con(E(e),i(I))}^{capacity}\right] \\
{}^{h}\delta H^{conduction} &= \sum_{e=1}^{nel}\sum_{i=1}^{4} \delta\theta_{con(e,i)}\, h_{con(e,i)}^{conduction} &&= \sum_{I=1}^{nnd}\left[\delta\theta_I \sum_{e=1}^{nel(I)} h_{con(E(e),i(I))}^{conduction}\right] \\
{}^{h}\delta H^{contact} &= \sum_{e=1}^{nelc}\sum_{i=1}^{4} \delta\theta_{con(e,i)}\; h_{con(e,i)}^{contact} &&= \sum_{I=1}^{nndc}\left[\delta\theta_I \sum_{e=1}^{nel(I)} h_{con(E(e),i(I))}^{contact}\right] \\
{}^{h}\delta H^{external} &= \sum_{e=1}^{nel}\sum_{i=1}^{4} \delta\theta_{con(e,i)}\, h_{con(e,i)}^{external} &&= \sum_{I=1}^{nnd}\left[\delta\theta_I \sum_{e=1}^{nel(I)} h_{con(E(e),i(I))}^{external}\right]
\end{aligned}
\qquad \text{(Eq. 6.38)}
$$

Plugging (Eq. 6.38) into (Eq. 6.16) then, we obtain

$$
\sum_{I=1}^{nnd} \delta\theta_I \cdot \left[{}^{capacity}h_I + {}^{cond}h_I + {}^{con}h_I - {}^{ext}h_I\right] = 0 \qquad \text{(Eq. 6.39)}
$$

where

$$
\begin{aligned}
{}^{capacity}h_I &= \sum_{e=1}^{nel(I)} h_{con(E(e),i(I))}^{capacity} = c_I\dot{\theta}_I \\
{}^{cond}h_I &= \sum_{e=1}^{nel(I)} h_{con(E(e),i(I))}^{conduction} \\
{}^{con}h_I &= \sum_{e=1}^{nel(I)} h_{con(E(e),i(I))}^{contact} \\
{}^{ext}h_I &= \sum_{e=1}^{nel(I)} h_{con(E(e),i(I))}^{external}
\end{aligned}
\qquad \text{(Eq. 6.40)}
$$

In (Eq. 6.40), nodal heat capacity c_I is computed from the expression

$$
c_I = \sum_{e=1}^{nel(I)} m_I c_{v_e} = \sum_{e=1}^{nel(I)} \frac{m_e c_{v_e}}{4} \qquad \text{(Eq. 6.41)}
$$

Finally, considering independent variations of nodal temperatures, (Eq. 6.39) results in nodal thermal equilibrium equations of the form

$$c_I \dot{\theta}_I = {}^{ext}h_I - \left[{}^{cond}h_I + {}^{con}h_I\right] \quad (I = 1 \dots nnd) \tag{Eq. 6.42}$$

6.3.3 Explicit Time Integration

6.3.3.1 Forward Difference Approximation

(Eq. 6.42) is a first order possibly nonlinear ordinary differential equation (ODE) of independent time variable and can be solved numerically using finite difference method. Explicit update formula can be obtained by referring to the differential equation corresponding to a known state, i.e. written for a typical time step t^k we have

$$c_I \dot{\theta}_I^k = {}^{tot}h_I^k \tag{Eq. 6.43}$$

where

$${}^{tot}h_I^k := {}^{ext}h_I^k - \left[{}^{cond}h_I^k + {}^{con}h_I^k\right] \tag{Eq. 6.44}$$

Forward difference approximation for nodal temperature rate reads as

$$\dot{\theta}_I^k \cong \frac{\theta_I^{k+1} - \theta_I^k}{\Delta t} \tag{Eq. 6.45}$$

With the insertion of (Eq. 6.45) into (Eq. 6.43) explicit update formula for θ_I^{k+1} is obtained as

$$\theta_I^{k+1} = \frac{\Delta t}{c_I} {}^{tot}h_I^k + \theta_I^k \tag{Eq. 6.46}$$

6.3.3.2 Numerical Stability

Forward difference approximation employed for time discretization of thermal equilibrium equations results in a conditionally stable stepping algorithm. As the numerical solution of volume-coupled thermo-mechanical problem at hand is considered stability limit posed by mechanical problem is much stricter than that posed by thermal counterpart and therefore stability issue is taken care of by mechanical problem only.

6.3.4 Thermo-Mechanical Coupling

Within the context of high-velocity contact-impact events thermo-mechanical coupling takes place due to two main reasons, namely:

- Heating due to frictional sliding during mechanical interactions (contact).
- Degradation of mechanical material properties during heating.

In reality thermal and mechanical events happen simultaneously. However from numerical standpoint it is very common to employ staggered schemes where mechanical and thermal problems are solved consecutively one after another. Note that staggered scheme here proposed utilizes same finite element discretizations for the solution of both physical disciplines.

7 Computational Tools and Procedures

7.1 Topological Data Structures (TDS)

Topological data structure is constructed to associate entities building up the geometry of a finite element discretization (FED). It is very useful in writing efficient geometry-based numerical algorithms like those used in adaptive element deletion and contact. Starting from the lowest dimension, points, segments, surfaces and volumes construct the building blocks of TDS of a given 3D FED (Pandolfi et al. 1998).

7.1.1 Data Structure for Linear Tetrahedra (DSLT)

Geometrically, a linear tetrahedral (LT) element is composed of 4 nodes, 6 edges and 4 facets. The data structure illustrated in Fig. 7.1 is defined for LT. Its use is made of extensively in constructing a TDS.

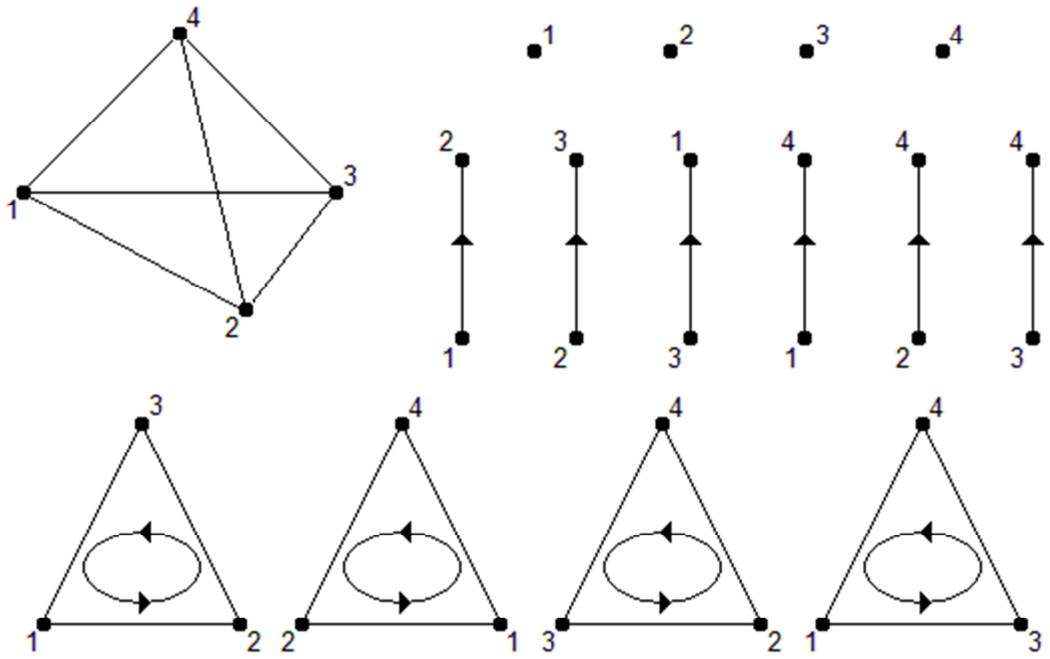

Fig. 7.1 Data structures for linear tetrahedra

7.1.1.1 Point type

Each node in a FED is associated with a unique point which has a structure as given in Fig. 7.2.

```
type type_topo_point
integer(4), pointer :: segs(:)
integer(4), pointer :: srfs(:)
integer(4), pointer :: vols(:)
end type type_topo_point
```

Fig. 7.2 Point type

Note that for type descriptions Fortran 90 programming syntax is employed. In this type following information is stored:

- segs: list of segments connected
- srfs: list of facets connected
- vols: list of volumes connected

7.1.1.2 Segment type

Segments are constructed by using edges of finite elements. Classical finite element connectivity (CON) and DSLT are required to identify edges of a given finite element. Each edge of a finite element is to be associated with a unique segment. Some attention needs to be paid in the construction of segment topology due to this uniqueness constraint. Segment type has a structure as given in Fig. 7.3.

```
type type_topo_segment
integer(4), pointer :: pts(:)
integer(4), pointer :: srfs(:)
integer(4), pointer :: els(:)
end type type_topo_segment
```

Fig. 7.3 Segment type

In segment type following information is stored:

- pts: list of points connected
- srfs: list of facets connected
- vols: list of volumes connected

7.1.1.3 Surface type

Surfaces are constructed using facets of finite elements. CON and DSLT are required to identify surfaces of a given finite element. Each facet of a finite element is to be associated with a unique surface. Surface type has a structure as given in Fig. 7.4.

```
type type_topo_surface
integer(4), pointer :: pts(:)
integer(4), pointer :: segs(:)
integer(4), pointer :: vols(:)
end type type_topo_surface
```

Fig. 7.4 Surface type

In surface type following information is stored:

- pts: list of points connected
- segs: list of segments connected
- vols: list of volumes connected

For surfaces located at the outer boundary size of vols array is one, whereas for others located inside it is two.

7.1.1.4 Volume type

Each element in a FED is associated with a unique volume which has a structure as given in Fig. 7.5.

```
type type_topo_volume
integer(4), pointer :: segs(:)
integer(4), pointer :: srfs(:)
integer(4), pointer :: nbors(:)
end type type_topo_volume
```

Fig. 7.5 Volume type

In this type following information is stored:

- segs: list of segments connected
- srfs: list of facets connected
- nbors: list volumes connected to the surfaces of current volume

7.1.1.5 Topology type

TDS for a given FED has a structure as given in Fig. 7.6.

```
type type_topology
type(type_topo_point), dimension(:), pointer :: points
type(type_topo_segment), dimension(:), pointer :: segments
type(type_topo_surface), dimension(:), pointer :: surfaces
type(type_topo_volume), dimension(:), pointer :: volumes
integer(4), dimension(:), pointer :: bnd_points
integer(4), dimension(:), pointer :: bnd_surfaces
integer(4), dimension(:), pointer :: bnd_layer
end type type_topology
```

Fig. 7.6 Topology type

In this type following information is stored:

- points: all unique points in TDS
- segments: all unique segments in TDS
- surfaces: all unique surfaces in TDS
- volumes: all unique volumes in TDS
- bnd_points: list of points located on the outer boundary
- bnd_surfaces: list of surfaces located on the outer boundary
- bnd_layer: list of volumes which have at least one node located on outer boundary.

Construction of a TDS takes place in the following order:

- Segments
- Surfaces
- Neighbors
- Volumes connected to points
- Boundary Surfaces
- Boundary Points
- Boundary Layer

7.2 Adaptive Element Deletion

In high velocity contact-impact simulations elements around the contact region experience very large deformations and therefore get severely distorted immediately. If not handled properly this results in elements with negative Jacobian and renders it impossible to continue the simulation. There are basically two different approaches that can be followed to address this problem:

- Mesh adaptivity
- Fixed mesh with element deletion

Adaptive methods utilize, most of the time, residual based error estimators for automatization. Adaptive techniques can be divided into two groups, namely Mesh Refinement and Remeshing.

Mesh refinement is based on subdivision of existing elements. Projection of nodal and history variables from old mesh onto new mesh (projection phase) can be performed very efficiently and accurately. However there is no improvement in element quality after subdivision therefore it is not possible to use this technique at rapidly deforming regions. It is best suited to increase solution accuracy and performance of the numerical algorithms around some critical regions like those evolving during low velocity contact events.

In remeshing, however, a completely new finite element discretization is generated. Therefore projection phase costs a lot of time which is prohibitive in solution algorithms based on explicit time integration. Elements with high quality can be generated during remeshing. Due to explosive character of concrete shape of the boundary at the contact region might become highly irregular and mesh generator might suffer to produce a new mesh from such a complicated boundary representation automatically. Moreover obvious need for frequent remeshing in explicit simulations is another negative prohibitive aspect of the approach.

In contrast to mesh adaptivity, technique based on element deletion can very time efficiently handle highly distorted elements. Method requires no projection phase because finite element discretization remains essentially the same during element deletion. Employment of a relevant criterion for element deletion is the most essential part of the method. Basically an element candidate for deletion should be stress free, i.e. fully unloaded, and highly deformed. These are the common characteristics of inelastic materials with localization properties, like concrete. There are several possible physically or geometrically motivated criteria that can be used for element deletion (Johnson 1977; Birnbaum et al. 1987; L. M. Taylor et al. 1989; Whirley et al. 1993; Hibbitt et al. 2001). In our simulations maximum principal strain has been used as primary criteria for element deletion.

Deleted elements do not contribute to the internal force calculation. However their contribution to the nodal masses is retained. A node is called as “free” if all the elements connected to it have been deleted. A free node continues its motion under the effect of body and external forces acting on it.

Deleted elements must be accounted for carefully in contact algorithm because some interior elements might come onto the outer boundary due to previously deleted elements. Finally note also that free nodes are skipped in contact algorithm.

```
type type_pair_data_contact
integer(4) :: DscMas = 0
integer(4) :: DscSlv = 0
real(8) :: Friction = 0.5D0
real(8) :: Tol = 1.0D-07
integer(4) :: MaxItn = 50
integer(4) :: Algo = 1          !0->1-Pass; 1->2-Pass
integer(4) :: ObjectType = 0    !0->Sphere; 1->Cone
integer(4) :: Ctype = 0         !0->Deformable-Deformable; 1->Deformable-Rigid
end type type_pair_data_contact
```

Fig. 7.7 Contact pair type

7.3 Contact Algorithm

7.3.1 Contact Pair Type

We base our contact algorithm on the assumption that contact takes place between two different FEDs. In other words, self-contact of an individual FED is not treated in formal sense. We keep all the data necessary to define a contact interaction between different discretizations in the type presented in Fig. 7.7.

7.3.2 Contact Search

Contact search is performed after computing predicted positions of the nodes in order to be able to construct list of node-to-surface contact finite elements. In the algorithm we follow a two-step procedure, namely contact detection followed by contact resolution.

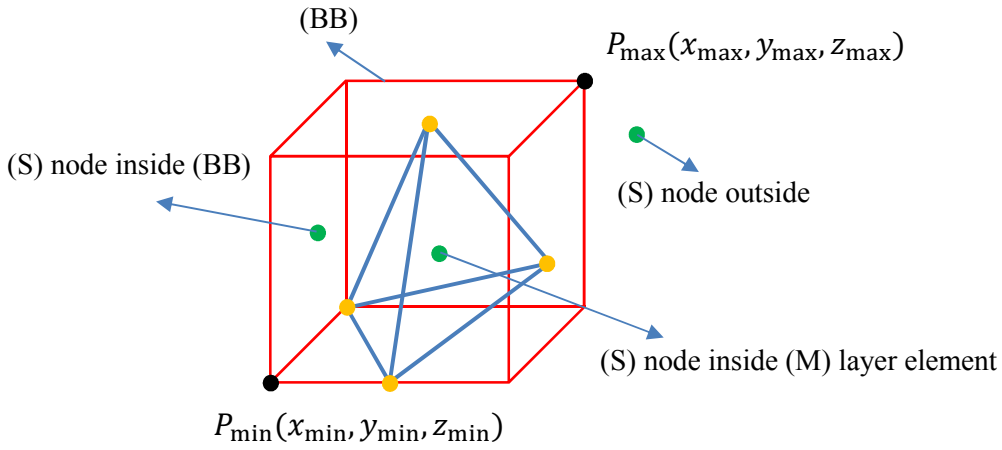

Fig. 7.8 Inside-outside checks

7.3.2.1 Contact Detection

7.3.2.1.1 Inside-Outside Checks

For algorithmic considerations we denote discretizations which build up the contact pair as “master” (M) and “slave” (S). During contact detection phase, in principle, we need to test precisely each node of (S) discretization located on the outer boundary for the violation of impenetrability constraint and construct list of (S) nodes penetrated into (M) boundary.

We perform two inside-outside checks to determine if a (S) node has penetrated into (M) layer element.

7.3.2.1.1.1 In-Out Bounding Box (BB) Check

First check is called bounding box (BB) check. A (BB) is first constructed for the candidate (M) layer element by computing the points $P_{\min}$ and $P_{\max}$ with respect to global Cartesian coordinate system (see Fig. 7.8). One can check easily if (S) node is inside the (BB) by performing range checks for each coordinate as given in (Eq. 7.1).

$$\begin{aligned} x_{\min} \leq x_S \leq x_{\max} \\ y_{\min} \leq y_S \leq y_{\max} \\ z_{\min} \leq z_S \leq z_{\max} \end{aligned} \qquad \text{(Eq. 7.1)}$$

(S) node is inside (BB) if all three checks in (Eq. 7.1) are passed successfully.

7.3.2.1.1.2 In-Out Element Check

If (S) node turns out to be inside the (BB) defined by candidate (M) layer element, we take another step and check if (S) node is also inside the (M) layer element itself. From (Eq. 4.53) and (Eq. 4.66) volume coordinates of (S) node with respect to (M) layer element can be written as

$$\xi_i = -\frac{1}{6V}\boldsymbol{A}_i \cdot \boldsymbol{x}_{S3} \quad (i = 1 \dots 4) \qquad \text{(Eq. 7.2)}$$

In (Eq. 7.2), $\boldsymbol{x}_{S3} := \boldsymbol{x}_S - \boldsymbol{x}_3$. (S) node is inside (M) layer element if all four conditions given in (Eq. 7.3) hold.

$$0 \leq \xi_i \leq 1 \quad (i = 1 \dots 4) \qquad \text{(Eq. 7.3)}$$

Candidate (S) node is marked as penetrated if two inside-outside checks given by (Eq. 7.1) and (Eq. 7.3) are all satisfied.

7.3.2.1.2 Moving Contact Sphere

As mentioned earlier contact interactions are defined by contact pairs. Then it is very natural to employ “bnd_layer” list of TDS corresponding to (M) discretization and “bnd_points” list of TDS corresponding to (S) discretization in contact detection phase. This straightforward approach brings a considerable loss in efficiency because many of the (S) nodes and (M) layer elements located outside the contact region are unnecessarily accounted for. To confine the relevant lists just around the contact region one can propose a simple solution. The solution requires the definition of a sphere for a given contact pair in the pre-processing stage. This sphere should be big enough to cover the contact region and capable of following it as it may possibly move and change position in time (see Fig. 7.16). For this purpose following type is defined for sphere:

```
type type_sphere_data_contact
integer(4) :: Active = 0       !0->inactive; 1->active
integer(4) :: Hook_Nd = -1     !hook node
integer(4) :: Hook_Dsc = -1
integer(4) :: RefCriteria = 0 !refresh criteria
                               !0 -> do NOT refresh
                               !1 -> at every time step
                               !2 -> by displacement amount
real(8) :: RefDisp = 1.0D0     !refresh displacement
real(8) :: Rad = 10.0D0        !radius
end type type_sphere_data_contact
```

Fig. 7.9 Contact sphere data type

Sphere is hooked to a node. In other words, sphere center is located at the current position of the hook node. Therefore it is essential that hook node always keeps closer in distance to the contact region throughout the whole simulation. In high velocity impact simulations, for the cases of our interest, the object called penetrator is much more rigid than the target object. Based on this assumption one can choose hook node from the FED belonging to projectile to ensure that the closeness requirement is always satisfied during the lifetime of simulation (see Fig. 7.10).

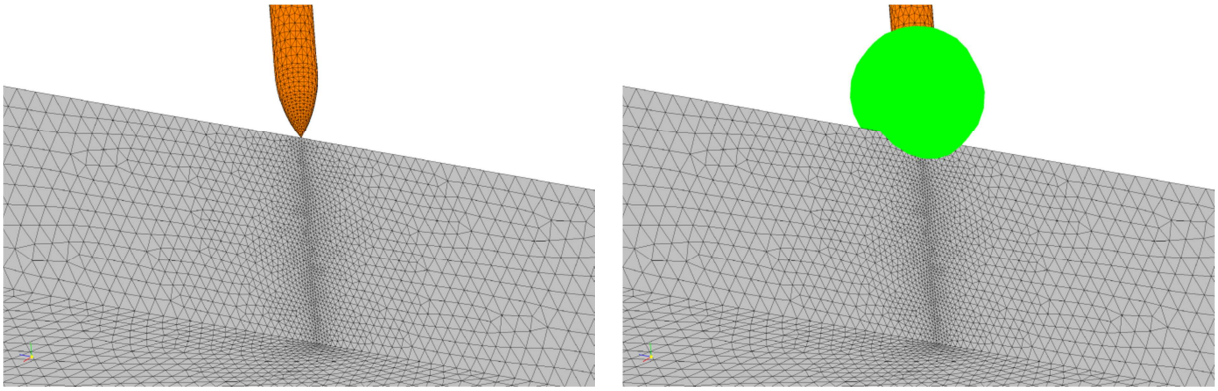

Fig. 7.10 Moving contact sphere

There are some lists constructed during the formation of contact sphere to be used in contact algorithm. Sphere data itself and all those lists are stored in another type presented in Fig. 7.11. Then one can resort to reduced “bnd_points_slave” and “bnd_layer_master” lists from contact sphere during contact detection phase. As one can note from Fig. 7.11 we have full lists for (M) and (S) discretizations separately. Full lists are constructed to be used in 2-pass contact algorithm.

7.3.2.2 Contact Resolution

Contact detection is followed by the construction of the contact discretization. The contact discretization proposed here is constructed based on 4-node node-to-surface (NTS) contact finite elements. For each (S) node penetrated, one needs to find a partner (M) facet located on the outer boundary of (M) discretization. Then penetrated (S) node together with its partner (M) facet constitutes one contact finite element. Among several possible alternatives we follow the strategy

emerged based on experience. Forthcoming subsections are devoted for the algorithmic steps followed.

```
type type_sphere_contact
type(type_sphere_data_contact) :: sphere_data
real(8), dimension(n_dim) :: c !center
integer(4), dimension(:), pointer :: bnd_points_master => null()
integer(4), dimension(:), pointer :: bnd_layer_master => null()
integer(4), dimension(:), pointer :: bnd_facets_master => null()
integer(4), dimension(:), pointer :: bnd_points_slave => null()
integer(4), dimension(:), pointer :: bnd_layer_slave => null()
integer(4), dimension(:), pointer :: bnd_facets_slave => null()
end type type_sphere_contact
```

Fig. 7.11 Contact sphere type

7.3.2.2.1 Locating partner (M) facet

The most essential part of the algorithm is the correct identification of partner (M) facet, for each penetrated (S) node. Due to discrete nature of time the solution to this problem is not unique. As discussed in section 4.5.1.3.2 one can locate partner (M) facet in two different ways.

7.3.2.2.1.1 Trajectory based location algorithm

According to this algorithm a candidate (M) facet is set to be partner if the trajectory of penetrated (S) node for the current time step intersects the plane defined by it from a point located inside its perimeter (see Fig. 7.12). To simplify computations it is assumed that trajectory of (S) node is a straight line.

First of all, for penetrated (S) node, list of candidate (M) facets located on the boundary are constructed. Dictated by experience, we do not follow a direct approach and use the boundary (M) facets connected to corresponding closest (M) node. Instead, we construct the list by populating the boundary (M) facets connected to the boundary nodes of owner (M) layer element which has already been located during contact detection phase.

7.3.2.2.1.2 Projection based location algorithm

According to this algorithm a candidate (M) facet is set to be partner if the projection of penetrated (S) node for the current time step intersects the plane defined by it from a point located inside its perimeter (see Fig. 7.12).

First of all, for penetrated (S) node, list of candidate (M) facets located on the boundary are constructed. For this purpose closest surface on the owner (M) layer element is found first. Then closest segment on closest surface is located. List of candidate (M) facets is finally constructed by

populating the boundary (M) facets connected to the closest segment. Some precautions need to be taken in the presence of local concave regions.

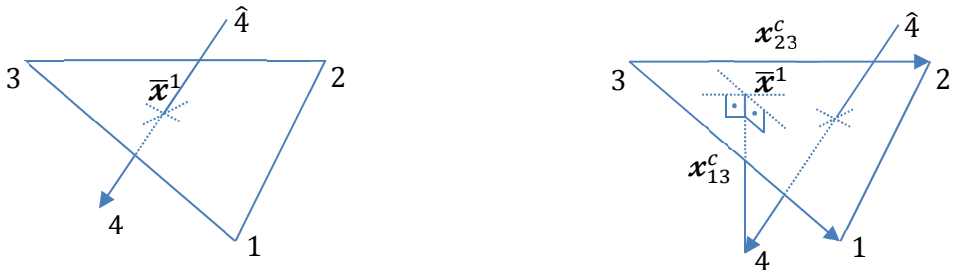

Trajectory based Projection based

Fig. 7.12 Location algorithms for partner (M) facet

7.3.2.2.1.3 2-Pass Algorithm

To better enforce contact constraints one can additionally solve the contact problem resulting as the roles of (M) and (S) discretizations are interchanged. In case of high-velocity contact-impact simulations in the first pass contact discretization is constructed primarily based on trajectory based location algorithm discussed above. For the second pass, however, always method based on closest-point projection is employed.

7.3.2.2.2 Contact Discretization

After all penetrated (S) nodes have been paired with one (M) facet, we take the final step and construct auxiliary contact discretization. For this purpose the types given in Fig. 7.13 and Fig. 7.14 are defined for contact node and contact finite element.

```
type type_contact_nd
character(1) :: dscr
integer(4) :: id
real(8), dimension(n_dim) :: uC
real(8), dimension(n_dim) :: LMincr
real(8), dimension(n_dim) :: LMiter
end type type_contact_nd
```

Fig. 7.13 Contact node

As soon as contact discretization has been generated one can employ the solution procedure based on Gauss-Seidel iteration (see section 4.7.5) to enforce contact constraints and to compute corrector position increments. Note that before passing data from the underlying 3D body discretizations to the contact discretization consecutive renumbering of the contact nodes is performed.

```
type type_contact_el
integer(4), dimension(ndpcel) :: con
integer(4) :: fct
character(1) :: ts
real(8) :: ksi1, ksi2
real(8), dimension(n_dim) :: g_iter
real(8), dimension(n_dim) :: L_iter
real(8), dimension(n_dim) :: Normal
real(8), dimension(n_dim) :: uSlip
real(8), dimension(ndpcel) :: alpha
real(8), dimension(ndpcel) :: gamma
real(8) :: theta
end type type_contact_el
```

Fig. 7.14 Contact element

7.4 Finite Element Program

To investigate the load-rate dependent behavior of concrete 3D explicit finite element research code, named as **Contact Impact and Fragmentation** (CIF), has been developed by the author using mixed programming approach. In this respect, for pre-processing and post-processing purposes, a graphical user interface (GUI) has been developed using C++ programming language (see Fig. 7.16). User interacts with GUI via forms and visual object selection mechanism implemented using OpenGL graphics routines. With CIF, user can perform interactive monitoring of nodes and elements as the simulation is still in progress.

Finite element meshes, used in simulations, are all generated using FEMAP software (**FEMAP 8.1**, ESP, Maryland Height, MO, USA). An interface has been developed to link CIF to FEMAP during pre-processing and post-processing. A new menu has been added to FEMAP, to be able to execute script files implemented, which bring simulation results obtained from CIF into FEMAP environment automatically with one click. Since the post-processor developed for CIF has some limited capacity, full post-processing can only be performed in FEMAP for now.

On the other hand to carry out finite element computations a program has been developed using Fortran programming language. The program is compiled both in the form of dynamic link library (DLL) and stand-alone executable (EXE). Former version is loaded from GUI during run time on a separate thread, whereas the latter one is aimed to carry out simulations in the so-called silent mode without GUI. Silent mode is attractive because it needs less memory as compared with interactive mode which runs together with GUI.

Material models are developed separately in the form of Fortran DLL s and linked into finite element program during run time, i.e. material models are not part of CIF program. For this purpose an interface has been developed by which one can register a material model in a straightforward

manner and then use in simulations. In this respect interface modules for rate and temperature dependent microplane material and Saint Venant-Kirchhoff hyperelastic material have been implemented.

Another program, named as **CIF-JOB**, is also maintained mainly to carry out parametric studies using CIF and browse in between several CIF projects (see Fig. 7.15). With this program it is possible to perform interactive monitoring of multiple simulation projects and to plot time history graphs of monitoring items for different projects onto the same graph (see Fig. 7.17).

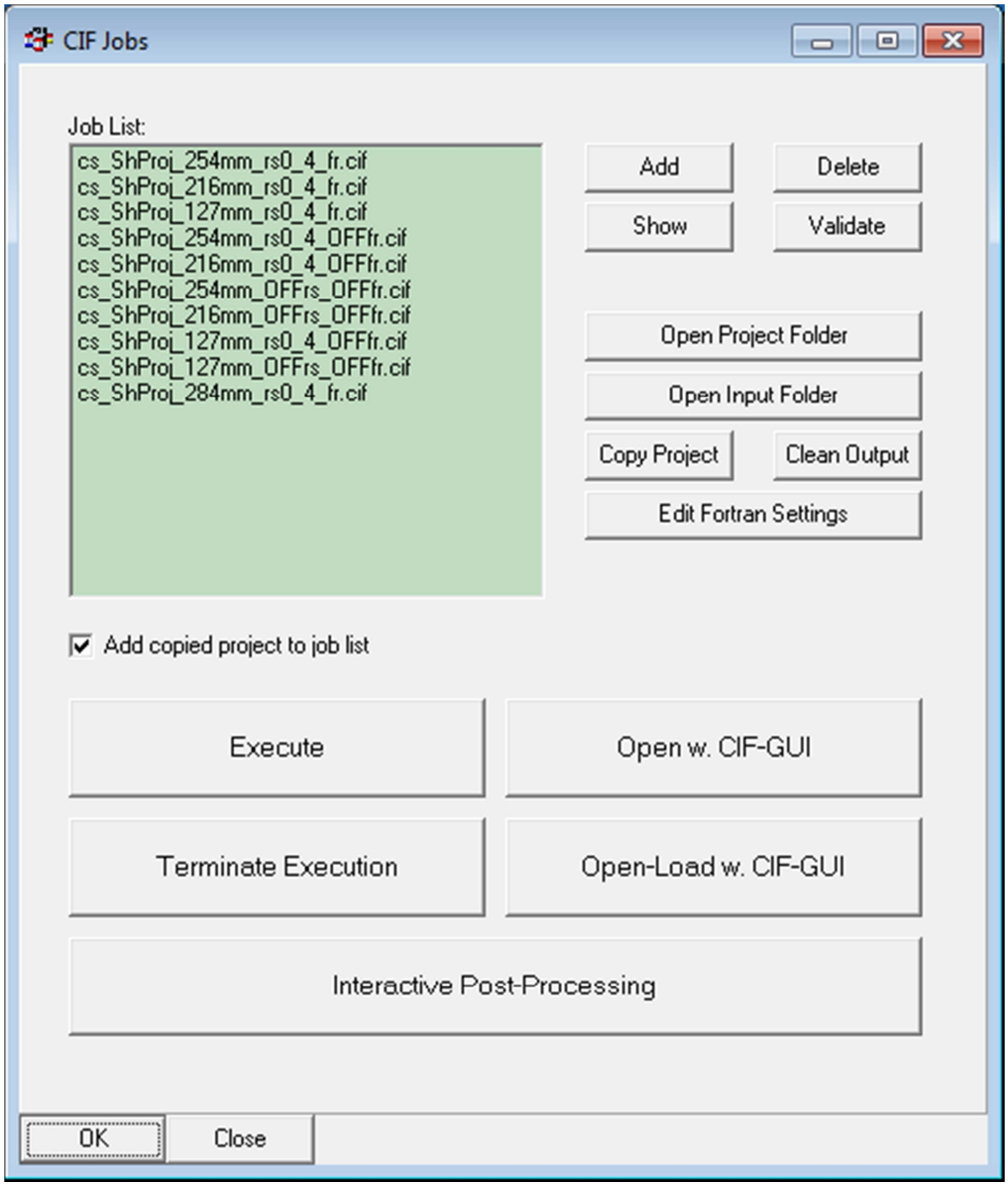

Fig. 7.15 CIF-JOB: Jobs list

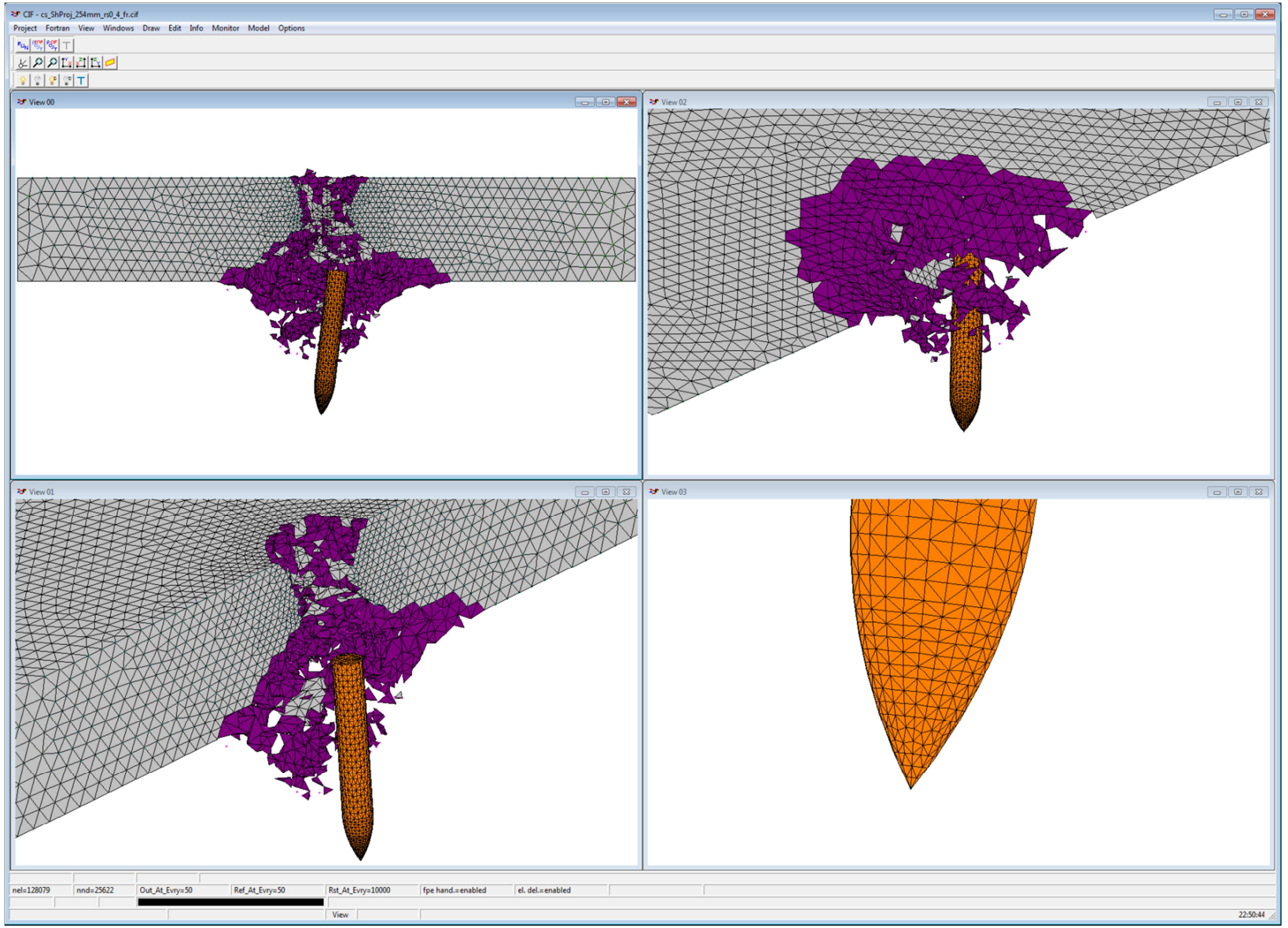

Fig. 7.16 CIF-GUI

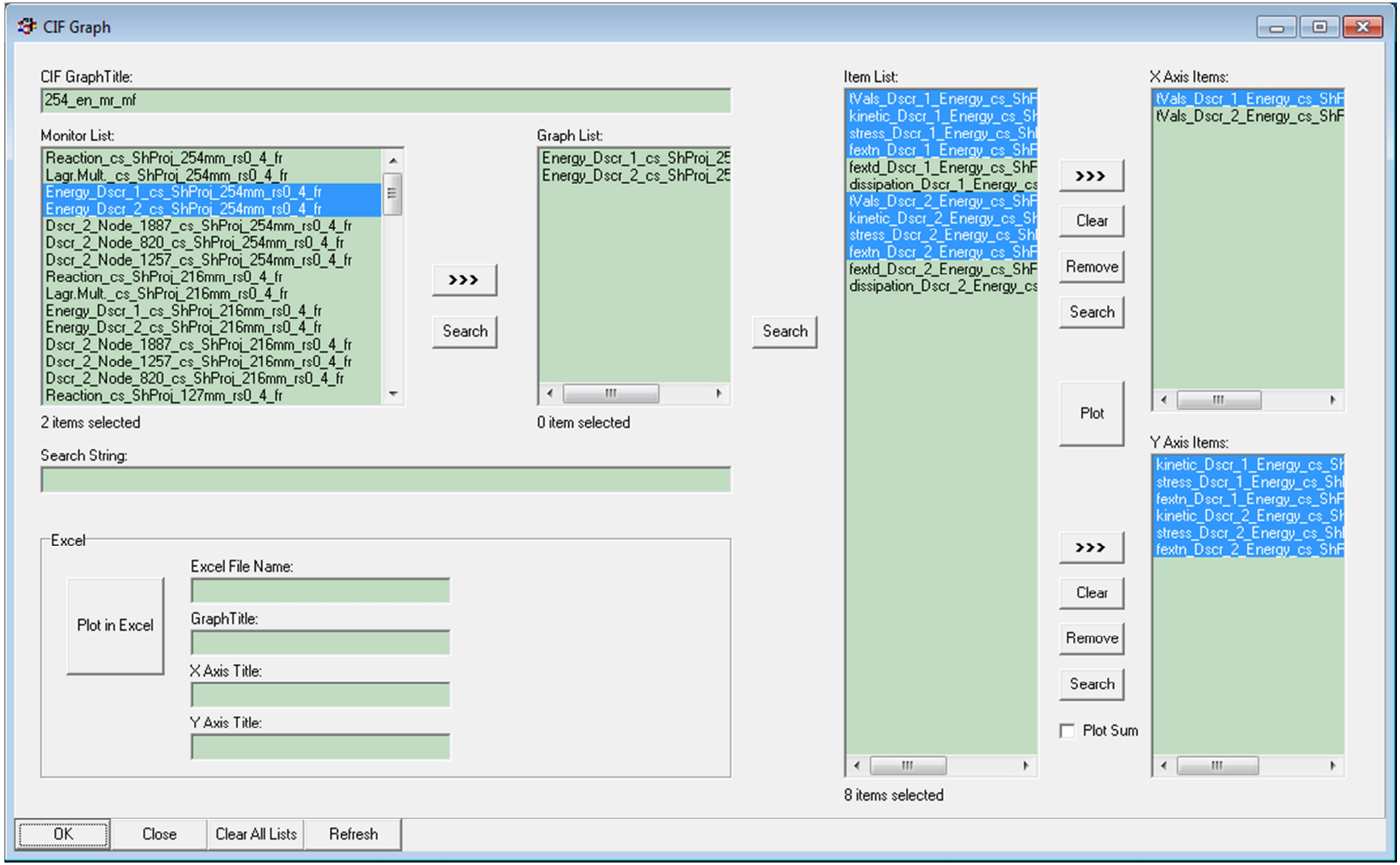

Fig. 7.17 CIF-JOB: Multi-project monitoring

8 Numerical Case Studies

8.1 Split Hopkinson Bar Test

8.1.1 Introduction

The experimental evidence (Malvar et al. 1998) shows that tensile behavior of concrete is strongly influenced by the loading rate. The uniaxial tensile behavior of concrete is difficult to investigate both experimentally and numerically. Therefore, indirect methods like split Hopkinson bar test, compact tension specimen test or some other alternatives are often employed. In (Reinhardt et al. 1986; Weerheijm 1992; Pedersen 2010) tensile behavior of concrete under dynamic loads has been studied by utilizing split Hopkinson bar test.

If the experimental results (Malvar et al. 1998) are evaluated based on the assumption that concrete behavior is purely linear elastic before tensile cracking, a progressive increase in tensile resistance with respect to strain rate is obtained beyond the critical value (approximately $10\ \mathrm{s}^{-1}$). The questions to be addressed are then:

(i) what is the reason for such a progressive increase and

(ii) whether the experimentally measured resistance can be attributed only to the material strength or there are some other factors to be taken into account when evaluating experimental results.

A deformable body subjected to impact loads is under dynamic equilibrium and consequently the applied load and reactions are not equal to each other due to presence of inertial forces. The applied load is balanced by inertial forces and internal forces, developing due to resistance of material to deformation. These internal forces are then transmitted through the body and build up the reaction forces. Up to a certain strain rate, the inertial component is insignificant and both applied load and reactions are nearly in static equilibrium, though they are higher than the corresponding values at static loading rates. This is termed as ‘rate sensitivity’ and is attributed totally to material behavior. Beyond critical strain rate inertial forces start becoming significant and, therefore, the applied load and reactions cannot be assumed to be in static equilibrium anymore. The relative magnitude of applied load with respect to the reactions keeps on increasing with increased loading rate. This is termed as ‘influence of structural inertia’ and cannot be attributed to the material resistance. Obviously, structural inertia is dependent on size and shape of the body. This suggests that the measured applied load during impact does not provide the true material strength but inherently has an inertial component and thus it can be referred to as ‘apparent strength’.

Behavior of various materials at high strain rates have been investigated experimentally in (Hopkinson 1914). Proposed experiment is based on the propagation of a compressive pulse, generated by an explosive charge or impacting bullet, on a long bar. Simply compressive loading wave is transmitted through the bar and is reflected back at the end as a tensile loading wave which then causes the fracture of brittle materials such as concrete, rock etc. Later on (Kolsky 1953) this technique has been made more feasible for practical measurements. It is known as split Hopkinson (pressure) bar (SHB) test which is schematically shown in Fig. 8.1.

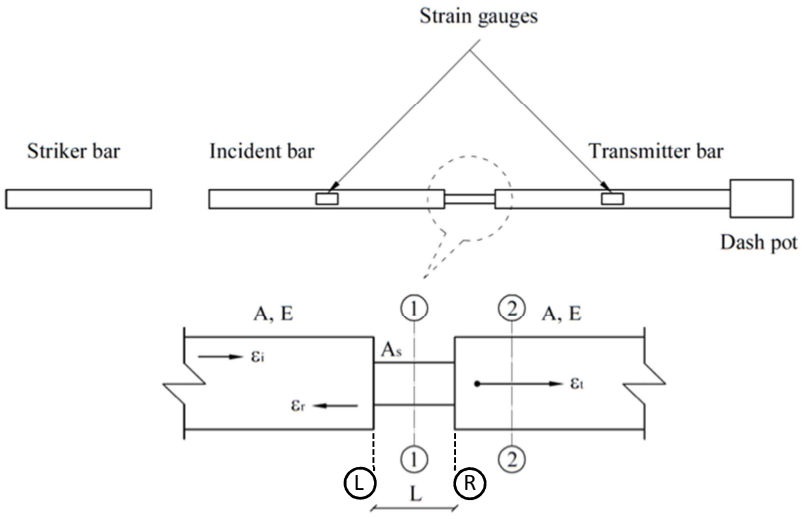

Fig. 8.1 Schematic of split Hopkinson bar (SHB)

Assuming that stress and strain is uniaxial during experiments and linear elastic material behavior (Ross 1989), dynamic equilibrium equation governing the motion of specimen, incident and transmitter bars collapses down to

$$\frac{\partial^2 u}{\partial t^2} = c\frac{\partial^2 u}{\partial x^2} \qquad \text{(Eq. 8.1)}$$

(Eq. 8.1) is known as one dimensional wave equation. In (Eq. 8.1), u is displacement and c is one dimensional elastic wave velocity given by

$$c = \sqrt{E/\rho} \qquad \text{(Eq. 8.2)}$$

where E, ρ are elastic modulus and mass density, respectively. In (Eq. 8.2) c denotes elastic wave velocity in incident and transmitter bars assuming that they are made of the same material. In the following, quantities related with specimen will be denoted with a subscript “s”.

An arbitrary wave of the form $u = f(ct - x)$ travelling in $+x$ direction is a solution to (Eq. 8.2). Assuming that the uniaxial strain is positive in compression, we obtain

$$\varepsilon = -\frac{\partial u}{\partial x} = f'(ct - x) \qquad \text{(Eq. 8.3)}$$

In (Eq. 8.3), f' denotes partial derivative with respect to $s := ct - x$. Particle velocity v is expressed in terms of f as

$$v = \frac{\partial u}{\partial t} = cf'(ct - x) \qquad \text{(Eq. 8.4)}$$

From (Eq. 8.3) and (Eq. 8.4), a relationship between particle velocity and strain is obtained as

$$v = c\varepsilon \qquad \text{(Eq. 8.5)}$$

Note that for a wave propagating in $-x$ direction (Eq. 8.5) takes the form

$$v = -c\varepsilon \qquad \text{(Eq. 8.6)}$$

Next we consider the displacements at sections L and R shown in Fig. 8.1. Displacement at section L is a combination of those due to incident and reflected waves, i.e.

$$u_{\mathrm{L}} = u_i(ct - x_{\mathrm{L}}) + u_r(ct + x_{\mathrm{L}}) \qquad \text{(Eq. 8.7)}$$

On the other hand, at section R displacement is due to transmitted wave only, i.e.

$$u_{\mathrm{R}} = u_t(ct - x_{\mathrm{R}}) \qquad \text{(Eq. 8.8)}$$

From (Eq. 8.7) and (Eq. 8.8), average strain in the specimen is obtained as

$$\varepsilon_s = -\frac{u_{\mathrm{R}} - u_{\mathrm{L}}}{L} \qquad \text{(Eq. 8.9)}$$

where L is the length of the specimen. From (Eq. 8.5), (Eq. 8.6) and (Eq. 8.9), the average strain rate in the specimen is obtained as

$$\dot{\varepsilon}_s = \frac{d\varepsilon_s}{dt} = \frac{v_{\mathrm{L}} - v_{\mathrm{R}}}{L} = \frac{c}{L}(\varepsilon_i - \varepsilon_r - \varepsilon_t) \qquad \text{(Eq. 8.10)}$$

Taking into account the fact that length of the specimen is so small as compared to the total length, strains at the both ends of the specimen can be assumed to be equal to each other, i.e.

$$\varepsilon_{\mathrm{L}} \cong \varepsilon_{\mathrm{R}} \quad \Longrightarrow \quad \varepsilon_i + \varepsilon_r = \varepsilon_t \qquad \text{(Eq. 8.11)}$$

Finally plugging (Eq. 8.11) into (Eq. 8.10) it is obtained that

$$\dot{\varepsilon}_s \cong -2\frac{c\varepsilon_r}{L} \qquad \text{(Eq. 8.12)}$$

Average stress in the specimen can be computed from transmitted strain as

$$\sigma_s A_s = \sigma A \quad \Longrightarrow \quad \sigma_s = E\varepsilon_t \frac{A}{A_s} \qquad \text{(Eq. 8.13)}$$

where A, A_s are cross-sectional area of the transmitter bar and specimen, respectively. High strain rates can be attained if ε_r is large, which can be achieved either by using a specimen diameter that is small compared to incident bar or in case when the bar material is much stiffer than the specimen.

The reflected and transmitted strain can be measured using strain gauges, and the stress in the specimen can be calculated as a function of strain rate by employing (Eq. 8.12) and (Eq. 8.13). By recording stresses σ_s at different strains ε_s, it is also possible to calculate fracture energy of concrete.

Using SHB for tensile loading, strain rates up to $10\ \mathrm{s}^{-1}$ can be obtained. For higher strain rates usually modified SHB (MSHB) is used, which is schematically shown in Fig. 8.2. In this test set-up the specimen is loaded in a quasi-uniaxial stress state and it is unbalanced since one end is in contact with the Hopkinson (incident) bar whereas the other end is free. MSHB test set up is very similar to flyer plate impact tests performed to determine spall strength of materials (Antoun et al. 2003). Typical strain rates in the range of $20 - 200 s^{-1}$ can be obtained with this technique (Schuler et al. 2006).

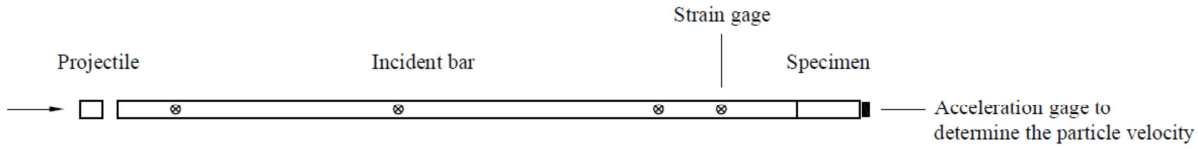

Fig. 8.2 Schematic of modified split Hopkinson bar (MSHB)

In MSHB test, acceleration time history at the free end of concrete specimen is recorded. Corresponding time history of the free surface velocity v_f is computed by applying numerical integration on recorded acceleration data. Free surface velocity is approximately equal to two times the corresponding particle velocity v_p, i.e.

$$v_f \cong 2v_p \qquad \text{(Eq. 8.14)}$$

As the fracture plane starts to form there is a sudden drop in free surface velocity (see Fig. 8.6). The difference between the first maximum and minimum free surface velocities, emanated from the formation of fracture plane, is called as pull-back velocity v_f^{pb}. Knowing pull-back velocity, corresponding tensile (spall) strength can be computed approximately from (Antoun et al. 2003)

$$f_t = \frac{1}{2}\rho_s c_s v_f^{pb} \underbrace{=}_{\text{(Eq.8.14)}} \rho_s c_s v_p^{pb} \quad \text{with} \quad c_s = \sqrt{E_s/\rho_s} \qquad \text{(Eq. 8.15)}$$

(Eq. 8.12), (Eq. 8.13) and (Eq. 8.15) are based on the assumption that material behavior is purely linear elastic before the formation of discrete crack(s). However, as will be shown later, this

assumption is critical for concrete like materials because the entire specimen already suffers significant level of damage at high strain rates before the formation of single (or multiple) discrete crack(s). Therefore pre-damaging of material must be taken into account for the determination of elastic wave velocity. Otherwise material strength predicted using (Eq. 8.15) can be highly overestimated.

8.1.2 Numerical Simulation

In (Schuler et al. 2006) series of experiments have been conducted using MSHB in order to explore load rate dependency of tensile strength and fracture energy of concrete. In this work, the experimental results have been evaluated based on elastic wave propagation and beyond the strain rate of approximately $10\ s^{-1}$ a progressive increase in dynamic-increase-factor (DIF) for tensile strength and fracture energy has been reported.

For the same experiments, set of numerical simulations has been performed using the recently developed 3D explicit finite element research code based on rate dependent microplane model. The geometry and dimensions of the problem are depicted in Fig. 8.3 together with corresponding finite element discretizations. Aluminum incident bar and concrete specimen are glued together and the diameter of both is $74.2\ mm$. The incident bar is loaded by the impact of $1.95\ kg$ steel hammer of the same diameter. Numerical simulation has been repeated for three different impact velocities, namely for $4.1\ m/s$ (Case-A), $7.6\ m/s$ (Case-B) and $11.1\ m/s$ (Case-C).

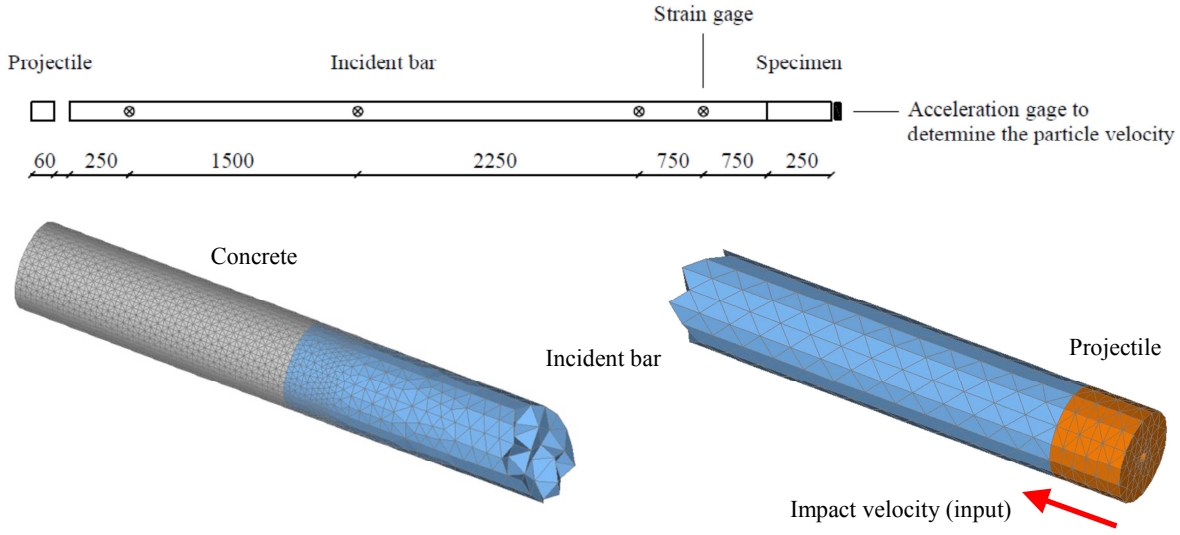

Fig. 8.3 Geometry, dimensions (in mm) and
FE discretization of concrete specimen, incident bar and projectile

For the concrete specimen rate sensitive microplane model is utilized whereas for steel projectile and aluminum incident bar simple linear elastic material behavior is adopted. The corresponding

material properties are given in Table 8.1. The concrete material properties for quasi-static loading are approximately the same as in the experiments. However, the values for tensile strength and fracture energy (see Table 8.1) slightly deviate from those specified by Schuler et al. (2006). The reason is the fact that for specified macroscopic properties the microplane parameters are automatically generated, which can result in macroscopic properties that can be slightly different than the specified values.

Table 8.1 Material properties

Material	Density [kg/m^3]	Elastic modulus [GPa]	Poisson's ratio	Compressive strength [MPa]	Tensile strength [MPa]	Fracture energy [J/m^2]
Concrete	2400.0	29.75	0.18	43.2	2.92	107.0
Steel	7800.0	210.0	0.33	-	-	-
Aluminum	2700.0	70.0	0.3	-	-	-

As discussed in section 5.2, the strain rate effect is incorporated into the microplane model based on rate process theory. According to this theory, the material strength increases approximately linear in semi log scale (A. S. Krausz et al. 1988) with respect to strain rate. Typical uniaxial tensile stress-strain curves obtained under different loading rates are plotted in Fig. 8.4 together with the one corresponding to quasi-static loading. The curves correspond to the element size of $\mathrm{h} = 5\ \mathrm{mm}$, which is also the average element size used for concrete finite elements in numerical simulations. The rate dependent concrete properties obtained for different strain rates are listed in Table 8.2.

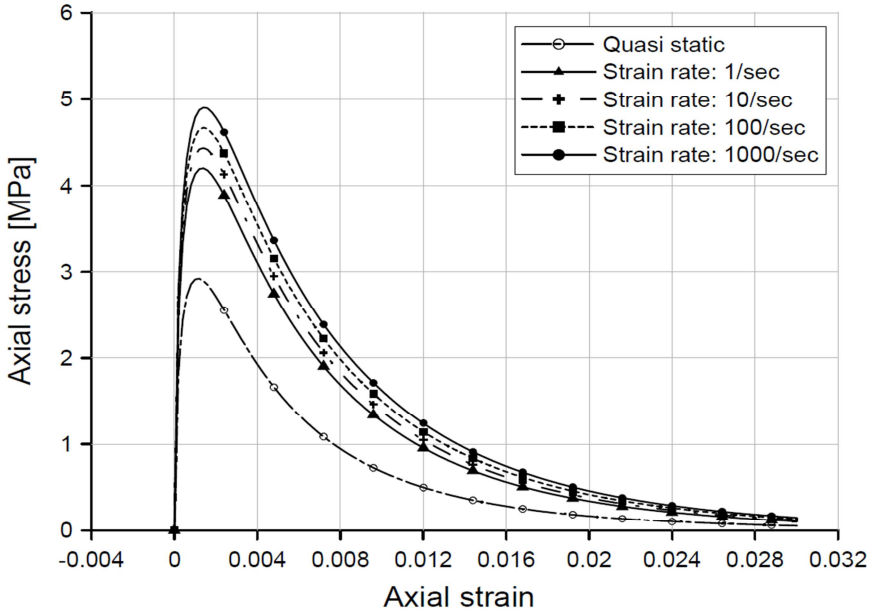

Fig. 8.4 Rate dependent tensile stress-strain curves – constitutive law

Table 8.2 Concrete properties from the rate dependent constitutive law

Strain rate [s^{-1}]	Young's modulus [GPa]	Comp. strength [MPa]	Tensile strength [MPa]	Fracture energy [J/m^2]
quasi-static	29.75	43.2	2.92	107
1	34.35	51.1	4.20	178
10	35.15	52.5	4.43	192
100	35.95	53.9	4.67	206
1000	36.70	55.4	4.90	221

The experimental results and macro material properties obtained eventually by processing them based on elastic wave propagation theory using (Eq. 8.15) are provided in Table 8.3 (Schuler et al. 2006).

Table 8.3 Experimental results and computed material properties (average values)

Case	Pull-back vel. v_f^{pb} [m/s]	Strain rate [s^{-1}]	Young's modulus [GPa]	Tensile strength [MPa]	Fracture energy [J/m^2]
A	2.63	33	40.1	12.9	288.5
B	3.36	68	38.7	16.2	334.5
C	3.67	80	39.9	18.0	-

As can be seen from Fig. 8.5 numerical results are in very good agreement with experiments in terms of the failure mode, assessed based on evolution of discrete cracks and formation of the fragments, for all three different impact velocities.

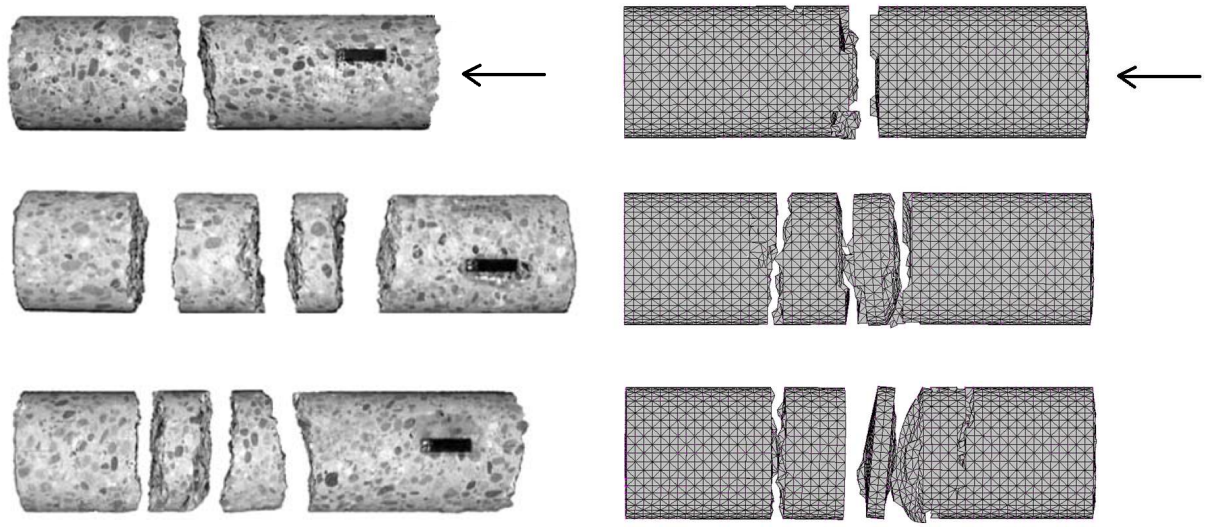

Fig. 8.5 Crack patterns for three impact velocities, left experiment and right numerical analysis with fragmentation (top 4.1 m/s, middle 7.6 m/s and bottom 11.1 m/s)

In (Schuler et al. 2006) axial strain at the glued end of the concrete specimen is approximated by an expression, whereas axial velocity at the free end is monitored with the aid of an acceleration gauge. These quantities are then used to compute equivalent elastic wave speed in concrete and pull-back velocity at the free end, from which dynamic material properties are then calculated. As can be inferred from Fig. 8.6, axial strain time history at the glued-end and axial velocity time history at the

free-end of the concrete specimen obtained from numerical simulation carried out for Case-A exhibit reasonably good agreement with those documented in (Schuler et al. 2006).

Based on successful comparisons above it can be concluded that numerical simulations carried out by 3D explicit finite element research code developed by the author are capable of successfully replicate experiments conducted in (Schuler et al. 2006). Therefore from this point on we carry on the discussion based on the results obtained from numerical simulations.

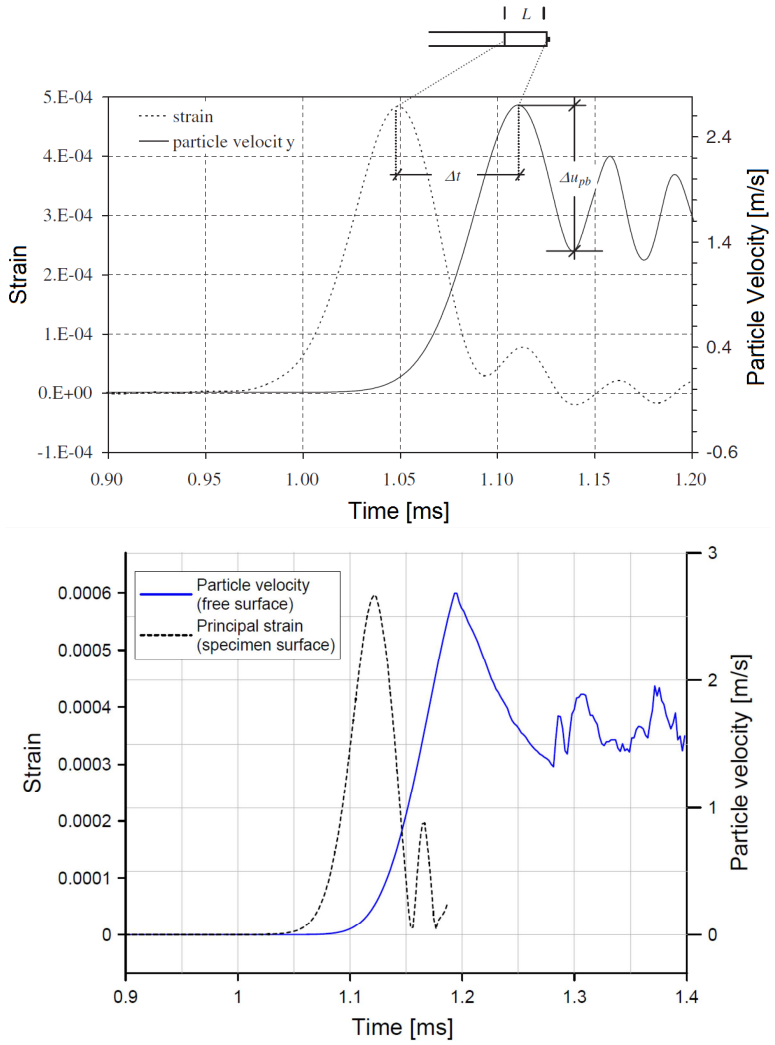

Fig. 8.6 Experimentally measured (top) and numerically predicted (bottom) strains and particle velocities

8.1.2.1 Rate dependent tensile strength

Typical time history graphs of axial stress and strain for cracked and un-cracked parts of concrete specimen and corresponding stress-strain diagrams are given, respectively, in Fig. 8.7 and Fig. 8.8 for Case-A. Note that data for these graphs are taken from finite elements located at the center of concrete specimen. For Case-A average strain rate is computed as approximately $34\ \mathrm{s}^{-1}$ (see Table 8.5). As can be inferred from Fig. 8.8-right uniaxial stress-strain diagram computed for this strain rate

does not lie in between those obtained from rate dependent constitutive law for strain rates $1\ s^{-1}$ and $100\ s^{-1}$. This contradiction can be explained by the three-dimensionality of stresses and strains, namely the reference element is in tension in lateral direction too.

Assessment of the numerical results reveals that un-cracked parts of the concrete specimen experience high level of tensile strains (damage) prior to formation of discrete cracks (see Fig. 8.7 and Fig. 8.8). It is also noteworthy to point out that before localization of damage into discrete cracks (softening) the overall stress level within the concrete specimen approaches to the tensile strength of the material.

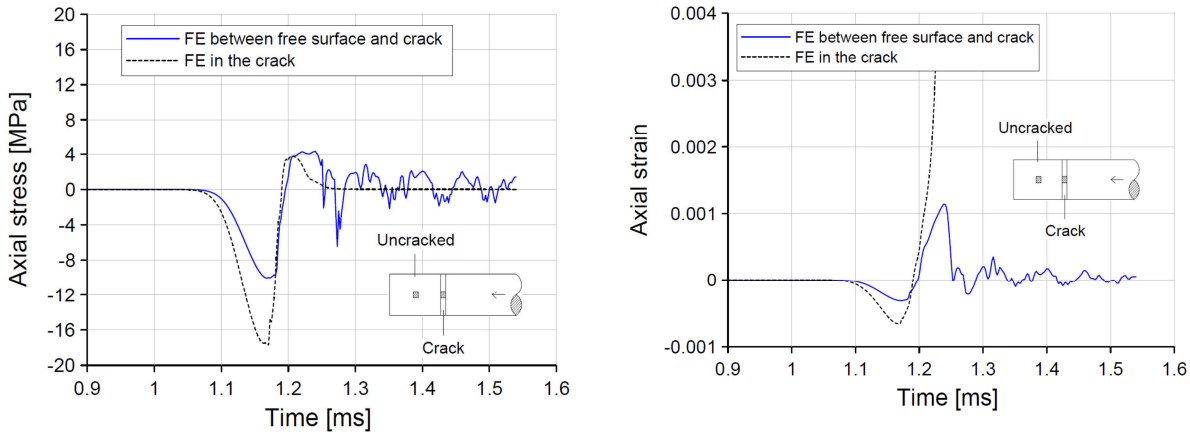

Fig. 8.7 Time evolution of stress (left) and strain (right)
in the finite element (center of the cross section)

Typical axial acceleration and axial displacement time history graphs for the un-cracked part of specimen is shown in Fig. 8.9-top. It is observed that maximum acceleration is attained after localization of the crack. At this instant inertial forces are partly in self-equilibrium (kinetic energy). Distributed damage of concrete, as have already been observed in the experiments of (Schuler et al. 2006) (Fig. 8.9-bottom), might be the consequence of the unbalanced portion of the inertial forces.

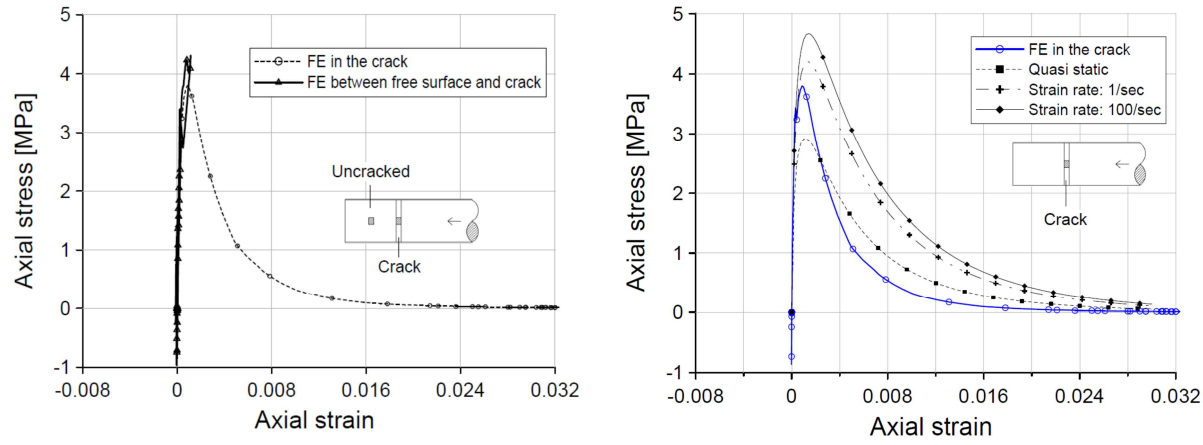

Fig. 8.8 Stress-strain relationships (left) in the finite element (center of the cross section) and comparison between stress-strain relationship in the crack and constitutive law (right)

As the discrete cracks form and start to propagate un-cracked parts of the body undergo elastic unloading. However up until to this point they have already been exposed to high level of damage, i.e. prior to unloading material behavior is not elastic (Fig. 8.8). To exemplify this maximum axial stresses attained and corresponding strains within the two elements, one located at the outer surface and the other at the center of the cross-section, between the free end of concrete specimen and the fully-developed discrete crack are listed in Table 8.4 for all three cases. The scalar damage variable ω is computed approximately from the ratio of tensile secant stiffness, calculated from corresponding maximum stress and strain given in Table 8.4, to initial elastic modulus listed in Table 8.2. As documented in Table 8.4, the computed level of damage is very high at un-cracked parts of the concrete specimen for all three cases. The reason for this is probably damage induced acceleration and resulting inertial forces.

Table 8.4 Numerically predicted concrete properties in the un-cracked part of the specimen

Case	**Max. stress [MPa]**		**Max. Strain [%]**		**Secant stiffness [MPa]**		**Damage**	
	center	surface	center	surface	center	surface	center	surface
A	4.31	3.60	0.114	0.046	3781	7826	0.87	0.74
B	4.45	4.16	0.176	0.076	2528	5474	0.92	0.82
C	4.02	3.61	0.109	0.057	3688	6333	0.88	0.79

Next rate dependent tensile strength values for concrete computed by different means are presented in Table 8.5. Note that strain rates listed are computed as the average value from a reference element just before it is cracked (Fig. 8.7-right) and are used here only to compute rate dependent tensile strength from constitutive law (Fig. 8.4). Virgin elastic modulus given by Table 8.1 and damaged secant stiffness presented in Table 8.4 are used to compute equivalent elastic wave velocity, which, together with pull-back velocities listed, is then used to compute rate dependent tensile strength from (Eq. 8.15). Direct numerical results from a reference cracked finite element are also presented.

Table 8.5 Numerically predicted data and their evaluation

Case	**Pull-back velocity v_f^{pb} [m/s]**	**Strain rate [s^{-1}]**	**f_t const. law [MPa]**	**f_t finite elements [MPa]**		**f_t (Eq. 8.15), damaged [MPa]**		**f_t (Eq. 8.15), elastic [MPa]**
		surface	surface	center	surface	center	surface	
A	2.81	34	4.56	3.80	4.36	4.23	6.09	11.87
B	2.81	52	4.64	4.27	4.46	3.46	5.09	11.87
C	2.85	83	4.67	3.59	4.30	4.24	5.56	12.04
Brittle material:								
A	0.8	34	4.56	4.63	4.84	3.4	4.45	3.38

After this brief information some conclusions will be drawn based on the results presented in Table 8.5. As can be seen pull-back velocities are very close to each other for all three cases. Based on this outcome one can claim that tensile strength should not change too much within investigated range of the strain rates. This is already confirmed by the rate dependent constitutive law for which tensile

strength ranges between 4.56 and 4.67 MPa. Direct numerical results from reference cracked finite elements also follow the same trend. The average tensile strength is below but fairly very close to the strength predicted by the constitutive law. This mismatch can be caused either by three dimensional stress (strain) state or by errors made in the computation of corresponding axial strain rate itself.

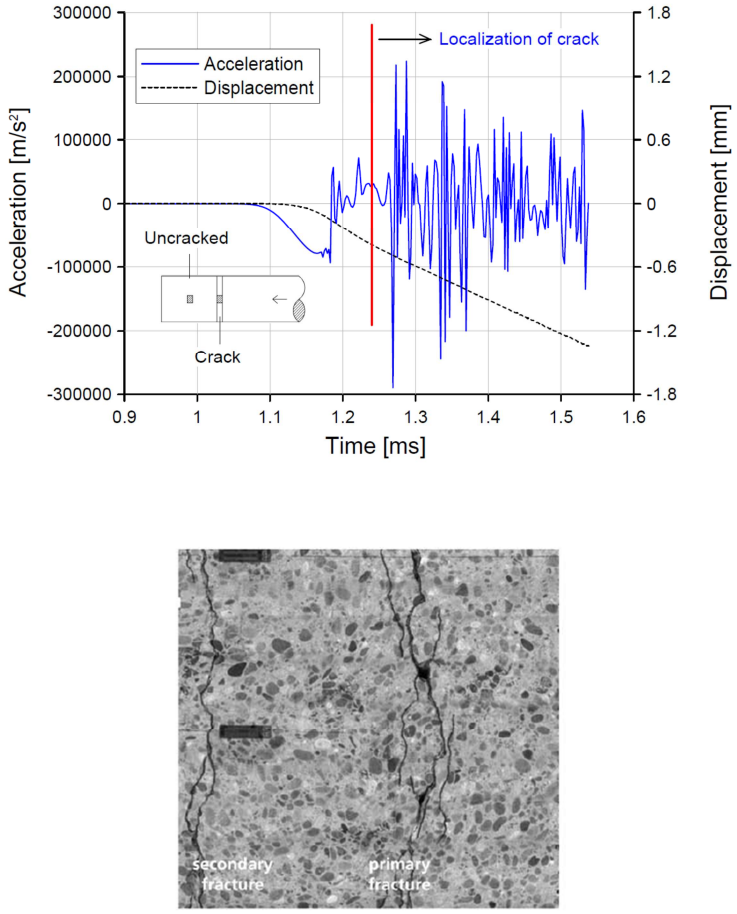

Fig. 8.9 Records of acceleration and displacement in the un-cracked part of the concrete specimen (left) and distributed damage observed in the experiments of Schuler et al. 2006

Furthermore, as can be seen from Table 8.5, the tensile strength predicted using (Eq. 8.15) based on pure linear elastic behavior of concrete specimen prior to discrete cracking is highly overestimated (apparent strength) for all three cases and follow neither constitutive law nor the numerical results obtained for any case. On the other hand the same computations carried out by taking pre-damaging of concrete into account yield results similar to those obtained from constitutive law and numerical analysis for all three cases.

The dynamic increase factors for tensile strength of concrete for different strain rates computed from

- results tabulated in Table 8.5
- results documented in (Schuler et al. 2006)
- rate-dependent constitutive law

are plotted in Fig. 8.10 together with vast amount of relevant experimental data from literature. It can be concluded that the numerical prediction and evaluation based on the wave equation, which accounts for damage of concrete, follow the rate dependent constitutive law. On the other hand the prediction based on the wave equation and elasticity significantly overestimates the true material strength. The comparison with the experimental data from the literature (see Fig. 8.10) also shows that the experimental results, that are all evaluated using wave equation and elasticity, fit the numerical prediction only when the results are evaluated in the same manner, i.e. assuming elastic behavior of concrete.

In (Schuler et al. 2006) pull-back velocity is measured and plugged in (Eq. 8.15) to compute tensile strength of the material assuming elastic behavior of concrete. In this way it is shown that there is a progressive increase in true tensile strength with respect to strain rate. However, the numerical results show that before localization of discrete macro cracks the entire specimen undergoes significant damage. Moreover, some parts of the specimen are observed to be even in the descending branch of the stress-strain curve. Therefore if the tensile stress wave propagation should be idealized as elastic wave propagation then damaged elastic modulus must be used to compute wave velocity and tensile strength must be calculated from (Eq. 8.15) based on such predicted wave velocity. It has been shown by numerical simulations that if this approach is used tensile strength computed from (Eq. 8.15) follow roughly the rate dependent constitutive law. Therefore progressive increase in tensile strength of concrete at high strain rates, as suggested by many researches and design codes, might need more careful and better interpretation, i.e. when the results of the experiments on Hopkinson bar are evaluated then damage before localization of discrete cracks should be accounted for. Another aspect of the problem is the fact that once the macro crack initiates, usually on one side of the specimen, there is not only a single crack but several cracks which branches before the specimen gets fully cracked over the entire cross-section (see Fig. 8.9). These effects are due to the activation inertia forces at the crack tip and are not accounted for by the evaluation of the results of experimental measurements using 1D wave propagation theory. Nevertheless, experimental evaluation techniques should be modified to account for these important phenomena.

Based on inadequate evaluation of the experimental results as discussed before, the progressive increase of tensile strength is considered to be a part of the constitutive model in most of the

commercial finite element programs available in the market. As discussed in (Ožbolt et al. 2011a-b, 2013b), the progressive increase of structural response observed at the macro scale (e.g. compact tension test) is a consequence of structural inertial forces and not a consequence of rate dependent strength of the material, i.e. the progressive increase in the tensile strength shall not be a part of the constitutive law, rather it should be predicted automatically from the dynamic analysis.

As discussed by (Ožbolt et al. 2006, 2011a), low quality concrete exhibit more damage before localization of cracks. Consequently, for low quality concrete the discrepancy between the true strength (rate dependent constitutive law) and the apparent strength predicted based on elastic wave propagation should be more transparent. On the other hand, for brittle materials like glass the apparent and true strength should be almost the same since for such materials there is almost no damage before localization of cracks. To illustrate this, the numerical analysis carried out for Case-A has been repeated for an elastic-brittle specimen by setting manually the fracture energy to a very small value as $G_F = 2.0\ \mathrm{J/m^2}$. The results are evaluated in the same manner as before and presented in a separate raw on Table 8.5. As can be seen, tensile strength computed based on elastic wave propagation is in the same order as that computed from rate-dependent constitutive law and numerical results. This affirms that the evaluation based on elastic wave propagation is valid only if there is no significant damage before cracking. Moreover, recent experimental results for glass also confirm that there is no progressive increase of DIF for tensile strength at high strain rates (Peroni et al. 2011).

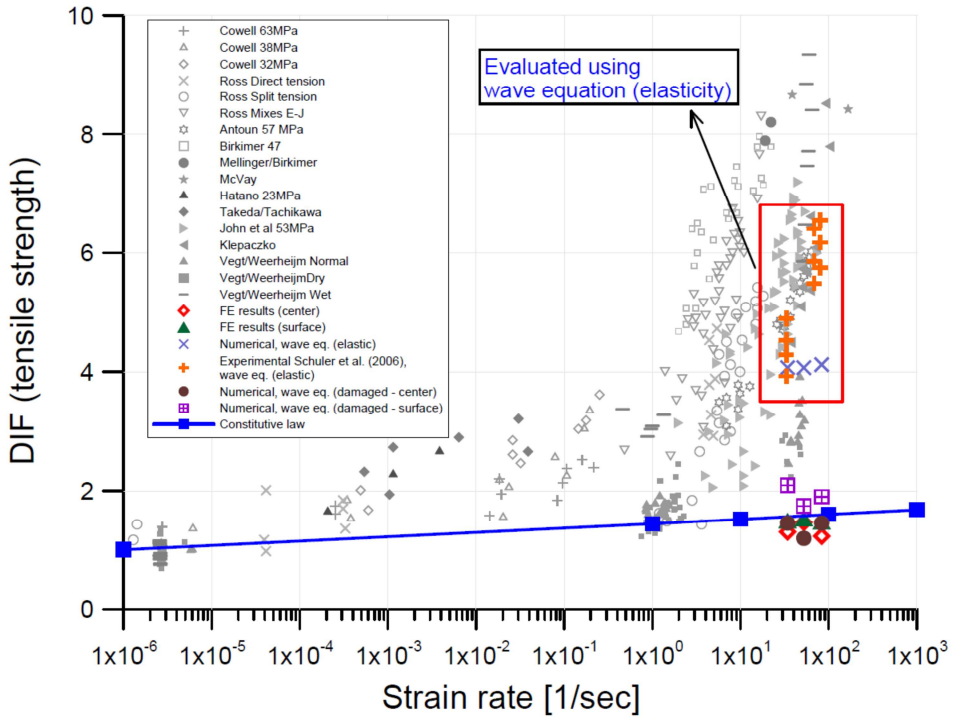

Fig. 8.10 Different evaluations of DIF for tensile strength (experimental and numerical results) compared with experimental data from the literature evaluated assuming elasticity

8.1.2.2 Rate dependent fracture energy

Similar to the rate dependent tensile strength, it is still not clear how the strain rate influences fracture energy of concrete. Experimental estimation of fracture energy at high strain rates is extremely difficult (Weerheijm et al. 2007; Vegt et al. 2009). It is because in such experiments multiple embedded cracks, which are not visible to the observer, might nucleate and propagate. In addition, overall concrete material experiences considerable amount of damage (micro-cracking) before the formation of discrete cracks. Based on these facts one might come up with highly overestimated values for fracture energy as the strain rate gets higher. For example in (Schuler et al. 2006) progressive increase of fracture energy with respect to strain rate beyond a critical value has been reported.

Table 8.6 Numerically evaluated fracture energy

Case	**Strain rate [s^{-1}]**	**G_F [J/m^2]**		**DIF**	
		center	surface	center	surface
quasi-static	-	107	107	1.0	1.0
A	34	84.10	116.95	0.79	1.09
B	52	124.12	110.32	1.16	1.03
C	83	154.97	104.43	1.45	0.98

To investigate the influence of strain rate on fracture energy, the numerical results obtained for three different cases are evaluated for the same crack used for tensile strength calculations. Within the context of crack band theory, fracture energy is calculated as the multiplication of area under the stress-strain curve (Fig. 8.8) with crack band (element size). In Table 8.6, the results for the cracked section, obtained at the center and surface of the specimen are shown. Note that similar to tensile strength, fracture energy is also not uniformly distributed over the cracked cross-section. In Fig. 8.11, experimental and numerical results together with some representative data from literature are given. As can be seen the numerical analyses result in DIFs slightly larger than one for fracture energy for the strain rate range of interest. They are even lower than the values predicted by rate dependent constitutive law. The reason for such behavior is not clear. Fracture energy is calculated (estimated) based on the maximum principal stress-strain relationship on the level of integration point of single finite element, at the center and on the surface of the cracked cross-section. According to definition, fracture energy should be calculated for Mode-I fracture, i.e. for uni-axial tension and it represents an average value over the entire crack surface. In the present case longitudinal direction is dominant, however, there are also tensile stresses in lateral direction due to inertia forces and due to the reflection of lateral loading waves. Moreover, during time history analysis direction of principal stresses and strains slightly changes and they are not coaxial. Having this in mind it is possible that the calculated fracture energy can be smaller than the value obtained

from quasi-static condition. Actually, one should calculate average value of fracture energy over the entire cracked cross-section. This is however not simple since there is often crack branching and direction of principal strains and stresses are different.

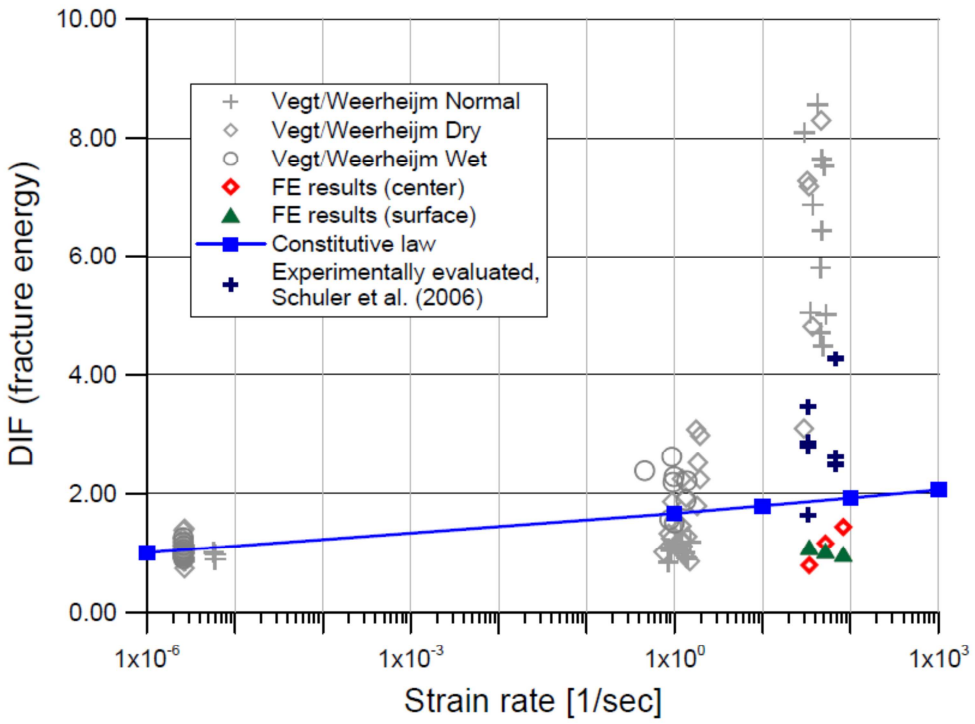

Fig. 8.11 Different evaluations of DIF for fracture energy (experimental and numerical results) compared with experimental data from the literature evaluated assuming elasticity

In contrast to numerical evaluation presented, the evaluations based on experimental results yield a progressive increase in fracture energy beyond a critical value of approximately $10\ \mathrm{s}^{-1}$. There are several reasons for this mismatch. First of all correct measurement of the total crack surface is not feasible at high strain rates due to rather complex crack topology. Therefore normally the total crack surface is underestimated during experimental evaluations. Micro-cracking (damage) prior to failure also contributes experimentally measured fracture energy. Moreover inertial effects around the crack zone also have a contribution. Filtering out all these effects would definitely close up the gap between numerically and experimentally computed fracture energies. Of course with the current state of the art experimental techniques it is not possible to make such measurements with required precision.

8.2 Compact Tension Specimen (CTS)

8.2.1 Introduction

CTS test is frequently used in engineering practice to determine tensile strength and fracture energy of concrete. In (Ožbolt et al. 2011a) loading rate sensitivity of CTS has been numerically investigated. The main conclusions drawn from this study can be summarized as follows:

- Material resistance increases linearly (in semi-log scale) with respect to loading rate up to a critical value. Up until this value material resistance is controlled by rate dependent constitutive law. On the other hand, beyond critical value there is a progressive increase in material resistance which is mainly controlled by inertial forces.
- Failure mode is rate dependent. For relatively low rates there is only one single monotonic discrete crack propagating almost perpendicular to the loading direction. As the loading rate is increased up to approximately $2.5\,\mathrm{m/s}$ failure mode changes from Mode-I to mixed mode and additionally crack branching is observed. Further increase in loading rate results in mixed failure mode together with multiple crack branching.
- Maximum crack velocity is attained before crack branching and it is computed approximately $600\,\mathrm{m/s}$ for normal strength concrete (uniaxial compressive strength $\cong 30\mathrm{MPa}$). Crack velocity drops down along the branches. Inertial forces at the crack tip are responsible for branching.

Currently there is no systematic procedure to test load rate sensitivity of CTS especially within the context of crack propagation and branching. Therefore set of experiments has been conducted recently using CTS to investigate rate dependent failure mode and crack branching. The results documented are then compared with results from (Ožbolt et al. 2011a) to assess the predictive capability of the numerical approach proposed therein. Due to technical reasons it was not possible to prepare the geometry of test set up and material properties exactly the same as one used in numerical simulations carried out in (Ožbolt et al. 2011a). For this reason, besides experiments, couple of additional numerical simulations has also been performed using explicit finite element research code developed by the author.

8.2.2 Experiments

The experiments have been conducted at MPA Institute, University of Stuttgart. Loading has been applied by prescribing displacements. During execution displacement rates up to $8\,\mathrm{m/s}$ has been reached.

8.2.2.1 Geometry, material properties and loading

Geometry and dimensions of CTS together with loading and boundary conditions are depicted in Fig. 8.12. In contrast to previous numerical study (Ožbolt et al. 2011a), CTS is positioned such that notch has horizontal alignment (see Fig. 8.12). Due to the technical reasons the load is applied only at one (bottom) surface of the notch through displacement control of the bottom loading frame. Top steel frame is fixed at the far end and served as reaction side. Before the experiment the top and bottom steel frames are glued to the corresponding notch surfaces. The photo of the test set-up is shown in Fig. 8.13.

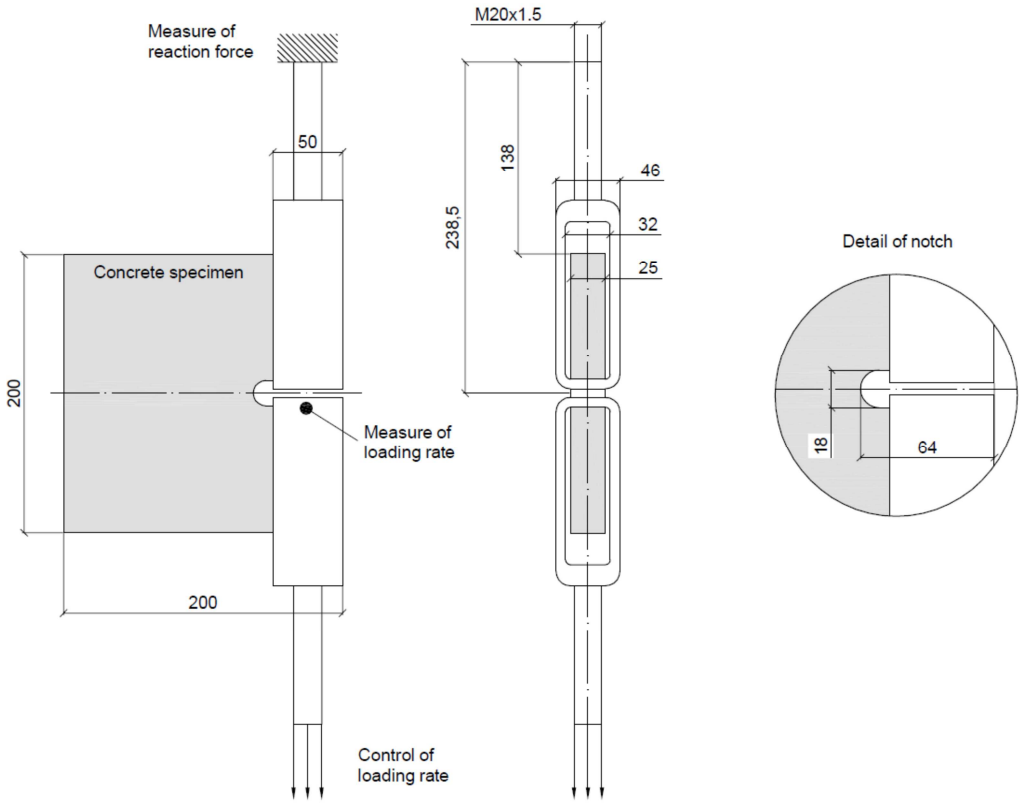

Fig. 8.12 Geometry of the CTS, top and bottom steel loading frames and detail of notch (all in mm)

The concrete specimens are cured 7 days under constant temperature of $20\ ^{\circ}\mathrm{C}$ and relative humidity (RH) of 100%. Subsequently the specimen is exposed to RH of 60% for approximately three weeks. Before casting CTS, the uniaxial compressive strength of concrete is measured on standard cylinders of $150\ \mathrm{mm}$ diameter and $300\ \mathrm{mm}$ height. The average strength (three specimens) is $f_c = 53\ \mathrm{MPa}$. Based on f_c, the concrete mechanical properties are estimated as: Young's modulus $E_c = 36\ \mathrm{GPa}$, Poisson's ratio $\nu = 0.18$, tensile strength $f_t = 3.8\ \mathrm{MPa}$ and fracture energy $G_F = 65\ \mathrm{J/m^2}$. Mass density of concrete is assumed to be $\rho_c = 2400\ \mathrm{kg/m^3}$ and maximum aggregate size is $8\ \mathrm{mm}$. The loading frames were made of normal steel with the following properties: Young's modulus $E_s = 210\ \mathrm{GPa}$, Poisson's ratio $\nu = 0.33$ and mass density $\rho_s = 7800\ \mathrm{kg/m^3}$.

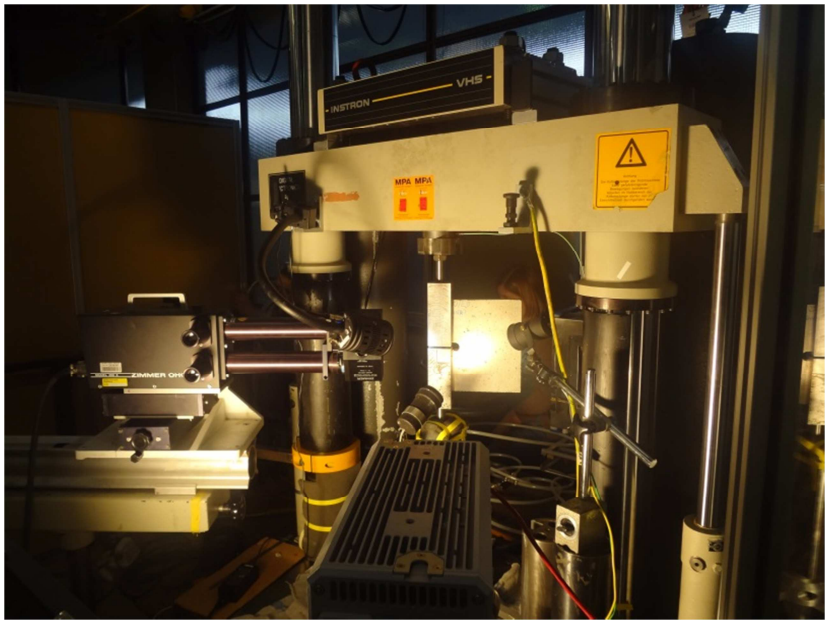

Fig. 8.13 Test set-up

Displacement rate at the both ends of bottom loading frame and the reaction at the far end of top steel frame are measured during experiments. High speed camera is used to estimate crack velocity. Displacement rates targeted at the far end of bottom loading frame vary between $0.1\ \mathrm{m/s}$ and $8.0\ \mathrm{m/s}$. Overall 12 experiments have been carried out.

8.2.2.2 Evaluation of experimental results

In Table 8.7, targeted and measured displacement rates at the far end of bottom loading frame, the displacement rate measured at the near end of bottom loading frame (near notch surface), reactions measured at the far end of top steel frame and cracking patterns observed are documented.

Table 8.7 Summary of experimental results

Test Nr.	Target disp. Rate [m/s]	Measured disp. Rate [m/s]	Disp. rate at contact [m/s]	Max. Reaction [kN]	Number of cracks
1	0.10	0.079	0.045	2.54	S
2	0.10	0.061	0.035	2.83	S
3	0.50	0.505	0.304	3.47	S
4	1.00	0.815	0.491	4.05	S
5	2.00	1.952	1.375	4.64	S
6	3.00	3.015	1.407	5.76	S
7	3.00	2.863	1.736	4.49	S
8	6.00	5.339	3.268	4.59	B
9	6.00	4.913	3.318	6.88	B
10	8.00	6.732	3.993	4.69	B
11	8.00	6.716	3.967	3.32	MB
12	8.00	6.774	4.298	5.66	B

S= single crack; B= branching; MB= multiple branching;

In Fig. 8.14 typical crack patterns for different loading rates are shown. It comes out that for the tested geometry and concrete properties there is only one single discrete crack up until the loading rates of about $2.0 - 3.0$ m/s. For relatively low loading rates, close to quasi static, the crack propagates almost perpendicular to the loading direction (Mode-I failure). On the other hand, for higher loading rates the crack trajectory becomes inclined with respect to the loading direction. In the experiments the first crack branching was observed at the displacement rate of approximately 3.3 m/s (see (d) in Fig. 8.14) and at the displacement rate of approximately 4.0 m/s even multiple crack branching is observed (case (e) and (f) in Fig. 8.14).

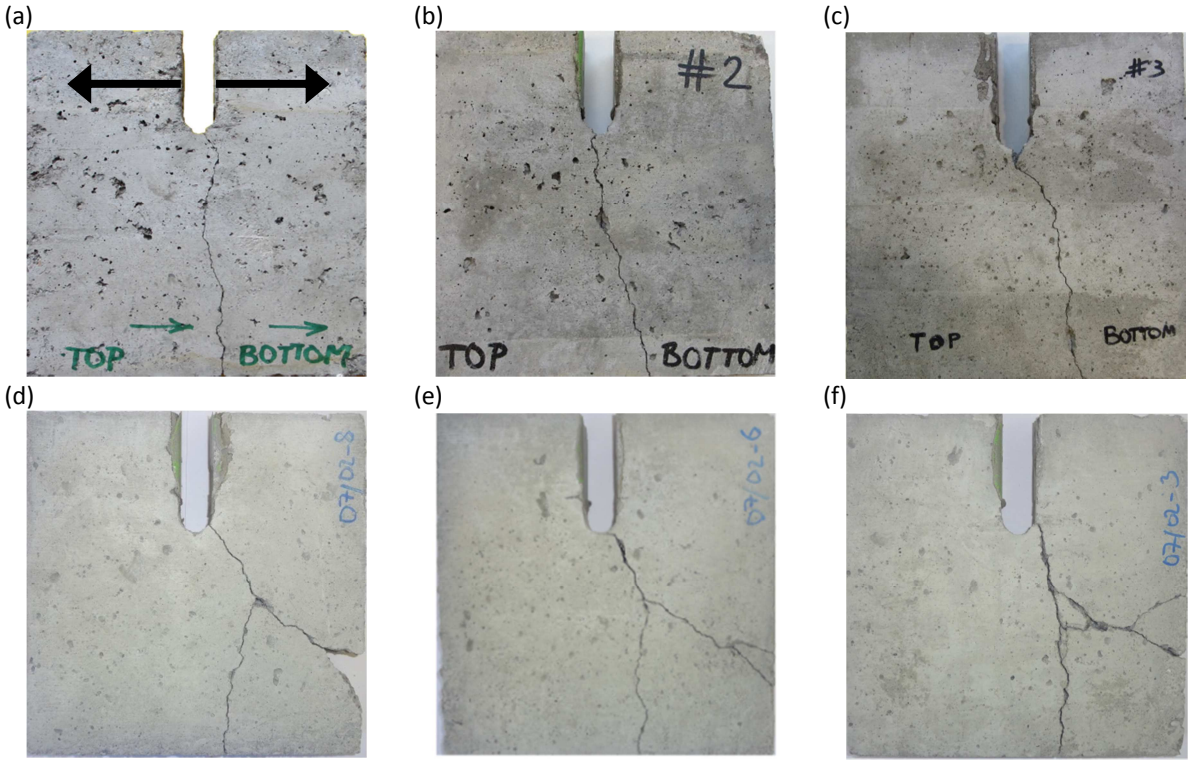

Fig. 8.14 Experimentally observed crack patterns for displacement rates
measured at the near end of bottom loading plate:
(a) 0.304 m/s, (b) 0.491 m/s, (c) 1.375 m/s, (d) 3.318 m/s, (e) 3.993 m/s and (f) 3.967 m/s

The crack velocity is estimated based on the evaluation of photos taken by high resolution camera FASTCAM APX-RS. With this camera it was possible to take 6 photos in the sequence of 19 ms from the crack initiation till crack branching. The highest crack velocity, detected during Test Nr. 12 (see Table 8.7), is around 800 m/s (see Fig. 8.15). The critical crack width was assumed to be 0.1 mm. It was possible to measure it from the camera resolution available and the corresponding measured frame window (area of measurement $= 70$x30 mm). The average crack velocity measured was approximately 420 m/s.

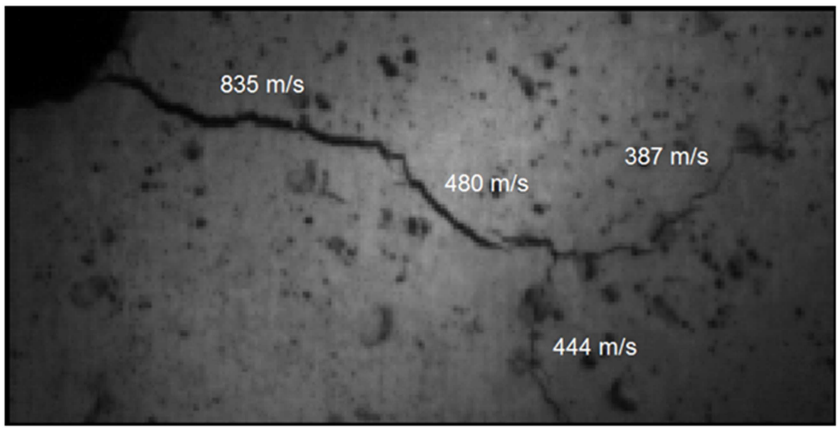

Fig. 8.15 Crack velocity before and after branching (Test Nr. 12)

The measured reaction-displacement curves are plotted in Fig. 8.16. The displacement is measured at the near end of bottom loading frame. As expected, the peak reaction increases with increase of displacement (loading) rate.

(a) (b)

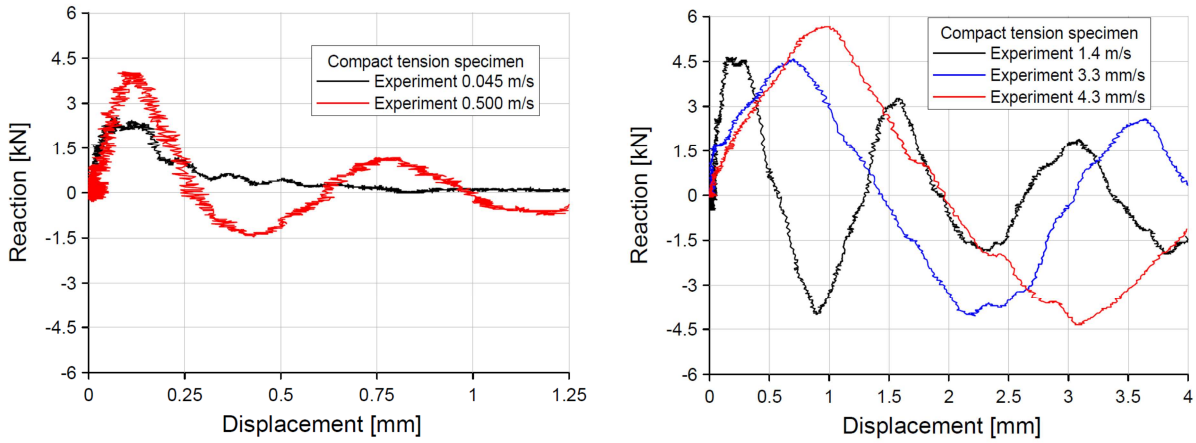

Fig. 8.16 Experimentally measured reaction-displacement response

As mentioned earlier, the geometry and material properties of CTS used for numerical study (Ožbolt et al. 2011a) and experiments performed later on are not identical. However the comparison of the results shows remarkably good agreement. The material properties for experiments and numerical study are given in Table 8.8.

Table 8.8 Material properties for experiments and numerical study (Ožbolt et al. 2011a)

	Density [kg/m^3]	Elastic modulus [GPa]	Poisson's ratio	Compressive strength [MPa]	Tensile strength [MPa]	Fracture energy [J/m^2]
Experiment	7800.0	36	0.18	53	3.8	65
Numeric	7800.0	30	0.18	40	3.5	90

As can be grabbed from Fig. 8.17, the numerical and experimental results, assessed in terms of failure mode and crack branching, are principally the same. Taking into account the facts that

numerical study (Ožbolt et al. 2011a) has been performed before the experiments presented herein and there has been no other similar experimental results published in the literature so far (according to our knowledge), it can be concluded that 3D finite element code used in (Ožbolt et al. 2011a) has a great predictive capability for the dynamic fracture of concrete.

(a) (b)

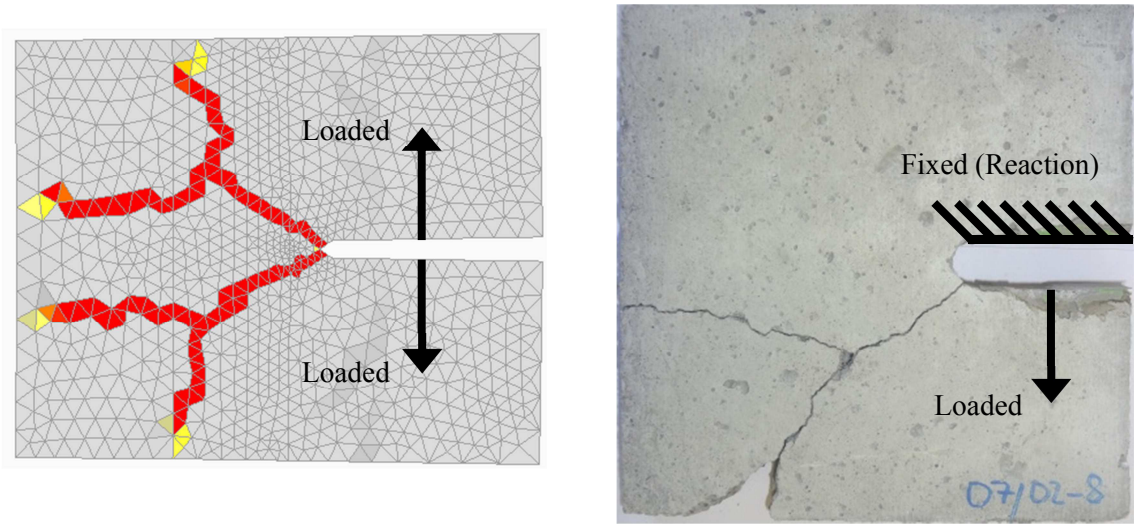

Fig. 8.17 Crack branching: (a) numerically predicted by (Ožbolt et al. 2011a) (loading rate 2.50 m/s) and (b) experimentally obtained (loading rate 3.30 m/s)

8.2.3 Numerical Study

For the experiments presented herein, set of numerical simulations has been performed using explicit finite element research code developed by the author. The material properties, geometry, boundary conditions and loading are exactly the same as in experiment (see Fig. 8.18). Linear tetrahedral finite elements are used to discretize concrete and steel parts. For steel parts linear elastic material behavior is adopted. Full bond is assumed between notch surfaces and steel plates. There is no contact in between at any other surfaces of concrete specimen as is the case for experiments. The displacement rates in the analysis are set to be equal to those measured during experiments (see Table 8.7-3rd column).

8.2.3.1 Comparison between numerical and test results

Numerical results obtained for eight different displacement rates are summarized in Table 8.9 together with corresponding experimental results. As can be seen, there is a very good agreement between numerical and experimental results in terms of reaction forces and crack patterns for all displacement rates investigated. In Fig. 8.20, comparison of crack trajectories for different displacement rates is given together with that obtained numerically for quasi-static loading. As is evident from Fig. 8.20, crack trajectory is perpendicular to the loading direction for relatively low

loading rates. On the other hand it becomes more and more inclined as the loading rate increases. There is crack branching at loading rate of about 3.3 m/s both numerically and experimentally. Comparison of crack trajectories and velocities is depicted in Fig. 8.19 for loading rate of 4.3 m/s. Maximum theoretical crack speed that can be attained in CTS specimen considered here is around 800 m/s. As soon as crack velocity attains this critical value crack branching occurs (Ožbolt et al. 2011a). Experimental and numerical reaction time history diagrams for four different loading rates are presented in Fig. 8.21. As can be grabbed from these diagrams experimental and numerical results are in very good agreement. For quasi static loading maximum reaction force is about $1.6\ \mathrm{kN}$, whereas it is equal to approximately $5.9\ \mathrm{kN}$ for loading rate of $4.3\ \mathrm{m/s}$ (i.e. DIF is equal to 3.69). Based on comparisons made so far, one can conclude that numerical analyses are quite successful in predicting concrete response for all loading rates.

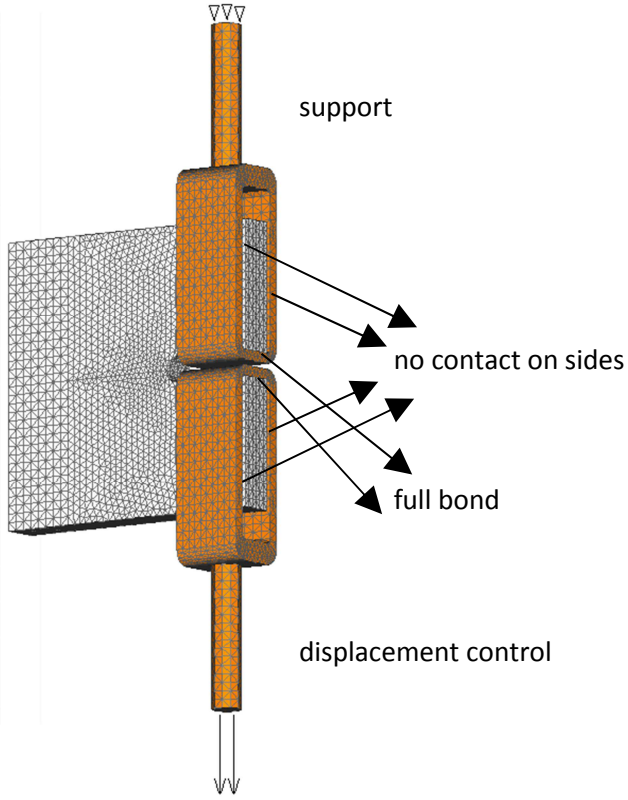

Fig. 8.18 3D finite element model of the CTS

It is very difficult to measure strain rate, crack opening rate, rate dependent tensile strength and fracture energy during experiments especially for very high loading rates. As the predictive capability of numerical tool used has been verified with successful comparisons presented so far, they will be all computed based on the results of numerical simulations.

Table 8.9 Summary of numerical and experimental results

Test Nr.	Disp. rate, analysis [m/s]	Disp. Rate, experiment [m/s]	Max. reaction, analysis [kN]	Max. reaction, experiment [kN]	# of cracks – test/an.
0	quasi-static	-	1.60	-	-/S
1	0.045	0.045	2.21	2.54	S/S
2	0.035	0.035	2.29	2.83	S/S
3	0.300	0.304	3.65	3.47	S/S
4	0.500	0.491	4.12	4.05	S/S
5	1.400	1.375	3.54	4.64	S/S
8	3.300	3.268	4.76	4.59	B/B
10	4.000	3.993	4.93	4.69	B/B
12	4.300	4.298	5.16	5.66	B/B

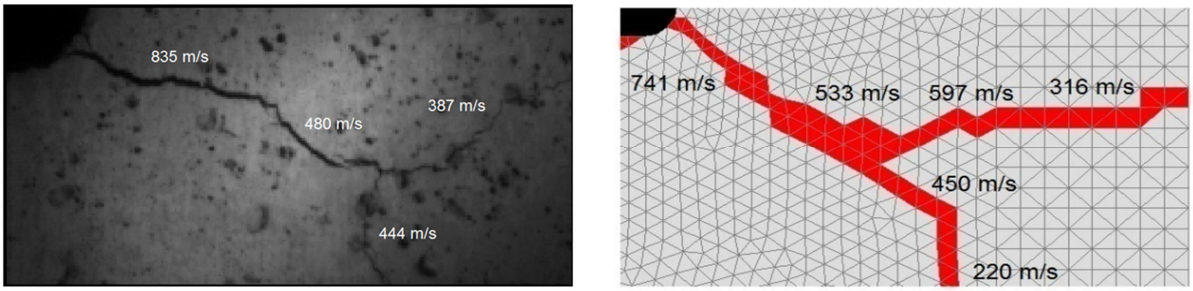

Fig. 8.19 Measured and numerically predicted crack velocities for loading rate 4.30 m/s

In Table 8.10, the results obtained from numerical simulations are summarized. All calculations have been performed on the first cracked finite element located at the notch tip. Time history diagrams for maximum principal stress and strain are plotted in Fig. 8.22 for different loading rates. Rate dependent tensile strength and fracture energy, listed in Table 8.10, have been calculated using these diagrams. Note that quasi-static counterparts of tensile strength and fracture energy are slightly lower than those computed by utilizing uniaxial constitutive equation. Tensile stresses developing in lateral direction (thickness direction) might have something to do with this reduction.

Table 8.10 Summary of numerical results

Test Nr.	Disp. rate, analysis [m/s]	Tensile strength [MPa]	Fracture energy [J/m^2]	Strain rate [s^{-1}]	Crack opening rate [m/s]
0	quasi-static	3.45 (3.80*)	45.20(65.00*)	--	--
2	0.035	4.52	38.0	3.20	0.03
5	1.400	4.63	46.3	45.30	1.38
8	3.300	4.68	50.8	56.80	4.48
12	4.300	4.64	48.3	77.20	5.55

*: constitutive law – quasi static uni-axial tension

(a)

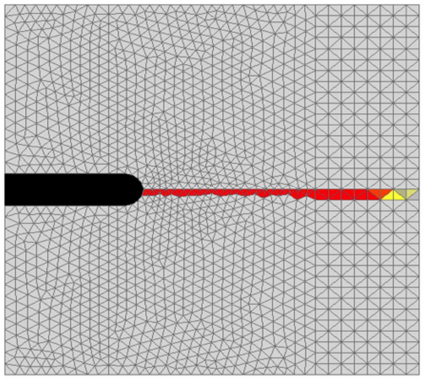

(b)

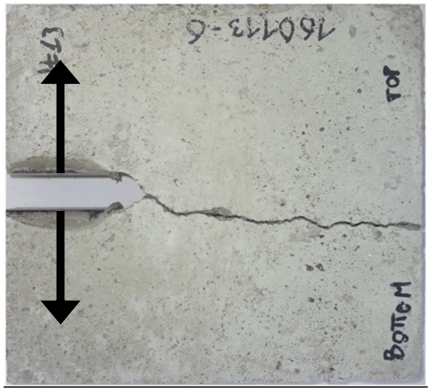

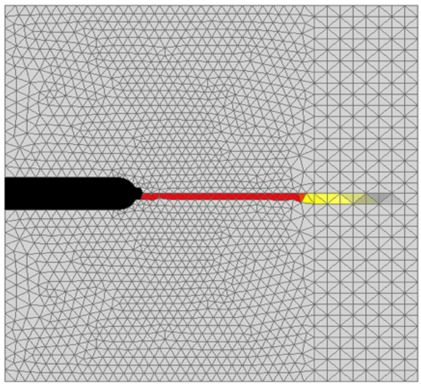

(c)

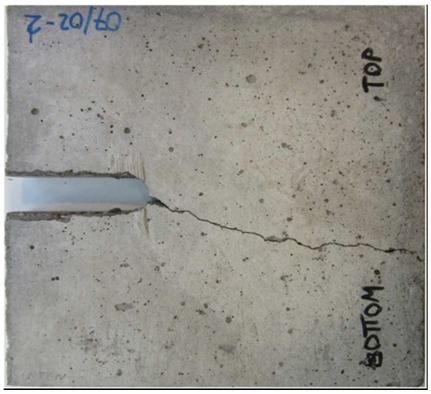

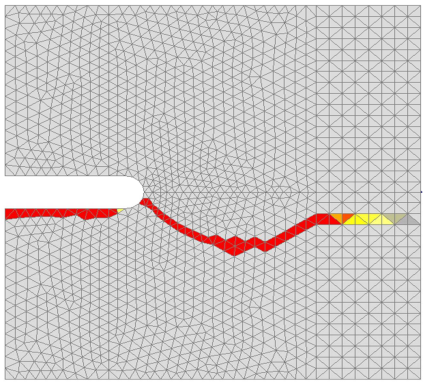

(d)

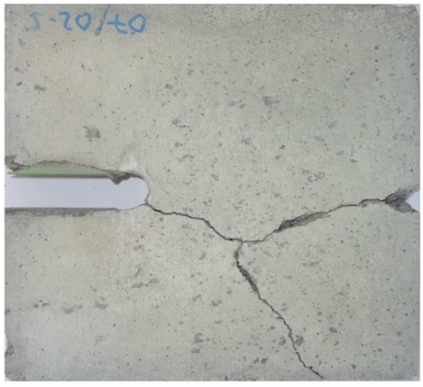

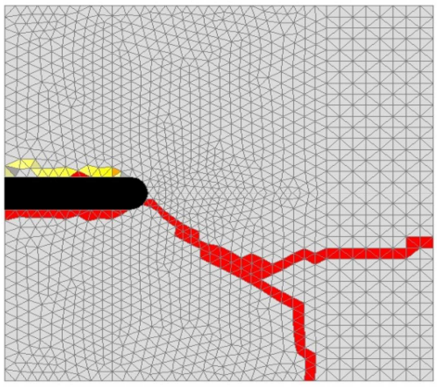

Fig. 8.20 Experimentally and numerically predicted crack patterns in terms of max. principal strains for: (a) quasi-static loading, (b) loading rate 0.035 m/s, c) 1.40m/s and (d) 4.30 m/s (red=critical crack opening of 0.20 mm)

(a)

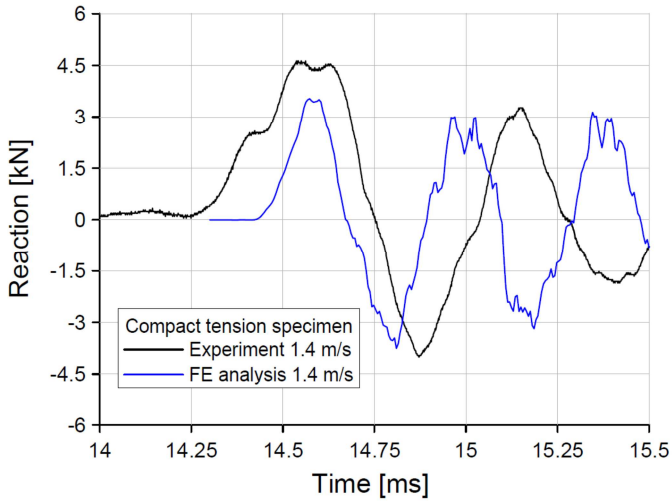

(b)

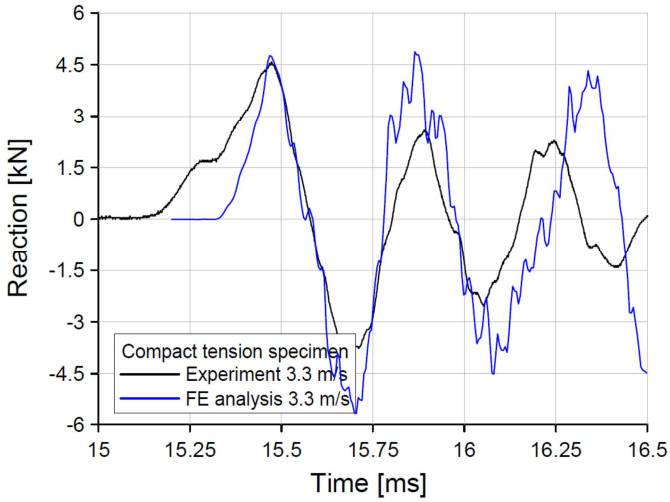

(c)

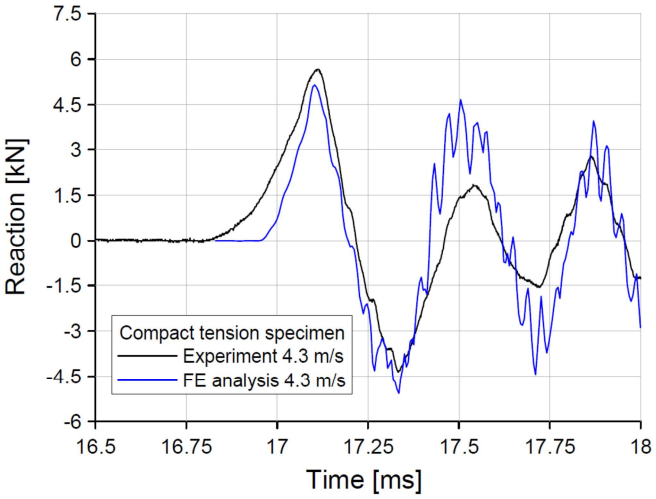

Fig. 8.21 Measured and numerically predicted Reaction-time response for displacement rates: (a) 1400 mm/s, (b) 3300 mm/s and (c) 4300 mm/s

Strain rate $d\varepsilon/dt$ given in Table 8.10 is computed from maximum principal strain time history diagram (see Fig. 8.22) at instant just before the tensile strength is reached. On the other hand, crack opening rate dw/dt is calculated from strain rate corresponding to localization of crack (softening), i.e. $dw/dt = (d\varepsilon/dt)h$, where h is the regularization parameter (equivalent element size) used in crack band approach to ensure mesh objective dissipation of energy (Bažant et al. 1983). As can be seen from Table 8.10, the crack opening rate approximately follows loading (displacement) rate, whereas, the strain rate increases much slower.

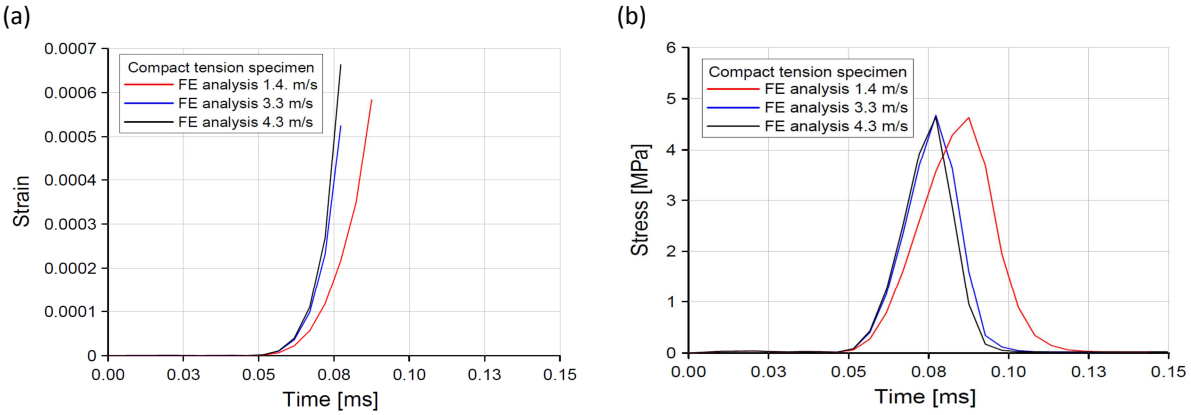

Fig. 8.22 Maximal principal strain and stress in the finite element where the crack is initiated

In Fig. 8.23, DIFs for tensile strength and fracture energy, computed from numerical results, are shown as a function of loading rate together with those computed directly from uniaxial rate dependent constitutive law. As can be seen, the tensile strength follows approximately the rate dependent constitutive law (Ožbolt et al. 2001, 2006). On the contrary fracture energy computed does not; actually it is almost independent of the strain rate. The reason for this could be the fact that, due to inertia forces at the crack tip, the part of the energy is consumed by damage that takes place before the crack is localized.

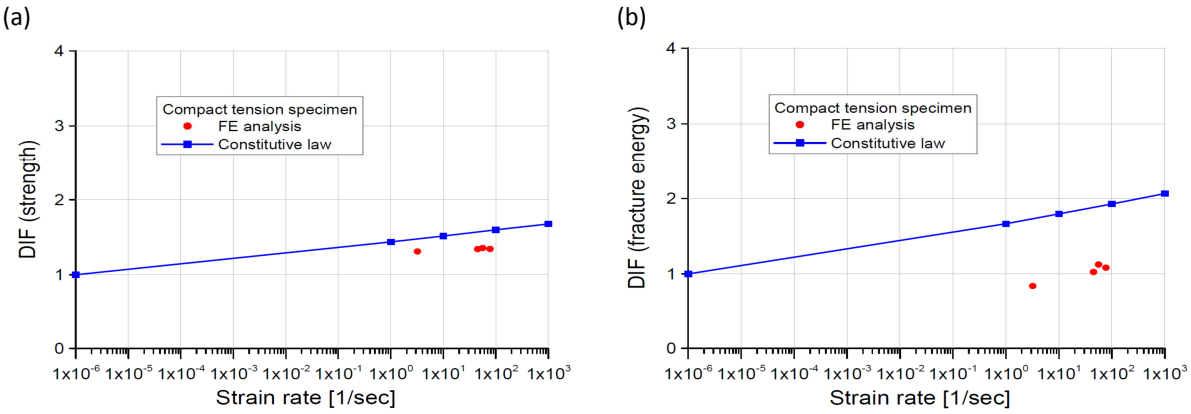

Fig. 8.23 DIF for tensile (a) and fracture energy (b) of concrete: measured in the finite element and resulting from the rate dependent constitutive law (microplane model)

In Fig. 8.24, DIFs for reaction force obtained from experiments and simulations are plotted together with normalized tensile strength obtained from constitutive law. As can be seen, normalized reaction

force increases linearly up to strain rate of approximately $50\ s^{-1}$, and there is a nice match up with normalized tensile strength within this range. As is obvious, reaction force is controlled by the rate dependent constitutive law in this range of strain rate. On the other hand, there is a progressive increase in normalized reaction force for higher strain rates (beyond $50\ s^{-1}$). Based on numerical results, it can be concluded that this progressive increase cannot be attributed to the tensile strength and fracture energy, which actually exhibit no progressive increase (see Fig. 8.23). As also discussed in detail by (Ožbolt et al. 2011a) this progressive increase is controlled by structural inertia. Meanwhile, it is noteworthy to point out that crack branching is observed for strain rates higher than $50\ s^{-1}$ both numerically and experimentally. Based on this observation it can be concluded that structural inertial forces are responsible for not only progressive increase in resistance but also crack branching.

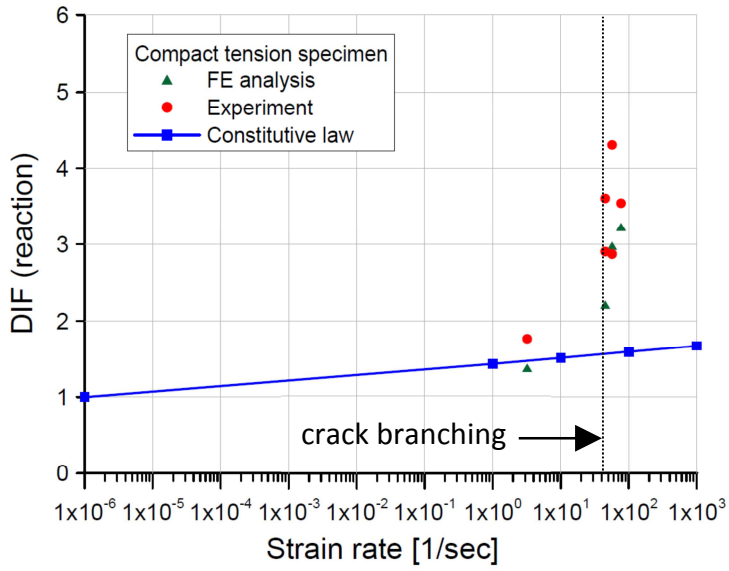

Fig. 8.24 DIF for reaction, predicted experimentally and numerically and compared with DIF for tensile strength of concrete from the rate dependent constitutive law (microplane model)

8.3 Projectile Penetration

8.3.1 Introduction

The response of target materials to projectile impact depends on (see (Cargile 1999))

- the impact conditions (velocity and projectile orientation relative to the target)
- characteristics of the projectile (geometry, mass, and strength)
- the properties of the target (dimensions and mechanical properties)

Although empirical and analytical approaches are available, numerical methods are best to handle various projectile penetration problems. In this respect, a successful numerical tool must account for the geometry of the target, large finite strains and deflections, strain rate effects, work hardening, heating or frictional effects, and the initiation and propagation of fracture.

For impact velocities less than $1000\ \mathrm{m/s}$, the impact event will generally involve conditions where the ratio of impact pressure to projectile strength is less than or approximately equal to one and the ratio of impact pressure to target strength is much greater than one. The projectiles should sustain only slight deformations, but the target will undergo significant deformations where the strength and compressibility of the materials play an important role.

Perforation is the complete piercing of a target with finite thickness by the projectile. This event includes the formation of the impact crater, may include the tunneling phase, and then an exit condition that will include the formation of an exit crater. All of these phases involve formation of cracks, plastic deformation as well as fragmentation and pulverization. From the perforation experiments performed by (Cargile 1999) on plain concrete slabs of different thicknesses it has been concluded that the modes of failure include combinations of brittle fracture, radial cracking and fragmentation only.

To test the performance of new 3D explicit finite element research code at very high loading rates series of numerical simulations have been performed for some of the mentioned projectile perforation experiments documented in (Cargile 1999). Quality of the results is assessed in terms of

- shape of the impact and exit craters
- projectile exit velocities
- projectile deformation
- formation of the radial cracks on the rear surface
- formation of the failure cone and fragmentation
- frictional heating and temperature distribution

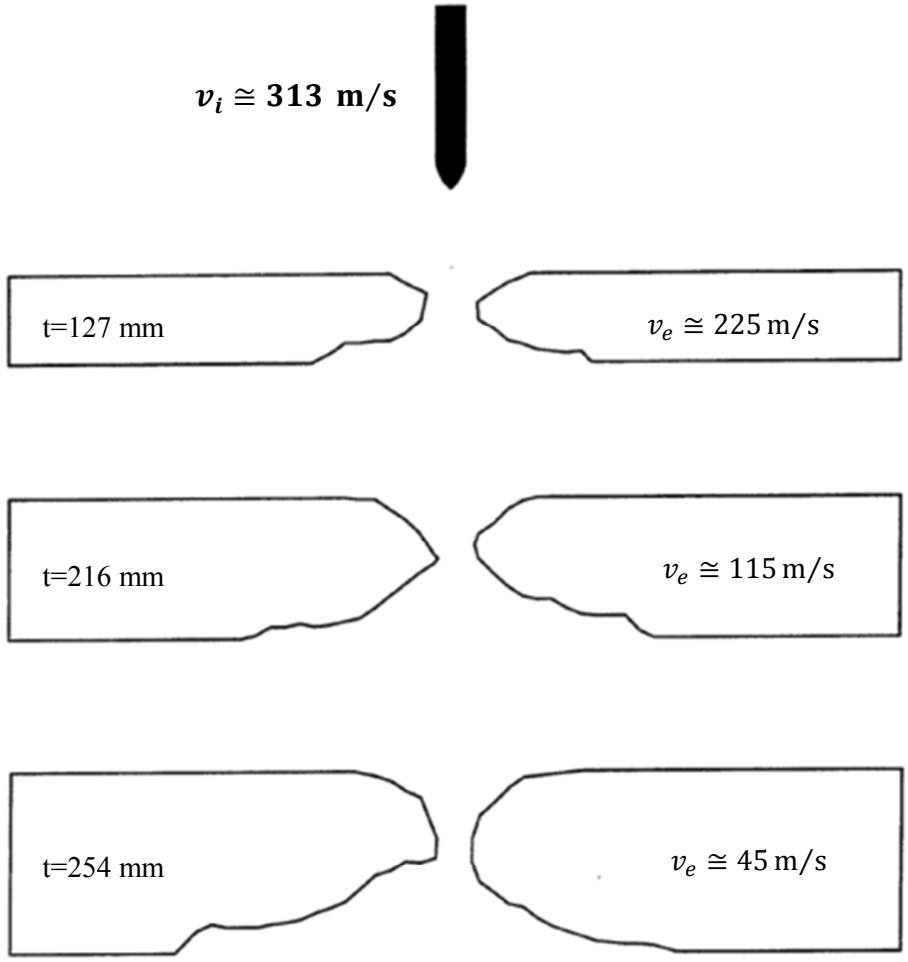

Fig. 8.25 Crater profiles for different slab thicknesses
together with corresponding exit velocities (Cargile 1999)

8.3.2 Perforation Experiments

The targets used in perforation experiments were circular slabs made of plain concrete (WES5000) having a nominal unconfined compressive strength of about 38 MPa. Circular slabs had a diameter equal to 30 times the projectile diameter to prevent boundary effects to pollute experimental results. Slabs of thicknesses 127 mm, 216 mm, 254 mm and 284 mm have been perforated during experiments.

Ogive-nose shaped projectiles of about 2.3 kg have been used during experiments. The diameter and length/diameter ratio of the projectiles was, respectively, 50.8 mm and 7. Projectiles were casted from 4340 steel rods and inner cavity of them was filled with sand. In all experiments projectile had an impact velocity of approximately 313 m/s with angle-of-obliquity less than 1 degree. During the experiments shape of the impact and exit craters after perforation together with corresponding exit velocities have been documented (see Fig. 8.25).

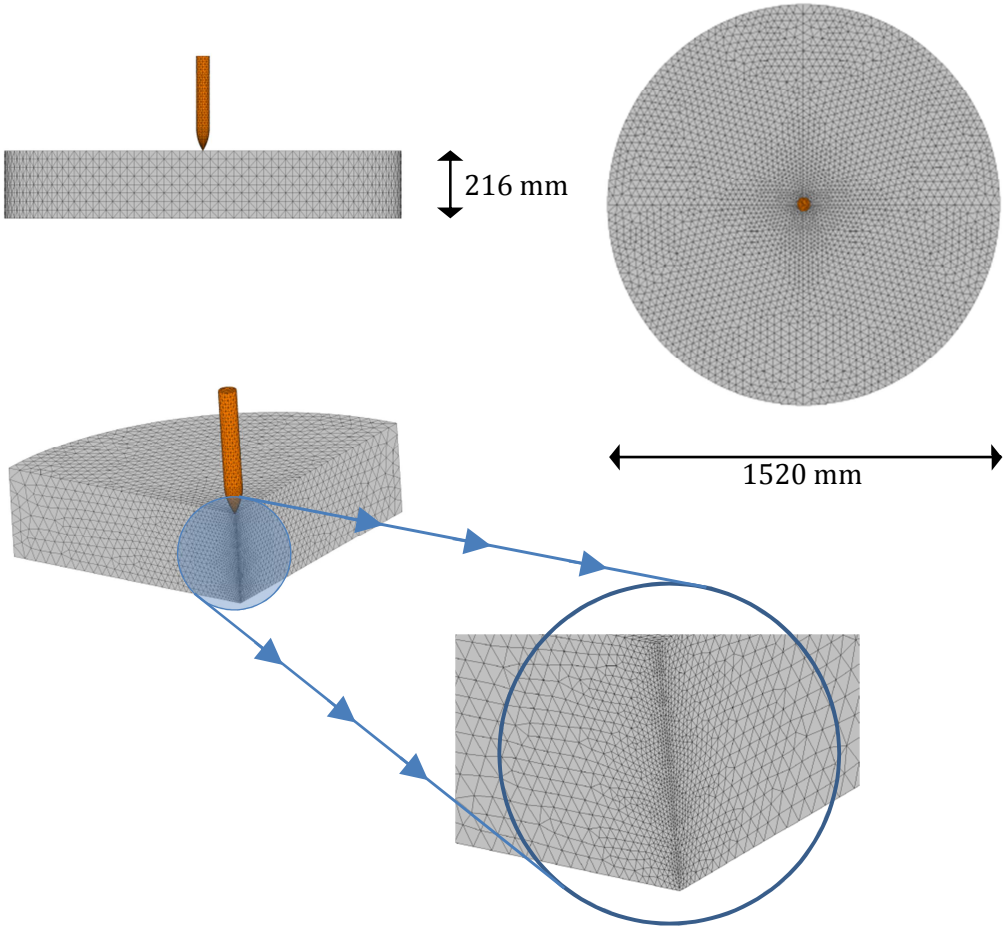

Fig. 8.26 Discretization of CS216

8.3.3 Numerical Simulations

8.3.3.1 Introduction

Finite element simulations have been performed for slab thicknesses $127\ \text{mm}$, $216\ \text{mm}$ and $254\ \text{mm}$. Circular slab and projectile have been discretized by standard linear tetrahedral finite elements (see Fig. 8.26 and Fig. 8.27). Simulations have been performed in three dimensions with full model without relying on any artificial symmetry boundary conditions. Total number of nodes and elements for each discretization used are listed in Table 8.11. Impact velocity has been defined as an initial condition on projectile. The nodes located on the sides of circular slab have been restrained in all directions. Gravity field has been ignored during calculations. No ad-hoc damping at global node level has been prescribed. Time increment has been set equal to 35% of the value computed based on stability criteria (CFL condition). Bulk viscosity pressure has been computed and added to the stress tensor coming from material model to prevent elements from collapsing down due to high velocity gradients. Element deletion technique based on maximum principal strain failure criteria has

been used to handle highly distorted elements. Failure value was set as equal to 1.0. Justification of this failure value will be made in subsequent subsection. Deleted elements are colored in yellow in figures presented. To accelerate contact search and hence the overall contact calculations use of contact sphere has been made (see section 7.3.2.1.2). 2-pass contact algorithm was preferred to tighten up the enforcement of contact constraints. Reactions, contact forces (Lagrange multipliers), energies and motion of one node located on projectile close to the nose have been monitored in all simulations. To simplify notation we will denote 127 mm circular slab, 216 mm circular slab and 254 mm circular slab as, respectively, CS127, CS216 and CS254 from this point onward.

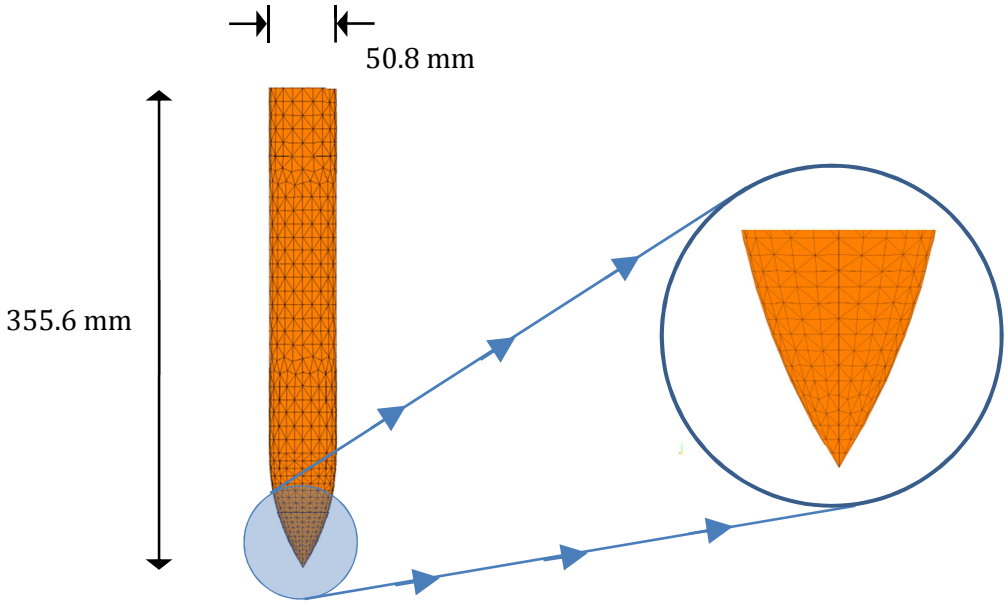

Fig. 8.27 Discretization of projectile

Rate dependent microplane material model has been used for concrete. In the model discrete cracks have been treated within the framework of continuum mechanics as smeared (crack strain) over the element volumes. Cracking strain value was set equal to 0.01. Cracked elements are colored in purple in figures presented. Mesh objectivity of the results is ensured by employing crack band regularization. On the other hand for steel case and sand filler Saint-Venant Kirchhoff hyperelastic material model is adopted assuming that projectile would undergo little or no deformation during perforation. Corresponding mechanical and thermal material properties are listed in Table 8.12 and Table 8.13.

Table 8.11 Total number of nodes and elements for circular slabs and projectile

	CS127	**CS216**	**CS254**	**projectile**
# of nodes	15249	19238	23564	2058
# of elements	73039	95892	119215	8864

A parametric study has been conducted in order to investigate the significance of rate dependency of concrete and friction (between circular slab and projectile) on the results. For this reason three sets of simulations, described in Table 8.14, have been carried out.

Table 8.12 Material properties (mechanical)

Material	Density [kg/m^3]	Elastic modulus [GPa]	Poisson's ratio	Compressive strength [MPa]	Tensile strength [MPa]	Fracture energy [J/m^2]
Concrete	2400	33	0.18	38	2.9	90
Steel	8010	200	0.3	-	-	-
Sand	1580	33	0.18	-	-	-

Table 8.13 Material properties (thermal)

Material	Heat capacity [J/kg/K]	Conductivity [W/m/K]	Diffusivity [m^2/s]
Concrete	900	0.2	9.3E-8
Steel	477	46.6	1.2E-5
Sand	900	0.2	1.4E-7

Table 8.14 Simulation sets

	SET-I		SET-II		SET-III	
	Rate effects	**Friction**	**Rate effects**	**Friction**	**Rate effects**	**Friction**
CS127	ON	ON	ON	OFF	OFF	OFF
CS216	ON	ON	ON	OFF	OFF	OFF
CS254	ON	ON	ON	OFF	OFF	OFF

8.3.3.2 Results

8.3.3.2.1 Exit Velocities

In Fig. 8.28, velocity time histories of a node located around the projectile nose are given for all simulation sets. Processing data from Fig. 8.28, a diagram showing variation of exit velocity with respect to slab thickness is obtained (see Fig. 8.29 and Table 8.15). As can be seen from Fig. 8.28, projectile velocity decreases in time in all simulations. Projectile perforates the target in each one of the simulations and has a constant mean residual velocity afterwards (exit velocity) as has already been pointed out in (Cargile 1999).

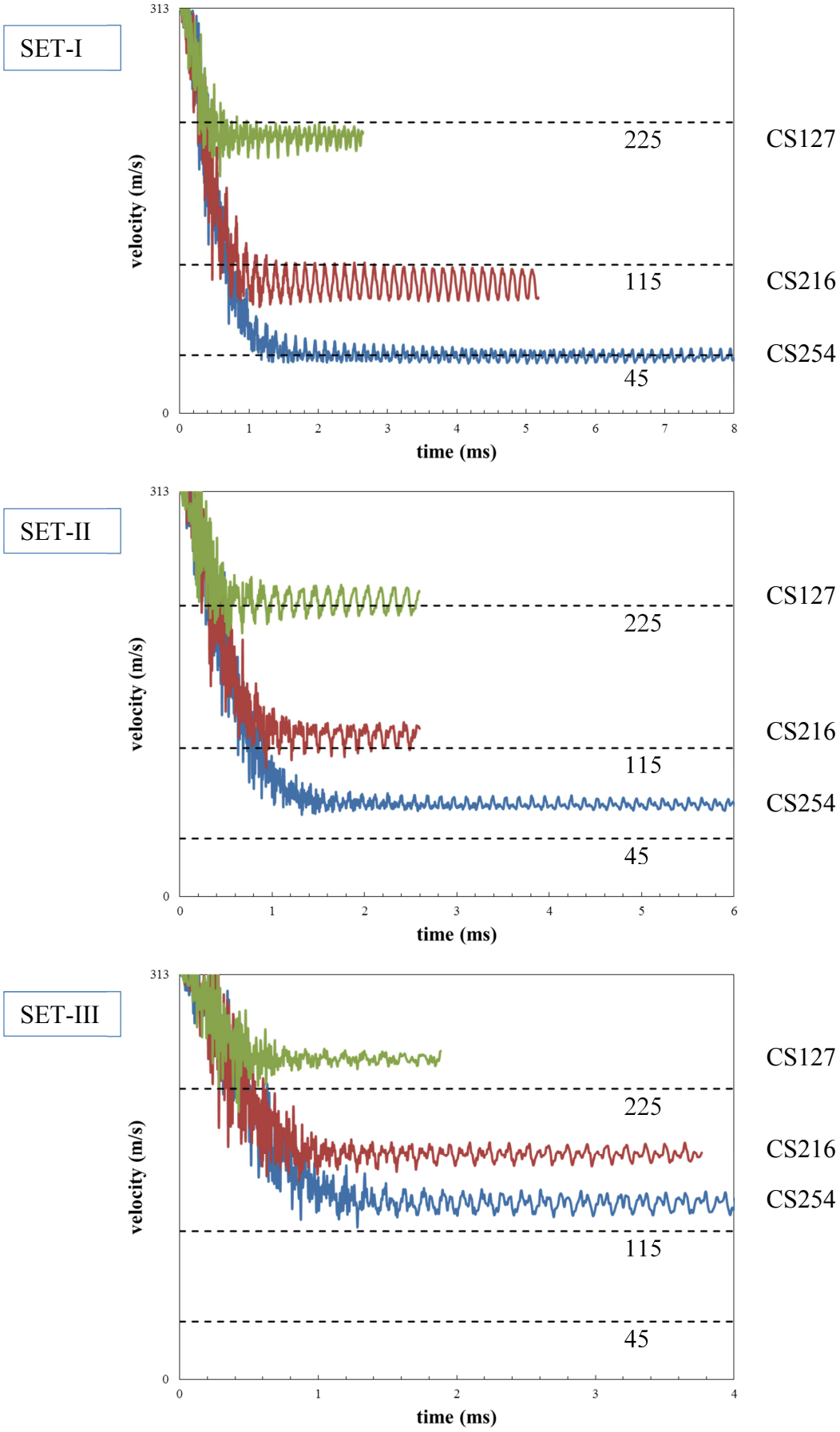

Fig. 8.28 Velocity time histories for all simulation sets together

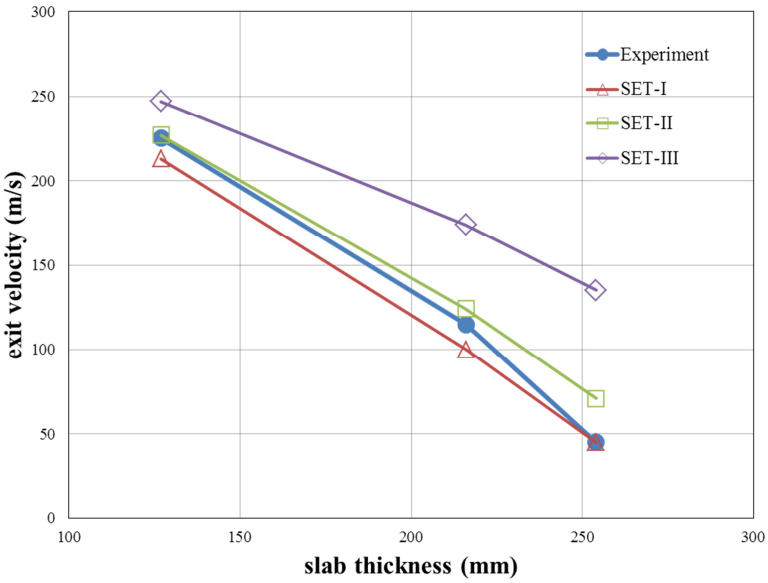

Fig. 8.29 Exit velocity versus slab thickness diagrams for all simulation sets together (see Fig. 8.28 and Table 8.15)

Table 8.15 Exit velocities (in m/s) for all simulations sets (see Table 8.14)

	Experiment	**SET-I**	**SET-II**	**SET-III**
CS127	225	213	227	247
CS216	115	100	124	174
CS254	45	45	71	135

Some remarkable conclusions can be drawn out of Fig. 8.29. As can be seen, for SET-I (rate:on; friction:0.5) and SET-II (rate:on; friction:0.0) exit velocities are very close to experimentally measured values for all range of slab thickness (see Table 8.15). It can then be concluded that rate dependent microplane model, in combination with bulk viscosity effects, is performing perfectly well for also very high loading rates. Therefore one can state that current model for rate dependency is adequate for impact velocities up to $1000\ \mathrm{m/s}$ and can be used conveniently without any modification. On the other hand, results obtained from SET-III (rate=off; friction=0.0) indicate that simulations performed without taking rate effects into account is not objective. Rate effects are very important for dynamic fracture of concrete and therefore must be properly accounted for. Friction also has a role in structural response, although not as much as rate effects do. Based on the current set of simulations, we observe that experimental results fall into the envelope defined by SET-I and SET-II. In general friction coefficient is also rate and temperature dependent and one might expect some improvements if those effects are taken into account properly. But it should be kept in mind that realistic prediction of these dependencies is very difficult to achieve.

In addition, we observe that exit velocity becomes very sensitive to rate effects as the thickness of slab is increased. While the difference between exit velocities for CS127 is only $20\,\mathrm{m/s}$, it increases up to $64\,\mathrm{m/s}$ for CS254, more than three times, from SET-II to SET-III. This can be explained by the time elapsed during perforation up until to the point where mean projectile velocity becomes constant (exit velocity). Note that beyond this point there are no more significant interactions in between circular slab and the projectile. It is about $0.5\,\mathrm{ms}$ for CS127 and $1.5\,\mathrm{ms}$ for CS254 (see Fig. 8.28). It is obviously much larger for thicker slabs and due to this fact concrete material has a chance to resist more, i.e. constitutive model is much more involved. That is why rate effects become much more apparent. Therefore thicker slabs build up a very challenging problem for the constitutive model utilized. And as we can see from Fig. 8.29 and Table 8.15, the exit velocity for CS254 obtained from SET-I is just on top of experimental value, and that obtained from SET-II is close to it fair enough. On the other hand, from the diagrams plotted for SET-I and SET-II we conclude that exit velocity changes only a little bit in case the friction is present (or not). While the difference between exit velocities for CS127 is $14\,\mathrm{m/s}$, it increases up to only $26\,\mathrm{m/s}$ for CS254. Obviously friction puts additional resistance to perforation. But as we see it is not as much as rate effects do and not very much sensitive to the thickness of the target.

Table 8.16 Diameters of impact and exit craters for all simulations sets (see Fig. 8.30) together with experimental results

Impact Crater (YZ/XZ)				
Thickness	**Experiment**	**SET-I**	**SET-II**	**SET-III**
127	198	180/169	191/169	202/191
216	227	218/205	218/205	264/248
254	236	204/191	233/218	263/264

Exit Crater (YZ/XZ)				
Thickness	**Experiment**	**SET-I**	**SET-II**	**SET-III**
127	395	332/320	318/305	334/332
216	580	546/616	502/570	615/615
254	715	688/570	688/713	639/641

units in mm

8.3.3.2.2 Crater Profiles

In Fig. 8.31 and Fig. 8.32, impact and exit crater profiles for all simulation sets are presented. Since there exists no symmetry in the problem profiles are given for sections parallel to YZ plane and XZ plane separately. Processing these figures, diagrams for the variation of impact-crater diameter and exit-crater diameter with respect to slab thickness are obtained (see Fig. 8.30). As can be seen from Fig. 8.30, Fig. 8.31, Fig. 8.32 and Table 8.16, impact-crater diameter is more or less the same for CS127, CS216 and CS254 in all simulation sets, i.e. slab thickness has no important role for the formation of impact crater, and it is significantly smaller than the diameter of exit-crater. On the

other hand, exit-crater diameter increases by a considerable amount as the slab thickness is increased. All these results are in very good agreement with experiments (see Table 8.16).

From Fig. 8.31 and Fig. 8.32, we realize that shape of the impact and exit craters does not change too much depending upon whether rate effects are included or not. That means that failure mode is not a primary function of rate-dependency but of global structural inertia forces which are present in all of the simulations. Remember that we have drawn a very similar conclusion out of the results obtained from the numerical simulation of CTS test in previous section (see section 8.2). If the crater profiles obtained by experiments (see Fig. 8.25) documented in (Cargile 1999) are compared with numerical results (see Fig. 8.31 and Fig. 8.32), we observe that for all simulation sets the diameter of the hole created by projectile is slightly larger than the value corresponding to experiment. It has already been pointed out in (Cargile 1999) that during posttest examination of the concrete slabs, material along the penetration path was found to be very weak and easily breakable. This material has stayed there just because of the presence of aggregate interlock or some other frictional mechanisms. In numerical simulations no such mechanism is explicitly incorporated. Therefore during numerical simulations this damaged material is also removed due to the motion of corresponding nodes. Introduction of some ad-hoc damping at global node level might help to slow down these nodes and keep the damaged material around the projectile in place throughout the simulation.

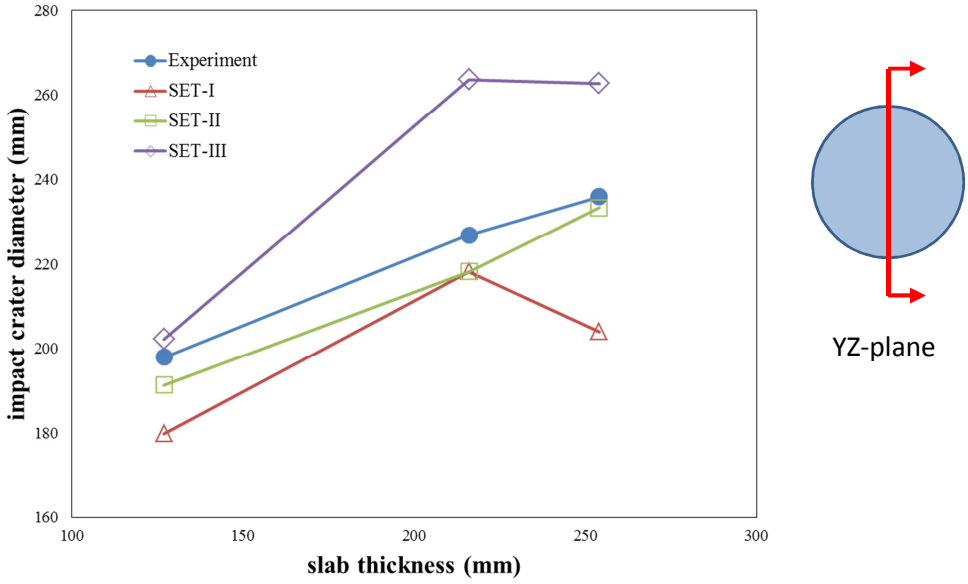

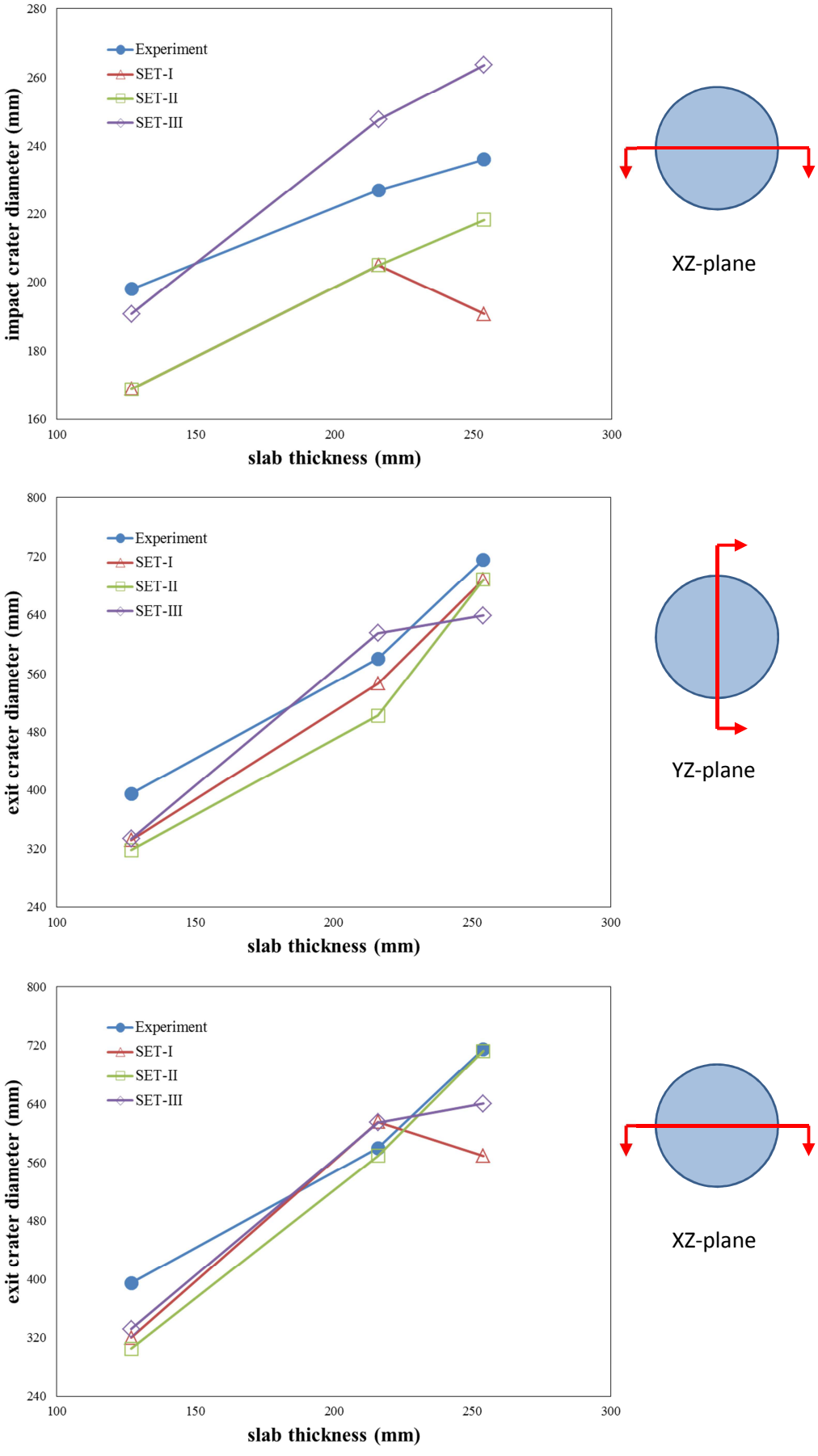

Fig. 8.30 Impact and exit crater diameters for all simulations sets

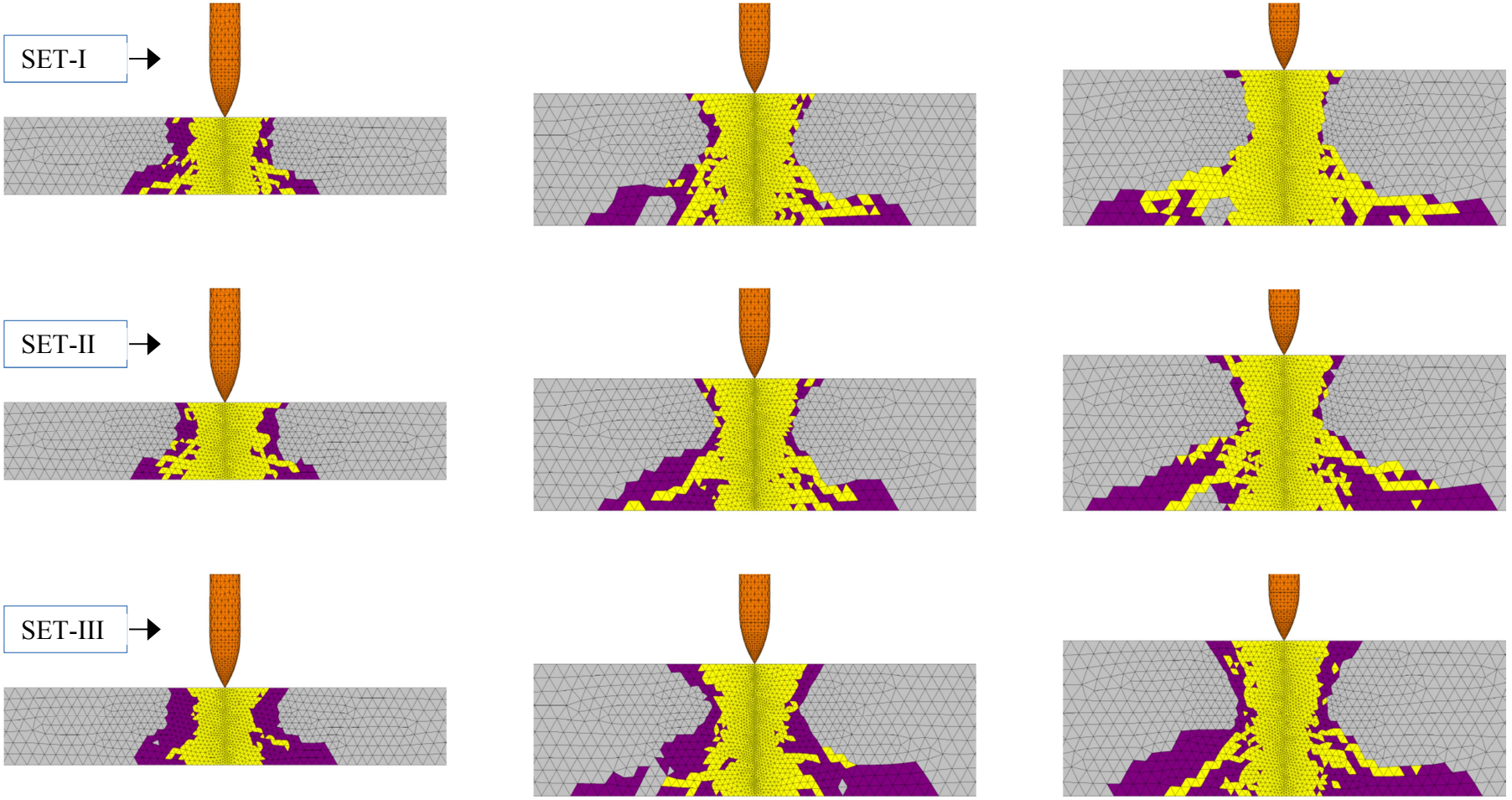

Fig. 8.31 Crater profiles (YZ-plane) for all simulation sets

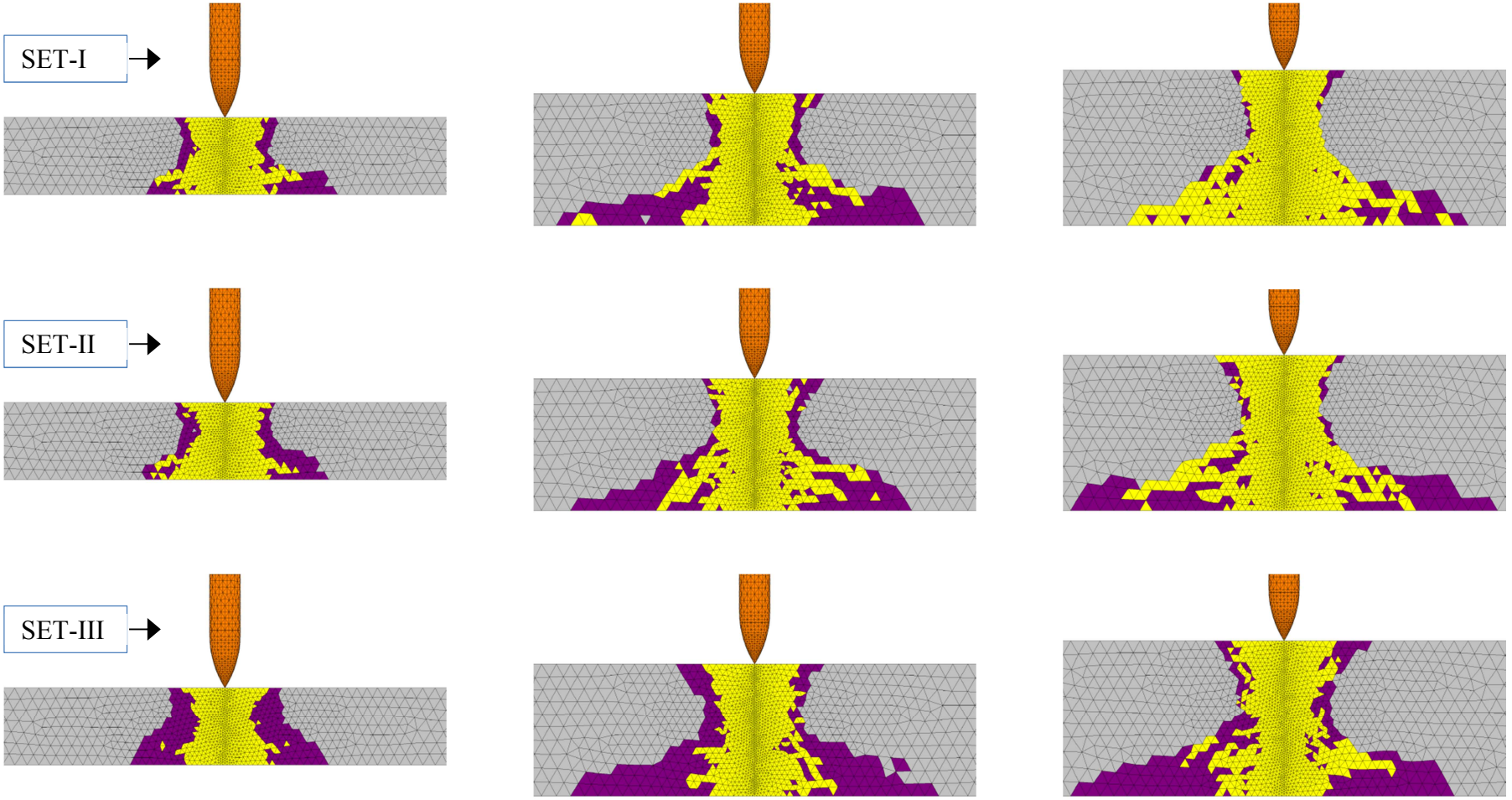

Fig. 8.32 Crater profiles (XZ-plane) for all simulation sets

8.3.3.2.3 Radial Cracks, Shear Cracks and Fragmentation

As soon as the compressive loading waves created by impact loading reaches the rear surface of the target and reflected back as a tensile loading wave, cracks start to form and propagate in radial direction. As the projectile penetrates deeper into the target, shear cracks might form at a certain depth depending upon the thickness of the target. These shear cracks then start to propagate and as soon as they reach to the back surface of the target the so-called failure cone is formed. Full formation of the failure cone corresponds to the point where target object loses its resistance against penetration. As can be seen from Fig. 8.33 and Fig. 8.34, for CS127 of SET-I formation of the radial cracks can be very well identified. However for this thin slab failure cone does not form completely and therefore slab resists to penetration with its full depth. Unfortunately even full depth is not enough to slow down the projectile and projectile perforates the target with a very high constant mean residual velocity of about $213\ \mathrm{m/s}$ (see Table 8.15). As the failure cone is not formed during perforation, there is not much fragmentation (see Fig. 8.35). On the other hand, for CS216 and CS254 for SET-I radial cracks as well as failure cone form and can be very well identified (see Fig. 8.36, Fig. 8.37, Fig. 8.39 and Fig. 8.40). For CS216, failure cone fully forms at penetration depth of about $198\ \mathrm{mm}$ (see Fig. 8.36), whereas for CS254 it takes place at penetration depth of about $220\ \mathrm{mm}$ (see Fig. 8.38). In other words these two slabs do not resist the penetration with full depth. As the failure cone fully forms for CS216 and CS254, there are considerable amount of fragments flying out from the rear surface of the target (see Fig. 8.38 and Fig. 8.41). In both cases target is pierced by the projectile and projectile has a certain constant mean residual velocity afterwards (see Table 8.15).

In (Cargile 1999), slabs of thickness $284\ \mathrm{mm}$ (CS284) have been also tested against penetration in order to identify perforation limit under given impact conditions. It has been found that projectile was not able to perforate the target in that case. We have added CS284 to simulation SET-I and carried out one additional simulation in order to see what will come out. As can be seen from Fig. 8.42, projectile stops at a penetration depth of about $150\ \mathrm{mm}$ for CS284. Therefore the perforation limit has to be somewhere in between $254\ \mathrm{mm}$ and $284\ \mathrm{mm}$ in full accordance with (Cargile 1999). Note that even if there was no perforation for CS284, target specimen has experienced considerable amount of damage during penetration (see Fig. 8.42).

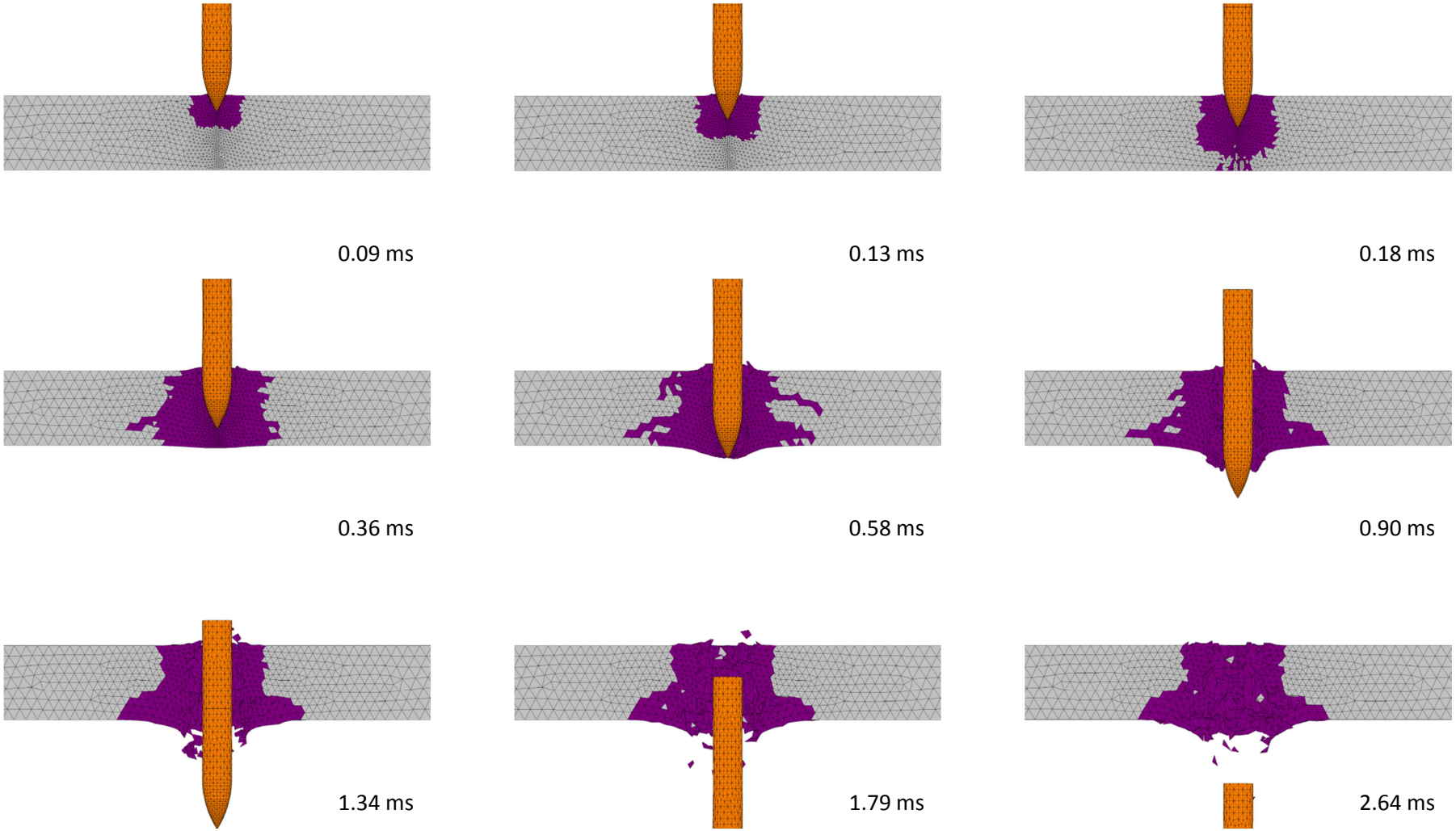

Fig. 8.33 Perforation process from section view for CS127 for SET-I

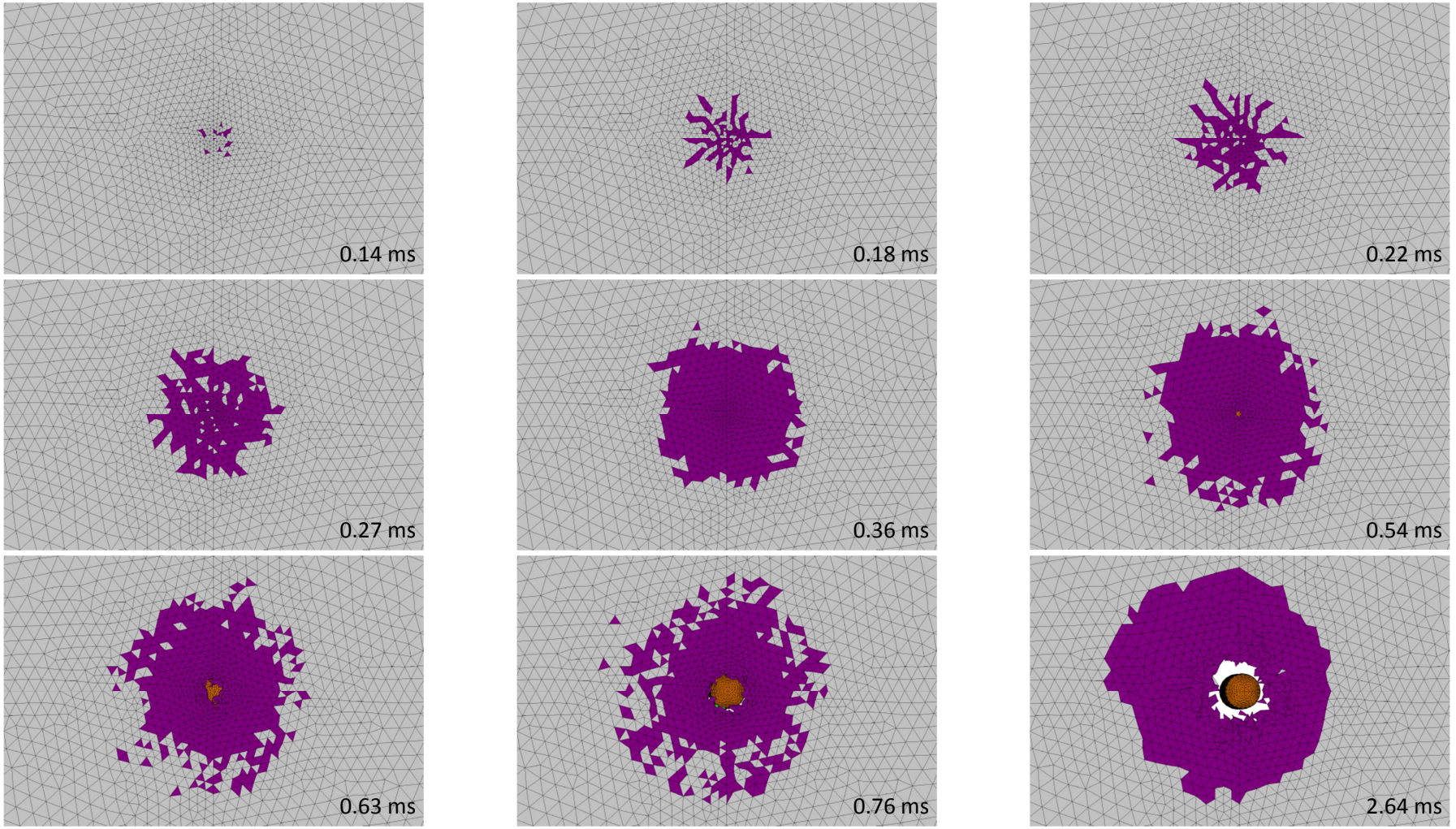

Fig. 8.34 Perforation process from back surface for CS127 for SET-I

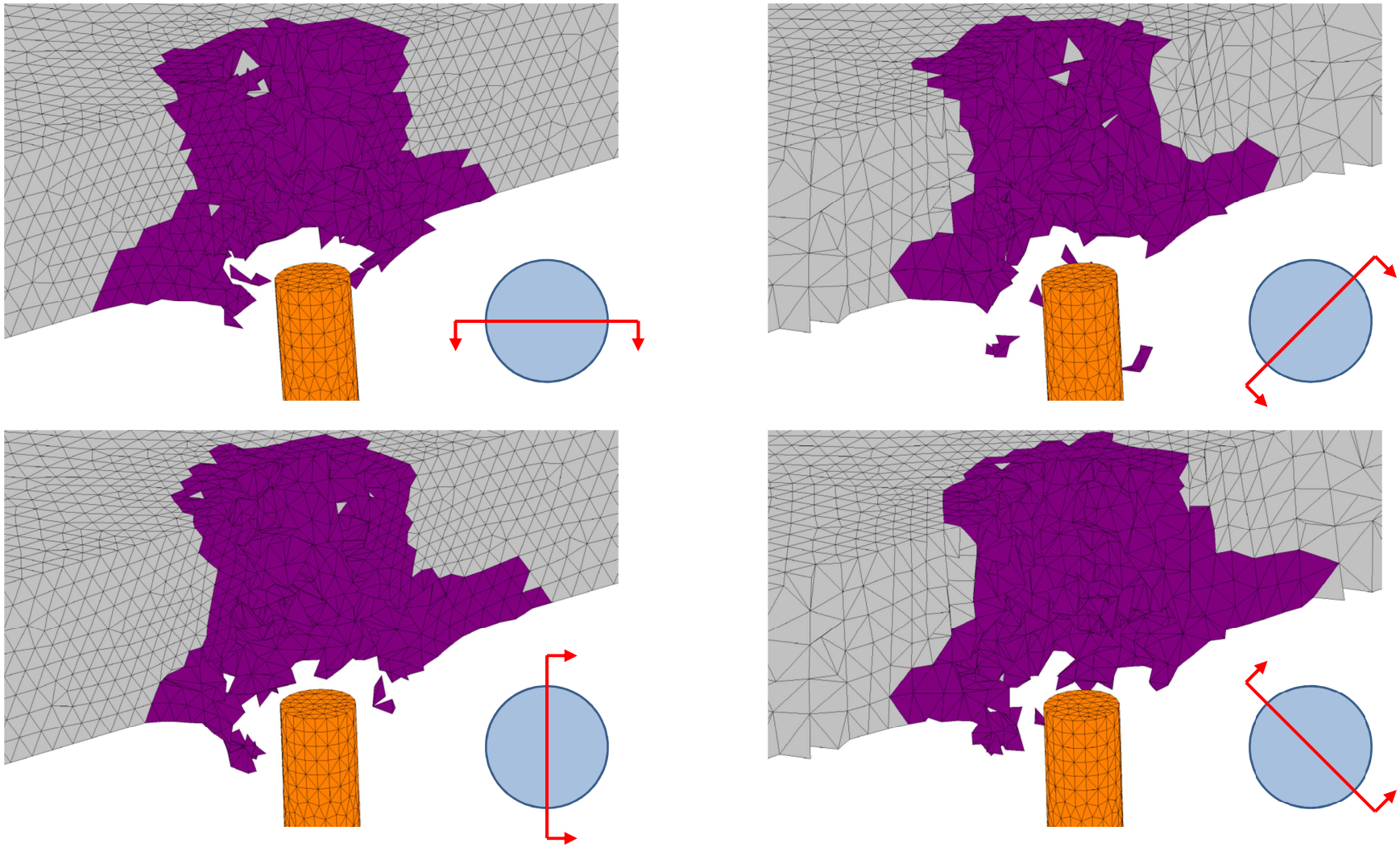

Fig. 8.35 Fragmentation patterns for CS127 for SET-I. Section views for different orientations

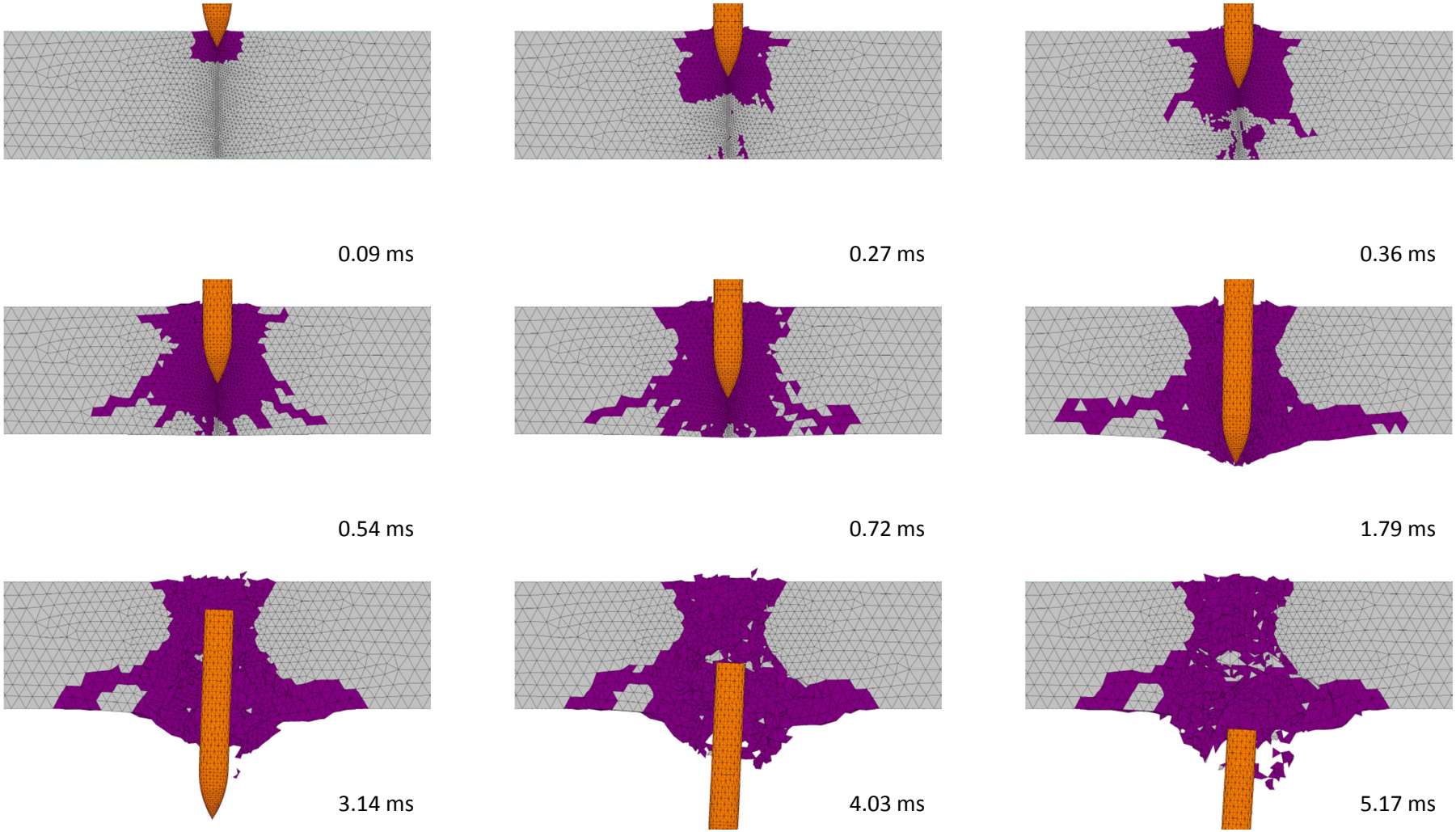

Fig. 8.36 Deformed shape section view for CS216 for SET-I

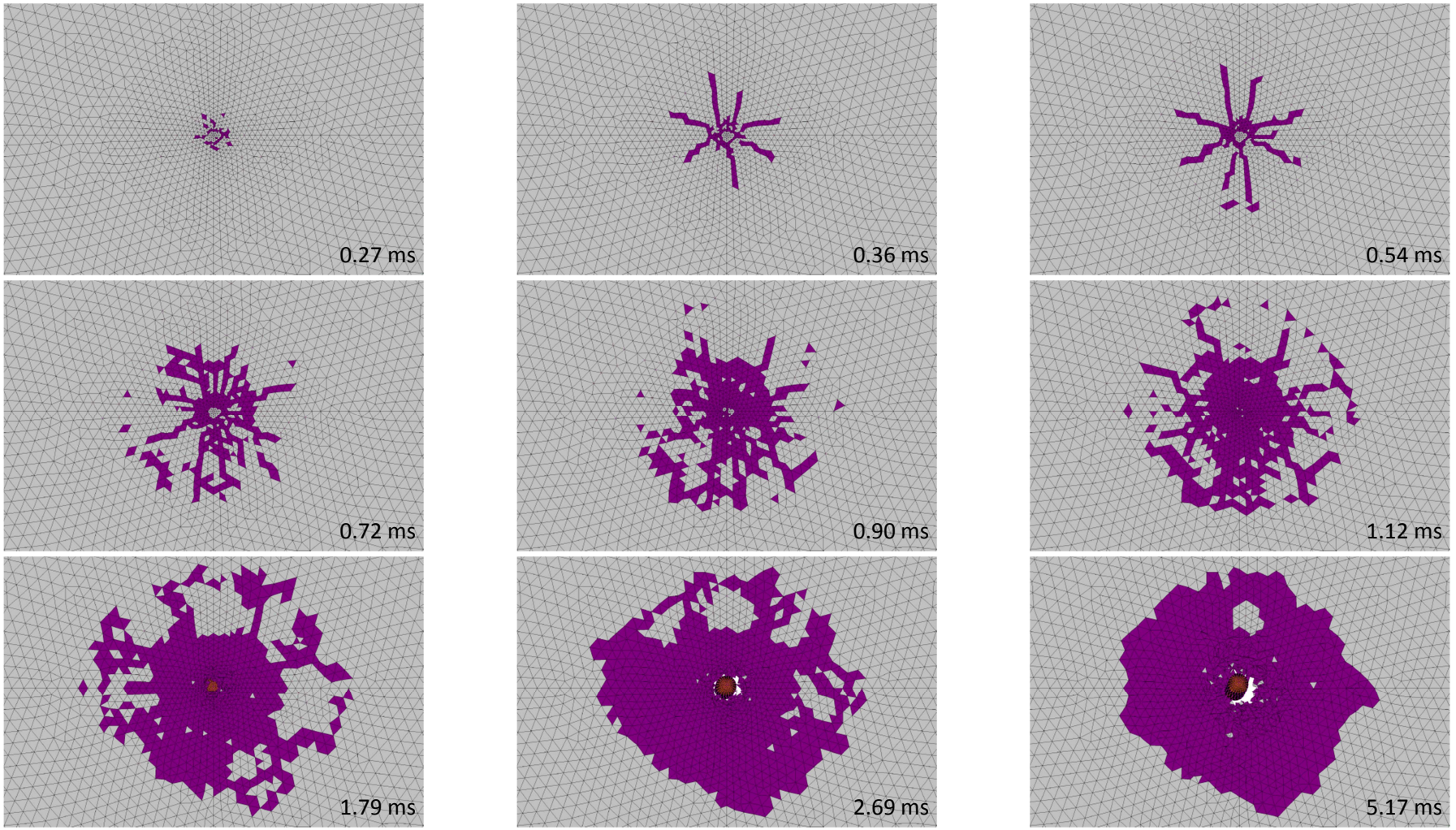

Fig. 8.37 Perforation process from back surface for CS216 for SET-I

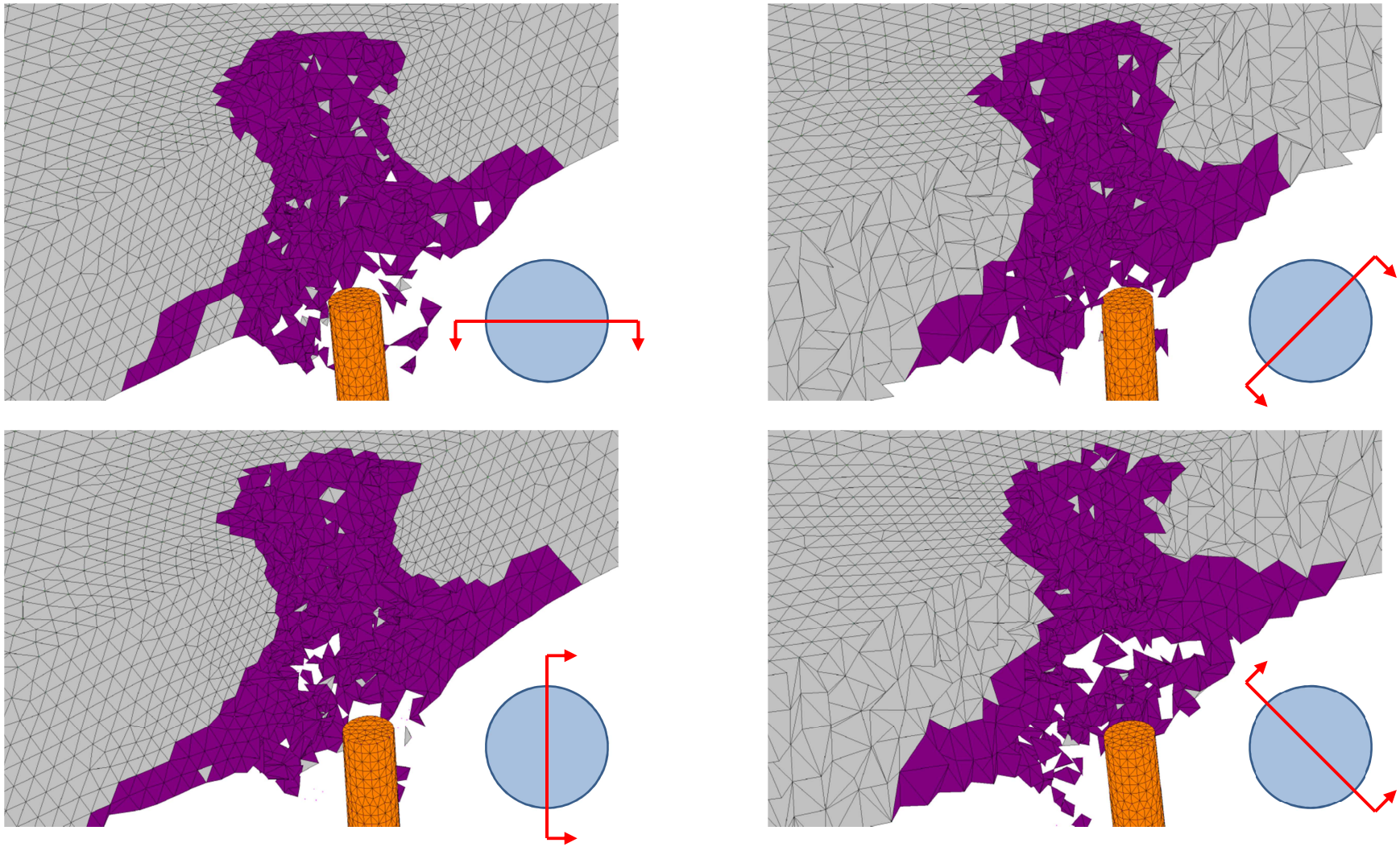

Fig. 8.38 Fragmentation patterns for CS216 for SET-I. Section views for different orientations

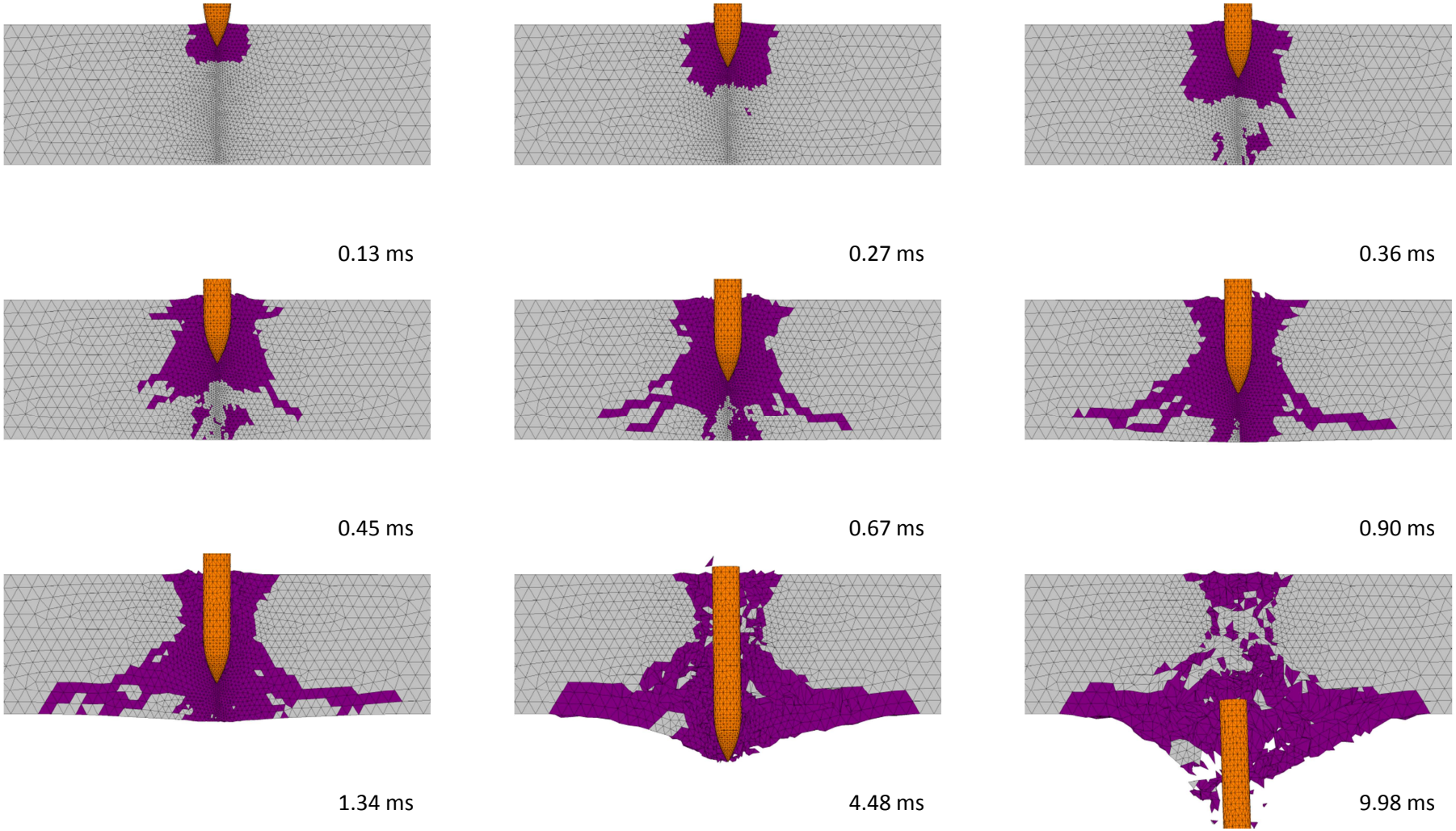

Fig. 8.39 Deformed shape section view for CS254 for SET-I

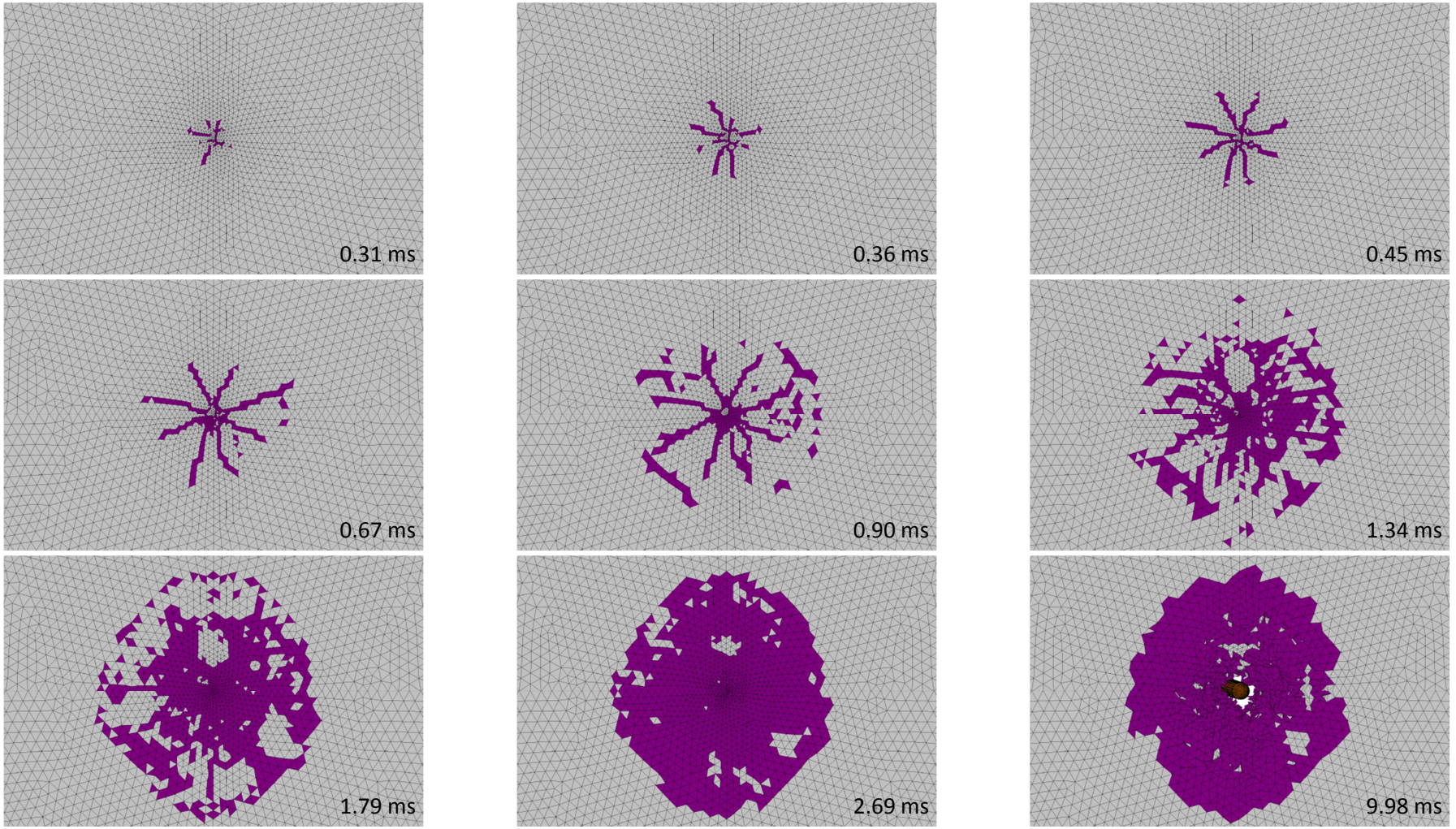

Fig. 8.40 Perforation process from back surface for CS254 for SET-I

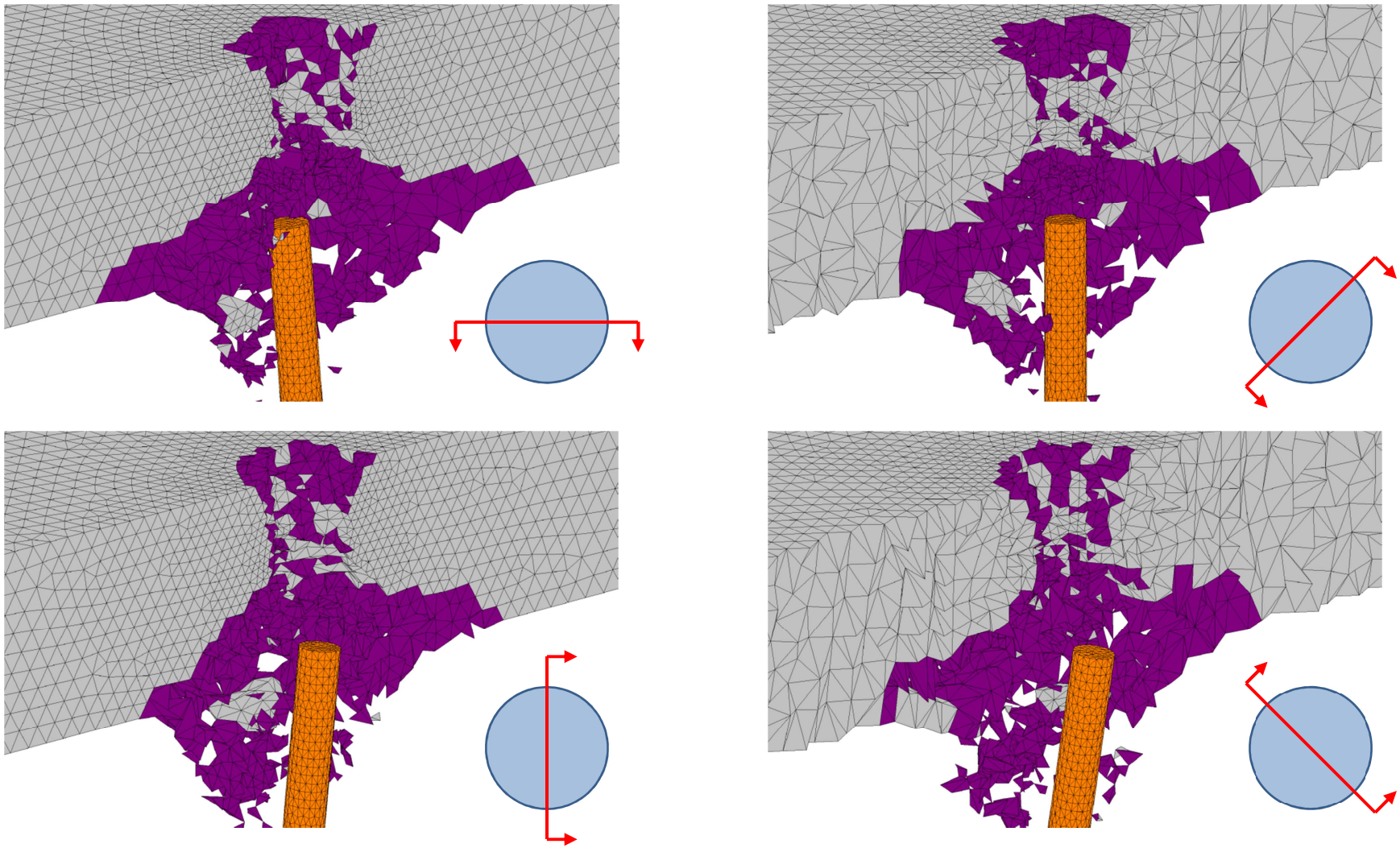

Fig. 8.41 Fragmentation patterns for CS254 for SET-I. Section views for different orientations

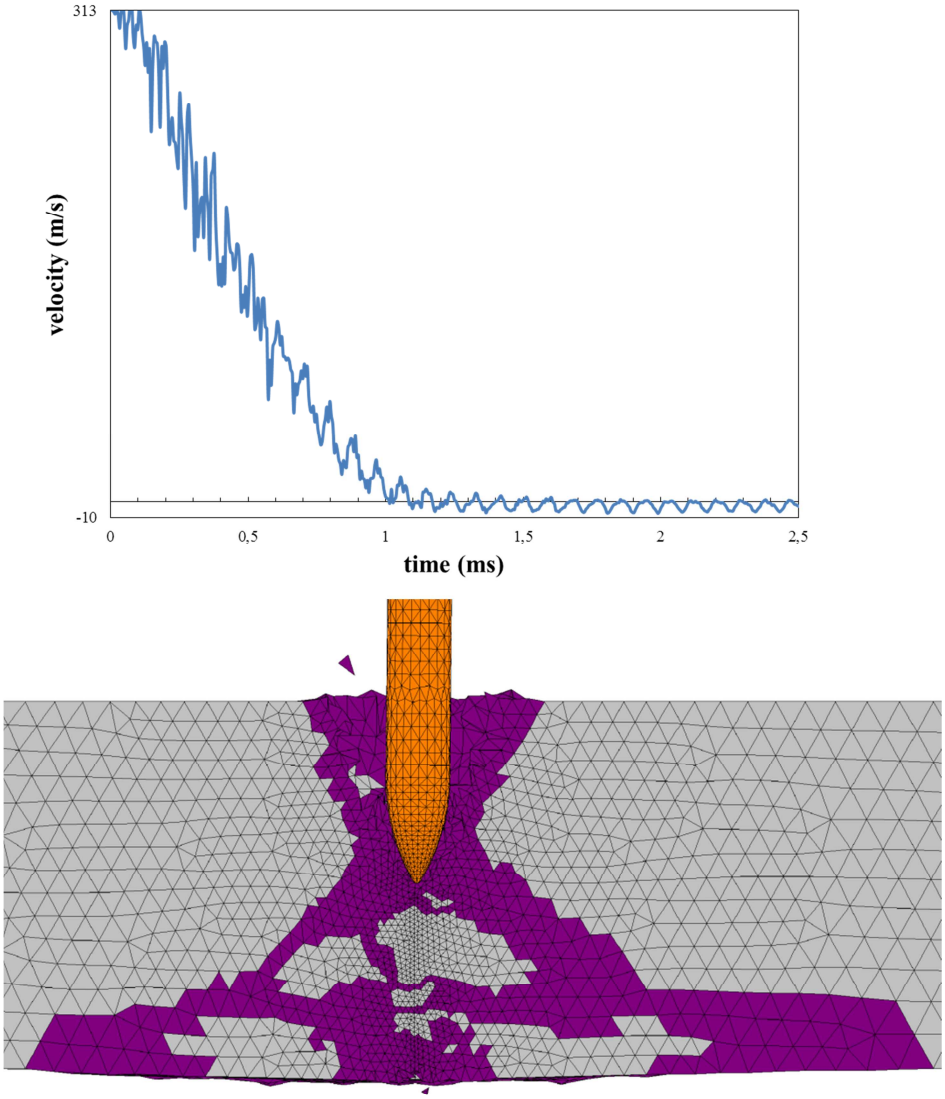

Fig. 8.42 Velocity time history and final deformed shape ($t = 2.68$ ms) for CS284 for SET-I

8.3.3.2.4 Projectile Deformation

In (Cargile 1999), projectile has remained almost undeformed during all perforation tests. But depending upon the thickness of the target specimen, certain level of rotation of the projectile as a rigid body has been observed. As can be seen clearly from Fig. 8.43, we obtain similar results from our numerical simulations too. Projectile is almost undeformed and rotates in each simulation, and as expected the amount of rotation increases with increasing slab thickness.

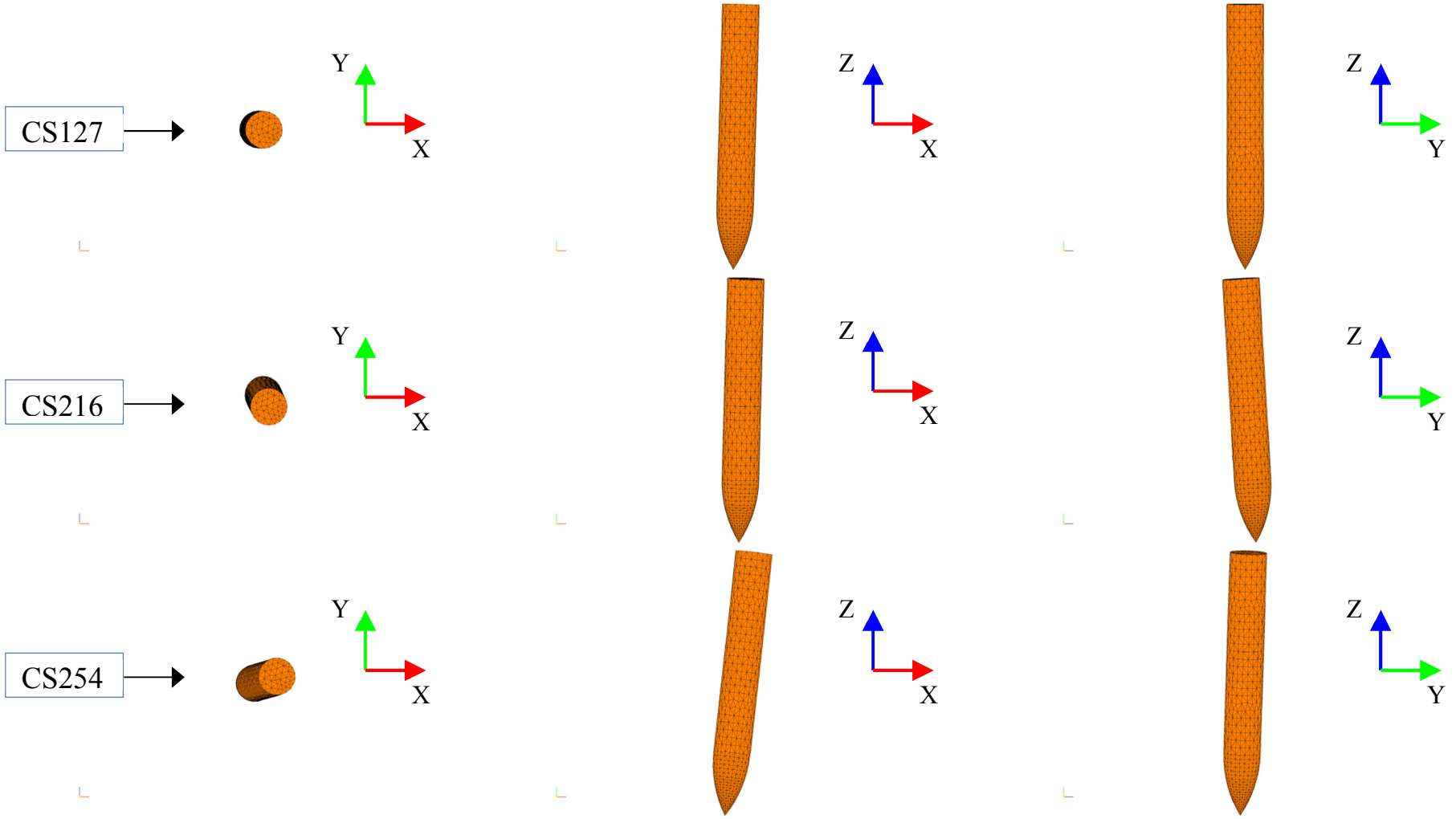

Fig. 8.43 Projectile shape after perforation for SET-I

8.3.3.2.5 Energy Transfer

In contrast to experiments, it is possible to investigate complex energy transfer during penetration events numerically. In Fig. 8.44, energy time history diagrams for SET-I is presented. For CS127 about 47% of total energy is transferred. This energy transfer ratio is 79% for CS216 and 86% for CS254. For CS127, 34% of this transferred energy is used to raise kinetic energy of the slab (KE(S)), 50% is used for concrete deformation and fracture (WE(S)) and 16% is the sum of energy dissipated during frictional sliding and parasitic contact energy stored due to residual gap vectors having possibly both normal and tangential components (WC). These distributions are KE(S)=26%; WE(S)=58%; WC=16% for CS216 and KE(S)=23%; WE(S)=58%; WC=19% for CS254 (see Fig. 8.44).

8.3.3.2.6 Thermal Effects

In the penetration experiments investigated out here, projectile remains essentially undeformed which implies that maximum temperature in the projectile should have been smaller than its melting temperature. It comes out so mainly because of projectile geometry, namely its sharp nose, impact velocity and angle (obliquity), thickness of the concrete slab and of course material properties of projectile and concrete. As has been discussed in section 5.3, concrete mechanical properties are temperature dependent. Level of heating might not be critical for projectile but maybe for concrete. In order to investigate this, set of thermo-mechanical simulations for SET-I (rate:on; friction:0.5) is conducted.

As can be seen from Fig. 8.45 and Fig. 8.46, crater shapes as well as exit velocities do not change much for all range of slab thickness when the temperature effects are accounted for. In Fig. 8.47 temperature contours are given for CS254 for different time instants, whereas in Fig. 8.48 those are presented for the projectile. For CS127, maximum temperatures attained in the slab and projectile are, respectively, $114\ ^0$C(S) and $520\ ^0$C(P). Those values are $95\ ^0\text{C}/144\ ^0$C (S) and $882\ ^0\text{C}/823\ ^0$C (P) for CS216/CS254. As can easily be seen from Fig. 5.7 and Fig. 5.8, even for the maximum temperatures attained, concrete material properties do not change significantly. In addition, in Fig. 8.49 temperature contours are given for projectile corresponding to time 1.17 ms. Different contour plots are given by gradually removing the finite elements located at the outer boundary of projectile (only those who have a surface on the outer boundary). From these contour plots it can be concluded that heat generated due to frictional sliding could propagate into the projectile only by couple of millimeters (around 10 mm) during perforation event. Local temperature increase at a material point is inversely proportional with volumetric heat capacity. As has already been stated in section 6.2, heat flux generated due to frictional sliding is equally distributed between projectile and concrete slab. As can be seen from Table 8.13, steel has a smaller volumetric heat capacity than

concrete. It means that for the same amount of net heat flux local temperature will increase faster in steel than concrete. Moreover, thermal conductivity of steel is orders of magnitude larger than concrete (see Table 8.13). That means that for the same spatial gradient of temperature, larger heat flux will be generated in steel than concrete. The ability of a material to conduct thermal energy relative to its ability to store thermal energy is called as thermal diffusivity. As can be seen from Table 8.13, thermal diffusivity of steel is orders of magnitude larger than concrete. Based on these observations it can be stated that within the context of frictional heating, heat will propagate much faster in steel than concrete. Therefore total volume of concrete slab which will experience heating is expected to be negligibly small. Based on all aforementioned results it can be concluded that for the perforation simulations considered here, temperature effects can be ignored conveniently. Note that in projectile penetration heat is not only generated due to frictional sliding. The energy released during crack propagation is also converted into heat. Some part of this energy is used to heat up the concrete. The quantification of this energy is rather difficult and, therefore, has not been taken into account in the computations.

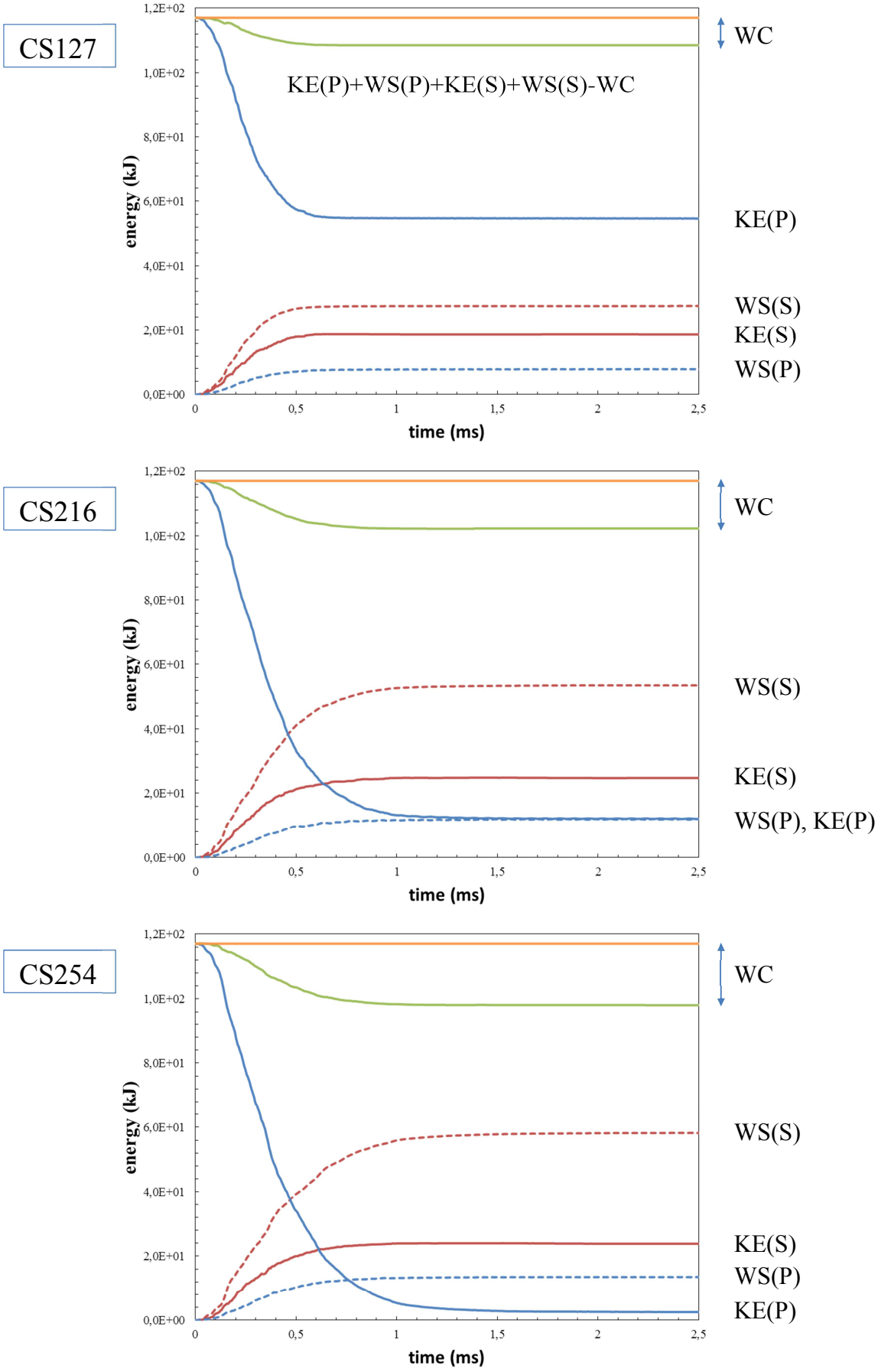

Fig. 8.44 Energy time histories for SET-I

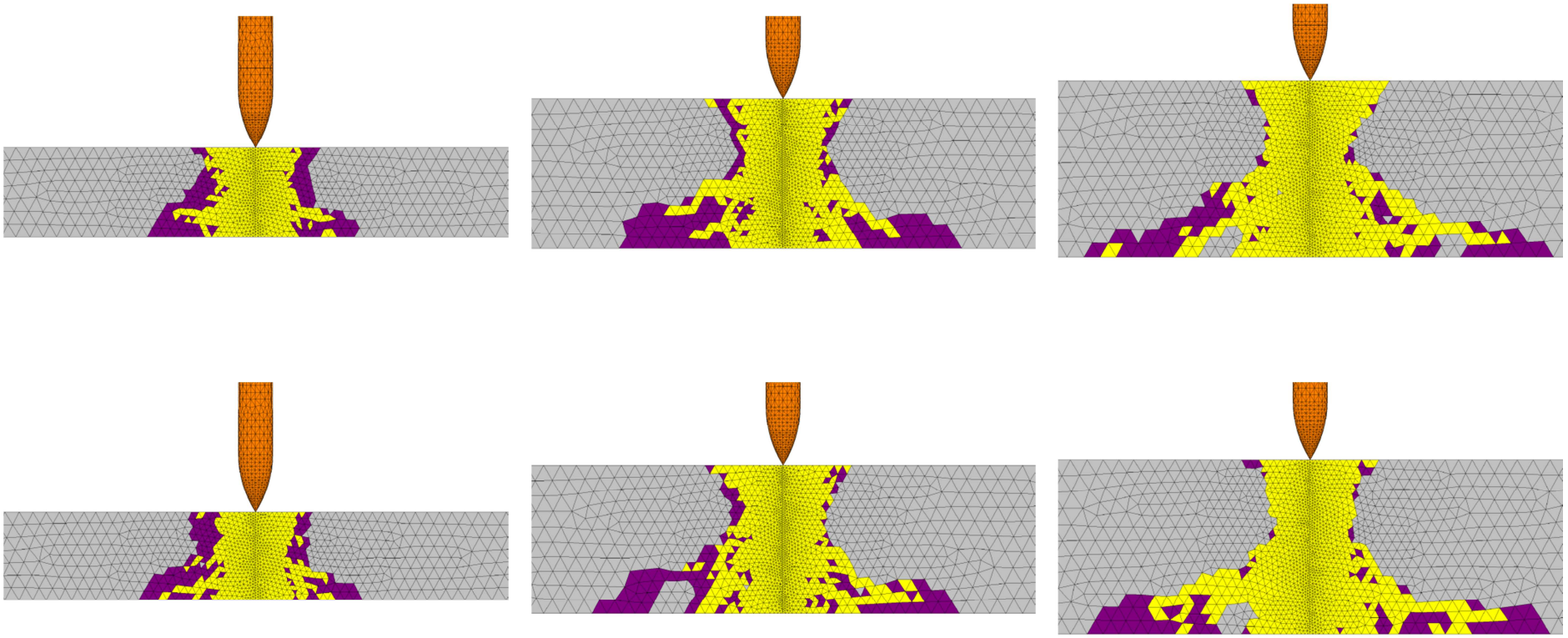

Fig. 8.45 Crater profiles (YZ-plane) with (top row) and without (bottom row) temperature effects for SET-I

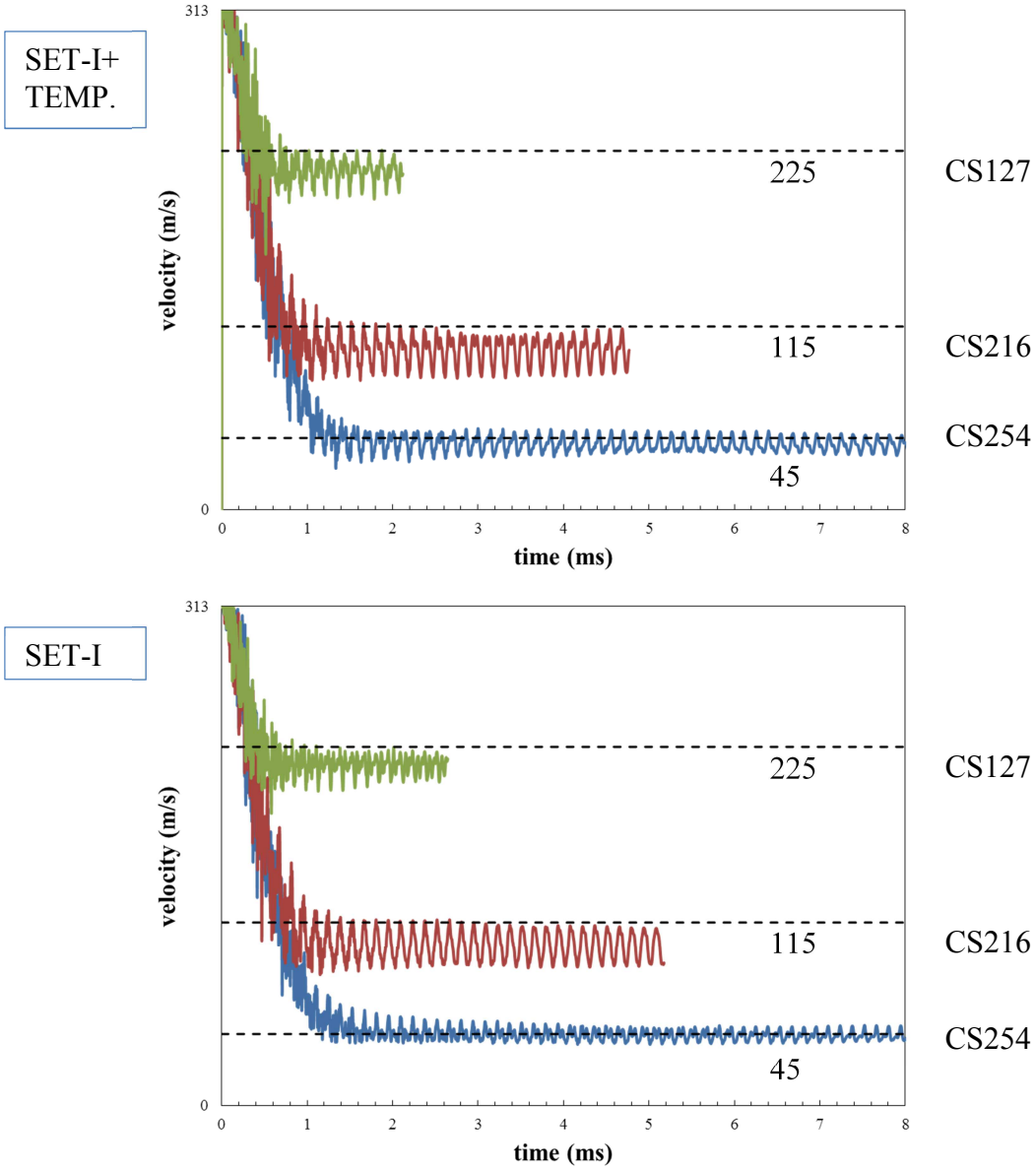

Fig. 8.46 Velocity time histories with and without temperature effects for SET-I

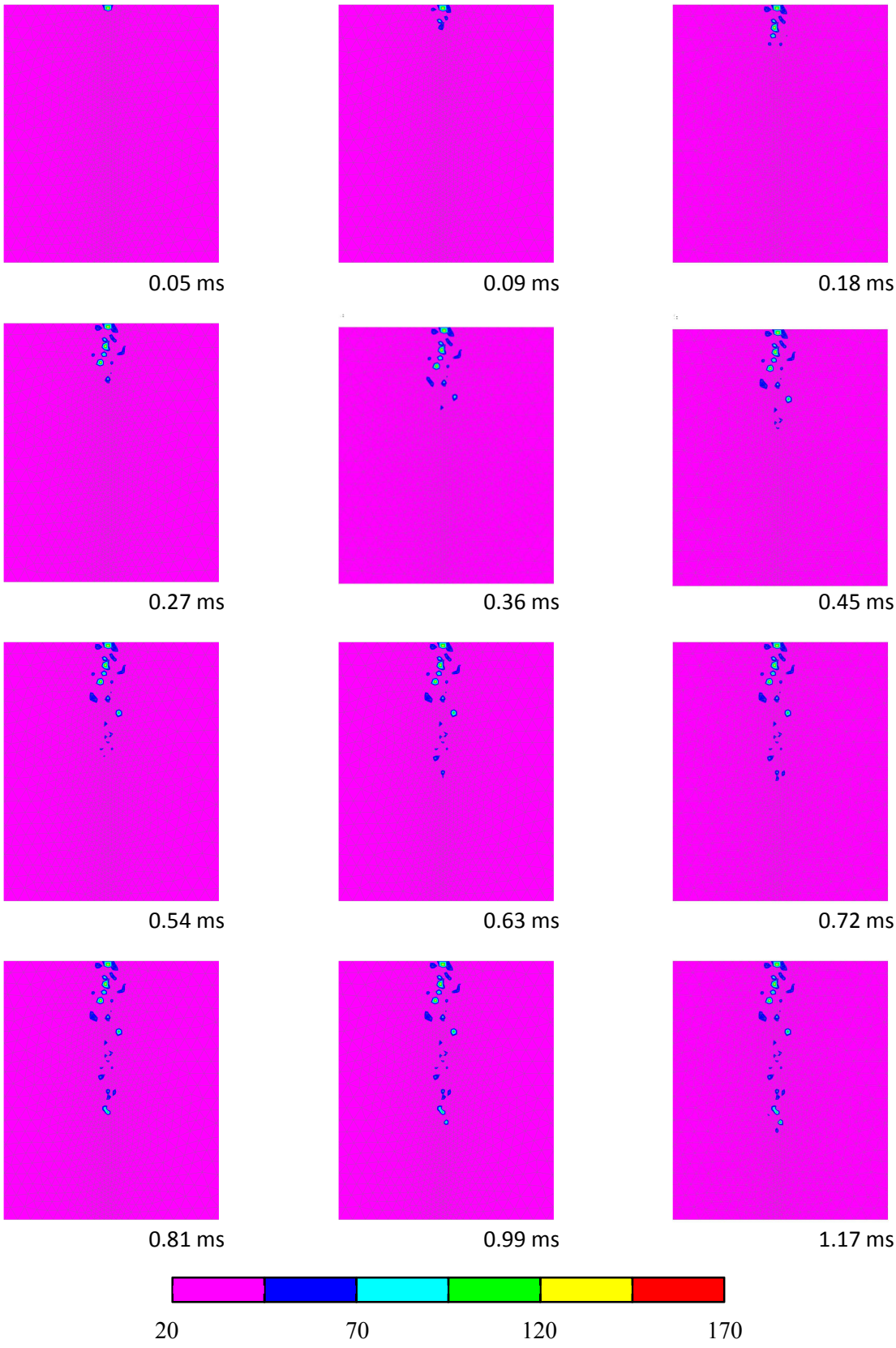

Fig. 8.47 Temperature contours for CS254 for SET-I

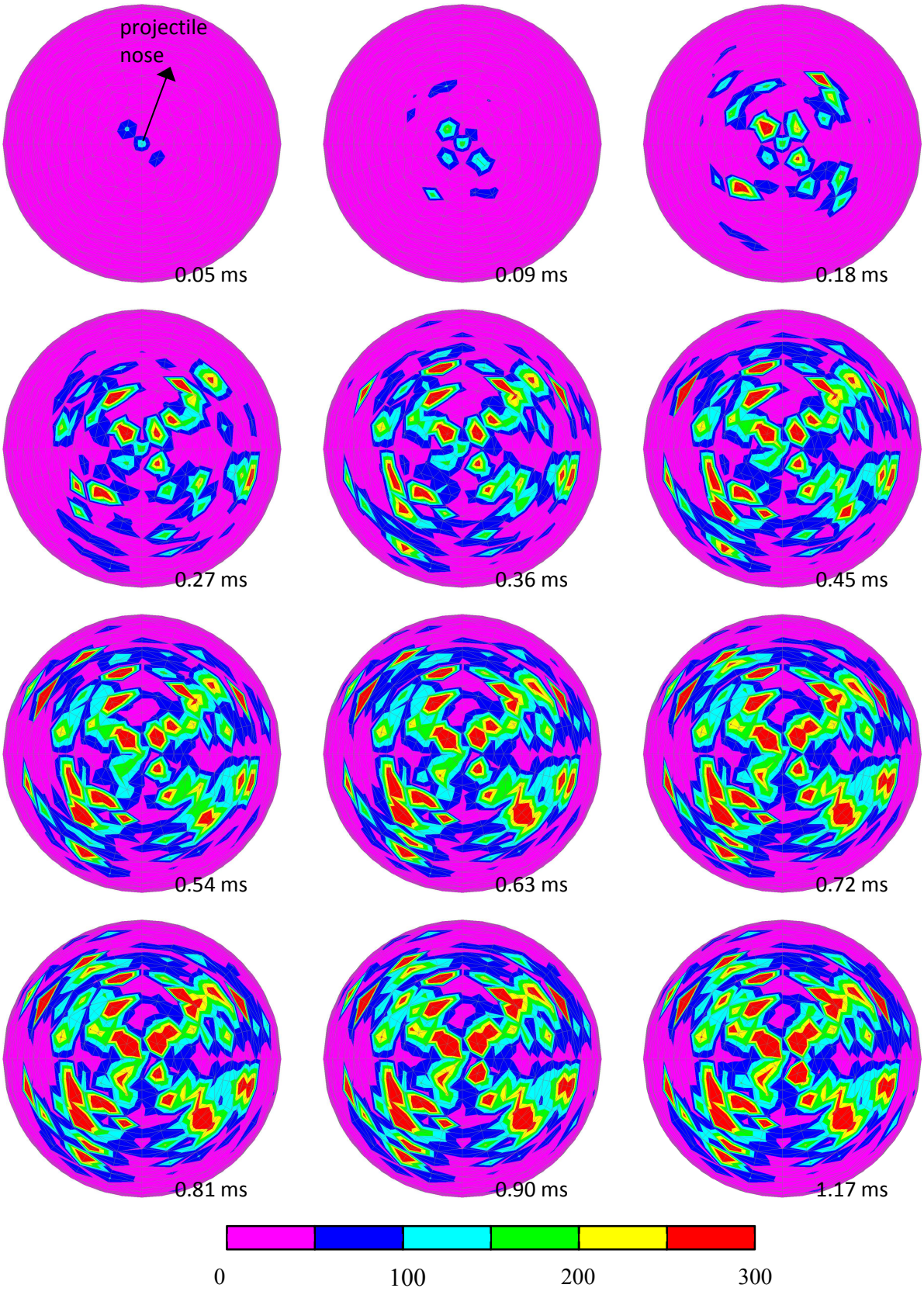

Fig. 8.48 Temperature contours at different time instants for CS254 for SET-I.
(Surface of the for projectile from front view)

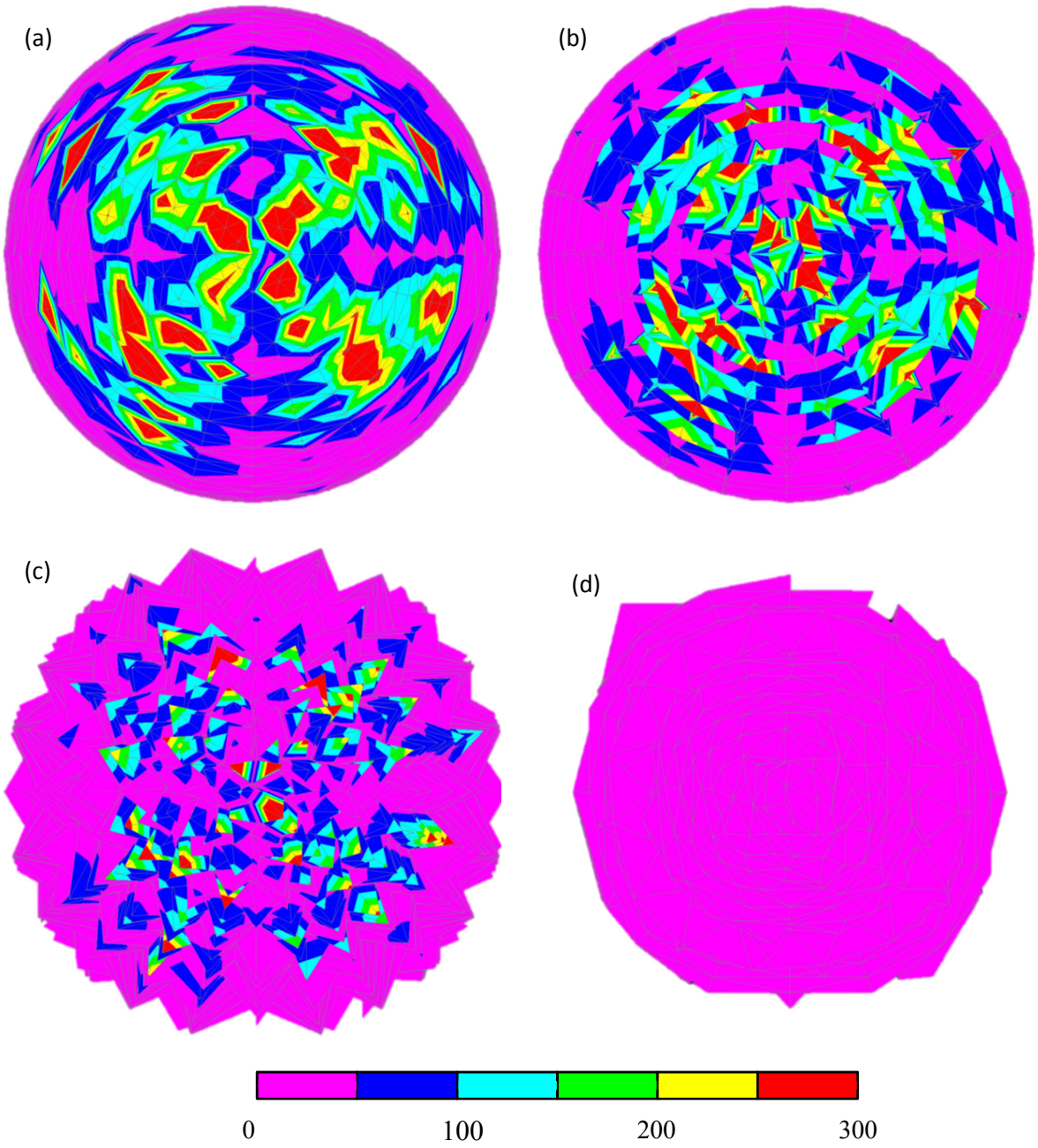

Fig. 8.49 Temperature distribution towards the interior (a-d) of the projectile at 1.17 ms

8.3.4 Failure Criteria

In principle, element deletion should be used only for inelastic softening type material models. Therefore it is ideal to put a stress limit together with some measures of inelastic deformations like plastic strain and damage parameter as a criterion for element deletion. Unfortunately, in practice it is not possible to use a deletion criterion based on stress because in some cases elements might undergo severe deformations prior to full relaxation of stress. In projectile penetration simulations performed in this study, highly deformed elements are not allowed to be present. There are several reasons for this:

- Local impenetrability constraint might be violated if there are highly deformed elements. In such a case simulation must be terminated unless such elements are deleted manually.
- Highly deformed elements could influence the performance of contact algorithm very much. Some non-physical contact situations, which should be avoided, might emerge.
- Number of self-contact events increases very much if highly deformed elements are allowed to be present. There is one version of self-contact algorithm in place but it has not yet been tested thoroughly and, therefore, is not active. That means that self-contact events are not handled in the computations which could also put into danger the standard contact algorithm employed between projectile and concrete slab.

Because of these technical reasons failure criteria based on stress should be avoided. Instead a failure criteria based on deformation has to be employed.

Recall that in all penetration simulations performed in this work, maximum principal strain has been used as a failure criteria and its value has been set to be equal to 1.0. In many commercial explicit finite element programs failure criteria are also based on a deformation measure like maximum principal strain, shear strain, instantaneous geometric strain etc. However, it seems that it is not checked prior to deletion whether a candidate element is free of stress or not for assessments based on deformation based failure criteria.

In projectile penetration simulations, it has been observed that stress state in some concrete elements around the contact region is almost hydrostatic compression. Such elements normally undergo very large deformations and still carry very high level of compressive stresses in the order of $1000\ \mathrm{MPa}$ when the maximum principal strain reaches the failure value. They fully unload at some point but corresponding maximum principal strain could be much larger than the failure value. Deletion of elements with extremely high level of stress might have severe consequences. Since such elements can still transmit force and resist projectile, deletion of them might numerically reduce the resistance of concrete slab. Consequently, failure mode, exit velocity and all other relevant features might drastically change and simulation results turn out to be failure criteria value dependent.

Based on above discussion, it is concluded that deletion of elements with very high stress is acceptable if and only if it does not change the results of numerical simulation significantly. Elements with very high stress can be conveniently deleted for penetration simulations if the following two conditions are satisfied:

- Contact algorithm should not be influenced from the deletion of elements with very high stress too much. As a concrete element gets into contact with projectile, it deforms and also its kinetic energy is increased. If this element is continuously in contact, after a while nodes of this element,

which contribute to contact, start to move together with projectile and, therefore, contact forces transmitted over such an element gradually lose their intensity. Only after then deletion of such an element will not disturb contact behavior and therefore is allowed even if it still carries very high stress. Otherwise resistance of concrete slab is artificially reduced and, as a natural consequence, exit velocity and failure mode are changed.

- Response of concrete slab should not be altered too much as the concrete elements with very high stress are deleted. This is only possible if there is an internal mechanism which brings back approximately the nodal forces removed due to element deletion. This effect, of course, should be produced by the undeleted elements connected to those nodes. The nodal internal forces in those elements should be adjusted such that dynamic equilibrium prior to element deletion is nearly recovered. As soon as an element with very high stress is deleted the acceleration of connected nodes suddenly changes in the following time step. Therefore relatively very high strain rates are generated artificially in the undeleted elements connected to those nodes. Due to material rate dependency and bulk viscosity pressure relatively large internal forces are produced, which replaces the nodal internal forces removed due to element deletion. Note that due to sudden change in stress in undeleted elements, damage grows faster and therefore slight reduction in the overall resistance is expected from the numerical simulations for optimum failure value, if it exists.

As can easily be deduced from above discussion, it is very difficult to predict an optimum failure value beforehand for deletion criterion based on maximum principal strain, especially from contact algorithm point of view, if there are some elements with very high stress at the onset of element deletion. For this reason, set of numerical simulations have been performed to study the sensitivity of numerical results with respect to failure value. Simulations have been performed for failure values 0.1, 0.5 1.0 and 1.5 using CS254 from SET-I (rate:on; friction:0.5).

As can be seen from Fig. 8.54, numerical simulations are very sensitive to the failure value especially for smaller ones. On the other hand, there is a convergence of results as the failure value is increased. Based on these observations, we can conclude that optimum value for failure should be somewhere in between 1.0 and 1.5. Comparing the exit velocity of projectile, shape of the impact and exit craters with experiments (see Fig. 8.52 and Fig. 8.54), optimum failure value turns out to be 1.0. Note that even if the failure value is set to 1.5, no significant change in the overall response is expected.

From the sensitivity study it is concluded that 1.0 could be used as a failure value for deletion criterion based on maximum principal strain. However it must be shown that the results of numerical

simulations are similar if the elements are deleted at the right time when they are fully unloaded. For this reason set of numerical simulations have been performed using again CS254 from SET-I (rate:on; friction:0.5). Due to numerical problems related with contact algorithm, it was not possible to use a projectile with sharp nose. Instead a projectile with smoothed nose has been used in these simulations. A new failure criterion has been implemented. It is again a failure criterion based on maximum principal strain. But for this criteria element is not deleted after the failure value is reached. In addition, norm of the stress tensor must be also below a given tolerance which is set to be 1.0 MPa. Overall two simulations have been performed. In the first simulation standard failure criterion based on maximum principal strain has been used with failure value equal to 1.0. On the other hand, in the second simulation new failure criterion again with failure value 1.0 has been used. As can be seen from Fig. 8.55 and Fig. 8.56, there are not many but definitely some elements which have been deleted with very high stress in the first simulation based on standard failure criterion. On the other hand for second simulation based on modified failure criterion stress level in all deleted elements is below the given tolerance (see Fig. 8.57 and Fig. 8.58). As can be seen from Fig. 8.56 and Fig. 8.58, failure mode in either case are fairly similar to each other. Moreover, from Fig. 8.59 (left) and Fig. 8.60 it can be concluded that the resistance of slab in either case is reasonably close to each other. As expected, response of concrete slab is slightly reduced for simulation based on standard failure criterion. This is good from practical point of view because numerical results stay on the safe side. Finally from Fig. 8.59 (right), we observe that contact behavior also does not change significantly. Based on these comparisons, it can be stated that for penetration simulations studied in this work, the deletion criteria based on maximum principal strain with failure value 1.0 can be used conveniently without checking additionally the state of stress inside the elements.

8.3.5 Rate Effects

It is of high importance to study the contribution of each rate effect, namely material rate sensitivity (MRS) based on micro-cracking and bulk viscosity (BV), to the results of numerical simulations. For this purpose two additional simulations have been performed using CS254 from SET-I (rate:on; friction:0.5). In the first simulation MRS for concrete has been turned on whereas BV for concrete has been turned off. In the second simulation opposite settings has been used as MRS-OFF and BV-ON. The important results of these simulations are documented in Fig. 8.61 together with those for case MRS-ON and BV-ON. As can be seen from Fig. 8.61, the resistance of slab is reduced dramatically, almost same amount, in either case. Based on this observation we can conclude that both MRS and BV are very important and should be included in the numerical simulations for correct prediction of concrete resistance against penetration.

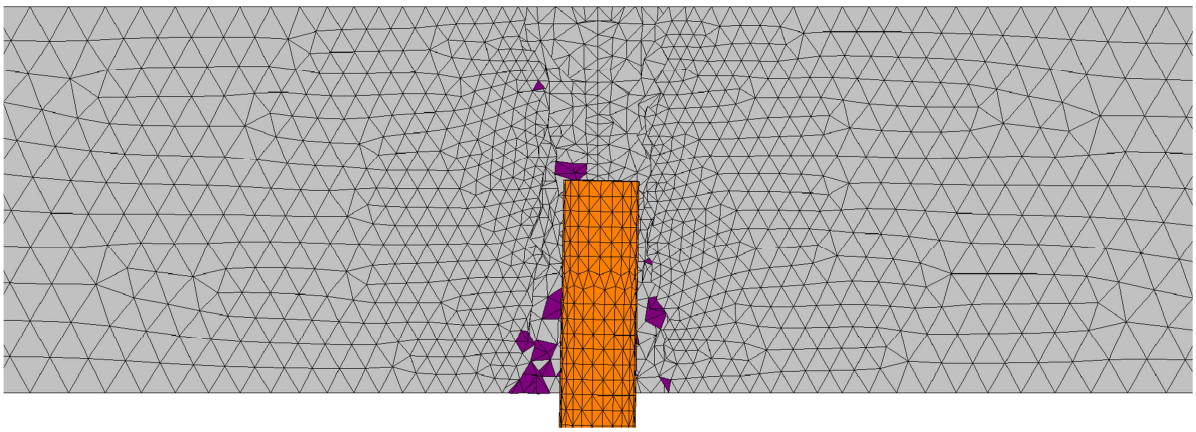

Fig. 8.50 Deformed shape at t $= 1.79$ ms for failure value 0.1

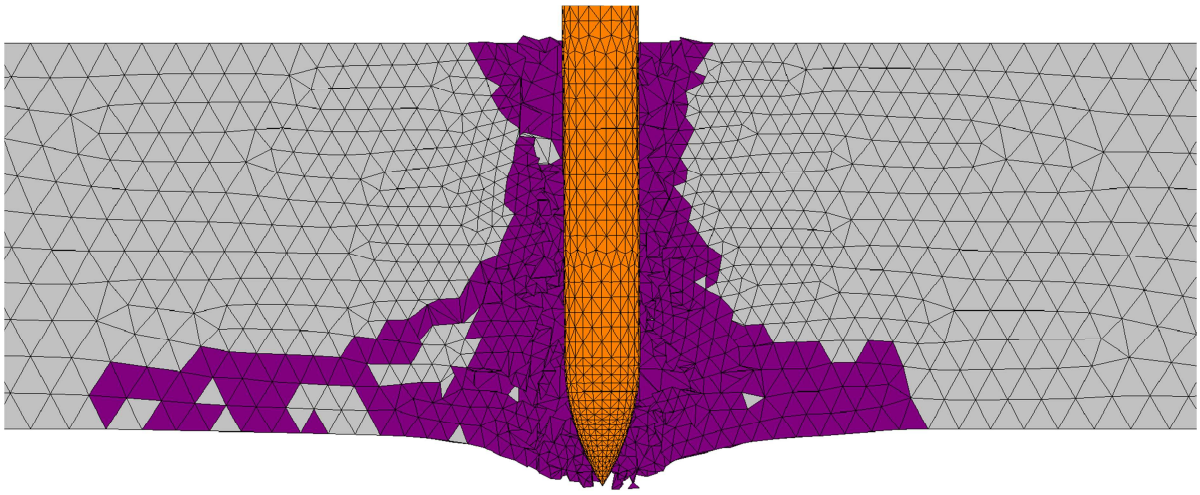

Fig. 8.51 Deformed shape at $t = 1.79$ ms for failure value 0.5

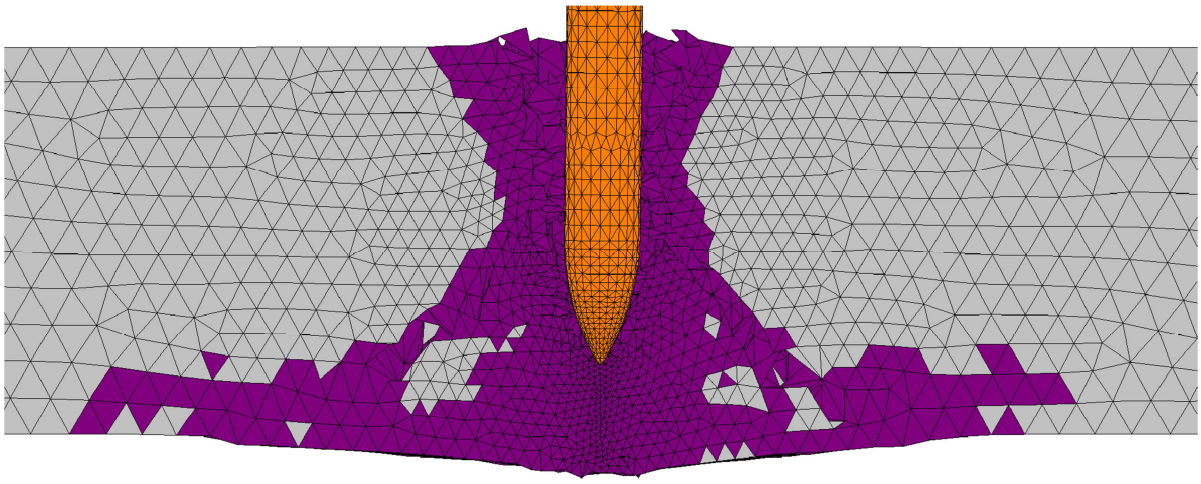

Fig. 8.52 Deformed shape at $t = 1.79$ ms for failure value 1.0

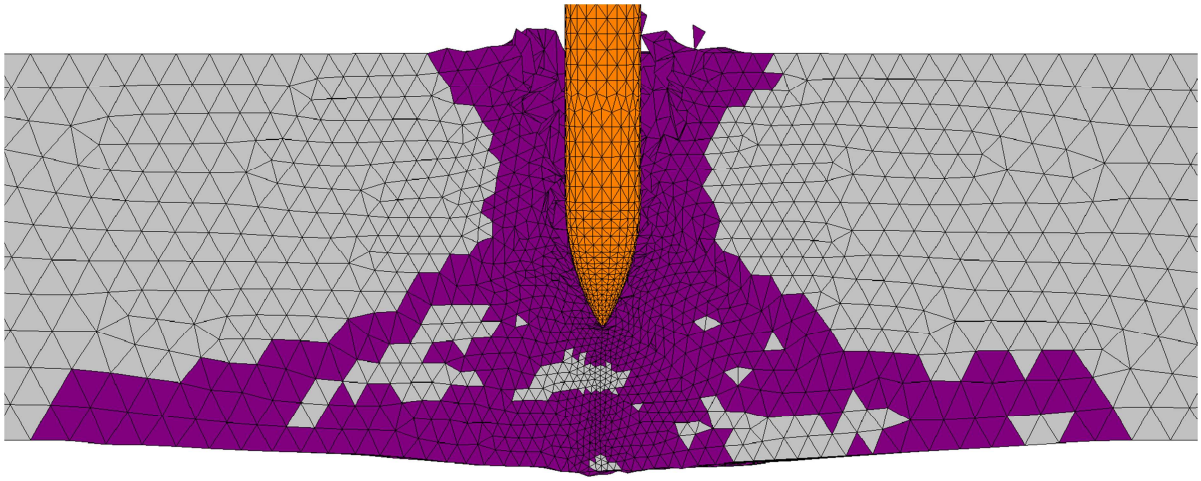

Fig. 8.53 Deformed shape at $t = 1.79$ ms for failure value 1.5

(a)

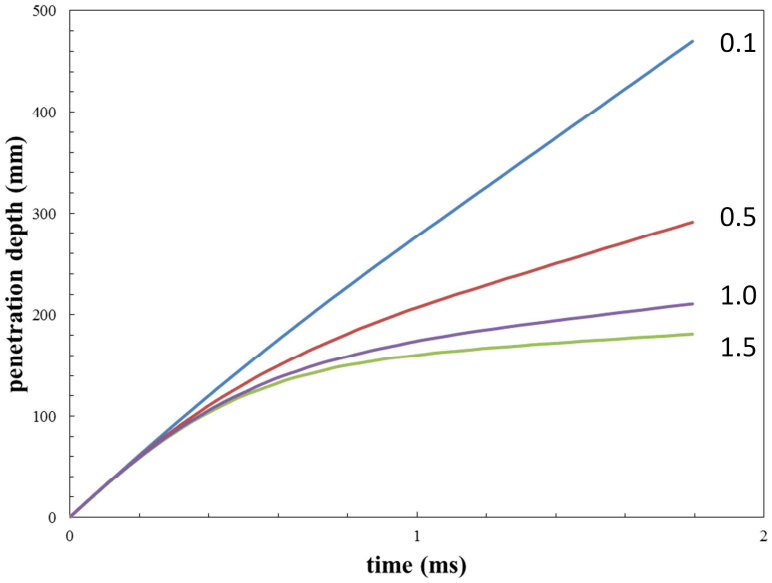

(b)

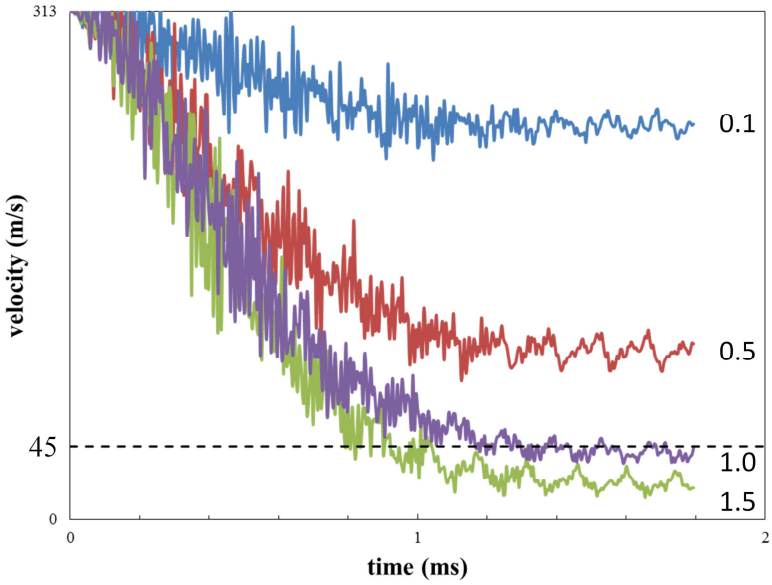

Fig. 8.54 Time history graphs. (a) Penetration depth vs. time. (b) Projectile velocity vs. time

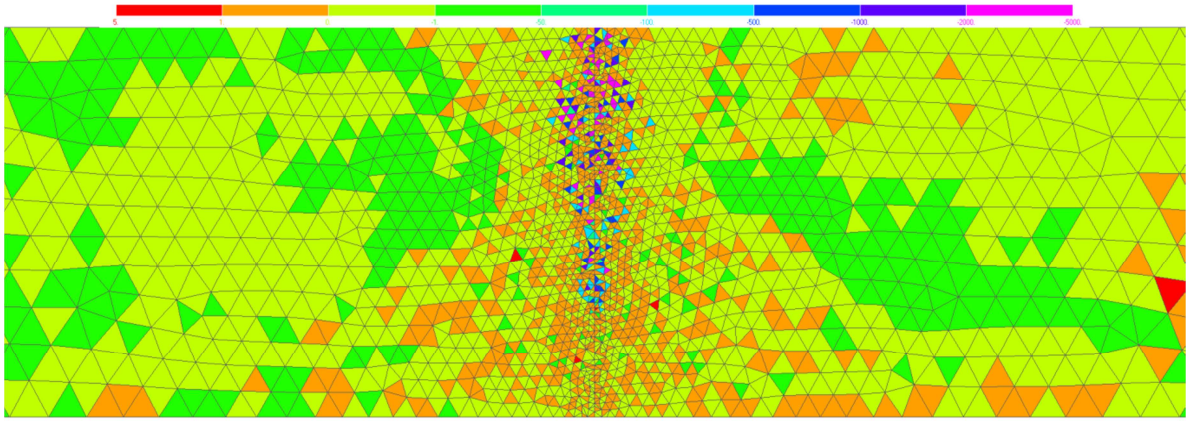

Fig. 8.55 Minimum principal stress contour plot at $t = 2.0$ ms for standard failure criterion

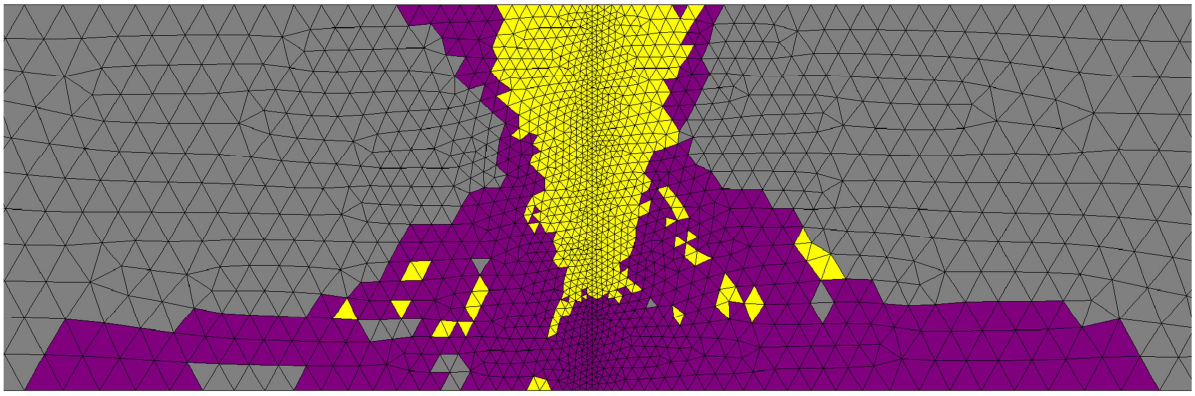

Fig. 8.56 Crater profiles (XZ-plane) for at $t = 2.0$ ms for standard failure criterion

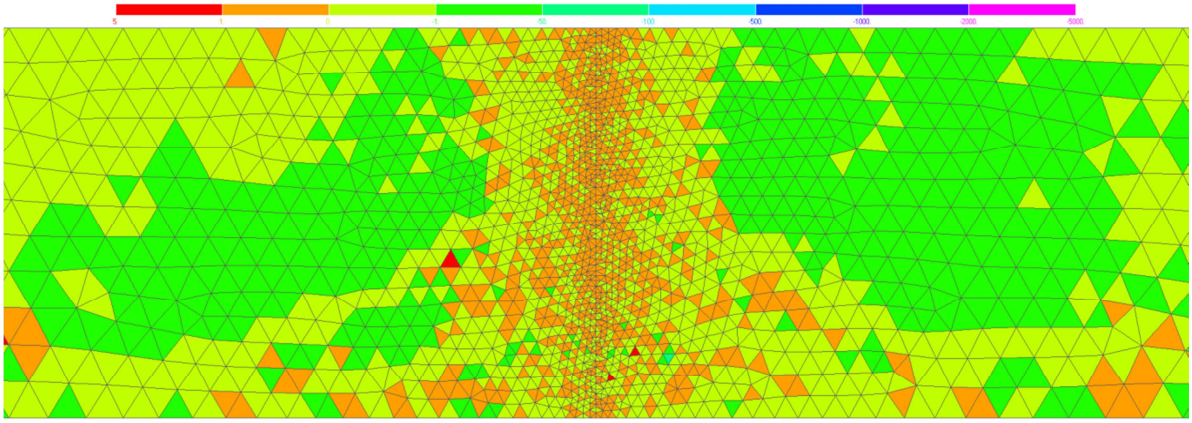

Fig. 8.57 Minimum principal stress contour plot at $t = 2.0$ ms for modified failure criterion

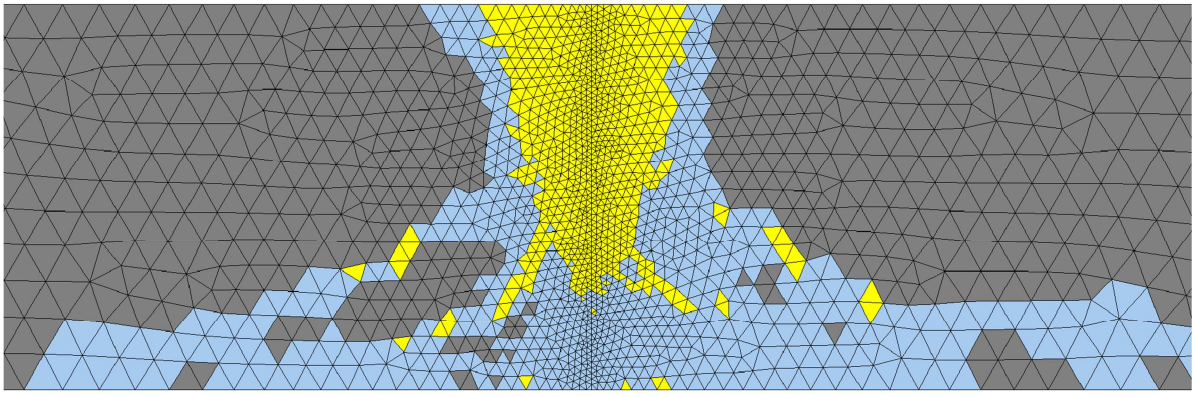

Fig. 8.58 Crater profiles (XZ-plane) for at $t = 2.0$ ms for modified failure criterion

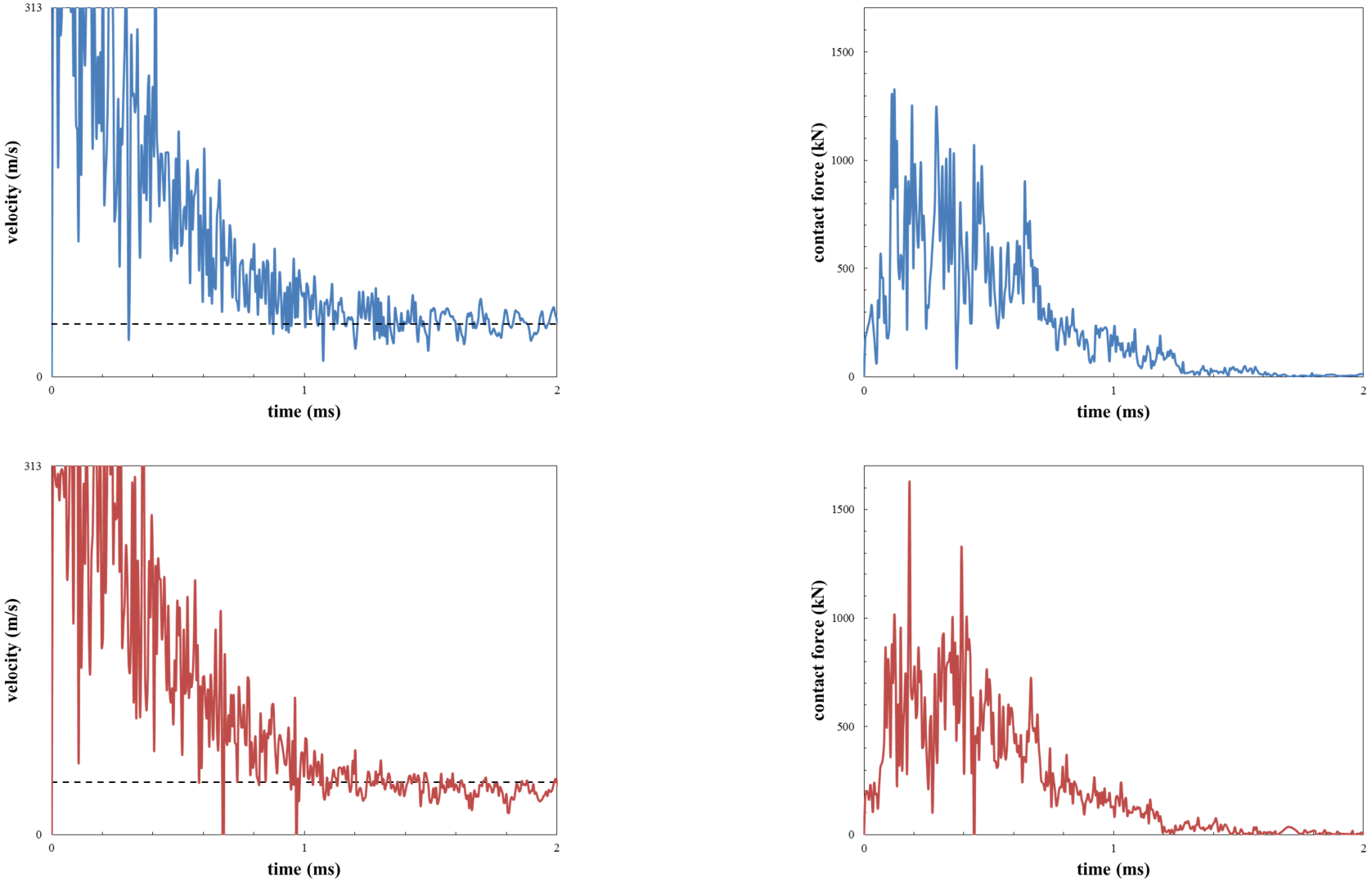

Fig. 8.59 Projectile velocity vs. time (left). Contact force vs. time (right)
Standard failure criterion (top) vs. Modified failure criterion (bottom)

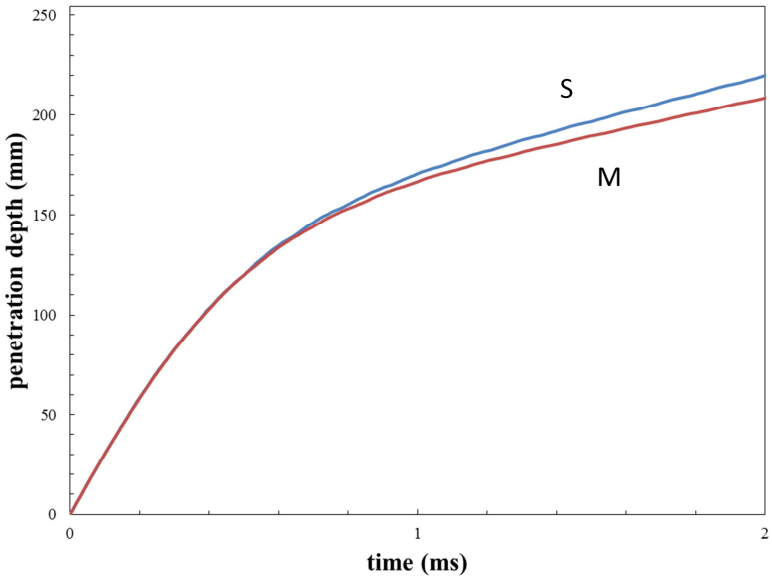

Fig. 8.60 Penetration depth vs. time for standard (S) and modified (M) failure criteria

(a)

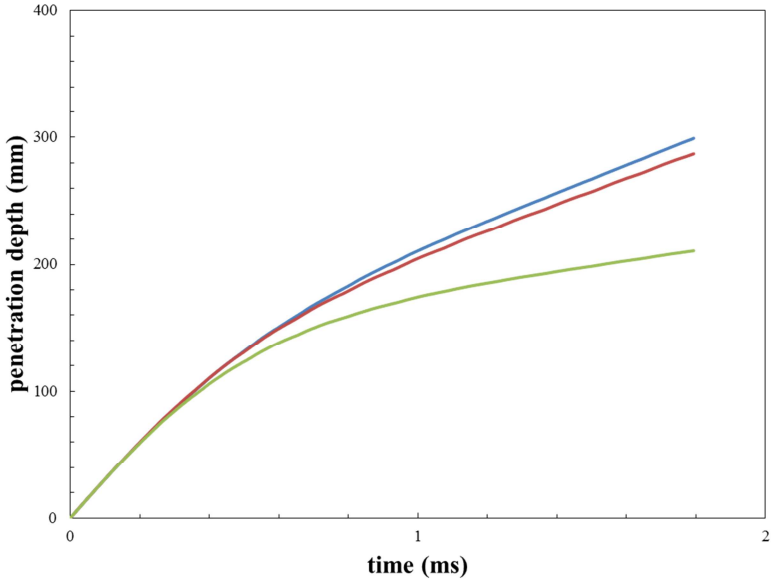

(b)

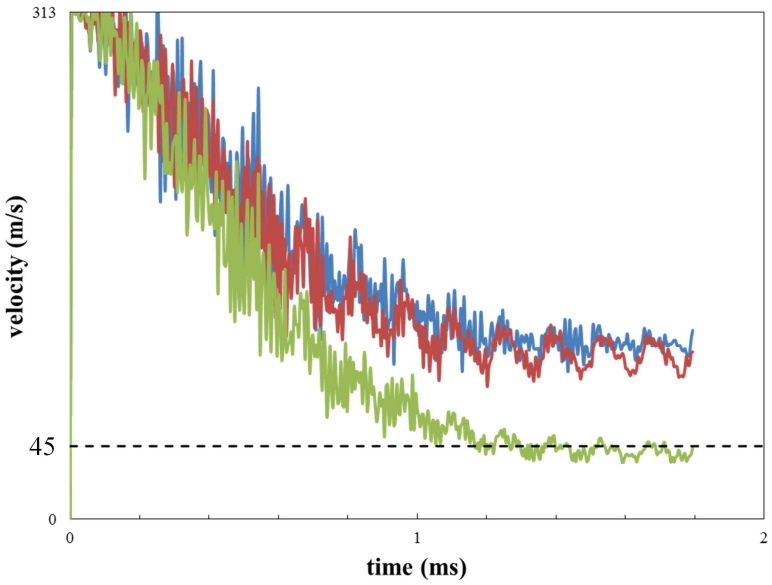

Fig. 8.61 Time history graphs. (a) Penetration depth vs. time. (b) Projectile velocity vs. time

9 Conclusions and Recommendations

9.1 Conclusions

In the present work a three-dimensional finite element code for nonlinear multi-body dynamic analysis of concrete is developed. The code is written in the framework of continuum mechanics following basic principles of irreversible thermodynamics. The explicit Lagrangian type of finite element formulation is employed using simple constant strain four node solid finite elements. As a constitutive law for concrete rate and temperature dependent microplane model based on relaxed kinematical constraint is used. Material model is further extended to account for large displacements and deformations. The crack band regularization method is employed to assure mesh objective results. Large-deformation frictional contact problem is solved by predictor-corrector type algorithm in which kinematical contact constraints are enforced by a Lagrange multiplier like penalty method. Kinematical contact constraints are formulated in both, total and rate form. Mohr-Coulomb type frictional constitutive behavior is adopted in tangential contact direction. Due to actual underlying penalty formulation, it is possible to utilize standard radial return mapping algorithm, frequently used for elastic-plastic materials, to perform constitutive update in tangential direction. Moreover, heat generated at the contact surface due to frictional sliding is also accounted for. The severe mesh distortions and pulverization of concrete are handled with a technique based on adaptive element deletion. Formation of the fragments is automated using adaptive element deletion without need for further intervention provided that the finite element mesh is sufficiently fine around the zone of interest.

The finite element code is then used in the numerical studies of plain concrete structures exposed to high strain rates and impact loads. The results of numerical analysis are compared with the experimental results. It is demonstrated that the proposed modeling approach, based on the standard simple finite elements and microplane model, is able to realistically simulate complex phenomena related to dynamic fracture of concrete, such as rate dependent resistance, rate dependent failure mode, crack velocity and crack branching.

The evaluation of experimental results indicates that the resistance of quasi brittle materials, like concrete, is an increasing function of strain (loading) rate. At the constitutive level rate effects can be modeled to a great extent based on the rate process theory, which results in a linear relationship between material resistance and loading rate (in semi-log scale). In opposite to common belief, it is shown that the progressive increase in material resistance beyond a certain critical strain rate (approximately $10\ \mathrm{s}^{-1}$), documented in many experiments, emanates mainly due to the different phenomena related to inertial forces (e.g. change of the failure mode, crack branching, damage and

softening) and cannot be attributed to the material behavior. If one incorporates this progressive increase in resistance into the material model directly and then uses it in dynamic fracture simulations, numerical results obtained become highly prone to errors due to double counting of the same effect. Unfortunately, many commercially used finite element codes available in the market employ material models equipped with this wrong rate dependency model. Instead one has to use a material model armed with linear (in semi-log scale) rate dependency model for full range of loading rate. If the material model is realistic, then progressive increase in resistance will automatically show up during dynamic simulations as the high structural inertial forces interact with the material constitutive law.

Structural inertial forces are not only responsible for progressive increase in material resistances. They also play an important role in the failure mode and crack branching phenomena observed at high loading rates. It is shown by means of numerical simulations that as the loading rate is increased failure mode changes from Mode-I to mixed mode and in some cases, depending upon the level of loading rate, crack branching is observed just like as in experiments even if the rate effect is turned off.

It is shown that in the case of Hopkinson bar experiment damage of the concrete specimen should be accounted when the experimental results are evaluated based on the elastic wave propagation theory. Common praxis is the assumption that concrete behavior before localization of cracks is linear elastic. However, the evaluation of numerical results shows that this assumption is unrealistic for concrete and leads to significant overestimation of resistance for higher strain rates. Actually, it seems that taking damage of concrete before localization of macro cracks into account, the influence of inertia can be eliminated from the evaluation of experimental results based on the elastic wave propagation theory. In this way the predicted material strength is the true and not the apparent strength.

The performance of rate dependent microplane material model at very high strain rates, of the order of $10^4\ \mathrm{s}^{-1}$, is also investigated. For this purpose projectile perforation experiments from the literature is simulated. During such perforation process, concrete material around the contact region experiences very large deformations in a very short period of time. For this reason microplane material model is extended to the large strain regime. Due to large deformations, motion function around the impact region rapidly loses its regularity. Assembly of particles located around the impact region does not behave like a solid any more but like a fluid or a gas. Then it becomes impossible to continue the simulation staying within the Lagrangian framework. To be able to retain computational framework intact, an adaptive technique based on element deletion is used. As the elements are

deleted and projectile penetrates further, new possible contact surfaces might evolve. A computational procedure coupling pre-processor based moving contact sphere and topological data structures is developed to accelerate contact search and make it possible to carry out such simulations within a reasonable period of time. After gathering all these numerical tools, a parametric study is conducted in order to investigate the effect of rate sensitivity of material and friction. The numerical results obtained are assessed in terms of exit velocity, shape of the impact and exit craters, projectile deformation, formation of the radial cracks and failure cone. It is found out that exit velocities for all range of slab thickness are fairly close to the experimental results if the rate sensitivity of the material is taken into account. On the other hand, for the simulations without rate sensitivity concrete becomes too soft and projectile perforates the target with a mean residual velocity much higher than the corresponding experimental values. Therefore it is concluded that the proposed model for the material rate dependency together with bulk viscosity effects is adequate for impact velocities up to $1000\ \mathrm{m/s}$ and can be used conveniently without any modification.

Friction also has an influence on the exit velocity but not as much as rate sensitivity. It is observed that rate effects become even more pronounced as the thickness of the slab is increased. This behavior can be explained by the time elapsed during perforation up until to the point where mean projectile velocity becomes constant (exit velocity). It is obviously much larger for thicker slabs and due to this fact concrete has a chance to resist more, i.e. constitutive model is much more involved. That is why rate effects become much more apparent. Therefore thicker slabs build up a very challenging problem for the constitutive model utilized. The presented numerical results with rate sensitivity are in very good agreement with the experiments in terms of exit velocities for thickest ($\mathrm{t} = 254\ \mathrm{mm}$) slab as well as others ($\mathrm{t} = 127$ and $\mathrm{t} = 216\ \mathrm{mm}$). It is observed that shape of the impact and exit craters does not change too much depending upon whether rate effects are included or not. That supports the claim that failure mode is not a primary function of material rate dependency but of global structural inertia forces, which are present in all of the simulations. In all simulations projectile has remained almost undeformed, similar to experiments. Due to full three dimensional simulations it was possible to capture rotation of the projectile as a rigid body which has been observed also in the experiments.

In addition set of numerical simulations has been performed to investigate sensitivity of the numerical results with respect to failure value, which is used to determine if an element will be deleted or not. It has been found out that there is an optimal value for element failure based on maximum principal strain which is around 1.0. It has also been shown that if the deletion criteria based on maximum principal strain with failure value 1.0 is used, elements can be deleted conveniently without checking additionally the state of stress inside the elements.

To investigate the significance of thermal coupling a set of thermo-mechanical penetration simulations have also been carried out. Based on computed temperature distributions, it can be concluded that for the given impact conditions, temperature effects can be ignored.

9.2 Recommendations

Finite element program used in the present work is developed by following one-body-one-discretization strategy. It means that each separate body in the system has its own finite element discretization completely independent from all others. In principle different bodies cannot recognize each other unless some mechanical interactions, like contact, are defined in between. This flexible structure together with explicit time integration and adaptive element deletion should readily be extended for parallel computations without any major modifications. Therefore, parallelization should be given top priority in order to reduce total computation time.

Development of more sophisticated material models for the projectile would be another interesting research direction. Because, then it would be possible to investigate more complex impact conditions where projectile experiences very large plastic deformations which in turn give rise to very high temperatures even larger than the melting point. It can be concluded that the modeling approach used in the simulation of impact problems is valid up until to the impact velocity of approximately $1000\ \mathrm{m/s}$. To figure out how much further one can still go with this model would also be interesting to study. Last but not least investigating load-rate dependent behavior of reinforced concrete would be also another fruitful research direction.

Bibliography

Antoun, T., Seaman, L., Curran, D.R., Kanel, G.I., Razorenov, S.V. & Utkin, A.V., 2003. *Spall fracture*, Springer, New York.

Armero, F. & Simo, J.C., 1992. A new unconditionally stable fractional step method for non-linear coupled thermomechanical problems. *International Journal for Numerical Methods in Engineering*, 35(4), pp.737–766.

Bažant, Z.P. & Oh, B., 1983. Crack band theory for fracture of concrete. *Materials and Structures*, RILEM 93 (16), pp.155–177.

Bažant, Z.P., Belytschko, T. & Chang, T.-P., 1984a. Continuum theory for strain-softening. *Journal of Engineering Mechanics*, 110(12), pp.1666–1692.

Bažant, Z.P. & Gambarova, P.G., 1984b. Crack shear in concrete: Crack band microplane model. *Journal of Structural Engineering*, 110(9), pp.2015–2035.

Bažant, Z.P. & Oh, B., 1986. Efficient numerical integration on the surface of a sphere. *ZAMM-Journal of Applied Mathematics and Mechanics/Zeitschrift für Angewandte Mathematik und Mechanik*, 66(1), pp.37–49.

Bažant, Z.P. & Prat, P.C., 1988a. Microplane model for brittle-plastic material: I. Theory. *Journal of Engineering Mechanics*, 114(10), pp.1672–1688.

Bažant, Z.P. & Prat, P.C., 1988b. Microplane model for brittle-plastic material: II. Verification. *Journal of Engineering Mechanics*, 114(10), pp.1689–1699.

Bažant, Z.P. & Ožbolt, J., 1992. Compression failure of quasibrittle material: Nonlocal microplane model. *Journal of Engineering Mechanics*, 118(3), pp.540–556.

Bažant, Z.P., 1995. Additive volumetric-deviatoric split of finite strain tensor and its implication for cracking models. In *Fracture Mechanics of Concrete Structures: Proc., 2nd Int. Conf. on Fracture Mech. of Concrete and Concrete Struct.(FraMCoS-2)*. pp. 515–534.

Bažant, Z.P., Xiang, Y. & Prat, P.C., 1996a. Microplane model for concrete. I: Stress-strain boundaries and finite strain. *Journal of Engineering Mechanics*, 122(3), pp.245–254.

Bažant, Z.P. & Ožbolt, J., 1996b. Numerical smeared fracture analysis: Nonlocal microcrack interaction approach. *International Journal for Numerical Methods in Engineering*, 39, pp.635–66l.

Bažant, Z.P., Caner, F.C., Adley, M.D., *et al.*, 2000a. Fracturing rate effect and creep in microplane model for dynamics. *Journal of Engineering Mechanics*, 126(9), pp.962–970.

Bažant, Z.P., Adley, M.D., Carol, I., *et al.*, 2000b. Large-strain generalization of microplane model for concrete and application. *Journal of Engineering Mechanics*, 126(9), pp.971–980.

Bažant, Z.P. & Jirásek, M., 2002. Nonlocal integral formulations of plasticity and damage: Survey of progress. *Journal of Engineering Mechanics*, 128(11), pp.1119–1149.

Bažant, Z.P. & Caner, F.C., 2014. Impact comminution of solids due to local kinetic energy of high shear strain rate: I. Continuum theory and turbulence analogy. *Journal of the Mechanics and Physics of Solids*, 64, pp.223–235.

Belytschko, T., Liu, W.K. & Moran, B., 1999. *Nonlinear finite elements for continua and structures*, Wiley, New Jersey.

Birnbaum, N., Cowler, M., Itoh, M., *et al.*, 1987. AUTODYN—An interactive non-linear dynamic analysis program for microcomputer through supercomputers. *Transactions of 9th Structural Mechanics in Reactor Technology*, pp.401–406.

Bischoff, P. & Perry, S., 1991. Compressive behaviour of concrete at high strain rates. *Materials and Structures*, 24(6), pp.425–450.

de Borst, R., 2002. Fracture in quasi-brittle materials: a review of continuum damage-based approaches. *Engineering Fracture Mechanics*, 69(2), pp.95–112.

de Borst, R., 2003. Numerical aspects of cohesive-zone models. *Engineering Fracture Mechanics*, 70(14), pp.1743–1757.

de Borst, R., Remmers, J.J., Needleman, A., *et al.*, 2004. Discrete vs smeared crack models for concrete fracture: bridging the gap. *International Journal for Numerical and Analytical Methods in Geomechanics*, 28(7-8), pp.583–607.

Bošnjak, J., 2014. *Explosive spalling and permeability of high performance concrete under fire – numerical and experimental investigations*, Institut für Werkstoffe im Bauwesen der Universität Stuttgart.

Camacho, G. & Ortiz, M., 1996. Computational modelling of impact damage in brittle materials. *International Journal of Solids and Structures*, 33(20), pp.2899–2938.

Camacho, G. & Ortiz, M., 1997. Adaptive Lagrangian modelling of ballistic penetration of metallic targets. *Computer Methods in Applied Mechanics and Engineering*, 142(3), pp.269–301.

Caner, F.C. & Bažant, Z.P., 2014. Impact comminution of solids due to local kinetic energy of high shear strain rate: II-Microplane model and verification. *Journal of the Mechanics and Physics of Solids*, 64, pp.236–248.

Cargile, J.D., 1999. *Development of a constitutive model for numerical simulation of projectile penetration into brittle geomaterials*, Technical Report SL-99-11, U.S. Army Engineer Research and Development Center, Vicksburg, MS.

Carpenter, N.J., Taylor, R.L. & Katona, M.G., 1991. Lagrange constraints for transient finite element surface contact. *International Journal for Numerical Methods in Engineering*, 32(1), pp.103–128.

Carter, B., Wawrzynek, P. & Ingraffea, A., 2000. Automated 3-D crack growth simulation. *International Journal for Numerical Methods in Engineering*, 47(1-3), pp.229–253.

Červenka, J., Bažant, Z.P. & Wierer, M., 2005. Equivalent localization element for crack band approach to mesh-sensitivity in microplane model. *International Journal for Numerical Methods in Engineering*, 62(5), pp.700–726.

Chen, E., 1994. Numerical simulation of dynamic fracture and failure in solids. *NASA STI/Recon Technical Report N*, 943, p.37705.

Couch, R., Albright, E. & Alexander, N., 1983. *JOY Computer Code*, Lawrence Livermore National Laboratory, UCID-19688.

Curbach, M. & Eibl, J., 1990. Crack velocity in concrete. *Engineering Fracture Mechanics*, 35(1), pp.321–326.

Dhir, R. & Sangha, R., 1974. Development and propagation of microcracks in plain concrete. *Matériaux et Construction*, 7(1), pp.17–23.

Dilger, W., Koch, R. & Kowalczyk, R., 1984. Ductility of plain and confined concrete under different strain rates. In *ACI Journal Proceedings*, 81(1), pp.73-81.

Dolbow, J. & Belytschko, T., 1999. A finite element method for crack growth without remeshing. *International Journal for Numerical Methods in Engineering*, 46, pp.131–150.

Donea, J. & Huerta, A., 2003. *Finite element methods for flow problems*, Wiley, New Jersey.

Donea, J., Huerta, A., Ponthot, J.-P., *et al.*, 2004. Arbitrary Lagrangian-Eulerian methods. *Encyclopedia of Computational Mechanics*.

Erhart, T., 2004. *Strategien zur numerischen Modellierung transienter Impaktvorgänge bei nichtlinearem Materialverhalten*, Institut für Baustatik und Baudynamik (Bauwesen) der Universität Stuttgart.

Erhart, T., Wall, W.A. & Ramm, E., 2006. Robust adaptive remeshing strategy for large deformation, transient impact simulations. *International Journal for Numerical Methods in Engineering*, 65(13), pp.2139–2166.

Fichant, S., La Borderie, C. & Pijaudier-Cabot, G., 1999. Isotropic and anisotropic descriptions of damage in concrete structures. *Mechanics of Cohesive-frictional Materials*, 4(4), pp.339–359.

Frank, A.O., Adley, M.D., Danielson, K.T., *et al.*, 2012. The high-rate brittle microplane concrete model: Part II: application to projectile perforation of concrete slabs. *Computers and Concrete*, 9(4), pp.311–325.

Freund, L., 1972a. Crack propagation in an elastic solid subjected to general loading□ I. Constant rate of extension. *Journal of the Mechanics and Physics of Solids*, 20(3), pp.129–140.

Freund, L., 1972b. Crack propagation in an elastic solid subjected to general loading□ II. Non-uniform rate of extension. *Journal of the Mechanics and Physics of Solids*, 20(3), pp.141–152.

Giry, C., Dufour, F. & Mazars, J., 2011. Stress-based nonlocal damage model. *International Journal of Solids and Structures*, 48(25), pp.3431–3443.

Grassl, P. & Jirásek, M., 2006. Plastic model with non-local damage applied to concrete. *International Journal for Numerical and Analytical Methods in Geomechanics*, 30(1), pp.71–90.

Hallquist, J.O., 2006. LS-DYNA Theory Manual. *Livermore Software Technology Corporation*.

Hansson, H. & Malm, R., 2011. Non-linear Finite Element Analysis of Deep Penetration in Unreinforced and Reinforced Concrete. *Nordic Concrete Research*, 44, pp.87–107.

Hassanzadeh, M., 1992. *Behaviour of fracture process zones in concrete influenced by simultaneously applied normal and shear displacements*, Building Materials, Lund University.

Hibbitt, Karlsson & Sorensen, 2001. *ABAQUS/Explicit: User's Manual*, Hibbitt, Karlsson and Sorenson Incorporated.

Hillerborg, A., Modéer, M. & Petersson, P.-E., 1976. Analysis of crack formation and crack growth in concrete by means of fracture mechanics and finite elements. *Cement and concrete research*, 6(6), pp.773–781.

Hirt, C., Amsden, A.A. & Cook, J., 1974. An arbitrary Lagrangian-Eulerian computing method for all flow speeds. *Journal of Computational Physics*, 14(3), pp.227–253.

Holzapfel, G., 2000. *Nonlinear solid mechanics: a continuum approach for engineering*, Wiley, Chichester.

Hopkinson, B., 1914. A method of measuring the pressure produced in the detonation of high explosives or by the impact of bullets. *Proceedings of the Royal Society of London. Series A*, 89(612), pp.411–413.

Huang, F., Wu, H., Jin, Q., *et al.*, 2005. A numerical simulation on the perforation of reinforced concrete targets. *International Journal of Impact Engineering*, 32(1), pp.173–187.

Hughes, T.J., 2012. *The finite element method: linear static and dynamic finite element analysis*, DoverPublications.

İrhan, B., 2003. *Comparsion of alternative kinematical approaches to finite element formulations with embedded strong discontinuities*, Institut für Mechanik (Bauwesen) der Universität Stuttgart.

Jirásek, M. & Zimmermann, T., 1998a. Analysis of rotating crack model. *Journal of Engineering Mechanics*, 124(8), pp.842–851.

Jirásek, M. & Zimmermann, T., 1998b. Rotating crack model with transition to scalar damage. *Journal of Engineering Mechanics*, 124(3), pp.277–284.

Jirásek, M., 1999. Computational aspects of nonlocal models. In *Proceedings of ECCM'99—European Conference on Computational Mechanics, August, Münich, Germany*.

Jirásek, M., 2000. Comparative study on finite elements with embedded discontinuities. *Computer Methods in Applied Mechanics and Engineering*, 188(1), pp.307–330.

Jirásek, M. & Patzák, B., 2001. Models for quasibrittle failure: Theoretical and computational aspects. In *Proceedings of ECCM'01—European Conference on Computational Mechanics, June, Cracow, Poland*.

Jirásek, M. & Belytschko, T., 2002. Computational resolution of strong discontinuities. In *Proceedings of Fifth World Congress on Computational Mechanics, WCCM V, Vienna University of Technology, Austria*.

Jirásek, M. & Marfia, S., 2005. Non-local damage model based on displacement averaging. *International Journal for Numerical Methods in Engineering*, 63(1), pp.77–102.

Jirásek, M. & Bauer, M., 2012. Numerical aspects of the crack band approach. *Computers and Structures*, 110, pp.60-78.

Johnson, G.R., 1977. EPIC-3, a computer program for elastic-plastic impact calculations in 3 dimensions. *Final Report, Jan. 1976-Feb. 1977 Honeywell, Inc., Hopkins, MN. Defense Systems Div.*, 1.

Vaz Jr, M. & Owen, D., 2001. Aspects of ductile fracture and adaptive mesh refinement in damaged elasto-plastic materials. *International Journal for Numerical Methods in Engineering*, 50(1), pp.29–54.

Ju, J., 1990. Isotropic and anisotropic damage variables in continuum damage mechanics. *Journal of Engineering Mechanics*, 116(12), pp.2764–2770.

Khoury, G.A., Grainger, B.N. & Sullivan, P.J.E., 1985. Transient thermal strain of concrete: literature review, conditions within specimen and behaviour of individual constituents. *Magazine of Concrete Research*, 37(132), pp.131–144.

Khoury, G.A., 2006a. Strain of heated concrete during two thermal cycles. Part 1: strain over two cycles, during first heating and at subsequent constant temperature. *Magazine of Concrete Research*, 58(6), pp.367–385.

Khoury, G.A., 2006b. Strain of heated concrete during two thermal cycles. Part 2: strain during first cooling and subsequent thermal cycle. *Magazine of Concrete Research*, 58(6), pp.387–400.

Khoury, G.A., 2006c. Strain of heated concrete during two thermal cycles. Part 3: isolation of strain components and strain model development. *Magazine of Concrete Research*, 58(7), pp.421–435.

Kipp, M., Grady, D. & Chen, E., 1980. Strain-rate dependent fracture initiation. *International Journal of Fracture*, 16(5), pp.471–478.

Koch, A., 2002. *Adaptive Finite-Elemente-Berechnungen der nichtlinearen Festkörpermechanik bei kleinen und grossen Verzerrungen*, Institut für Mechanik (Bauwesen) der Universität Stuttgart.

Kolsky, H., 1953. *Stress waves in solids*, Clarendon Press, Oxford.

Kožar, I. & Ožbolt, J., 2010. Some aspects of load-rate sensitivity in visco-elastic microplane material model. *Computers and Concrete*, 7(4), pp.317–329.

Krausz, A.S. & Krausz, K., 1988. *Fracture kinetics of crack growth*, Springer.

Larcher, M., 2009. Development of discrete cracks in concrete loaded by shock waves. *International Journal of Impact Engineering*, 36(5), pp.700–710.

Larsson, R. & Runesson, K., 1996. Element-embedded localization band based on regularized displacement discontinuity. *Journal of Engineering Mechanics*, 122(5), pp.402–411.

Lemaitre, J., 1984. How to use damage mechanics. *Nuclear Engineering and Design*, 80(2), pp.233–245.

Leppänen, J., 2006. Concrete subjected to projectile and fragment impacts: Modelling of crack softening and strain rate dependency in tension. *International Journal of Impact Engineering*, 32(11), pp.1828–1841.

Linder, C., 2003. *An arbitrary Lagrangian-Eulerian finite element formulation for dynamics and finite strain plasticity models*, Institut für Baustatik und Baudynamik (Bauwesen) der Universität Stuttgart.

Linder, C. & Armero, F., 2007. Finite elements with embedded strong discontinuities for the modeling of failure in solids. *International Journal for Numerical Methods in Engineering*, 72(12), pp.1391–1433.

Liu, Y., Ma, A. & Huang, F., 2009. Numerical simulations of oblique-angle penetration by deformable projectiles into concrete targets. *International Journal of Impact Engineering*, 36(3), pp.438–446.

Lu, Y. & Xu, K., 2004. Modelling of dynamic behaviour of concrete materials under blast loading. *International Journal of Solids and Structures*, 41(1), pp.131–143.

Malvar, L.J. & Ross, C., 1998. Review of strain rate effects for concrete in tension. *ACI Materials Journal*, 95(6), pp.735-739.

Martha, L.F., Wawrzynek, P.A. & Ingraffea, A.R., 1993. Arbitrary crack representation using solid modeling. *Engineering with Computers*, 9(2), pp.63–82.

Marusich, T. & Ortiz, M., 1995. Modelling and simulation of high-speed machining. *International Journal for Numerical Methods in Engineering*, 38(21), pp.3675–3694.

Matuska, D. & Durrett, R., 1978. The HULL Code, Finite Difference Solution to the Equations of Continuum Mechanics. *Air Force Armaments Technology Laboratory Report No. AFATL-TR-78-125*.

Mazars, J. & Pijaudier-Cabot, G., 1989. Continuum damage theory-application to concrete. *Journal of Engineering Mechanics*, 115(2), pp.345–365.

Mazars, J. & Pijaudier-Cabot, G., 1996. From damage to fracture mechanics and conversely: a combined approach. *International Journal of Solids and Structures*, 33(20), pp.3327–3342.

McGlaun, J.M., Thompson, S. & Elrick, M., 1990. CTH: a three-dimensional shock wave physics code. *International Journal of Impact Engineering*, 10(1), pp.351–360.

van Mier, J., 1984. *Strain-softening of concrete under multiaxial loading conditions*, Technische Hogeschool Eindhoven.

Mihashi, H. & Wittmann, F., 1980. Stochastic Approach to Study the Influence of Rate of Loading on Strength of Concrete. *HERON*, 25(3).

Mindess, S. & Diamond, S., 1982. The cracking and fracture of mortar. *Matériaux et Construction*, 15(2), pp.107–113.

Moës, N. & Belytschko, T., 2002. Extended finite element method for cohesive crack growth. *Engineering Fracture Mechanics*, 69(7), pp.813–833.

Mohr, O., 1900. Welche Umstände bedingen die Elastizitätsgrenze und den Bruch eines Materiales? *Zeitschrift des Vereins Deutscher Ingenieure*, 46, pp.1524–1530 & 1572–1577.

Nielsent, C.V., Pearce, C.J. & Bicanic, N., 2004. Improved phenomenological modelling of transient thermal strains for concrete at high temperatures. *Computers and Concrete*, 1(2), pp.189–209.

Ogden, R.W., 1997. *Non-linear elastic deformations*, Courier Dover Publications.

Oliver, J., 1989. A consistent characteristic length for smeared cracking models. *International Journal for Numerical Methods in Engineering*, 28(2), pp.461–474.

Oliver, J., 1996a. Modelling strong discontinuities in solid mechanics via strain softening constitutive equations. Part 1: Fundamentals. *International Journal for Numerical Methods in Engineering*, 39(21), pp.3575–3600.

Oliver, J., 1996b. Modelling strong discontinuities in solid mechanics via strain softening constitutive equations. Part 2: Numerical simulation. *International Journal for Numerical Methods in Engineering*, 39(21), pp.3601–3623.

Ortiz, M. & Suresh, S., 1993. Statistical properties of residual stresses and intergranular fracture in ceramic materials. *Journal of Applied Mechanics*, 60, pp.77–84.

Ortiz, M. & Pandolfi, A., 1999. Finite-Deformation Irreversible Cohesive Elements For Three-Dimensional Crack-Propagation Analysis. *International Journal for Numerical Methods in Engineering*, 44, pp.1267–1282.

Ožbolt, J. & Eligehausen, R., 1995. Modeling of reinforced concrete by the non-local microplane model. *Nuclear engineering and design*, 156(1), pp.249–257.

Ožbolt, J., Li, Y. & Kožar, I., 2001. Microplane model for concrete with relaxed kinematic constraint. *International Journal of Solids and Structures*, 38(16), pp.2683–2711.

Ožbolt, J. & Reinhardt, H.-W., 2002. Numerical study of mixed-mode fracture in concrete. *International Journal of Fracture*, 118(2), pp.145–162.

Ožbolt, J., Kožar, I., Eligehausen, R., *et al.*, 2005a. Instationäres 3D Thermo-mechanisches Modell für Beton. *Beton-und Stahlbetonbau*, 100(1), pp.39–51.

Ožbolt, J. & Reinhardt, H.-W., 2005b. Rate dependent fracture of notched plain concrete beams. *CONCREEP 7*, pp.57–62.

Ožbolt, J., Rah, K.K. & Meštrovic, D., 2006. Influence of loading rate on concrete cone failure. *International Journal of Fracture*, 139(2), pp.239–252.

Ožbolt, J., Periškic, G., Reinhardt, H.-W., *et al.*, 2008. Numerical analysis of spalling of concrete cover at high temperature. *Computers and Concrete*, 5(4), pp.279–293.

Ožbolt, J., Sharma, A. & Reinhardt, H.-W., 2011a. Dynamic fracture of concrete-compact tension specimen. *International Journal of Solids and Structures*, 48(10), pp.1534–1543.

Ožbolt, J. & Sharma, A., 2011b. Numerical simulation of reinforced concrete beams with different shear reinforcements under dynamic impact loads. *International Journal of Impact Engineering*, 38(12), pp.940–950.

Ožbolt, J. & Sharma, A., 2012. Numerical simulation of dynamic fracture of concrete through uniaxial tension and L-specimen. *Engineering Fracture Mechanics*, 85, pp.88–102.

Ožbolt, J., Bošnjak, J., Periškic, G., *et al.*, 2013a. 3D numerical analysis of reinforced concrete beams exposed to elevated temperature. *Engineering Structures*.

Ožbolt, J., Bošnjak, J. & Sola, E., 2013b. Dynamic Fracture of Concrete Compact Tension Specimen: Experimental and Numerical Study. *International Journal of Solids and Structures*.

Ožbolt, J., Sharma, A., İrhan, B. & Sola, E., 2014. Tensile Behavior of Concrete under High Loading Rates. *International Journal of Impact Engineering*, 69, pp.55–68.

Pandolfi, A. & Ortiz, M., 1998. Solid modeling aspects of three-dimensional fragmentation. *Engineering with Computers*, 14(4), pp.287–308.

Pandolfi, A. & Ortiz, M., 2002. An efficient adaptive procedure for three-dimensional fragmentation simulations. *Engineering with Computers*, 18(2), pp.148–159.

Pantuso, D., 1997. *A finite element procedure for the analysis of thermo-mechanical solids in contact*, MIT Department of Mechanical Engineering.

Pantuso, D., Bathe, K.-J. & Bouzinov, P.A., 2000. A finite element procedure for the analysis of thermo-mechanical solids in contact. *Computers and Structures*, 75(6), pp.551–573.

Pedersen, R.R., Simone, A. & Sluys, L.J., 2006. Continuous-discontinuous modelling of dynamic failure of concrete using a viscoelastic viscoplastic damage model. In *III European Conference on Computational Mechanics* . pp. 370–370.

Pedersen, R.R., 2010. *Computational modelling of dynamic failure of cementitious materials*, Delft University of Technology.

Periškic, G., 2009. *Entwicklung eines 3D thermo-hygro-mechanischen Modells für Beton unter Brandbeanspruchung und Anwendung auf Befestigungen unter Zuglasten*, Institut für Werkstoffe im Bauwesen der Universität Stuttgart.

Peroni, M., Solomos, G., Pizzinato, V., *et al.*, 2011. Experimental investigation of high strain-rate behaviour of glass. *Applied Mechanics and Materials*, 82, pp.63–68.

Petrangeli, M. & Ožbolt, J., 1996. Smeared crack approaches-material modeling. *Journal of Engineering Mechanics*, 122(6), pp.545–554.

Pijaudier-Cabot, G. & Bažant, Z.P., 1987. Nonlocal damage theory. *Journal of Engineering Mechanics*, 113(10), pp.1512–1533.

Pijaudier-Cabot, G. & Mazars, J., 2001. Damage models for concrete. *Handbook of Materials Behavior Models*, 2, pp.500–512.

Pivonka, P., Ožbolt, J., Lackner, R., *et al.*, 2004. Comparative studies of 3D-constitutive models for concrete: application to mixed-mode fracture. *International Journal for Numerical Methods in Engineering*, 60(2), pp.549–570.

Rabczuk, T. & Belytschko, T., 2004. Cracking particles: a simplified meshfree method for arbitrary evolving cracks. *International Journal for Numerical Methods in Engineering*, 61(13), pp.2316–2343.

Rashid, Y., 1968. Ultimate strength analysis of prestressed concrete pressure vessels. *Nuclear Engineering and Design*, 7(4), pp.334–344.

Reinhardt, H.-W., Körmeling, H. & Zielinski, A.J., 1986. The split Hopkinson bar, a versatile tool for the impact testing of concrete. *Materials and Structures*, 19(1), pp.55–63.

Reinhardt, H.-W. & Weerheijm, J., 1991. Tensile fracture of concrete at high loading rates taking account of inertia and crack velocity effects. *International Journal of Fracture*, 51(1), pp.31–42.

Rieger, A. & Wriggers, P., 2004. Adaptive methods for thermomechanical coupled contact problems. *International Journal for Numerical Methods in Engineering*, 59(6), pp.871–894.

Ross, C., 1988. Split-Hopkinson pressure bar tests ESL-TR-88-82, HQ AF Engineering and Services Center, Tyndall AFB, FL.

Rots, J.G., Nauta, P., Kuster, G., *et al.*, 1985. Smeared crack approach and fracture localization in concrete, *HERON*, 30(1).

Rots, J.G., 1988. *Computational modeling of concrete fracture*, Delft University of Technology.

Rots, J.G., 1992. Removal of finite elements in strain-softening analysis of tensile fracture. *Proceedings FraMCoS I (ed. ZP Bazant), Elsevier Publishers, London/New York*, pp.330–338.

Ruiz, G., Ortiz, M. & Pandolfi, A., 2000. Three-dimensional finite-element simulation of the dynamic Brazilian tests on concrete cylinders. *International Journal for Numerical Methods in Engineering*, 48(7), pp.963–994.

Ruiz, G., Pandolfi, A. & Ortiz, M., 2001. Three-dimensional cohesive modeling of dynamic mixed-mode fracture. *International Journal for Numerical Methods in Engineering*, 52(1-2), pp.97–120.

Schneider, U., 1982. *Properties of materials at high temperatures, concrete*, 2nd ed. RILEM technical committee 44-PHT. Kassel: University of Kassel.

Schuler, H., Mayrhofer, C. & Thoma, K., 2006. Spall experiments for the measurement of the tensile strength and fracture energy of concrete at high strain rates. *International Journal of Impact Engineering*, 32(10), pp.1635–1650.

Schwer, L.E. & Day, J., 1991. Computational techniques for penetration of concrete and steel targets by oblique impact of deformable projectiles. *Nuclear Engineering and Design*, 125(2), pp.215–238.

Simo, J.C. & Rifai, M., 1990. A class of mixed assumed strain methods and the method of incompatible modes. *International Journal for Numerical Methods in Engineering*, 29(8), pp.1595–1638.

Simo, J.C., Oliver, J. & Armero, F., 1993. An analysis of strong discontinuities induced by strain-softening in rate-independent inelastic solids. *Computational Mechanics*, 12(5), pp.277–296.

Simo, J.C. & Hughes, T.J., 1998. *Computational inelasticity*, Springer.

Stabler, J., 2000. *Computational modelling of thermomechanical damage and plasticity in concrete*, University of Queensland.

Stroeven, P., 1973. *Some aspects of the micromechanics of concrete*, Stevin Laboratory, Technological University of Delft.

Taylor, G.I., 1938. Plastic strain in metals. *Journal of the Institute of Metals*, 62, pp.307–324.

Taylor, L.M. & Flanagan, D.P., 1989. PRONTO 3D: A three-dimensional transient solid dynamics program.

Travaš, V., Ožbolt, J. & Kožar, I., 2009. Failure of plain concrete beam at impact load: 3D finite element analysis. *International Journal of Fracture*, 160(1), pp.31–41.

Tu, Z. & Lu, Y., 2010. Modifications of RHT material model for improved numerical simulation of dynamic response of concrete. *International Journal of Impact Engineering*, 37(10), pp.1072–1082.

Vegt, I.W.J. & Breugel, K., 2009. The rate dependency of concrete under tensile impact loading - fracture energy and fracture characteristics. In *Proceedings of 13th ISIEMS*.

Wall, W.A., 1999. *Fluid-Struktur-Interaktion mit stabilisierten Finiten Elementen*, Institut für Baustatik und Baudynamik (Bauwesen) der Universität Stuttgart.

Weerheijm, J., 1992. *Concrete under impact tensile loading and lateral compression*, TU Delft, the Netherlands.

Weerheijm, J. & Van Doormaal, J., 2007. Tensile failure of concrete at high loading rates: New test data on strength and fracture energy from instrumented spalling tests. *International Journal of Impact Engineering*, 34(3), pp.609–626.

Wells, G. & Sluys, L., 2000. Three-dimensional embedded discontinuity model for brittle fracture. *International Journal of Solids and Structures*, 38(5), pp.897–913.

Wells, G. & Sluys, L., 2001. A new method for modelling cohesive cracks using finite elements. *International Journal for Numerical Methods in Engineering*, 50(12), pp.2667–2682.

Whirley, R.G. & Engelmann, B.E., 1993. DYNA3D: A nonlinear, explicit, three-dimensional finite element code for solid and structural mechanics, User manual. Revision 1.

Wriggers, P. & Miehe, C., 1994. Contact constraints within coupled thermomechanical analysis a finite element model. *Computer Methods in Applied Mechanics and Engineering*, 113(3), pp.301–319.

Wriggers, P., 2006. *Computational contact mechanics*, Springer.

Xu, X.-P. & Needleman, A., 1994. Numerical simulations of fast crack growth in brittle solids. *Journal of the Mechanics and Physics of Solids*, 42(9), pp.1397–1434.

Zavarise, G., Wriggers, P., Stein, E., *et al.*, 1992. Real contact mechanisms and finite element formulation a coupled thermomechanical approach. *International Journal for Numerical Methods in Engineering*, 35(4), pp.767–785.

Zavarise, G., Wriggers, P. & Schrefler, B., 1995. On augmented Lagrangian algorithms for thermomechanical contact problems with friction. *International Journal for Numerical Methods in Engineering*, 38(17), pp.2929–2949.

Zavarise, G., Bacchetto, A. & Gänser, H., 2005. Frictional heating in contact mechanics A methodology to deal with high temperature gradients. *Computational Mechanics*, 35(6), pp.418–429.

Zhang, X., Ruiz, G., Yu, R., *et al.*, 2009. Fracture behaviour of high-strength concrete at a wide range of loading rates. *International Journal of Impact Engineering*, 36(10), pp.1204–1209.

Zhang, B. & Bicanic, N., 2002. Residual Fracture Toughness of Normal-and High-Strength Gravel Concrete after Heating to 600 °C. *ACI Materials Journal*, 99(3), pp.217-226.

Zienkiewicz, O.C. & Taylor, R.L., 2005. *The finite element method for solid and structural mechanics*, Butterworth-Heinemann.

Curriculum Vitae

Personal Data

Name:	Barış İrhan
Date of Birth:	April 10, 1977
Place of Birth:	Ankara, Turkey
Parents:	Cemil İrhan and Rabiye İrhan
Marital status:	Married
Nationality:	Turkish

Education

1983-1988	Yalçın Eskiyapan Primary School, Ankara, Turkey
1988-1991	Yahya Kemal Beyatlı Secondary School, Ankara
1991-1994	Ankara Yüce Science High School, Ankara
1994-1999	B.S., Civil Engineering Middle East Technical University
1999-2002	M.S., Civil Engineering Middle East Technical University
2001-2003	M.Sc., Computational Mechanics of Materials and Structures (COMMAS) University of Stuttgart
2011-2014	Ph.D., Institute of Construction Materials University of Stuttgart

Experience

2000-2001	Graduate Teaching Assistant, Structural Mechanics Laboratory Middle East Technical University
2003-2004	Graduate Research Assistant at the Institute for Computational Mechanics Technical University of Munich
2005-2006	Graduate Research Assistant at the Institute of Construction Materials University of Stuttgart
2008-present	Software Development Engineer PROYA, Ankara, Turkey